AN ABSTRACT OF THE DISSERTATION OF

Dong-Shan Yang for the degree of Doctor of Philosophy in Civil Engineering presented on March 10, 1999. Title: Deformation-Based Seismic Design Models for Waterfront Structures.

Redacted for Privacy

Abstract approved: _____

Stephen E. Dickenson

Recent experience demonstrates that waterfront structures are vulnerable to earthquake damage. The poor seismic performance of these facilities has been primarily due to liquefaction of backfill and/or foundation soils and the lack of seismic design standards for waterfront structures. The seismic performance of waterfront structures is a key issue in the evaluation of the unimpeded operations of the port system and affiliated facilities following earthquakes. The widespread economic consequences of earthquake-induced damage to waterfront structures and required serviceability of port components after earthquakes highlight the need for improved performance-based design methods.

The weak foundation soils and high water tables that are common at ports result in a high vulnerability to seismically-induced ground failures and corresponding damage to adjacent structures. Liquefaction of backfill and foundation soils next to waterfront structures contributes to an increase in active lateral earth pressures against walls, loss of stability of rock dike, excessive ground settlements, and lateral soil movements. Current pseudostatic methods are not well suited to account for the

influence of excess pore pressure generation as well as amplification of acceleration. In order to limit earthquake-induced deformations of waterfront structures, various ground treatment strategies have been used to mitigate liquefaction hazards at numerous ports. However, very few guidelines exist for specifying the extent of remedial soil treatment required to insure the serviceability of the waterfront components after a design-level earthquake.

This research has investigated the seismic response of waterfront structures, specifically concrete caissons and pile-supported wharves, during past earthquakes. A numerical model was validated by comparing the computed response to field performance. A series of parametric studies were conducted for waterfront structures in improved soils. The effectiveness of soil improvement in controlling permanent seismically-induced deformations of the waterfront structures is evaluated as functions of wall geometry, the density of backfill soils, the stiffness of piles, the extent of the improved soil, and the characteristics of the strong ground motions. The results were synthesized into simplified, practice-oriented design charts for deformation-based analysis, and preliminary guidelines for estimating the extent of ground treatment that is required given allowable deformation limits for the caissons and pile-supported systems.

Deformation-Based Seismic Design Models for Waterfront Structures

by

Dong-Shan Yang

A DISSERTATION

submitted to

Oregon State University

in partial fulfillment of
the requirements for the
degree of

Doctor of Philosophy

Presented March 10, 1999
Commencement June 1999

Doctor of Philosophy dissertation of Dong-Shan Yang presented on March 10, 1999

APPROVED:

Redacted for Privacy

Major Professor, representing Civil Engineering

Redacted for Privacy

Chair of Department of Civil, Construction, and Environmental Engineering

Redacted for Privacy

Dean of Graduate School

I understand that my dissertation will become part of the permanent collection of Oregon State University libraries. My signature below authorizes release of my dissertation to any reader upon request.

Redacted for privacy

Dong-Shan Yang, Author

ACKNOWLEDGEMENT

The author would like to express his sincere thanks to his advisor, Professor Stephen E. Dickenson, for his assistance, guidance, and invaluable suggestions throughout this research.

The research was funded by a grant from National Science Development Foundation, Taiwan. Their supports are gratefully acknowledged.

Lastly, the author wishes to express his deepest appreciation to his wife, Yu, and his sons, Joe and Jackie, for their support, understanding, and endless encouragement throughout this research.

TABLE OF CONTENTS

TABLE OF CONTENTS (CONTINUED)

TABLE OF CONTENTS (CONTINUED)

TABLE OF CONTENTS (CONTINUED)

Page

LIST OF FIGURES

LIST OF FIGURES (CONTINUED)

LIST OF FIGURES (CONTINUED)

LIST OF FIGURES (CONTINUED)

LIST OF FIGURES (CONTINUED)

LIST OF FIGURES (CONTINUED)

LIST OF FIGURES (CONTINUED)

LIST OF TABLES

LIST OF TABLES (CONTINUED)

DEFORMATION-BASED SEISMIC DESIGN MODELS FOR WATERFRONT STRUCTURES

1 INTRODUCTION

1.1 Background

A number of port and harbor facilities throughout the world are located in highly seismic regions, and recent experience demonstrates that waterfront retaining structures are vulnerable to earthquake damage. In several instances waterfront components have been badly damaged despite the occurrence of ground motions of only moderate intensity. The poor seismic performance of these facilities has been due, in large part, to the deleterious foundation and backfill soils that are commonly prevalent in the marine environment and the lack of design standards for many of the waterfront structures that make up the port system. In order to understand the vulnerability of waterfront retaining structures at ports and harbors to earthquake damage and primary modes of failure, it is important to learn the lessons from past case studies. Werner and Hung (1982) have summarized 12 prior earthquakes from which documented damage to port and harbor facilities has been provided. The most significant source of earthquake-induced damage to port and harbor facilities has been porewater pressure buildup in the loose-to-medium dense, saturated cohesionless soils that prevail at marine environment. Liquefaction of backfill and foundation soils next to retaining structures contributes to an increase in active lateral earth pressures against retaining walls, loss of passive soil resistance below the dredge line, and excessive settlements and lateral soil movements. In several cases, for example the

Port of Kobe during the 1995 Hyogoken-Nanbu Earthquake, ground deformations associated with liquefaction-induced failure of caissons have extended as much as 150 m into backland areas damaging waterfront components and suspending port operations (Inagaki, et al., 1996; Werner, 1998).

The waterfront retaining structures consist of rigid (gravity) type walls, such as concrete caissons and block walls, and flexible sheetpile walls and pile-supported systems. They usually represent the critical elements of ports and harbors. These retaining structures play a significantly important role to ensure that transportation system, lifelines, and other relevant facilities of ports and harbors are normally operational during earthquakes. Earthquakes have caused severe damage to port facilities from strong ground shaking, ground deformation, liquefaction, and permanent deformation of waterfront retaining structures, in many historic earthquakes. In some cases, these deformations were negligibly small; whereas in some cases waterfront retaining structures have collapsed, such as substantial lateral and rotational movement of quay walls and sheetpile bulkheads as well as buckling and yielding of pile-supported systems. The damaging effects due to earthquake have been reflected in the loss of function of major ports and have resulted in the regional and even worldwide economic impacts. The performance of ports in the Osaka Bay region during the Hyogoken-Nanbu (Kobe) Earthquake of January 17, 1995 provides pertinent examples of the seismic vulnerability of port facilities. The widespread damage to the Port of Kobe during this earthquake caused $5.5 billion repair cost and $6 billion of indirect losses due to closure of the Kobe Port during only the first year after the earthquake (Werner and Dickenson, 1996).

In view of these physical and economic consequences caused by earthquakes, the design of waterfront retaining structures to mitigate seismic hazards becomes one of the ultimate goals for the earthquake engineers. The main issues arise from how to limit the seismically-induced deformations of critical port components (i.e., gravity quay walls, pile-supported wharf, rock dike) to an acceptable level. It is important to consider how various major causes are evaluated and how they perform in an acceptable level in the seismic design of waterfront retaining structures against earthquakes. The poor seismic performance of port facilities and economic impact of earthquake-induced damage highlight the need for improved performance-based design methods. The performance-based design is the design of port facilities to insure that damage will be limited to negligible levels so that port operations are not impeded during a moderate earthquake, and earthquake-induced damage is controlled to a repairable extent during larger earthquake. The performance-based design methods improve the limitation in the conventional seismic design methods that are based on the force balance against the designed seismic force. Although numerous ports and governmental agencies with facilities in seismically active regions have adopted deformation-based seismic performance requirements for waterfront retaining structures (Ferritto, 1997), however, very few guidelines exist for specifying the performance-based design procedures in current standards-of-practice. In view of the lack of standardized performance-based approach for critical components at ports, the recommendations of Pacific Earthquake Engineering Research Center (PEER) Port Workshop have been proposed as follows.

1. Establish a performance-based approach for evaluating the response of existing port system components to major earthquake scenario.
2. Develop retrofit technologies to improve the performance of port components to earthquake loading.
3. Develop performance-based design criteria for the seismic design of new port system components, suitable for subsequent translation into design guidelines.
4. Develop system-based seismic risk evaluation and management procedures for port systems, which will allow optimization of seismic design and retrofit options for port facilities and minimize economic loss.

1.2 Current Design Philosophy

In light of the economic importance of port facilities, the levels of design earthquake motions are specified as two-level design approach as follows:

- *Level 1*: Operating Level Earthquake (OLE) motion having a 50% probability of exceedance in 50 years, approximately a return period of about 72 years.
- *Level 2*: Contingency Level Earthquake (CLE) motion having 10% probability of exceedance in 50 years, approximately a return period of 475 years.

For port facilities, the waterfront structures are designed to resist these two levels of shaking. Under Level 1 earthquake motion events, current codes are defined as the structure operations are not interrupted and any damage that occurs will be repairable in a short period of time. Expected ground peak accelerations for these events are about 0.25g. Under Level 2 earthquake motion events, the structure

damage is controlled, economically repairable, and is not endangered to life safety. Expected ground peak accelerations for these events are about 0.5g.

The application of these two-level design approaches may not be the same due to the requirement of performance goals at ports. For example, Navy facilities may be defined as essential construction by their mission requirement based on the needs for emergency operability. Level 2 earthquake motion for these essential structures is defined as 10% probability of exceedance in 100 years (Ferritto, 1997). Another example of the application of two-level approach is Port of Oakland after 1989 Loma Prieta Earthquake which defines Level 2 earthquake motion with a probability of exceedance of 20% in 50 years (Erickson et al., 1998). For a specific port, the decision of determination of the probability levels for Level 1 and Level 2 earthquake motions is to be made by the user based on seismic risk evaluation for port systems and relative costs between loss and construction. Housner (1975) suggested that seismic performance requirements for port components should reflect the importance of the component to these system requirements as shown in Table 1-1. Once the performance requirements are established, the performance-based design of port facilities should satisfy the performance requirements in terms of design criteria in order to minimize earthquake-induced deformation of port components against varying levels of earthquake motions. Port components that are difficult to maintain after given earthquake and/or higher importance such as Class A and B in Table 1-1 should be treated.

Table 1-1: Seismic Performance Requirements for Port Components (Housner, 1975)

Class	*Description*	*Seismic Performance Requirements and Design Standards*
A	Components for which collapse or damage might lead to severe consequences in terms of risks to life safety, disruption of port operations, repair or replacement costs, or risks to the environment.	Stringent
B	Components important but not vital to port operations, and whose damage would not pose significant risks to life safety or to the environment, and would not lead to unacceptably large repair or replacement costs.	High
C	Easily repairable components not important to port operations, and whose damage would not pose significant risks to life safety or to the environment.	Moderate

1.3 Current Design Methods

In present research, seismic design considerations are summarized for two major types of port structures – gravity type quay walls and pile-supported systems. The reason to choose these two types of port structures is that gravity type quay wall, such as concrete caissons and concrete block walls, is the simplest type of retaining structure at ports. It is a good start to evaluate the uncertainties, i.e., soil characteristics, generation of excess pore pressures, and ground motion characteristics, involved in the proposed numerical model. Complicate pile-supported systems in the manner of nonlinear soil-pile interaction can be then efficiently established and developed.

1.3.1 Rigid Type Gravity Walls

Gravity type walls are the oldest and simplest type of retaining structures as shown in Figure 1-1. The current standards-of-practice for seismic design of gravity type retaining walls are mainly based on pseudostatic, limit equilibrium, seismic pressure-based mechanics (i.e., Okabe, 1926, Mononobe and Matsuo, 1929, Seed and Whitman, 1970, Ebeling and Morrison, 1993). The seismic loading is modeled with seismic coefficients, which are a function of the maximum accelerations associated with the design earthquakes. Pseudostatic lateral earth pressure forces and the inertia force of wall are most typically the only seismic design forces considered. Quay walls are designed to resist overturning, sliding, and tilting when subjected to seismic forces, although some horizontal wall movement is tolerated. Although hydrodynamic pressures acting on the wall can be incorporated in the design, the excess pore pressures generated in loose-to-medium dense saturated sandy backfill soils are only approximately accounted for, or generally ignored. For example, the seismic design of waterfront retaining structures in Japan and at many ports of United States has not accounted for the effects of pore pressure buildup in the adjacent soils. These excess pore pressures have resulted in liquefaction in the adjacent backfills and the underlying soils and hence have increased lateral forces on the retaining structures. Common design methods either treat potentially liquefiable soils as heavy fluids (i.e., zero shear strength and fluid unit weight equal to the saturated unit weight of the soil) or post-liquefaction residual shear strengths are used in undrained stability analyses. In either case, limit equilibrium methods are used to obtain factors of safety against potential failure modes such as sliding, overturning, bearing capacity and deep-seated

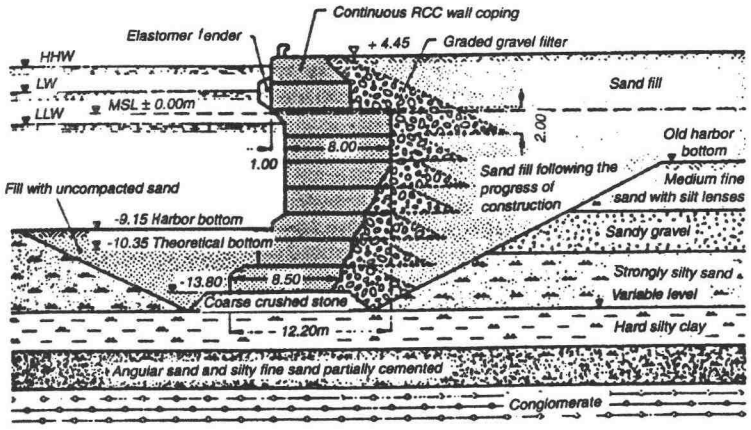

(a) Concrete block type (EAU, 1990)

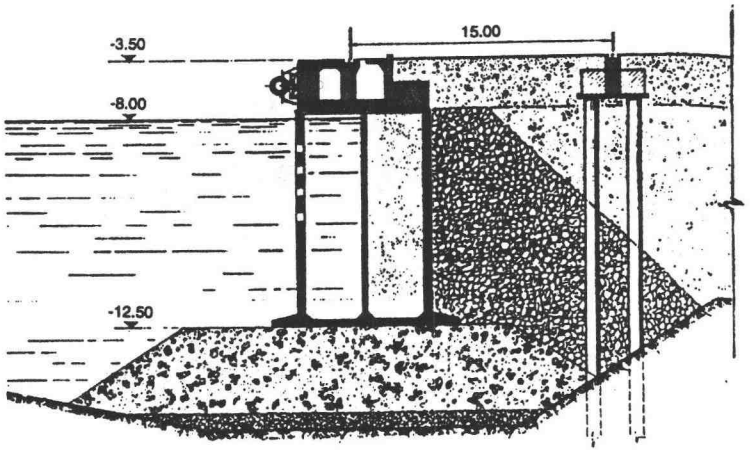

(b) Concrete caisson type (Contri, et al., 1986)

Figure 1-1: Gravity type retaining structures

foundation failures. The resulting factors of safety are only approximately correlated to the permanent deformations that may be realized during the design level earthquake.

Enhancements to the standard pseudostatic methods of analysis have been made by numerous investigators (Richards and Elms, 1979, Whitman and Liao, 1985). These methods incorporate a permanent displacement-based approach and they represent improved methods for the seismic design of gravity retaining walls in non-liquefiable soils. These rigid-body, "sliding block" type displacement analyses are not, however, well suited to account for the influence of excess pore pressure development in the foundation and backfill soils. In order to address this deficiency limit equilibrium-based methods for predicting seismic displacements of slopes and retaining walls with liquefiable soils have also been developed (Byrne, et al., 1994).

1.3.2 Pile-Supported Wharves in Sloping Dikes

In the design of flexible type waterfront retaining wall systems, piles are typically used as foundation elements for waterfront components as well as cargo-handling and infrastructure components at ports. Both batter piles and vertical piles are commonly used at ports. Figure 1-2 shows typical cross section of pile-supported wharf and surrounding soils at Port of Oakland.

In pseudostatic, limit equilibrium analysis methods the soil deformation is determined using rigid-body, sliding block, Newmark's analysis (1965) in which the soil on the potential failure surface is assumed to be rigid-perfectly plastic material. If the inertia forces acting on a potential failure mass become large enough that the total driving forces exceed the available resisting forces, the factor of safety against sliding for a specified block of soil will drop below 1.0. Newmark used this analogy to

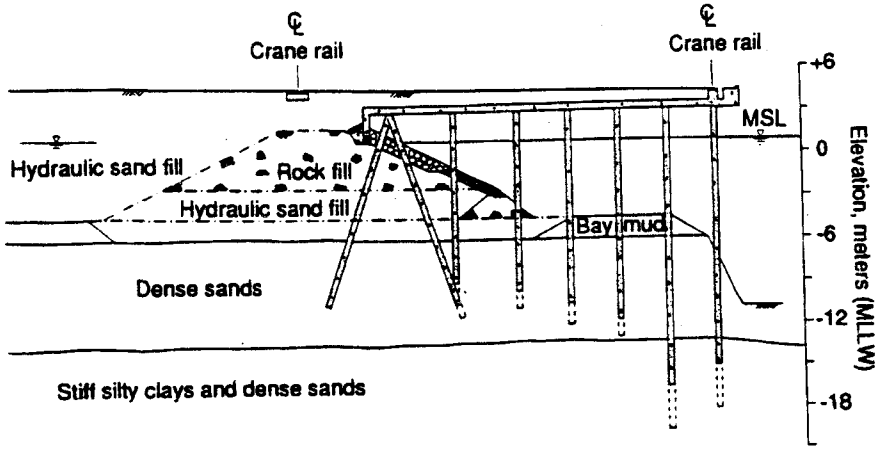

Figure 1-2: Typical cross section of pile-supported wharf at Port of Oakland

develop a method for prediction of the permanent displacement of a slope subjected to any motion. When the ground motion acceleration exceeds the yield acceleration, defined as minimum pseudostatic acceleration required to produce instability of the soil block (factor of safety = 1), the soil block begins to move downwards. The displacement of soil block is then determined by double integrating the area of the earthquake acceleration time history that exceeds the yield acceleration. However, when the pile-supported structures are embedded in sloping dikes, Newmark's analysis becomes very complicated. Enhancement to pseudostatic analysis methods has been established by using numerical models including uncoupled model and coupled model. In uncoupled model, slope deformations and the response of structural components are computed separately. The slope deformations are first determined by Newmark's approach and these soil deformations are then used as input information in numerical models. In coupled model the slope displacements and structural

elements are determined simultaneously. This coupled type model usually requires using two-dimensional numerical modeling techniques.

Soil-pile interaction is considered to be a complex phenomenon and has been largely simplified in dynamic analysis and design. The seismic design of pile foundation can be, in general, categorized as four groups: (1) empirical methods; (2) pressure-based methods; (3) displacement-based methods; and (4) numerical methods. The difficulty mainly arises from the complexity of the stress-strain relationships of the soil, particularly when pore pressure rise and liquefaction occurs. In general, the dynamic analysis of soil-pile interaction is actually a three-dimensional problem. The model should consider not only both transverse and longitudinal motions, but should include vertical, rocking and torsional motions. Thus, the models that consider all of the motions become theoretical practice. A number of simplified analytical and numerical models which incorporate various levels of complexity associated with soil, soil-pile interface, and superstructure under static and dynamic loading have been developed (Matlock and Reese, 1960; Reese and Cox, 1975; Meyersohn, et al., 1992; Finn, et al., 1994; Stewart, et al., 1994; Martin and Lam, 1995; Chen and Poulos, 1997). The numerical model is considered as the most efficient and well-suited method for analyzing problems of complicated geometry, such as piles in layer soils and sloping ground, which is not easily handled with analytical or semi-analytical formulations. At present, treating the pile as a beam or column supported on a Winkler-type foundation, i.e., by a series of independent horizontal or vertical springs (p-y curve approach, p = soil resistance, y = pile deflection) distributed along pile's length, has been a worldwide used model for estimating pile-head deflection, bending

moment, and settlement. Enhancement of this model has been to make the Winkler springs nonlinear and then solve for the pile deflections using a finite difference or finite element discretization under either static or dynamic loading. These springs represent the action of the soil-pile foundation when the structure is displaced due to various applied forces, i.e., lateral, vertical, and moment forces.

As a result of soil liquefaction, the pile head acceleration would be amplified or attenuated and pile head displacement as well as the pile bending moment would be greatly increased in most cases. These tendencies are more pronounced when liquefaction-induced soil movements are triggered during earthquake. Hence, the response of piles to these horizontal free-field soil displacements becomes an important issue for the analysis and design of the pile-supported structures. These free-field displacements caused by earthquake are movements of the soil that occur at a distance from the piles such that they are not affected by the presence of the piles or if the piles are not present. The effects of earthquake-induced free-field soil movements can be taken into consideration in soil-pile interaction model by either reducing the stiffness of the liquefied soil or using undrained residual shear strength.

1.4 Ground Treatment for Mitigating Liquefaction Hazards

Soil improvement techniques have been used to mitigate liquefaction hazards to waterfront retaining walls at numerous ports throughout the world (Iai et al., 1994b). All other factors being equal, the effectiveness of the soil improvement is a function of the level of densification and the volume of soil that is treated. Although few case histories exist for the performance of improved soils subjected to design-

level earthquake motions, experience has shown that caissons in improved soils have performed much more favorably than have adjacent caissons at unimproved sites which experienced widespread damage (Iai et al., 1994b). In general, soil improvement methods mitigate liquefaction hazards by increasing the shear strength (and relative density) of potentially liquefiable soils, and decreasing the excess pore pressures generated during earthquakes. The effectiveness and economy of any method, or combination of methods, will depend on geologic and hydrologic factors as well as site factors. Detailed descriptions of these strategies can be found in the reports of Ferritto (1997) and Werner (1998). An overview of the available liquefaction remediation measures is provided in Table 1-2.

The Japan Port and Harbour Research Institute (PHRI, 1997) has produced one of the few design guidelines that exist for specifying the extent of soil improvement adjacent to waterfront retaining structures. In the PHRI approach, the recommended extent of ground treatment is shown in Figure 1-3. The stability of the caisson is evaluated using standard limit equilibrium methods in which a dynamic pressure and a static pressure corresponding to an earth pressure coefficient K=1.0 are applied along plane CD due to liquefaction of the unimproved soil. These guidelines for establishing the soil improvement area and evaluating caisson stability are valuable design tools, however, they do not address the seismically-induced deformation of the caisson and backfill soils.

Current design guidelines of soil improvement for pile-supported systems are not well developed. The use of soil improvement techniques has been primarily based on port authority standards.

Table 1-2: Liquefaction Remediation Measures (Ferritto, 1997)

Method	Principle	Most Suitable Soil Conditions or Types	Maximum Effective Treatment Depth	Relative Costs
1) Vibratory Probe a) Terraprobe b) Vibrorods c) Vibrowing	Densification by vibration; liquefaction-induced settlement and settlement in dry soil under overburden to produce a higher density.	Saturated or dry clean sand; sand.	20 m routinely (ineffective above 3-4 m depth); > 30 m sometimes; vibrowing, 40 m.	Moderate
2) Vibrocompaction a) Vibrofloat b) Vibro-Composer system.	Densification by vibration and compaction of backfill material of sand or gravel.	Cohesionless soils with less than 20% fines.	> 20 m	Low to moderate
3) Compaction Piles	Densification by displacement of pile volume and by vibration during driving, increase in lateral effective earth pressure.	Loose sandy soil; partly saturated clayey soil; loess.	> 20 m	Moderate to high
4) Heavy tamping (dynamic compaction)	Repeated application of high-intensity impacts at surface.	Cohesionless soils best, other types can also be improved.	30 m (possibly deeper)	Low
5) Displacement (compaction grout)	Highly viscous grout acts as radial hydraulic jack when pumped in under high pressure.	All soils.	Unlimited	Low to moderate
6) Surcharge/buttress	The weight of a surcharge/buttress increases the liquefaction resistance by increasing the effective confining pressures in the foundation.	Can be placed on any soil surface.	Dependent on size of surcharge/buttress	Moderate if vertical drains are used
7) Drains a) Gravel b) Sand c) Wick d) Wells (for permanent dewatering)	Relief of excess pore water pressure to prevent liquefaction. (Wick drains have comparable permeability to sand drains). Primarily gravel drains; sand/wick may supplement gravel drain or relieve existing excess pore water pressure. Permanent dewatering with pumps.	Sand, silt, clay.	Gravel and sand > 30 m; depth limited by vibratory equipment; wick, > 45 m	Moderate to high
8) Particulate grouting	Penetration grouting-fill soil pores with soil, cement, and/or clay.	Medium to coarse sand and gravel.	Unlimited	Lowest of grout methods
9) Chemical grouting	Solutions of two or more chemicals react in soil pores to form a gel or a solid precipitate.	Medium silts and coarser.	Unlimited	High
10) Pressure injected lime	Penetration grouting-fill soil pores with lime	Medium to coarse sand and gravel.	Unlimited	Low

Table 1-2 (Continued): Liquefaction Remediation Measures (Ferritto, 1997)

Method	Principle	Most Suitable Soil Conditions or Types	Maximum Effective Treatment Depth	Relative Costs
11) Electrokinetic injection	Stabilizing chemical moved into and fills soil pores by electro-osmosis or colloids in to pores by electrphoresis.	Saturated sands, silts, silty clays.	Unknown	Expensive
12) Jet grouting	High-speed jets at depth excavate, inject, and mix a stabilizer with soil to form columns or panels.	Sands, silts, clays.	Unknown	High
13) Mix-in-place piles and walls	Lime, cement or asphalt introduced through rotating auger or special in-place mixer.	Sand, silts, clays, all soft or loose inorganic soils.	> 20 m (60 m obtained in Japan)	High
14) Vibro-replacement stone and sand columns a) Grouted b) Not grouted	Hole jetted into fine-grained soil and backfilled with densely compacted gravel or sand hole formed in cohesionless soils by vibro techniques and compaction of backfilled gravel or sand. For grouted columns, voids filled with a grout.	Sands, silts, clays.	> 30 m (limited by vibratory equipment)	Moderate
15) Root piles, soil nailing	Small-diameter inclusions used to carry tension, shear, compression.	All soils.	Unknown	Moderate to high
16) Blasting	Shock waves an vibrations cause limited liquefaction, displacement, remolding, and settlement to higher density.	Saturated, clean sand; partly saturated sands and silts after flooding.	> 40 m	Low

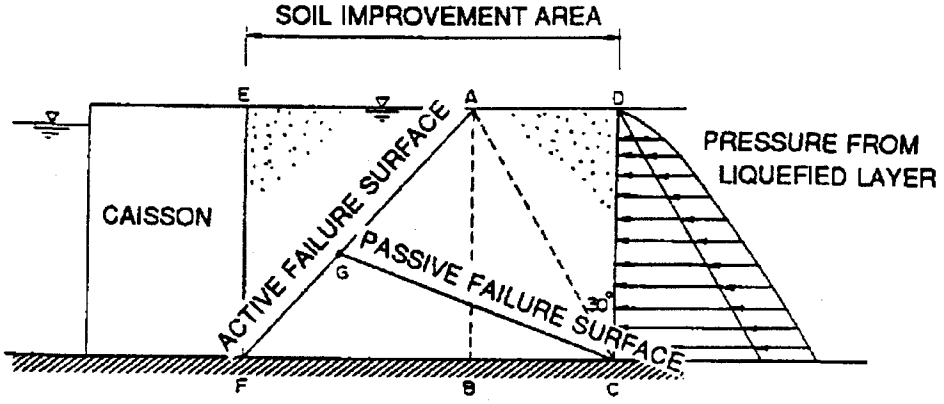

Figure 1-3: Schematic diagram for investigation of stability with respect to pressures applied from the liquefied sand layer (PHRI, 1997)

1.5 Objectives and Scope of Work

In view of the consequences of the earthquake-induced damage to waterfront retaining walls, this research has investigated the seismic response of port and harbor facilities in unimproved and in improved soils during past earthquakes. The major issues of this research can be categorized as three primary groups: (1) the seismic response of waterfront retaining walls and pile-supported wharves from case histories by recent earthquakes; (2) evaluating the effectiveness of soil improvement methods which limit earthquake-induced deformations of waterfront retaining walls to acceptable levels; (3) the development of improved seismic design procedures for various waterfront retaining walls.

1.5.1 Objectives

The objectives of this research have been concluded as follows:

1. Extensive review of case studies to investigate seismic performance of port and harbor facilities during earthquakes;
2. Extensive literature review to evaluate current standards-of-practice seismic design methods for waterfront structures;
3. Validate and calibrate a numerical dynamic nonlinear effective stress model for analyzing seismic soil-structure interaction (SSI) of waterfront structures;
4. Apply the numerical model to generalized waterfront configurations with sensitivity studies of key geotechnical and structural parameters (i.e., the density

of backfill soils, wall geometry, pile stiffness, characteristics of ground motions, the extent of the improved soil);

5. Model the application of soil improvement for reducing the permanent deformations of waterfront structures;
6. Develop straightforward, practice-oriented design charts and guidelines for the analysis and design of waterfront structures.

1.5.2 Scope of Work

1.5.2.1 Validate Numerical Model and Apply for Gravity Walls

This task is to validate and calibrate proposed numerical model to known seismic performance of gravity type waterfront retaining walls by case histories. Five well-documented case histories for the seismic performance of gravity type retaining walls are first chosen and reviewed. The causes and failure modes of these retaining structures subjected to earthquake damage are identified. The important design variables associated with the properties and responses of retaining structures and surrounding soils, which will be used and evaluated in parametric studies, are determined. Once the model is validated and calibrated by case studies, a series of parametric studies associated with soil density, wall geometry, and ground motion characteristics are then conducted. The results of the parametric study are presented in the form of simplified design charts for performance-based analysis of concrete caisson, as well as preliminary guidelines for estimating the extent of ground treatment that is required given allowable deformation limits for the quay wall.

1.5.2.2 Validate Numerical Model for Piles in Competent and Liquefiable Soils

This task is to validate the performance of single pile under static lateral loading in level ground and in sloping ground, and dynamic loading for pile in liquefiable soils. The representative parameters and model considerations for soil-pile interaction analysis in the proposed numerical model are evaluated and established. These design-related parameters will be applied for the parametric studies.

1.5.2.3 Validate and Apply Model for Pile-Supported Wharves

This task is to validate the applicability of proposed numerical model to earthquake damage by case study. Once the model is validated and calibrated using case history, a series of parametric studies are then conducted. The results are synthesized into design charts for deformation-based analysis of pile-supported system in unimproved and in improved soils, and simplified guidelines for estimating the extent of ground treatment that is required given allowable deformation limits for the pile-supported wharf is proposed.

1.6 Report Organization

This report is divided into eight chapters. The remainder of this report includes the following chapters: Chapter 2 contains the outlines of current seismic design methods related to gravity type retaining walls; Chapter 3 contains the outlines of considerations of advanced numerical modeling; Chapter 4 contains the performance of gravity type waterfront retaining structures during past earthquakes (case study);

Chapter 5 contains parametric study for gravity type retaining walls; Chapter 6 contains the seismic behavior of pile-supported wharves (case study); Chapter 7 contains parametric study of pile-supported wharves in sloping rockfill. Chapter 8 contains summary and conclusion and recommendations for future work.

2 CURRENT METHODS OF SEISMIC ANALYSIS AND DESIGN FOR GRAVITY WALLS - PSEUDOSTATIC METHODS

2.1 Introduction

A number of different approaches to waterfront retaining structures, such as gravity walls, anchored bulkheads, bridge abutments, tieback walls, and pile supported wharf, have been developed and used at ports and harbors for past several decades. Numerous standards-of-practice for seismic design of waterfront retaining structures can be found in the literature (Werner and Hung, 1982; Ebeling and Morrison, 1993; PHRI, 1997; Werner, 1998).

Gravity type walls are the oldest and simplest type of retaining structures. They are the walls that rely on their weight to resist the forces exerted by the soil they retain. There are three major classes of gravity type quay walls that exist at ports, namely (1) cast-in-place concrete block type; (2) precast concrete block type; and (3) concrete caisson type. The cast-in-place block type walls are placed where soil conditions are firm and where construction under reasonably dry conditions can be carried out. Precast block type walls can be placed on firm or soft soil conditions and they involve relatively simple construction techniques that are not hindered by the presence of shallow seawater or ground water. Caisson type walls are typically constructed where water is deep. Caisson "boxes" filled with granular material (i.e., soil, or concrete construction debris) are built onshore, transported to the waterfront, and sunk into position. The caissons are usually placed on a prepared foundation pad of granular fill and backfilled with sand and rubble. Block type walls, either cast-in-

place or precast type, are more susceptible to seismic effects than are caisson type walls due to earthquake-induced sliding between layer of blocks.

Under static conditions, retaining walls are acted upon by body forces related to the mass of the wall, by soil pressures, and by external forces. A properly designed retaining wall will achieve equilibrium of these forces without inducing shear stresses that approach the shear strength of the soil, i.e., factor of safety ~ 1.5 against sliding and ~ 3 against bearing failure. However, during an earthquake, inertial forces and changes in soil strength (partially due to soil liquefaction) may violate equilibrium and cause permanent deformation of the wall. Gravity walls usually fail by rigid-body mechanisms, such as sliding, overturning, or deep-seated (global) instability. These failure mechanisms are shown in Figure 2-1.

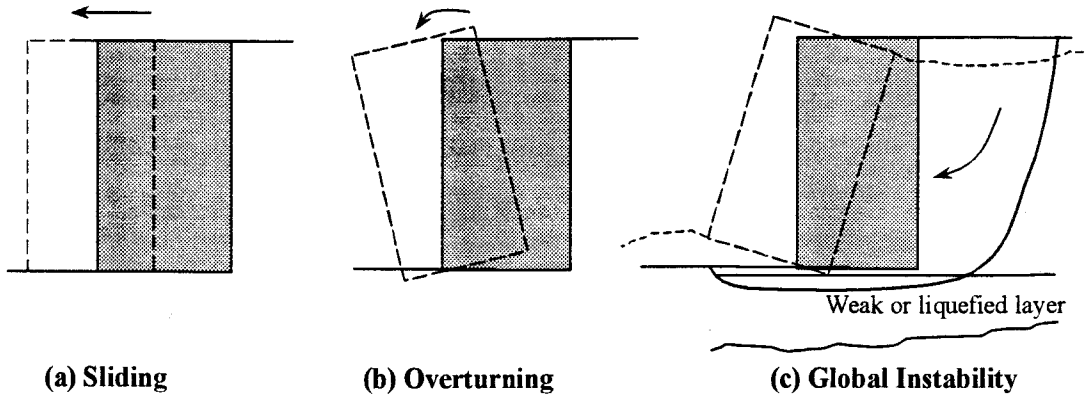

Figure 2-1: Typical failure mechanisms for gravity type retaining walls

The sliding mode of failure occurs when the lateral pressures on the back of the wall produce a thrust that exceeds the available sliding resistance on the base of the wall. The overturning mode of failure occurs when moment equilibrium is not

satisfied. Deep-seated (global) instability mode of failure occurs when the soils behind and/or beneath the walls are weak, which may cause slope instability or bearing capacity failure of the soils. In view of these failure mechanisms, the seismic design of gravity type walls should consider lateral earth pressure, inertial forces, dynamic water pressures, and additional lateral forces due to liquefied soil behind the wall. The seismic design of retaining walls has involved estimating the forces acting upon the wall during earthquake shaking and then ensuring that the wall can resist external forces. Because the actual forces imposed upon the walls during an earthquake are much more complicated, seismic forces on retaining walls are usually estimated using simplified pseudostatic procedures (Ebeling and Morrison, 1993). These methods commonly use rigid-body, limit equilibrium methods of analysis. Pseudostatic seismic coefficients (k_h *and* k_v) are determined as a fraction of the maximum peak accelerations generated by the design earthquake motions. The dynamic earth pressures are then calculated by adding these inertia effects to the wall. The seismic coefficients are commonly estimated as one-third to one-half of the peak horizontal ground surface acceleration. For example, retaining structure design in Japanese practice, the horizontal seismic coefficients, k_h, are determined by the following relationship (Noda et al., 1975):

$$k_h = (a/g) \qquad \text{for a} \leq 0.2\ \text{g}$$

$$k_h = 1/3\ (a/g)^{1/3} \qquad \text{for a} > 0.2\ \text{g}$$

where a is the peak horizontal ground surface acceleration and g is the gravity acceleration. The figure developed by Noda et al. (1975), as shown in Figure 2-2, has

been updated by Nozu et al. (1997a), and is shown in Figure 2-3 in which it includes a more recent assessment of the seismic performance of retaining structures.

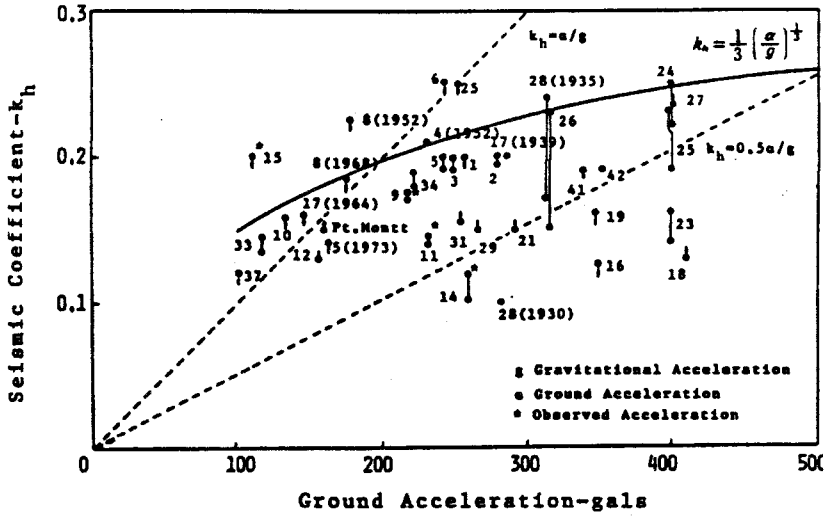

Figure 2-2: Relation between seismic coefficient and ground acceleration (Noda et al., 1975)

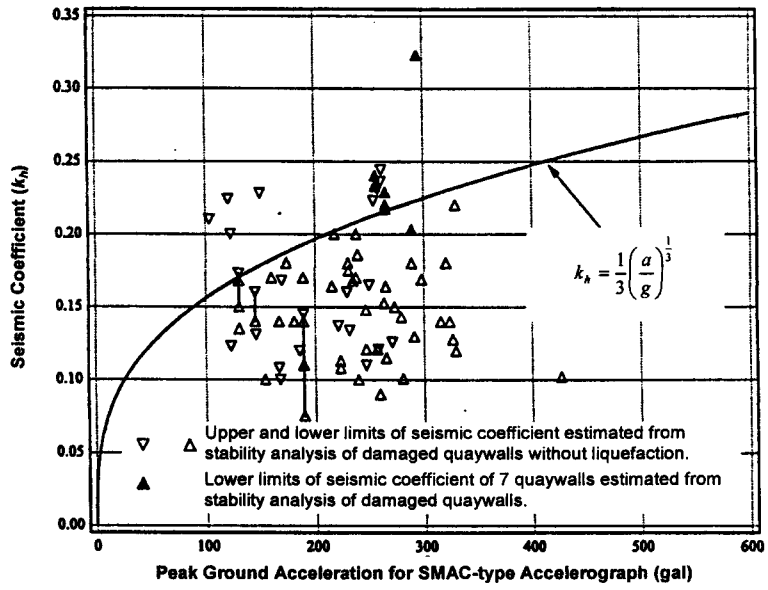

Figure 2-3: Coefficient estimated from damaged quaywall (after Nozu et al., 1997a)

In the following sections two different design approaches, i.e., *seismic pressure-based approach* and *permanent displacement-based approach*, will be presented. Due to simplicity and wide applicability, only Mononobe-Okabe method for seismic pressure-based approach will be introduced and outlined herein.

2.2 Seismic Pressure-Based Approach (Mononobe-Okabe Method)

The Mononobe-Okabe analysis for dynamic lateral pressures is a straightforward extension of the Coulomb sliding wedge theory in which earthquake effects are taken into account by the addition of horizontal and vertical inertia pseudostatic accelerations to a Coulomb active wedge. Due to the simplicity it is widely used in practice.

2.2.1 Active and Passive Earth Pressure

The basic assumptions of Mononobe-Okabe method for dry cohesionless soils are: (1) the wall moves sufficiently to mobilize the minimum active pressure; (2) when the minimum active pressure acts against the failure with the maximum shearing resistance mobilized all along the plane sliding surface; (3) the soil wedge acts as a rigid body with earthquake accelerations acting uniformly throughout the wedge (Seed and Whitman, 1970). The typical approach is to estimate the forces acting on a wall and then to design the wall to resist those forces with a factor of safety (FS) high enough to produce acceptably small deformations, i.e., FS = 1.1 ~ 1.2 against sliding and FS > 2.0 against bearing failure. The forces acting on active wedge

in a dry cohesionless backfill for the Mononobe-Okabe analysis are shown in Figure 2-4, where ϕ = the internal friction angle of soil; δ = the wall friction angle; β = the inclination of backfill surface behind the wall; θ = the slope of the back of the wall to the vertical; k_h = pseudostatic horizontal acceleration/g; k_v = pseudostatic vertical acceleration/g; and W = weight of sliding wedge.

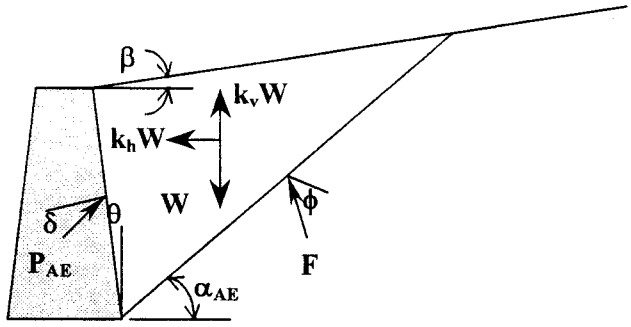

Figure 2-4: Forces acting on active wedge in Mononobe-Okabe method

The inertia terms represent the effect of the earthquake on the backfill, assuming that the backfill behaves as a rigid body so that the accelerations can be considered uniform throughout. The angle of critical failure surface, α_{AE}, is inclined at an angle

$$\alpha_{AE} = \phi - \psi + \tan^{-1}\left[\frac{-\tan(\phi-\psi-\beta)+C_{1E}}{C_{2E}}\right] \qquad (2\text{-}1)$$

where

$$\psi = \tan^{-1}\left[k_h/(1-k_v)\right]$$

$$C_{1E} = \sqrt{\tan(\phi-\psi-\beta)\left[\tan(\phi-\psi-\beta)+\cot(\phi-\psi-\theta)\right]\left[1+\tan(\delta+\psi+\theta)\cot(\phi-\psi-\theta)\right]}$$

$$C_{2E} = 1+\left\{\tan(\delta+\psi+\theta)\left[\tan(\phi-\psi-\beta)+\cot(\phi-\psi-\theta)\right]\right\}$$

The active thrust, P_{AE}, is the driving force in causing lateral displacement and tilting of the retaining walls. The active force determined by the equilibrium of the wedge is expressed as follows:

$$P_{AE} = \frac{1}{2}\gamma H^2 (1-k_v) K_{AE} \tag{2-2}$$

where γ = unit weight of backfill soil; H = wall height; K_{AE} = active earth pressure coefficient with earthquake effect expressed as follows:

$$K_{AE} = \frac{\cos^2(\phi-\theta-\psi)}{\cos\psi\cos^2\theta\cos(\delta+\theta+\psi)\left[1+\sqrt{\frac{\sin(\delta+\phi)\sin(\phi-\beta-\psi)}{\cos(\delta+\theta+\psi)\cos(\beta-\theta)}}\right]^2} \tag{2-3}$$

In Mononobe-Okabe analysis, k_v, pseudostatic vertical acceleration/g, when taken as one-half to two-thirds the value of k_h, only affects P_{AE} by less than 10%, therefore, k_v is usually ignored when the Mononobe-Okabe method is used to estimate P_{AE} for typical wall designs (Seed and Whitman, 1970).

The corresponding expression for the passive thrust which is the resistance force provided by soils is given as follows:

$$P_{PE} = \frac{1}{2}\gamma H^2 (1-k_v) K_{PE} \tag{2-4}$$

$$K_{PE} = \frac{\cos^2(\phi+\theta-\psi)}{\cos\psi\cos^2\theta\cos(\delta-\theta+\psi)\left[1+\sqrt{\frac{\sin(\delta+\phi)\sin(\phi+\beta-\psi)}{\cos(\delta-\theta+\psi)\cos(\beta-\theta)}}\right]^2} \tag{2-5}$$

The critical failure surface for Mononobe-Okabe passive conditions is inclined from horizontal by an angle

$$\alpha_{PE} = \psi - \phi + \tan^{-1}\left[\frac{\tan(\phi+\psi+\beta)+C_{3E}}{C_{4E}}\right] \quad (2\text{-}6)$$

where

$$C_{3E} = \sqrt{\tan(\phi-\psi+\beta)\left[\tan(\phi-\psi+\beta)+\cot(\phi-\psi+\theta)\right]\left[1+\tan(\delta+\psi-\theta)\cot(\phi-\psi+\theta)\right]}$$

$$C_{4E} = 1+\left\{\tan(\delta+\psi-\theta)\left[\tan(\phi-\psi+\beta)+\cot(\phi-\psi+\theta)\right]\right\}$$

The Mononobe-Okabe equation has been developed for dry, cohesionless soils, therefore, it does not account for the potentially important increases in lateral pressure that may occur because of porewater pressure buildup in loose, saturated cohesionless soils below the water table. Most retaining walls are designed with drains, i.e., wick or geotextile systems, to prevent static porewater pressure buildup within the backfill. This is not possible for retaining walls in waterfront areas, where most earthquake-induced wall failures have been observed. When the soil is saturated with water such as in waterfront areas, the generation of seismically-induced excess pore water pressures becomes an important factor that would affect the performance of waterfront retaining structures. In general, the total water pressures that act on retaining walls in the absence of seepage within the backfill can be divided into two components: (1) hydrostatic pressure, which increases linearly with depth and acts on the wall before, during, and after earthquake shaking, and (2) hydrodynamic pressure, which results from the dynamic response of the wall itself. The effects of water on wall pressures are presented in the following section.

2.2.2 Seaward Hydrodynamic Pressure

For the presence of water in front of the wall, the Westergaard procedure (1931) is usually used for computing the hydrodynamic water pressures, which are superimposed on the static water pressure distribution along the front of the wall. The pressures derived in Westergaard's solution is for the case of a vertical, rigid dam retaining a semi-infinite reservoir of water that is excited by harmonic, horizontal motion of its rigid base.

$$p(y) = \frac{7}{8}\frac{a_h}{g}\gamma_w\sqrt{yH} \tag{2-7}$$

where

$p(y)$ = hydrodynamic water pressure at depth y.

a_h = horizontal acceleration, g.

γ_w = unit weight of water.

H = water depth in the reservoir.

The resultant hydrodynamic thrust, P_{wd}, is given by

$$P_{wd} = \frac{7}{12}\frac{a_h}{g}\gamma_w H^2 \tag{2-8}$$

The total lateral thrust due to the water is the sum of the hydrostatic and hydrodynamic thrusts as follows:

$$P_{w,total} = P_{ws} + P_{wd} \tag{2-9}$$

where P_{ws} = hydrostatic thrust = $\frac{1}{2}(\gamma_w H^2)$.

2.2.3 Water in Backfill Soils

The presence of water in the backfill behind a retaining wall can influence the seismic loads that act on the wall: (1) by altering the inertial forces within the backfill, (2) by developing hydrodynamic pressures within the backfill, and (3) by allowing excess pore water pressure buildup within the backfill.

For *restrained porewater conditions*, i.e., the permeability of the soil is small enough (typically $k \leq 10^{-3}$ cm/sec) so that the porewater moves with the soil during earthquake shaking, the Mononobe-Okabe can be modified to account for the presence of porewater within the backfill. Representing the excess porewater pressure in the backfill by the pore pressure ratio, $r_u = u_{excess}/\sigma'_v$, the active soil thrust acting on the walls can be calculated from equation 2-2 using

$$\gamma = \gamma_b(1-r_u) \tag{2-10}$$

$$\psi = \tan^{-1}\left[\frac{\gamma_{sat} k_h}{\gamma_b(1-r_u)(1-k_v)}\right] \tag{2-11}$$

An equivalent hydrostatic thrust based on fluid of unit weight, $\gamma_{eq}=\gamma_w+r_u\gamma_b$, should be added to the soil thrust using

$$P_{ws} = \frac{1}{2}\gamma_{eq} H^2 \tag{2-12}$$

where H = water depth. It should be noted that as r_u approaches 1, i.e., in a liquefiable backfill soil, equivalent hydrostatic thrust is calculated by equivalent unit weight, γ_{eq} = γ_{sat}. For the case of partially submerged backfill, soil thrusts may be calculated by

using an average unit weight based on the relative volumes of soil within the active wedge that are above and below the water surface as follows:

$$\bar{\gamma} = \lambda^2 \gamma_{sat} + (1 - \lambda^2)\gamma_d \qquad (2\text{-}13)$$

where

λ = relative water depth with respect to wall height, in decimal.

γ_{sat} = saturated unit weight of soil.

γ_d = dry unit weight of soil.

Then, the hydrostatic thrust and hydrodynamic thrust must be added to the soil thrust.

For *free porewater conditions*, i.e., the permeability of the backfill soil is very high (typically k ≥ 1 cm/sec), so that the porewater may remain essentially stationary while the soil skeleton moves back and forth, hydrodynamic water pressures could be developed and must be added to the computed soil and hydrostatic pressures to obtain the total loading on the wall.

Although hydrodynamic pressures acting on the wall can be incorporated in the design, the excess pore pressures generated in loose- to medium dense saturated sandy backfill soils are only approximately accounted for. Common design methods either treat potentially liquefiable soils as heavy fluids (i.e., zero shear strength and fluid unit weight equal to the saturated unit weight of the soil) or post-liquefaction residual shear strengths are used in undrained stability analyses. In either case, limit equilibrium methods are used to obtain factors of safety against potential failure modes such as sliding, overturning, bearing capacity and deep-seated foundation

failures. The resulting factors of safety are only approximately correlated to the permanent deformations that may be realized during the design level earthquake.

2.3 Permanent Displacement-Based Approach

Although seismic pressure-based approaches, i.e., Mononobe-Okabe method, provide significant indication on the seismic loads acting on the waterfront retaining walls, the post-earthquake serviceability of such walls at ports is more related to the allowable permanent deformations that occur during earthquakes. Therefore, alternative approaches based on allowable (or limited) permanent wall displacements, i.e., permanent displacement-based approach, proposed by Richards-Elms (1979) and Whitman-Liao (1985) will be presented in the following sections.

2.3.1 Richards-Elms Method

An alternative method on the basis of allowable permanent wall displacements is proposed by Richards and Elms (1979) for consideration of the post-earthquake serviceability of retaining walls. This method involves calculation of the wall weight that would be required to ensure that permanent displacements are less than or equal to allowable value determined from the importance of structures. Richards and Elms suggested that acceleration less than the expected peak ground acceleration be used in design due to the fact that peak acceleration exists for only a very short period of time during transient earthquake loading. It implies that some relative slip occurs between the wall and its supporting soil mass. This method assumes a rigid-plastic behavior of

the backfill soil and the acceleration field is constant throughout the backfill soil. This means that amplification of earthquake motion can not be taken into account. Richards and Elms indicated that force increased over those predicted by the Mononobe-Okabe analysis occurred because of the inertia effects of the wall itself. The omission of such effects in the Mononobe-Okabe analysis can lead to a serious underestimate of the total force on a wall. The seismic forces acting on gravity retaining wall are shown in Figure 2-5, where W_w is the weight of the wall and B is the reaction force at the base with horizontal and vertical component F and N, respectively.

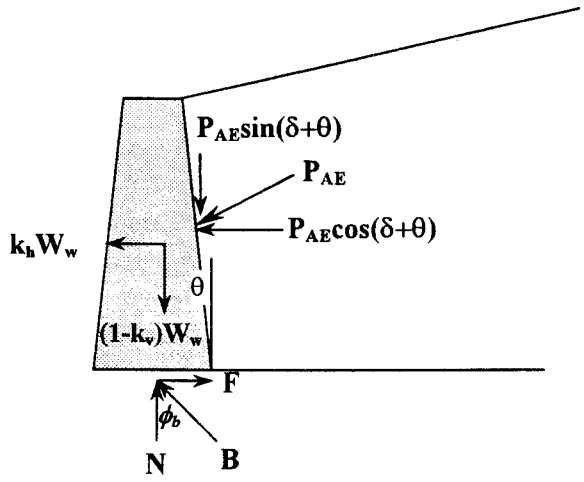

Figure 2-5: Seismic forces on gravity retaining wall (Richards and Elms, 1979)

Application of the Richards-Elms method requires evaluation of the yield acceleration for the wall-backfill system. The *yield acceleration* is defined as the level

of acceleration that is just large enough to cause the wall to slide on its base, i.e., FS = 1 against sliding. From force equilibrium

$$N = (1 - k_v)W_w + P_{AE}\sin(\delta + \theta) \tag{2-14}$$

$$F = P_{AE}\cos(\delta + \theta) + k_h W_w \tag{2-15}$$

At sliding $F = N\tan\phi_b$ in which ϕ_b is the friction angle at the base of the wall. Thus

$$P_{AE}[\cos(\delta + \theta) - \sin(\delta + \theta)\tan\phi_b] = W_w[(1 - k_v)\tan\phi_b - k_h] \tag{2-16}$$

Replacing k_h with $(1-k_v)\tan\psi$ as defined before, thus

$$W_w = \frac{[\cos(\delta + \theta) - \sin(\delta + \theta)\tan\phi_b]}{(1 - k_v)(\tan\phi_b - \tan\psi)} P_{AE} \tag{2-17}$$

When the acceleration is equal to the yield acceleration, a_y, yield acceleration can be computed from equation 2-16 by replacing k_h with a_y.

$$a_y = \left[\tan\phi_b + \frac{P_{AE}\sin(\delta + \theta)\tan\phi_b - P_{AE}\cos(\delta + \theta)}{W_w}\right] g \tag{2-18}$$

In equation 2-18, k_v is assumed to be zero and P_{AE} can be computed using the Mononobe-Okabe method. Since the Mononobe-Okabe method requires that a_y be known, the solution of equation 2-18 must be obtained iteratively.

Newmark (1965) carried out the sliding block analysis for four different earthquakes and scaled the records in each case to a maximum acceleration of 0.5g and a maximum velocity of 30 in/sec in order to compare the displacement characteristics of the results. Franklin and Chang (1977) extended Newmark's work and analyzed 169 horizontal and 10 vertical corrected accelerograms as well as

several synthetic records. Franklin and Chang drew upper bound envelope curves for various groupings of acceleration records and is shown in Figure 2-6.

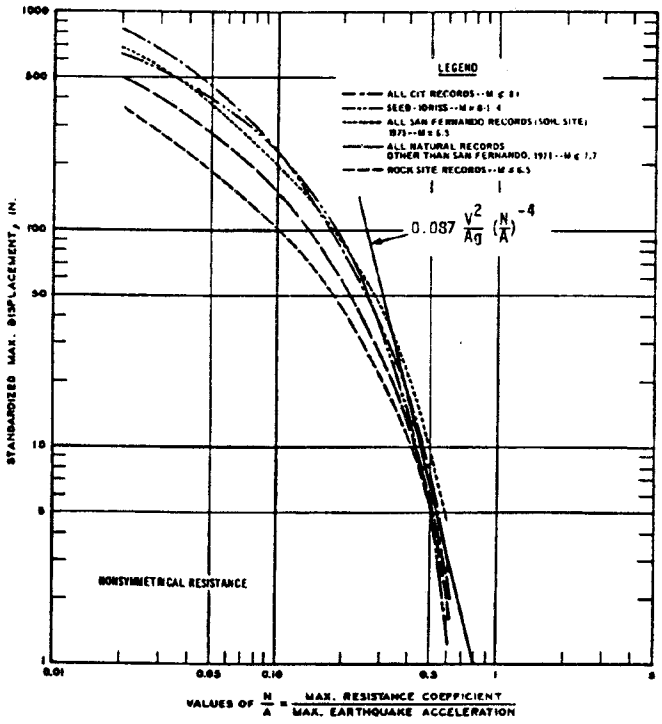

Figure 2-6: Upper bound envelop curves of permanent displacements for all natural and synthetic records (Franlin and Chang, 1977)

Using the results of sliding block analyses by Franklin and Chang, Richards and Elms proposed the following expression for permanent displacement, d, of a wall

$$d = 0.087 \frac{V^2 \left(\frac{N}{A}\right)^{-4}}{Ag} \tag{2-19}$$

where N is coefficient of limiting wall acceleration, A is coefficient of maximum acceleration, V is maximum velocity. Equation 2-19 can be expressed as an alternative form as follows:

$$d = 0.087 \frac{v_{\max}^2 a_{\max}^3}{a_y^4} \tag{2-20}$$

where v_{max} is the peak ground velocity (= V), a_{max} is the peak ground acceleration (= Ag), and a_y is the yield acceleration (= Ng). The above procedures are reversible. If an allowable permanent displacement is specified, a_y is calculated using equation 2-20. The wall weight required to limit the permanent displacement to the allowable permanent displacement is then calculated using equation 2-17 by simply changing $\tan\psi\,[= k_h/(1-k_v)]$ with a_y/g assuming that k_v is equal to zero. Finally, apply a factor of safety ranging from 1.1 to 1.2 to the weight of the wall.

2.3.2 Whitman-Liao Method

Whitman and Liao (1985) improved Richards-Elms procedure by using a statistical method (probabilities of exceedance) to address sources of uncertainty in the displacement controlled procedure. One of the simplifying assumptions made in the Richards-Elms model is that the acceleration field is uniform within the backfill. Thus, the input ground acceleration is constant throughout the backfill and amplification of motion cannot be taken into account. Nadim and Whitman (1983) reveal that non-uniformity of accelerations within the backfill can affect the amount of wall movement significantly. Finite element analyses of the effects of the dynamic

response of the backfill on wall displacement also show that amplification occurs when input motions coincide with the natural period of the backfill and produce considerably greater permanent displacement than the rigid block model used by Richards and Elms. Nadim (1980) also indicates that the combination of tilting and sliding mechanism generally increase wall displacements over those produced by sliding only such as that of Richards-Elms method. In view of those uncertainties in the Richards and Elms model, Wong (1982) has suggested an alternative equation for the expected displacements based on computed wall displacements for 56 ground motions and various values of N/A as follows:

$$d = \frac{37V^2}{Ag \bullet e^{9.4N/A}} \tag{2-21}$$

or

$$d = \frac{37v_{\max}^2}{a_{\max}} exp\left(\frac{-9.4a_y}{a_{\max}}\right) \tag{2-22}$$

Notations described above are the same as previously defined, i.e., equation 2-19 and equation 2-20. Whitman and Liao (1985), combining all of the modeling errors, characterizes the permanent wall displacement as a lognormally distributed random variable with mean value

$$\overline{d} = \frac{37v_{\max}^2}{a_{\max}} exp\left(\frac{-9.4a_y}{a_{\max}}\right)\overline{QM} \tag{2-23}$$

and variance

$$\sigma_{\ln d}^2 = \left(\frac{9.4g}{a_{\max}}\right)^2 \sigma_{a_y}^2 + \sigma_{\ln M}^2 + \sigma_{\ln Q}^2 \tag{2-24}$$

Suggested values of the means and standard deviations of the ground motion, soil resistance, and model error factors are listed in Table 2-1.

Table 2-1: Mean and Standard Deviation Values for Gravity Wall Displacement (Whitman and Liao, 1985)

Factor	*Mean*	*Standard Deviation*
Model Error	$\overline{M} = 3.5$	$\sigma_{\ln M} = 0.84$
Soil Resistance	$\overline{a_y} = a_y\left(\overline{\phi}, \overline{\delta}\right)$	$\sigma_{a_y} = 0.04 \sim 0.065$
Ground Motion	$\overline{Q} = 1$	$\sigma_{\ln Q} = 0.58 \sim 1.05$

Thus, using equations (2-23) and (2-24), the probability of exceeding any particular value of $d_{allowable}$ can be computed. Whitman and Liao suggest that a conservative design (corresponding to a probability of exceedance of 5%) can be obtained by assuming $d_{allowable} = 4\ d_{perm}$, where d_{perm} is calculated from Equation (2-22). A less conservative design (corresponding to a probability of exceedance of 10%) can be obtained by $d_{allowable} = 2.5\ d_{perm}$.

2.4 Discussion

While permanent displacement-based approaches have produced improved methods for the seismic design of gravity retaining walls in non-liquefiable soils, these rigid-body, "sliding block" type displacement analyses are not well suited to account for the influence of excess pore pressure development in the foundation and backfill soils. In order to address this deficiency limit equilibrium-based methods for

predicting seismic displacements of slopes and retaining walls with liquefiable soils have also been developed (Byrne, et al., 1994).

The waterfront retaining structures at ports are usually encountered with several unique conditions such as saturated soils, balanced static water forces, and hydraulically placed loose sandy soils. These soil conditions are very suspicious to liquefaction damage. The application of pseudostatic methods for marine environment is not directly accounted for strain softening behavior in liquefiable soils. Furthermore, the important aspects of soil-structure interaction are not modeled. These conditions limit the applicability of pseudostatic methods for waterfront structures. Because of complexity of soil-structure interaction, pseudostatic design procedures are usually based on numerous simplifying assumptions. In view of the simplifying assumptions in the pseudostatic methods for waterfront retaining structures, prediction of permanent wall displacements requires the use of a nonlinear analysis. A suitable analysis should be capable of accounting for nonlinear, plastic behavior of the soil and of the interfaces between the soil and wall elements. The state-of-art nonlinear, effective stress analysis for predicting earthquake-induced displacements of retaining walls will be presented in the following chapter (Chapter 3).

3 DYNAMIC ANALYSIS APPROACH – NUMERICAL MODELING

3.1 Introduction

Current standards-of-practice using pseudostatic methods for analyzing the seismic response of waterfront retaining structures is mainly due to (1) the pseudostatic methods provide a simple and straightforward procedure for most engineers routinely to perform and interpret their analysis; (2) the soil and structural parameters required for the analysis can be easily obtained from field and laboratory tests or well-established geotechnical correlations; (3) the enhancement of pseudostatic methods has been calibrated and improved by many database from case studies. However, pseudostatic methods, using a constant pseudostatic acceleration to represent actual earthquake loading, seem to be over-simplified in the sense of very complex, transient, and dynamic effects of earthquake motions. For example, Werner and Dickenson (1995) indicated that the pseudostatic seismic coefficients used for caisson type quay walls at the Port of Kobe were 0.1 ~ 0.15. These values were way below the actual earthquake acceleration experienced during 1995 Kobe Earthquake. Furthermore, past experiences also indicated that pseudostatic analysis could be not reliable for strain softening behavior in liquefiable soils.

3.1.1 Advantages of Numerical Methods over Pseudostatic Methods

In light of limitations of pseudostatic methods, numerical nonlinear effective stress analysis approaches are recommended. The primary advantages of numerical

models include (1) capable of accounting for nonlinear, plastic behavior of the soil and of the interfaces between the soil and wall elements; (2) irregular embankment and structure geometries can be modeled; (3) dynamic soil behavior, strain softening of liquefiable soils, soil-structure interaction, and permanent deformations can be more accurately evaluated; (4) complex, transient, dynamic effects of earthquake motions can be more reasonably represented; (5) it is easy to perform sensitivity studies for the influence of various parameters on the seismic response of soils and structures.

Although these advantages of numerical models have been recognized, uncertainties in the numerical models usually arise from the facts that (1) requisite soil parameters for a constitutive soil model may not be always available and engineering judgement according to geotechnical correlations by individuals may cause the variations; (2) given the highly variable nature of ground motion characteristics, the use and interpretation of earthquake motions may result in quite variable computed structure deformations; (3) very few of the available numerical models have been validated and calibrated by well-documented case histories of seismic performance of actual retaining structures.

3.1.2 Overview of Numerical Methods

A sophistical numerical analysis should be able to account for nonlinear, inelastic behavior of the soil and soil-structure interaction. The numerical model is to analyze the actual nonlinear response of soil-structure interaction using direct numerical integration in the time domain. By integrating the equation of motion in

small time steps, any linear or nonlinear stress-strain model, i.e., constitutive soil model, can be used. At the beginning of each time step (usually very small in the finite difference method), the stress-strain relationship is referred to obtain the appropriate soil properties to be used in that time step. By this approach, a nonlinear elastic-plastic stress-strain relationship can be followed in a set of small incrementally linear steps.

For level or gently sloping sites one-dimensional technique may be useful, however, for those problems associated with sloping, irregular ground surfaces, the presence of structures, and tunnel, two-dimensional or even three-dimensional techniques are required. Techniques for the solution of such problems have been developed using either frequency-domain methods or time-domain methods. Prediction of permanent displacement of waterfront retaining walls requires, at least, the use of a nonlinear, two-dimensional analysis.

In this chapter, an explicit finite difference code FLAC (Fast Lagrangian Analysis of Continua, Itasca Consulting Group, 1995) is introduced and the discussion of formulations and numerical modeling considerations in FLAC is also presented.

3.2 Overview of FLAC

The FLAC program employs an explicit finite difference method for modeling nonlinear static and dynamic problems in two dimensions. Motions in response to external forces are approximated by finite difference equations applied to model zones, which describe the modeled continuum. At each time step, incremental strains

are computed for each zone, and corresponding stress increments are derived from a constitutive law governing the material's stress-strain behavior. The general calculation sequence embodied in FLAC is illustrated in Figure 3-1.

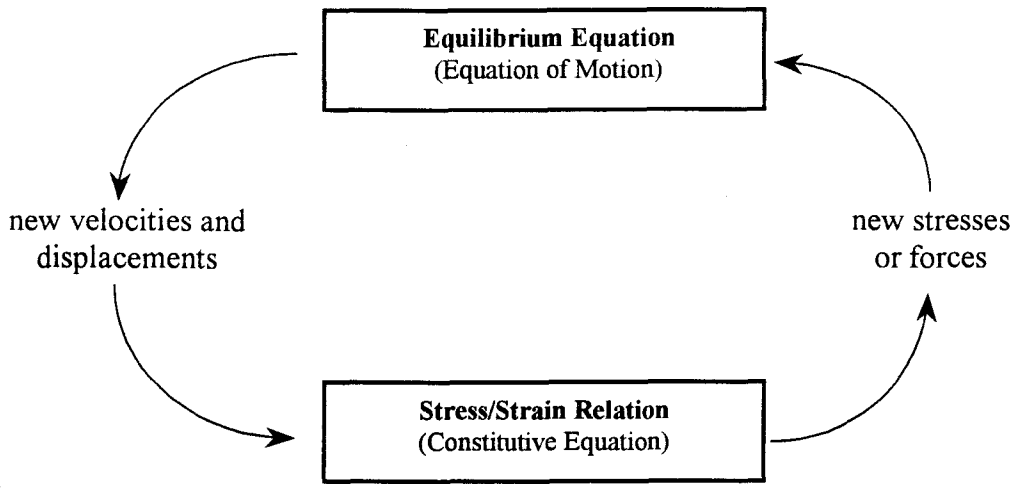

Figure 3-1: Basic explicit calculation cycle in FLAC model

This procedure first invokes the equations of motion to derive new velocities and displacements from stresses and forces. Then, strain rates are derived from velocities, and new stresses from strain rates. It takes one time step for every cycle around the loop. Each box in Figure 3-1 updates all of its grid variables from known values that remain fixed while control is within the box. For example, the lower box takes the set of velocities already calculated and, for each element, computes new stresses. The velocities are assumed to be frozen for the operation of the box, i.e., the newly calculated stresses do not affect the velocities. This assumption can be justified by choosing a time step so small that information can not physically pass from one

element to another in that interval. These computation cycles are repeated until internal stresses are in equilibrium with external forces.

3.3 Constitutive Soil Model

There are seven constitutive laws provided in FLAC. But only a constitutive law consisting of the Mohr-Coulomb failure criterion in a linear elastic-perfect plastic framework will be discussed in this section since the Mohr-Coulomb model is the conventional model for plasticity in soil and rock mechanics.

3.3.1 Elastic-Perfectly Plastic Behavior

The different models in FLAC are characterized by their yield function, hardening/softening functions and flow rule. The yield functions for each model define the stress combination for which plastic flow takes place. These functions or criteria are represented by one or more limiting surfaces in a generalized stress space with points below or on the surface being characterized by an incremental elastic or plastic behavior, respectively. The plastic flow formulation in FLAC rests on basic assumptions from plasticity theory that the total strain increment may be decomposed into elastic and plastic parts, with only the elastic part contributing to the stress increment by means of an elastic law. Figure 3-2 shows a typical stress-strain diagram for soils.

The stress-strain behavior of most real soils is characterized by an initial linear portion and a peak, or failure, stress followed by softening to a residual stress. In limit

analysis, it is common to ignore the strain softening (or work softening) feature of the stress-strain diagram and to take the stress-strain diagram to consist of two straight lines, i.e., elastic part and perfectly plastic part as shown by the dashed lines in Figure 3-2. A hypothetical material exhibiting this property of continuing plastic flow at constant stress is called an ideally plastic, or perfectly plastic, material. Plastic flow occurs when a stress-point in stress space reaches the perfectly-plastic yield surface. The kinematics of the plastic flow may be expressed as plastic strain rates (or plastic strain increments). The total strain rate is composed of elastic and plastic parts. The elastic strain parts are related to the stress rates through Hook's law and the plastic parts depend on the state of stress through an appropriate kinematic assumption on the deformations.

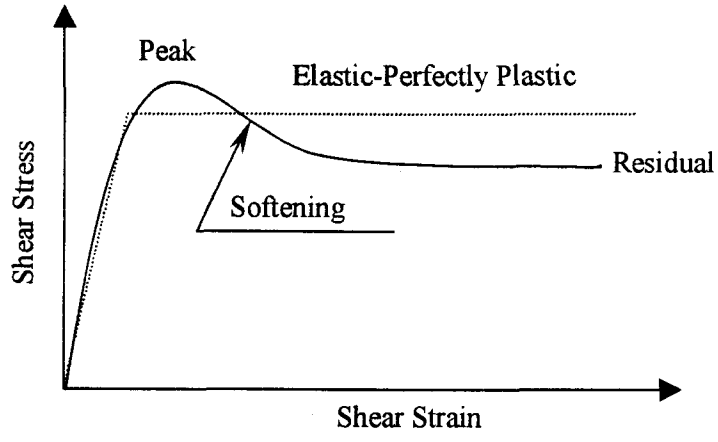

Figure 3-2: Stress-strain relationhip for ideal and real soils

3.3.2 Mohr-Coulomb Model

It is generally assumed that plastic flow occurs when, on any plane at any point in a soil mass, the shear stress, τ, reaches an amount that depends linearly on the cohesion stress, c, and the normal stress (compressive stress), σ: $\tau = c + \sigma \tan \phi$. The angle ϕ is the angle of internal friction of a soil. The constants c and ϕ can be treated simply as parameters which characterize the total resistance of the soil media to shear.

Values of σ, τ satisfying the Coulomb yield criterion are represented in Figure 3-3 by two straight lines which start from the point $(c \cdot cot\phi, 0)$ and inclined at angles of amount ϕ to the positive σ-axis. If a state of stress σ_1, σ_2, σ_3 is such that the Mohr circles lie within the wedge-shaped region, i.e., below the Mohr-Coulomb failure envelop, the soil remains in the linear elastic range. Plastic flow of the soil can occur when the largest of the circles touches the two straight lines. However, when the principal stress components σ_1, σ_2, σ_3 are used as coordinates, the Coulomb yield curve in two-dimensional becomes the Coulomb yield *surface* in the three-dimensional.

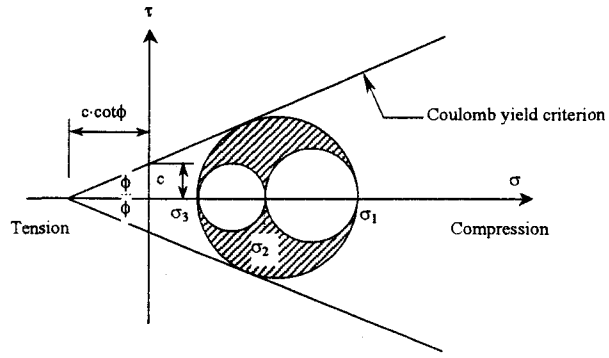

Figure 3-3: Mohr's representation of a stress and the Coulomb yield criterion

In FLAC, the Mohr-Coulomb failure criterion (shear yield function) with tension cutoff (tensile yield function) is employed. The elastic behavior of the soil is defined by bulk and shear moduli, and the shear strength is defined by friction angle and cohesion. In the FLAC implementation of this model, principal stresses σ_1, σ_2, σ_3 are used. The principal stresses and principal directions are evaluated from the stress tensor components and ordered. An elastic trial for the stress increment is first computed from the total strain increment using the incremental form of Hook's law. The corresponding stresses are then evaluated. If they violate the yield criteria (i.e., the stress point representation lies above the yield function in the generalized stress space), plastic deformations take place. In this case, only the elastic part of the strain increment can contribute to the stress increment; the latter is corrected by using the plastic flow rule to ensure that the stresses lie on the composite yield function. This procedure is outlined as follows:

3.3.2.1 Step 1: Incremental Elastic Law

The principal stresses and principal directions are evaluated from the stress tensor components and ordered.

$$\sigma_1 \leq \sigma_2 \leq \sigma_3 \tag{3-1}$$

Note that compressive stresses are negative in FLAC notation.

The corresponding principal strain increments $\Delta\varepsilon_1$, $\Delta\varepsilon_2$, $\Delta\varepsilon_3$ are decomposed as elastic and plastic parts.

$$\Delta\varepsilon_i = \Delta\varepsilon_i^e + \Delta\varepsilon_i^p \qquad i = 1,3 \tag{3-2}$$

Note that the plastic components are non-zero only during plastic flow. The incremental expression of Hook's law can be expressed as follows.

$$\begin{aligned}\Delta\sigma_1 &= \alpha_1\Delta\varepsilon_1^e + \alpha_2\left(\Delta\varepsilon_2^e + \Delta\varepsilon_3^e\right)\\ \Delta\sigma_2 &= \alpha_1\Delta\varepsilon_2^e + \alpha_2\left(\Delta\varepsilon_1^e + \Delta\varepsilon_3^e\right)\\ \Delta\sigma_3 &= \alpha_1\Delta\varepsilon_3^e + \alpha_2\left(\Delta\varepsilon_1^e + \Delta\varepsilon_2^e\right)\end{aligned} \qquad (3\text{-}3)$$

where $\alpha_1 = K + 4\,G/3$ and $\alpha_2 = K - 2\,G/3$ and K = bulk modulus and G = shear modulus.

3.3.2.2 Step 2: Yield Functions

The failure criterion is represented in the plane (σ_1, σ_3). Two governing yield functions associated with shear yield function and tension yield function are employed in the Mohr-Coulomb model.

$$f^s = \sigma_1 - \sigma_3 N_\phi + 2c\sqrt{N_\phi} \quad \text{(shear yield function)} \qquad (3\text{-}4)$$

$$f^t = \sigma^t - \sigma_3 \quad \text{(tension yield function)} \qquad (3\text{-}5)$$

where ϕ is the friction angle of the soil, c, the cohesion, σ^t, the tensile strength and $N_\phi = (1+\sin\phi) / (1-\sin\phi)$. A function $h(\sigma_1, \sigma_3) = 0$ is defined which is represented by the diagonal between the representation of $f^s = 0$ and $f^t = 0$ in the (σ_1, σ_3) plane as shown in Figure 3-4.

An elastic trial violating the failure criterion is represented by a point in the (σ_1, σ_3) plane located either in shear domain or tension domain. If in shear domain, shear failure is declared, and the stress point is brought back to the curve $f^s = 0$. If in

tension domain, tensile failure takes place, and the stress point is brought back to $f^t = 0$. A plastic correction must be applied to the elastic trial to give the new stress state.

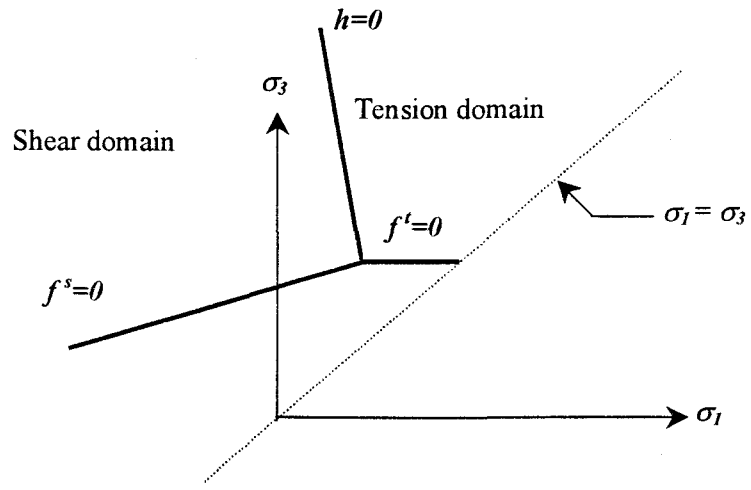

Figure 3-4: Domain used in the definition of the flow rule in Mohr-Coulomb model

3.3.2.3 Step 3: Plastic Corrections

First consider shear failure. The flow rule has the form

$$\Delta\varepsilon_i^p = \lambda^s \frac{\partial g^s}{\partial \sigma_i} \qquad i = 1,3 \qquad (3\text{-}6)$$

where $\Delta\varepsilon_i^p$ is plastic strain increments, λ^s is a scalar proportionality factor, and g^s is shear potential function.

$$g^s = \sigma_1 - \sigma_3 N_\psi$$
$$N_\psi = \frac{1+\sin\psi}{1-\sin\psi} \qquad (\psi = \text{dilation angle}) \qquad (3\text{-}7)$$

The flow rule in equation (3-6) becomes

$$\begin{aligned} \Delta\varepsilon_1^p &= \lambda^s \\ \Delta\varepsilon_2^p &= 0 \\ \Delta\varepsilon_3^p &= -\lambda^s N_\psi \end{aligned} \tag{3-8}$$

Since the elastic strain increments are equal to the total minus plastic strain increments, $\Delta\varepsilon_i^e = \Delta\varepsilon_i - \Delta\varepsilon_i^p$, the equation (3-3) becomes

$$\begin{aligned} \Delta\sigma_1 &= \alpha_1\Delta\varepsilon_1 + \alpha_2\left(\Delta\varepsilon_2 + \Delta\varepsilon_3\right) - \lambda^s\left(\alpha_1 - \alpha_2 N_\psi\right) \\ \Delta\sigma_2 &= \alpha_1\Delta\varepsilon_2 + \alpha_2\left(\Delta\varepsilon_1 + \Delta\varepsilon_3\right) - \lambda^s\alpha_2\left(1 - N_\psi\right) \\ \Delta\sigma_3 &= \alpha_1\Delta\varepsilon_3 + \alpha_2\left(\Delta\varepsilon_1 + \Delta\varepsilon_2\right) - \lambda^s\left(-\alpha_1 N_\psi + \alpha_2\right) \end{aligned} \tag{3-9}$$

Let the new and old stress state be N and O, respectively. Therefore,

$$\sigma_i^N = \sigma_i^O + \Delta\sigma_i \qquad i = 1,3 \tag{3-10}$$

Substituting equation (3-9) into equation (3-10) and yields

$$\begin{aligned} \Delta\sigma_1^N &= \sigma_1^I - \lambda^s\left(\alpha_1 - \alpha_2 N_\psi\right) \\ \Delta\sigma_2^N &= \sigma_2^I - \lambda^s\alpha_2\left(1 - N_\psi\right) \\ \Delta\sigma_3^N &= \sigma_3^I - \lambda^s\left(-\alpha_1 N_\psi + \alpha_2\right) \end{aligned} \tag{3-11}$$

where

$$\begin{aligned} \sigma_1^I &= \sigma_1^O + \alpha_1\Delta\varepsilon_1 + \alpha_2\left(\Delta\varepsilon_2 + \Delta\varepsilon_3\right) \\ \sigma_2^I &= \sigma_2^O + \alpha_1\Delta\varepsilon_2 + \alpha_2\left(\Delta\varepsilon_1 + \Delta\varepsilon_3\right) \\ \sigma_3^I &= \sigma_3^O + \alpha_1\Delta\varepsilon_3 + \alpha_2\left(\Delta\varepsilon_1 + \Delta\varepsilon_2\right) \end{aligned} \tag{3-12}$$

where the superscript ***I*** is used to represent the elastic guess obtained by adding to the old stresses, elastic increments computed using the total strain increments. The last parameter left is λ^s. The λ^s may now be defined by requiring that the new stress point

be located on the shear yield surface. Therefore, λ^s can be obtained by substituting σ_1^N and σ_3^N for σ_1 and σ_3 in $f^s = 0$ and yield

$$\lambda^s = \frac{\sigma_1^I - \sigma_3^I N_\phi + 2c\sqrt{N_\phi}}{(\alpha_1 - \alpha_2 N_\psi) - (\alpha_2 - \alpha_1 N_\psi) N_\phi} \tag{3-13}$$

Similar procedures can be expected in the case of tensile failure. Tensile potential function, g^t, and λ^t are used in the flow rule.

$$\Delta\varepsilon_i^p = \lambda^t \frac{\partial g^t}{\partial \sigma_i} \qquad i = 1,3 \tag{3-14}$$

and new stress states can be expressed as follows:

$$\begin{aligned} \Delta\sigma_1^N &= \sigma_1^I + \lambda^t \alpha_2 \\ \Delta\sigma_2^N &= \sigma_2^I + \lambda^t \alpha_2 \\ \Delta\sigma_3^N &= \sigma_3^I + \lambda^t \alpha_1 \end{aligned} \tag{3-15}$$

and

$$\lambda^t = \frac{\sigma^t - \sigma_3^I}{\alpha_1} \tag{3-16}$$

3.3.2.4 Summary of Analysis Procedures in Mohr-Coulomb Model

1. An elastic trial, σ_{ij}^I, is first computed by adding to the old stress components, increments calculated by application of Hook's law to the total strain increment for the step.

2. Principal stresses $\sigma_1^I, \sigma_2^I, \sigma_3^I$ and corresponding principal directions are calculated and ordered.

3. If these stresses violate the composite yield criterion, a plastic correction must be applied to the elastic trial to give the new stress state.

4. If shear failure is declared, new stresses are evaluated from equation (3-11) using equation (3-13) for λ^s. If tension failure is declared, new stresses are evaluated from equation (3-15) using equation (3-16) for λ^t.

5. The stress tensor components in the system are then calculated from the principal values by assuming that the principal directions have not affected by the occurrence of a plastic correction.

The behavior of elastic-perfectly plastic materials is used because of its simplicity and wide applicability. Although this formulation significantly simplifies real soil behavior, it is still capable of satisfaction predictions for geotechnical engineering problems.

3.4 Model for Pore Pressure Generation

The pore pressure generation and liquefaction resistance of saturated cohesionless soil was modeled using an incremental form of the simplified, stress-based procedures developed by Seed and his co-workers (Martin et al., 1975; Seed and De Alba, 1986). The liquefaction resistance of the soil is adjusted to account for initial static shear stresses and overburden stresses as described by Seed and Harder (1990). By coupling of this scheme with the dynamic analysis, effective stresses are

continuously updated as pore pressures gradually increase in loose to medium dense sandy soils.

After developing the static state of stress, the initial stresses and elastic moduli are stored for subsequent use in the dynamic analysis. Pore pressures are driven by cyclic shear stresses that are continuously tracked for each element during dynamic analysis. For each element of the model mesh (or zone), the cumulative damage, D, is updated every time a shear cycle is completed. The cumulative damage is expressed as:

$$D = \sum \frac{1}{N_{liq}} \tag{3-17}$$

where N_{liq} is the number of cycles required to produce initial liquefaction. After every cycle, the current value of cumulative damage, D, is related to the pore pressure ratio ($r_u = u / \sigma'_{vo}$) by an empirical function such that a soil subjected to random amplitude shear stress cycles reaches a pore pressure ratio of unity when $D = 1$. In the dynamic analysis, the simple linear function, $r_u = D$, is adopted. The effective stresses and corresponding soil strength are monitored until the state of initial liquefaction (i.e., zero effective stress) is reached. At this point the strength of the soil is modeled using undrained residual strengths (Stark and Mesri, 1992). In addition, the post-liquefaction volume change of the sand deposits following the generation of excess pore pressures in the soil has been estimated using the established relationship between the factor of safety against liquefaction and volumetric strain (Ishihara and Yoshimine, 1991). This method for modeling pore pressure generation and liquefaction related ground movements has been found to yield reasonable

displacements for a variety of seismic design applications (Inel et al., 1993; Roth and Inel, 1993; Dickenson and McCullough, 1998).

3.5 Soil Parameters

The complete description of the soil parameters in FLAC associated with Mohr-Coulomb constitutive soil model requires the input of the soil elastic parameter such as shear and bulk moduli, and soil strength parameter such as friction angle and cohesion. A framework for determining these parameters from the available test data or well-established engineering relationship is summarized herein.

3.5.1 Elastic Parameters

The shear and bulk moduli are required to define the elastic behavior of the soil. Since both moduli vary with mean stress, an empirical formula derived by Hardin (1978) is employed to describe the variation:

$$G = Kp_a\left(\frac{\sigma'_m}{p_a}\right)^n \tag{3-18}$$

where G is the low-strain shear modulus, p_a is the atmospheric pressure, σ'_m is the effective mean stress, and K and n are dimensionless constant which can be determined from laboratory tests or back-calculated from the empirical relationship associated with shear wave velocity. The shear modulus defined by equation (3-18) varies with depth in the static (gravity) analysis and then keep constant throughout the

dynamic run. The corresponding bulk modulus is computed from the expression as follows:

$$B = \frac{2(1+\nu)}{3(1-2\nu)}G \tag{3-19}$$

where B is bulk modulus and ν is Poisson's ratio. Poisson's ratio is very difficult to determine experimentally and almost always estimated in practice. It could be estimated by empirical expressions as follows:

$$\nu = \frac{K_0}{1+K_0} \quad \text{(for sand)} \qquad \text{or} \tag{3-20}$$

$$\nu = 0.5 \quad \text{(for undrained analysis of saturated clay)} \tag{3-21}$$

where K_0 is coefficient of earth pressure at rest which can be estimated using the empirical equation proposed by Mayne and Kulhawy (1982)

$$K_0 = (1 - Sin\phi')OCR^{Sin\phi'} \tag{3-22}$$

where ϕ' is effective friction angle and OCR is overconsolidation ratio of the soil.

3.5.2 Strength Parameters

The soil shear strength, $\tau = c + \sigma tan\phi$, is defined by the cohesion, c, and the friction angle, ϕ, as aforementioned in section 3.3.2. These values can be easily determined by laboratory tests. It is well known that friction angle varies with mean stress in a nonlinear fashion. The Mohr-Coulomb failure criterion assumes a linear failure envelop in stress space as shown in Figure 3-3 and yields reasonable results in

engineering practice. Therefore, constant values of c and/or ϕ are used in the same layer throughout the static and dynamic analysis.

3.6 Dynamic Loading (Input Motions)

FLAC models a region of material subjected to external and/or internal dynamic loading by applying a dynamic input boundary condition at either the model boundary or internal gridpoints. The dynamic input is represented by plane wave propagating upward through the underlying material. The dynamic input can be applied in the form of (1) an acceleration time history; (2) a velocity time history; (3) a stress (or pressure) time history; or (4) a force time history. The sources of the dynamic input in this research are obtained from recorded free-field acceleration time histories. A detailed description of the use of recorded free-field acceleration time histories for each case history evaluated herein will be presented in the next chapter (Chapter 4).

3.7 Boundary Conditions

A static analysis considering the effect of gravity is performed to simulate the stress conditions before the dynamic analysis. In static (gravity) analysis, both sides of the model are fixed in the horizontal direction and both directions, vertical and horizontal, are fixed at the bottom of the model. In dynamic analysis, the boundary conditions at both sides of the model are accounted for the free-field motion which

would exist in the absence of the structure, i.e., outward waves originating from the structure are properly absorbed.

3.8 Damping

In real material, part of the elastic energy of a traveling wave is always converted to heat. The conversion is accompanied by a decrease in the amplitude of the wave. For a dynamic analysis, the damping in the numerical simulation should attempt to reproduce the energy losses in the natural system when subjected to a dynamic loading. Real soils dissipate elastic energy hysteretically, by the slippage of grains with respect to each other. As a result, their energy dissipation characteristics are insensitive to frequency. It is difficult to reproduce this type of damping numerically because of the problem with path dependence, which makes results difficult to interpret (Cundall, 1976). Alternatively, in time-domain programs, Rayleigh damping is commonly used. This form of damping consists of two types of damping, mass-proportional and stiffness-proportional. Mass-proportional damping applies to the grid points a force which is proportional to the particle velocity but in the opposite direction. Stiffness-proportional damping applies a force to the zones, which is proportional to the incremental stress and in the same sense. Either form of damping may be used separately or in combination. The use of both forms of damping in combination is termed Rayleigh damping.

Mass-proportional damping decreases in a nonlinear way with frequency, whereas stiffness-proportional damping increases linearly with frequency. Rayleigh damping is frequency-dependent, but by choosing a center frequency, at which the

gradients of the two curves balance out, it is possible to have damping that is nearly independent of frequency over a fairly wide spectrum on low frequency side and high frequency side of the center frequency. If the highest predominant frequency is three times greater than the lowest predominant frequency, then there is a 3:1 range that contains most of the dynamic energy in the spectrum. In this way, hysteretic damping (independent of frequency) is simulated approximately. Then, natural frequency of the system, $f\,(=\omega/2\pi)$, is obtained by choosing angular frequency, ω, to lie in the center of the range of frequencies, i.e., 3:1 flat range. For geological materials and for structural systems, damping ratio is usually in the range of 2-5% and 2-10%, respectively. Therefore, in the present study, Rayleigh damping coefficients are chosen in accordance to a critical damping ratio of 5%. Natural frequency of the model is obtained either from running the model with dynamic loading but no damping or based on the following relationship:

$$f = \frac{\sum_{i=1}^{n} V_{si} \times h_i}{4H^2} \tag{3-23}$$

where f = natural frequency, V_{si} = shear wave velocity of layer i, h_i = layer thickness of layer i, and H = thickness of subsoil profile. This approach tends to be somewhat conservative side of the system but reflects the simplification made for the model. The validation of case studies indicates that the results using this simplified approach yield favorably reasonable agreement.

3.9 Structural Elements

The structural elements specified in FLAC can be grouped into four forms: (1) beam element; (2) pile element; (3) cable element; and (4) support member. The uses of beam element and pile element in the present study represent concrete caisson and pile-supported wharf, respectively. The beam element simulates concrete caisson that contains the soil in it and the slippage between beam elements and soil grids is not allowed, whereas pile elements allow the relative slippage between element and grid. However, the relative slippage between the caisson and the soil behind the caisson can be modeled using interface feature embodied in the code. This feature allows the model to simulate the relative movement between the caisson and the soil behind it as expected during earthquake shaking.

Beam elements are two-dimensional elements with three degree-of-freedom (x-translation, y-translation, and rotation) at each end node. Beam elements can be joined together with one another and/or the grid. Beam elements are used to represent a structural member in which bending resistance and limited bending moments are important. A beam element is defined by its material and geometric properties, which are assumed to be constant for each element. In general, the beam is assumed to behave as a linearly elastic material with no failure limit. However, a maximum moment (plastic moment) may be specified. The input parameters of beam element are specified by rather simple manner. They are cross-sectional area, elastic modulus, and the moment of inertia of the element. These properties are very easily obtained from available manuals.

Pile elements are two-dimensional elements that can transfer normal and shear forces and bending moments to the grid. Piles interact with adjacent grids via shear and normal coupling springs. The coupling springs are connectors that transfer forces and motions between the pile elements and the grid at the pile element nodes. The shear and normal behavior of the pile-grid interface is represented as a spring-slider system at the pile nodes. The maximum shear and normal force that can be developed along the pile-grid interface are the function of the cohesive strength of the interface and the stress-dependent frictional resistance along the interface. The maximum spring shear and normal force per length of the pile can be defined as follows.

$$\frac{F_s^{\max}}{L} = cohesion + \sigma_c^{'} \times \tan\phi \times perimeter \tag{3-24}$$

$$\frac{F_n^{\max}}{L} = cohesion + \sigma_c^{'} \times \tan\phi \times perimeter \tag{3-25}$$

where $F_s^{\max}$ and $F_n^{\max}$ are the maximum shear force and maximum normal force of the spring respectively, σ'_c is the mean effective confining stress normal to the pile element, and *perimeter* is the exposed perimeter of the element. The stiffness of the springs is just the slope of shear or normal force versus relative displacement between the pile node and the grid. This relationship is expressed in the Figure 3-5.

These coupling spring approach is similar as those used in p-y curves method except that the simplified bilinear elasto-plastic force-displacement relationship is adopted herein.

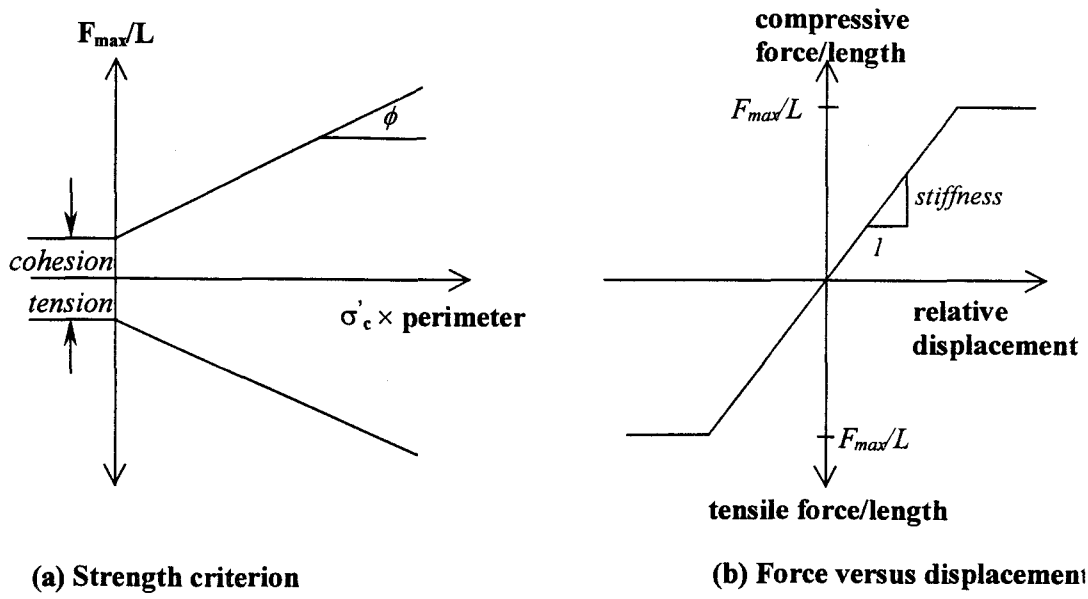

(a) Strength criterion **(b) Force versus displacement**

Figure 3-5: Material behavior of coupling spring for pile elements

4 SEISMIC PERFORMANCE OF GRAVITY RETAINING WALLS: FIELD CASES AND NUMERICAL MODELING

4.1 Introduction

The poor seismic performance of gravity type waterfront retaining walls has been primarily due to liquefaction of backfill and/or foundation soils. The waterfront structures have suffered failure due to sliding, overturning, loss of bearing capacity, and deep-seated shear failure. In addition, earthquake-induced movement of the walls has resulted in damaging lateral and vertical soil movements in backland areas. During the 1995 Hyogoken-Nanbu (Kobe) Earthquake, for example, ground deformations associated with liquefaction-induced failure of caissons have extended as much as 150 m into backland areas damaging waterfront components and suspending port operations at the Port of Kobe.

An early stage of this research involves the validation of the numerical analysis procedure for modeling the seismic performance of gravity type concrete caissons. The numerical models were first validated by comparing field performance of five well-documented case studies of caissons in unimproved and in improved soils during recent earthquakes to the computed response. Once the numerical models were calibrated using case studies, a series of parametric studies were then conducted and the results were synthesized into design charts for deformation-based analysis of concrete caissons, and simplified guidelines for estimating the extent of ground treatment that is required given allowable deformation limits for the concrete caissons.

4.2 Validation of the Numerical Model – Five Case Studies

After an extensive review of the literature five well documented case studies were selected. The case histories included: (1) two caissons at the Port of Kobe, i.e., Port Island and Rokko Island, which were affected by the M_w 6.9, 1995 Hyogoken Nanbu Earthquake (as described by Inagaki, et al., 1996), (2) two sites at Kushiro Port, i.e., Pier 2 and Pier 3, which were affected to differing degrees during the M_{JMA} 7.8, 1993 Kushiro-Oki Earthquake (Iai et al., 1994b; PHRI, 1994), and (3) one caisson at Akita Port, i.e., Gaiko Wharf, subjected to the M_{JMA} 7.7, 1983 Nihonkai-Chubu Earthquake (Hamada, 1992b). Requisite data for the case studies included: the geometry of the caisson, foundation pad and backfill, acceleration time histories recorded near the site, site specific geotechnical data, and pre- and post-earthquake wall geometry.

For each case study, the recorded free-field acceleration time histories were utilized. At each site the two perpendicular horizontal motions were combined vectorially to produce the acceleration time history acting normal to the quay wall. The acceleration records used at the base of the FLAC models were either computed from the recorded ground surface motions using the equivalent linear dynamic soil response program SHAKE91 (i.e., Kushiro and Akita case study) or directly used recorded motions at the site (i.e., Kobe case study) corresponding to the same depth of the model base. The dynamic soil properties used in SHAKE91 (Idriss and Sun, 1992) were obtained from measured *insitu* soil properties, or derived from established correlation with standard geotechnical parameters. The general location of each case study is shown in Figure 4-1.

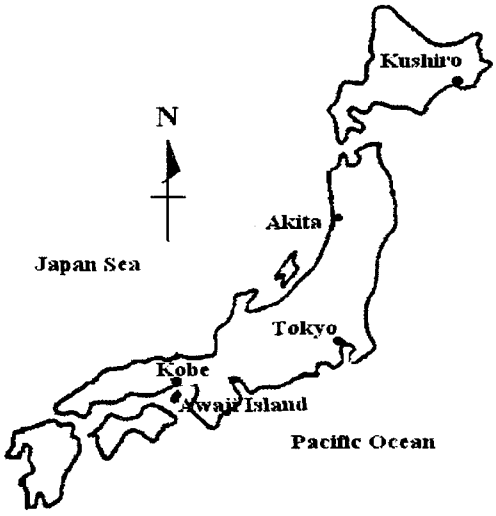

Figure 4-1: Location of case study

4.2.1 Hyogoken-Nanbu (Kobe) Earthquake (Case 1 and Case 2, 1995)

During the 1995 Hyogoken-Nanbu (Kobe) Earthquake (M_w 6.9), a great number of caisson type quay walls were damaged in Kobe Port, Japan (Werner and Dickenson, 1995; Inagaki et al., 1996). At the time of the earthquake, the port had 186 quay walls, about 90 percent of which were caisson type walls. These concrete caissons were subjected to very strong earthquake motion of 0.54g and 0.45g peak ground acceleration in the horizontal and vertical directions, respectively. Lateral deformations at the top of the caissons were about 5 m maximum and 3 m average, and inclined about 4 degrees towards the sea (Inagaki et al, 1996). Virtually all of the 240 berths at Kobe Port were closed indefinitely after the earthquake (i.e., only 6 of the 240 berths were serviceable to any degree). Repair costs for the port have been estimated at about $10 billion, and repair time to restore total operations at the port took roughly two years from the time of the earthquake. The severe earthquake

damage to waterfront retaining walls was primarily due to (1) liquefaction of backfill and foundation soils, and (2) the large initial forces on the caissons. The earthquake-induced liquefaction resulted in large horizontal ground displacements, damage to buried lifeline facilities, deep foundation, and waterfront structures.

The earthquake was a right-lateral strike-slip type with the epicenter of 15 km north of Awaji Island shown in Figure 4-1 and the hypocenter depth of 14.3 km below sea level. The maximum horizontal acceleration of 0.8g was observed in Kobe City. The Port of Kobe has been built almost entirely on reclaimed land. Sandy soil was placed over soft marine clay deposits (Werner and Dickenson, 1995). Two man-made islands, Port Island and Rokko Island as shown in Figure 4-2, have been constructed at the Kobe Port since 1966. The first stage of Port Island was completed in 1981 after 15 years of construction, and Rokko Island was completed in 1991 after 20 years of reclamation work. The second (final) stage of Port Island was almost completed when the earthquake hit Kobe Port in January 1995.

The direction of predominant motion from loci of the earthquake motion at Port of Kobe, as shown in Figure 4-3, is North-West to South-East, which is approximately perpendicular to the direction of the earthquake fault. The direction components of the projected accelerations perpendicular to the face lines of the quaywalls are shown in Figure 4-2. These direction components of the earthquake motions are one of the most relevant quantities acting as an inertia force to affect the seismic performance of the quay walls. They could change the behavior of the soils beneath and behind the caisson including excess pore water pressure increase in these soils.

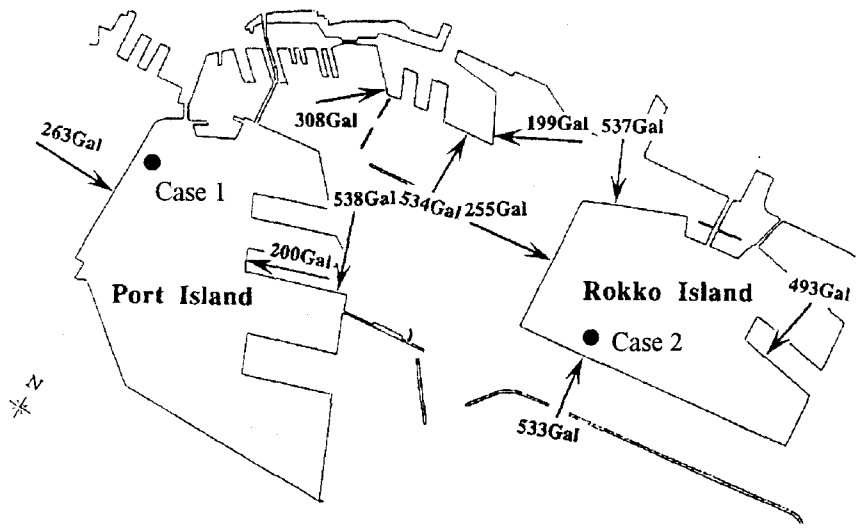

Figure 4-2: Two man-made islands, Port Island and Rokko Island, at Kobe Port and direction components of the projected accelerations (Inagaki et al., 1996)

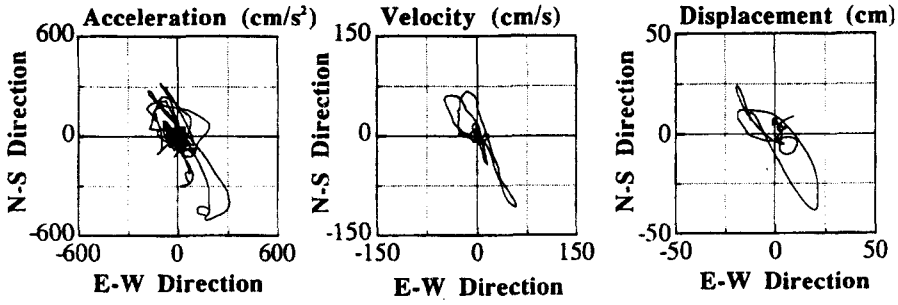

Figure 4-3: Loci of the earthquake motion at Kobe Port (Inagaki et al., 1996)

The acceleration components parallel to the face lines of the quaywalls also affect the performance of the quaywalls but their influence is indirect. A set of the earthquake motions recorded at downhole array on Port Island was obtained at depths of 0 m, 16 m, 32 m, and 83 m and the peak horizontal accelerations in the North-South and East-West component are shown in Figure 4-4.

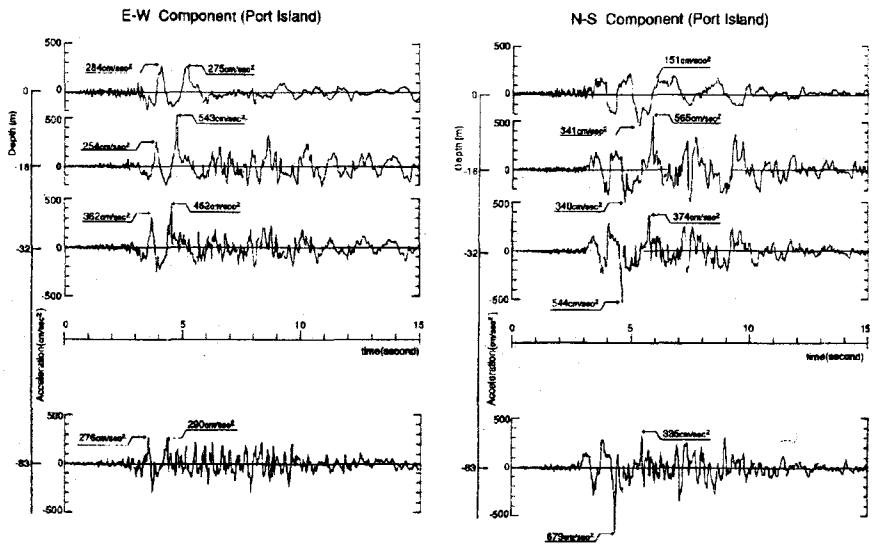

Figure 4-4: Recorded accelerations at Port Island (Toki, 1995)

Understanding the importance of the direction components of the earthquake motion, the recorded acceleration time history, as shown in Figure 4-4, perpendicular to the face lines of caissons will be used in the Case 1 and Case 2. Detailed description will be given in the following sections.

4.2.1.1 Case 1: Port Island

4.2.1.1.1 Site Description

Port Island is an artificial island due south of Kobe's central business district, and was constructed in two phases. In the first phase, between 1966 and 1981, 436-hectare area was reclaimed. In the second phase, the island was then extended southward by reclaiming 319 additional hectares.

Several soil improvement methods such as sand drain and pre-loading methods were utilized in the areas where major structures were built to accelerate consolidation of the alluvial marine clay. Vibration compaction and sand compaction pile methods were used in order to compact fills as a countermeasure against liquefaction and minimize differential settlement for the bearing layers where structures are supported by spread foundation. The improvement zones at Port Island is shown in Figure 4-5. Figure 4-5 shows that the areas where soil improvement has been implemented are located primarily within the interior of the island, i.e., at areas of commercial development not associated with shipping and cargo handling. There was very little soil improvement being performed at the shipping berths and wharves along the periphery of the Port Island. The penetration resistances obtained by Standard Penetration Test (SPT N-value) ranges from 5 to 10 blows/0.3m before treatment, and increasing to 18 to 31 blows/0.3m after treatment.

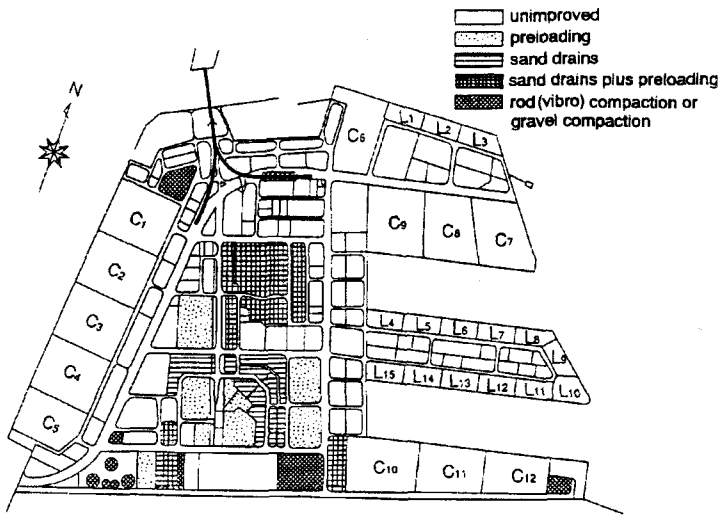

Figure 4-5: The improvement zones at Port Island (Watanabe, 1981)

4.2.1.1.2 Soil Conditions

Port Island was developed by barge-dumping granular soil onto a roughly 10~15 m thick layer of very soft to soft marine clay. The soils used for backfill were largely decomposed granite (Masado) excavated from the Rokko Mountains and Awaji Island and Pliocene deposits of mudstone, sandstone and conglomerate of Kobe Group from western Kobe, and to a lesser degree of Pleistocene marine clay and gravel of Osaka Group and dredged sands. The backfill soils range in classification from SP/SM to SW/SM. The SPT N-value ranges from 5 to 10 blows/0.3m in the backfill soil, resulting in high susceptibility to liquefaction. The range of grain-size distribution curves of Masado, and the mud stone-origin and tuff-origin sandy soils, which were used as backfill soils for Port Island and Rokko Island, respectively, is shown in Figure 4-6. About 80 percent of Masado grain-size distribution lies within the range of potential liquefaction (0.01mm < grain size < 5mm) and about 50 percent lies within the range of high possibility of liquefaction (0.03mm < grain size < 3mm).

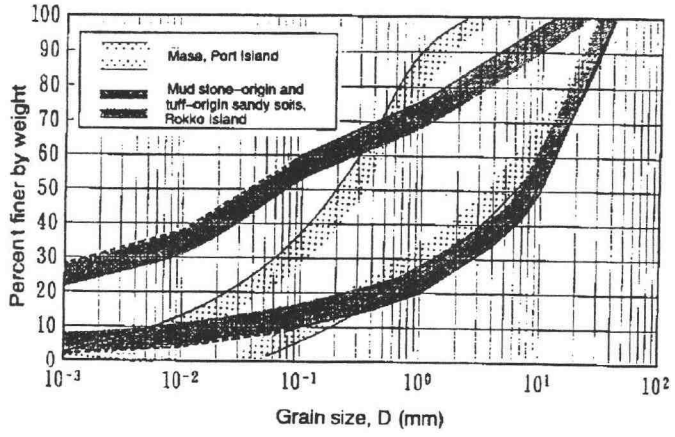

Figure 4-6: Grain size distribution curves for backfill soils at Port Island and Rokko Island (Yasuda et al., 1996)

From the ground surface down, the soil profile at Port Island consists of approximately 15~20 m of loose hydraulically placed sand fill underlain by 15 m of soft to medium stiff marine clay; 30~35 m of interlayered dense gravelly sand and stiff clay; 20 m of stiff marine clay; and interbedded very dense sand and stiff to hard clay to the maximum depth of the borings at 90 m. The soil profile at Port Island downhole strong motion instrument array station is shown in Figure 4-7.

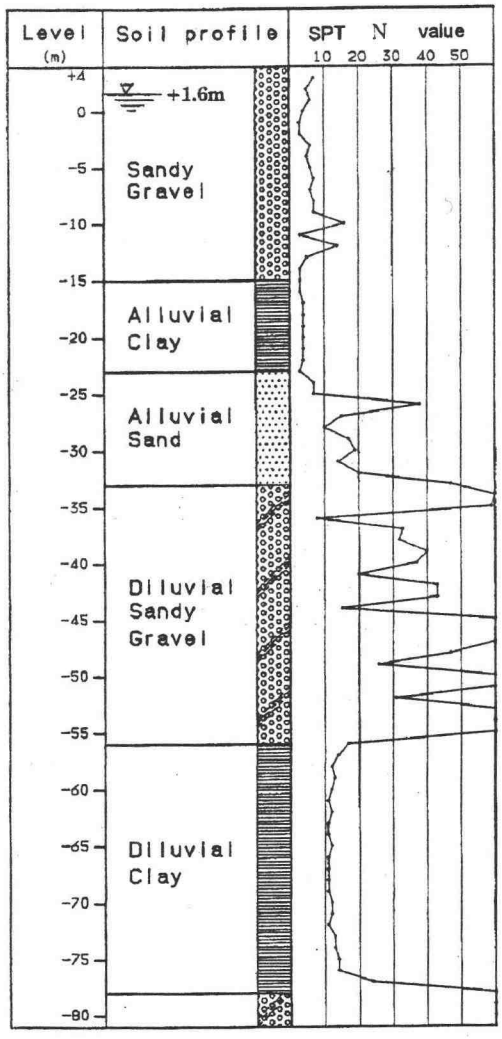

Figure 4-7: Soil profile at the site of vertical array of seismograph (Shibata et al., 1996)

4.2.1.1.3 Earthquake Damage

The extensive occurrence of liquefaction in the sandy backfill at almost every pier within the Port of Kobe has been investigated and sand boils have been observed at various sites as shown in Figure 4-8.

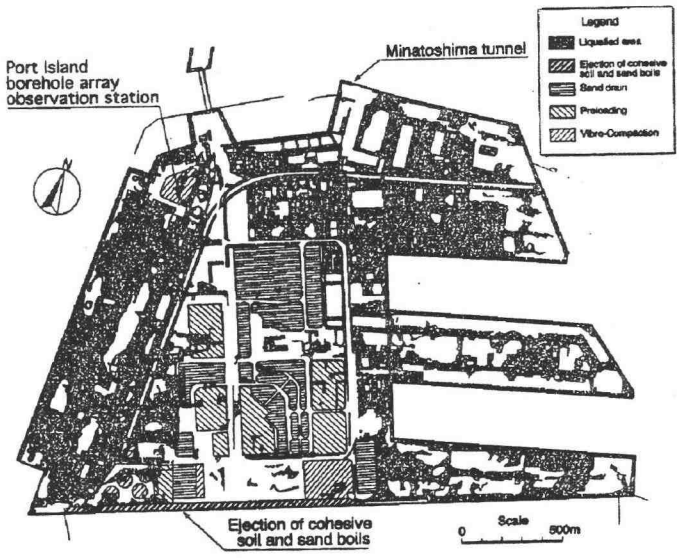

Figure 4-8: Distribution of liquefaction at Port Island and areas where soil improvement techniques were used (Shibata et al., 1996)

The ground surface settlements due to extensive liquefaction were measured at various locations on Port Island following the earthquake. The ground distortion caused widespread damage to lifeline systems such as gas and water pipes, and resulted in large restoration costs. The settlement of the ground surface sufficiently far from the waterfront was estimated by surveying the difference in elevation between supposedly subsided flat ground areas and objects such as pile-supported buildings which were apparently free from any settlement (Ishihara, et al., 1996). The survey

result of settlements observed on the ground surface at Port Island is shown in Figure 4-9. The maximum measured settlement up to 90 cm and average value of 50 cm can be observed on Port Island.

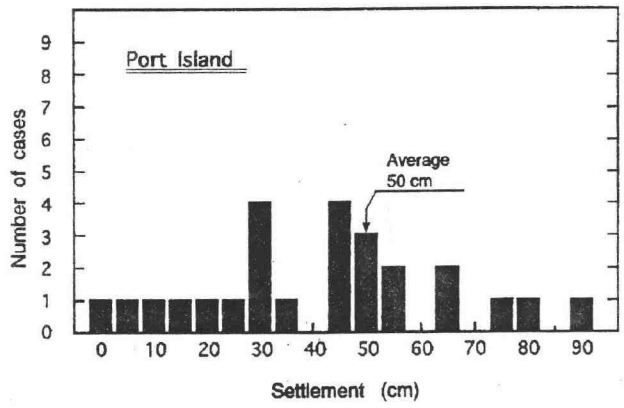

Figure 4-9: Settlements observed on the ground surface at Port Island (Ishihara et al., 1996)

During Kobe Earthquake, lateral displacements associated with liquefaction-induced failure of caissons have extended as much as 150 m into backland areas damaging waterfront components and suspending port operations. Measurements of lateral displacement were basically made on the ground by measuring the openings of ground cracks starting from a fixed reference point located far enough inland where no cracks were observed. By summing up those openings from the reference point, the lateral displacements in the direction perpendicular to the quay wall line were obtained. Figure 4-10 shows the distribution of lateral displacement behind the quaywall obtained from different locations and comparison between measured and

numerical prediction will be presented in the latter section. The lateral displacements were generally large near waterfront and decreased with distance into backland.

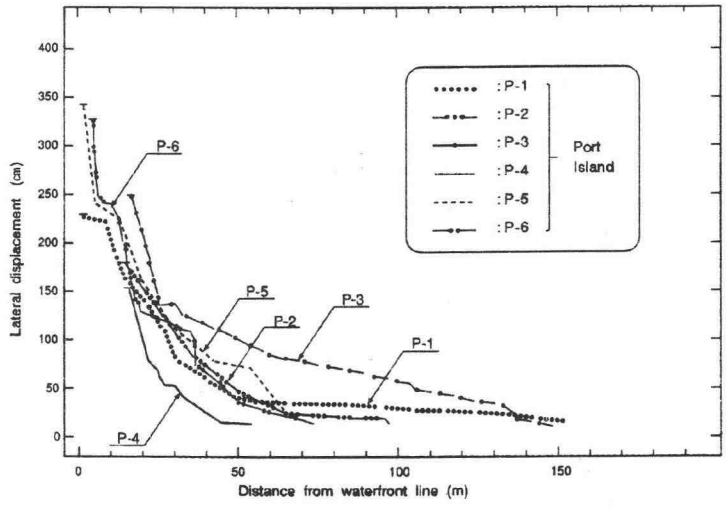

Figure 4-10: Distribution of lateral displacement behind the quaywall (Ishihara, et al., 1996)

Typical damage to concrete caisson quay walls at Port Island before and after earthquake is shown in Figure 4-11. As shown in this figure, the caisson moved seaward by approximately 3 meters and settled differentially 1 meter, with inclination of about 3 degrees on average. The damage of concrete caissons was mainly due to liquefaction of backfill soil (Inagaki et al., 1996). This lateral and vertical deformation was common at the port in the aftermath of the 1995 Hyogoken-Nanbu Earthquake. The horizontal and vertical displacements measured and calibrated by the Global Positioning System along the perimeter of Phase 1 of Port Island are shown in Figure 4-12 and Figure 4-13, respectively. The measurements of seaward displacements indicates that predominant displacement tend to occur in the North-South direction,

which is consistent with the direction of earthquake motion. In general, the caissons suffering damage of seaward lateral displacements of 1 to 5 m have been observed at Port Island as a result of liquefaction in the soils behind or beneath the caisson.

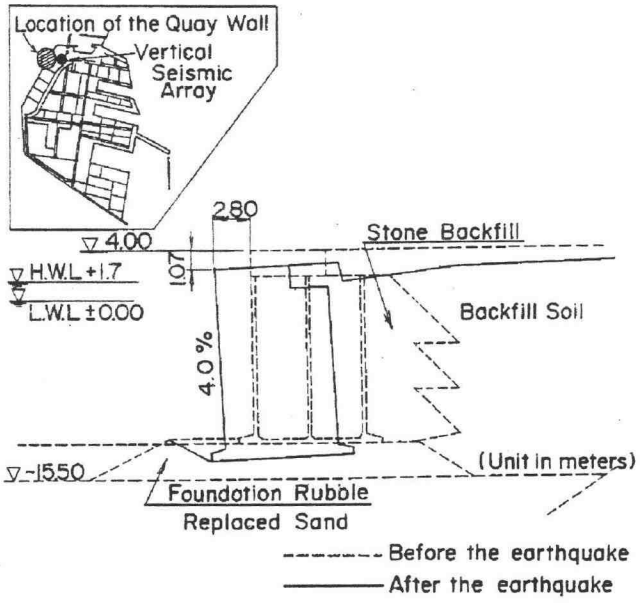

Figure 4-11: Deformation of caisson at Port Island (Inagaki et al., 1996)

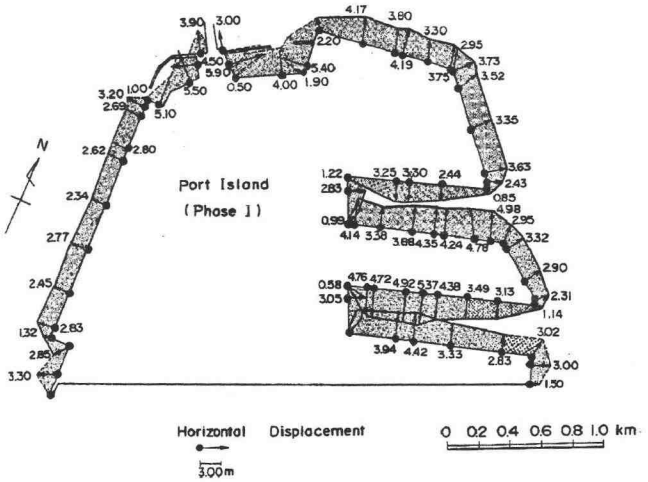

Figure 4-12: Horizontal displacements at the top of the caissons (Inagaki et al., 1996)

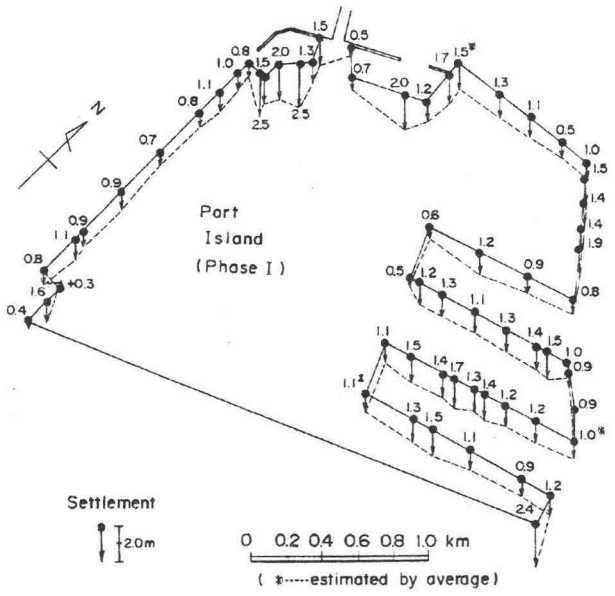

Figure 4-13: Vertical displacements at the top of the caissons (Inagaki, et al., 1996)

The seismic design procedures used for caissons at Port of Kobe have been based primarily on psuedostatic method using a variety of seismic coefficients. Seismic coefficient used in the design of the caissons at Port Island was 0.1. The design of caissons did not take the effects of liquefaction of foundation and backfill soils into account, i.e., purely subjected to earthquake inertia forces. The values of seismic coefficients obtained from seismic zone maps, which provide the seismic coefficients for seismic design in Japan in 1959 and 1978, are shown in Figure 4-14. In both maps, Kobe lies in the region rating the highest seismic coefficient. It should be noted that the range of seismic coefficients was reduced from 0.15-0.25 to a value of 0.15 in the latter code. The final seismic coefficient in 1959 code was decided from taking into consideration the kind and importance of the structure, and the condition

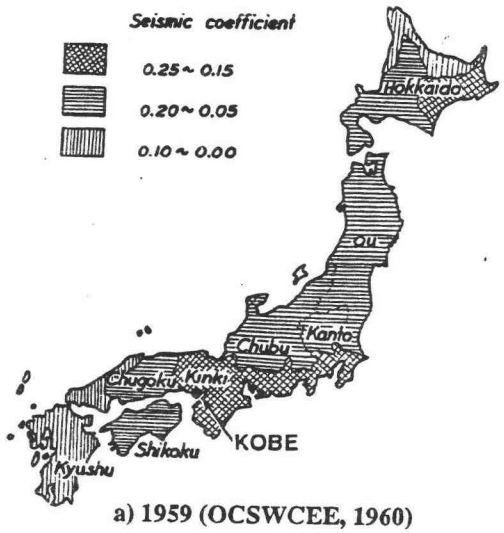

a) 1959 (OCSWCEE, 1960)

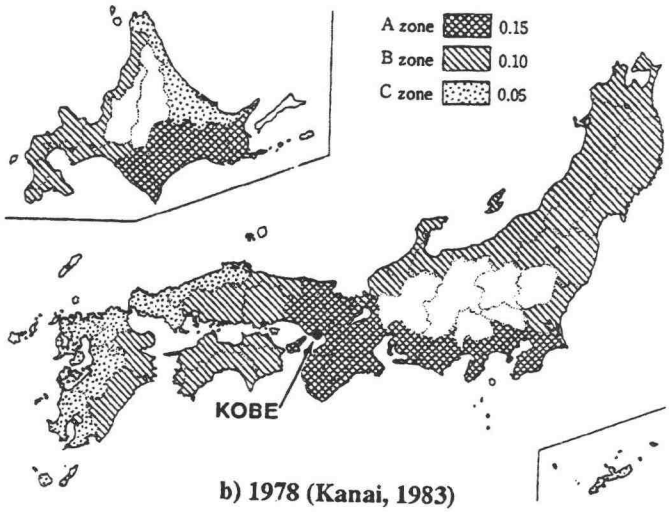

b) 1978 (Kanai, 1983)

Figure 4-14: Horizontal seismic coefficients used for design of port facilities in Japan

of the foundation. However, no information was available regarding the factors used in the code to represent the soil conditions and the importance of the structure. The factors of safety incorporated into the seismic design of the caissons were 1.0 and

1.1~1.2 for sliding and overturning, respectively. The level of shaking during the earthquake, as previously indicated in Section 4.2.1 by the peak horizontal ground acceleration of 0.54 g, obviously exceeded the limiting condition considered in the seismic design of a caisson wall at Port of Kobe.

4.2.1.2 Case 2: Rokko Island

4.2.1.2.1 Site Description

Rokko Island, which is located in the east of Port Island, is also a reclaimed island. Rokko Island was constructed between 1972 and 1990 by excavating soil materials from Suma and from the Rokko Mountains. The total area of Rokko Island is approximately 580 hectares.

As described in Section 4.2.1.1, several soil improvement methods were also utilized at Rokko Island. Once again, the purpose of the soil improvement was not for the mitigation of liquefaction during earthquake. Only one zone, where a tram depot was to be built at Rokko Island, was compacted by sand compaction method to prevent the occurrence of liquefaction. Most of the soil improvement work was advanced to the bottom of the alluvial soft clay. The improvement zones at Rokko Island is shown in Figure 4-15. As shown in this figure, there was only small part of the soil improvement being implemented along the periphery of the Rokko Island. The average SPT N-value ranges from 8 to 10 blows/0.3m and from 14 to 18 blows/0.3m in untreated and in treated subsoil, respectively.

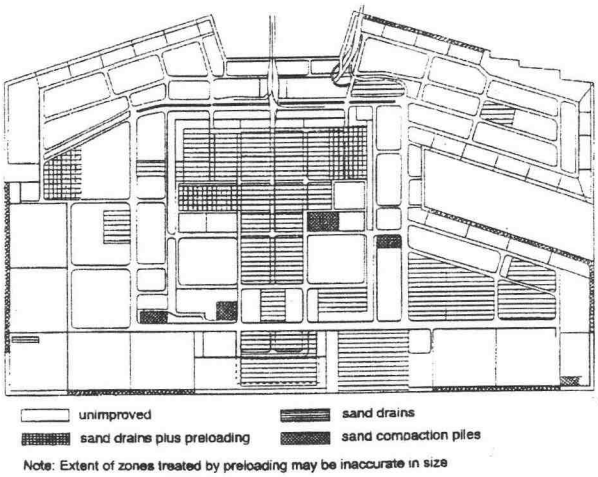

Figure 4-15: Improvement zones at Rokko Island (Yasuda et al., 1996)

4.2.1.2.2 Soil Conditions

The fill used in the inland portions of Rokko Island contains a large portion of crushed mudstone and siltstone material. The northern section of Rokko Island was reclaimed first using Masado as used at Port Island, and later the southern section was reclaimed using both debris of the Kobe Group and waste fill from construction sites. The subsurface conditions at Rokko Island are fairly similar to those at Port Island. Soil profile consists of loose sandy fill (F) with SPT N-values of 5~10 blows/0.3m, soft to medium stiff marine clay (Ac), and interlayered very dense sand and stiff to hard clay (Dsc) as shown in Figure 4-16.

4.2.1.2.3 Earthquake Damage

A number of sand boils were observed along the periphery of the Rokko Island. The distribution of soil liquefaction on Rokko Island and area where various

soil improvement techniques were used is shown in Figure 4-17. The degree of liquefaction was much less severe as compared to Port Island.

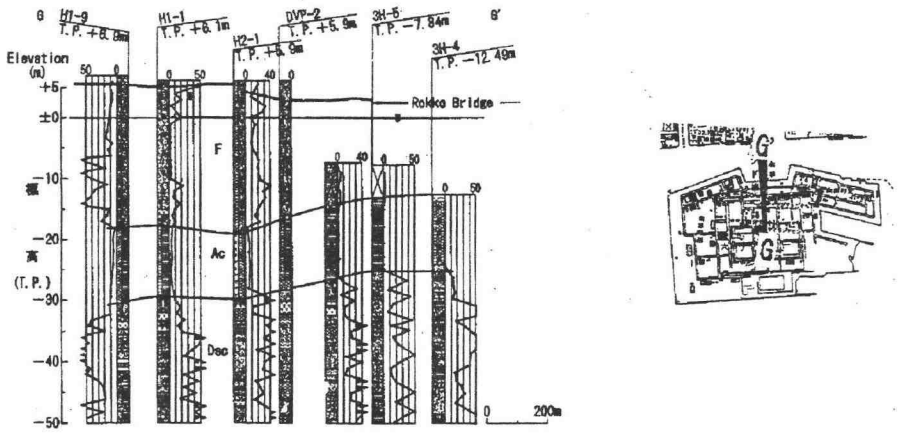

Figure 4-16: Soil profiles along G-G' at Rokko Island (Hamada et al., 1996)

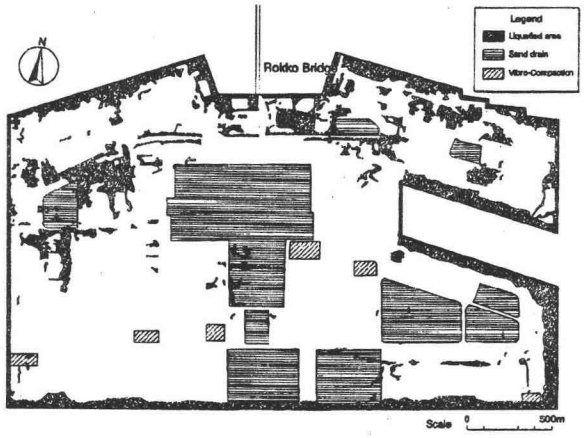

Figure 4-17: Distribution of liquefaction at Rokko Island and areas where soil improvement techniques were used (Shibata et al., 1996)

The maximum ground surface subsidence was reported to be about 3 meters just behind the caisson. There were many deep ground cracks parallel to the caisson

due to the seaward movement of the caisson. The results of inland ground settlement survey, similar procedures as mentioned in Section 4.2.1.1, are presented in Figure 4-18 with maximum settlement of 50 cm and an average value of 40 cm.

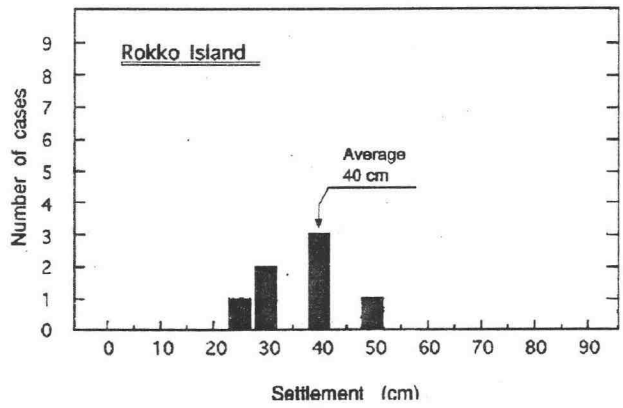

Figure 4-18: Settlements observed on the ground surface at Rokko Island (Ishihara, et al., 1996)

Typical damage to concrete caisson at Rokko Island before and after earthquake is shown in Figure 4-19. As shown in this figure, the caisson moved seaward by approximately 5 meters, settled 2 meters, and inclined about 4 to 5 degrees on average. The backfill soils behind the walls sank accordingly as in the same magnitude as those in the horizontal wall movement. No collapse or overturning of the caisson walls was observed. The magnitude of displacement and settlement at the top of the caisson, shown in Figure 4-19, is larger than that measured at Port Island. As mentioned in Section 4.2.1, the direction of predominant motion is North-West to South-East. The caisson is subjected to larger inertia force; therefore, it yields larger displacement and settlement. This is consistent with the directional components

of the accelerations shown in Figure 4-2, in which 0.54g was observed in the direction of North-South. The horizontal and vertical displacements measured and calibrated by the Global Positioning System along the perimeter of Rokko Island are shown in Figure 4-20 and Figure 4-21, respectively.

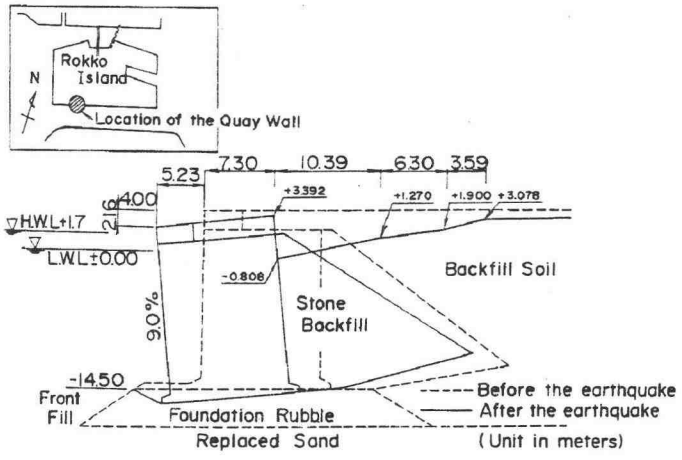

Figure 4-19: Deformation of caisson at Rokko Island (Inagaki et al., 1996)

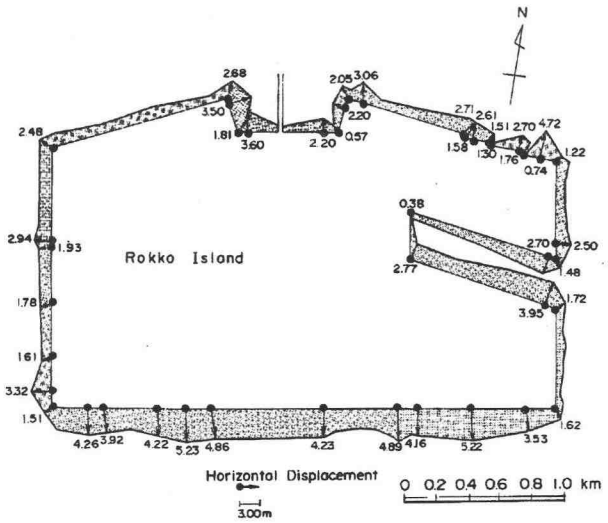

Figure 4-20: Horizontal displacements at the top of the caissons at Rokko Island (Inagaki et al., 1996)

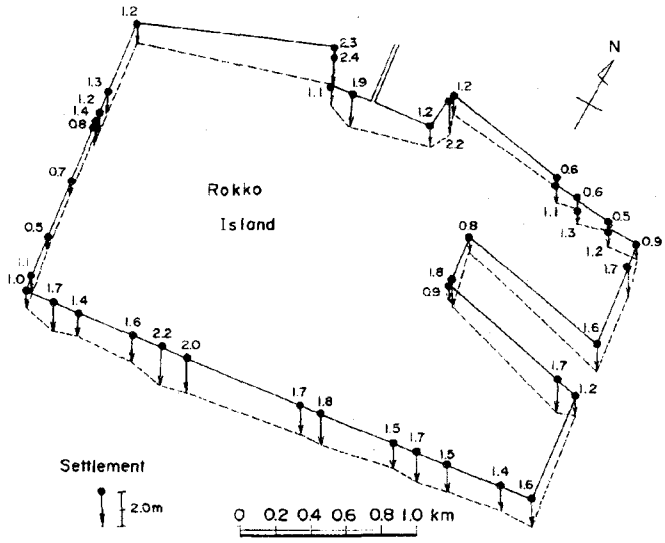

Figure 4-21: Vertical displacements at the top of the caissons at Rokko Island (Inagaki et al., 1996)

4.2.1.3 Analyses of Numerical Models at Kobe Port

Detailed description of numerical modeling considerations has been provided in Chapter 3. In the following sections only specific description of the modeling considerations associated with each case study will be given.

4.2.1.3.1 Port Island

The geometry of Port Island model indicated in Figure 4-2 and labeled as Case 1 is used. The model geometry is shown in Figure 4-22. The model is analyzed using a mesh of 60 by 15 zones. The input soil parameters for Port Island model are provided shown in Table 4-1. The soil parameters used in the analysis are mainly derived from Inagaki et al. (1996).

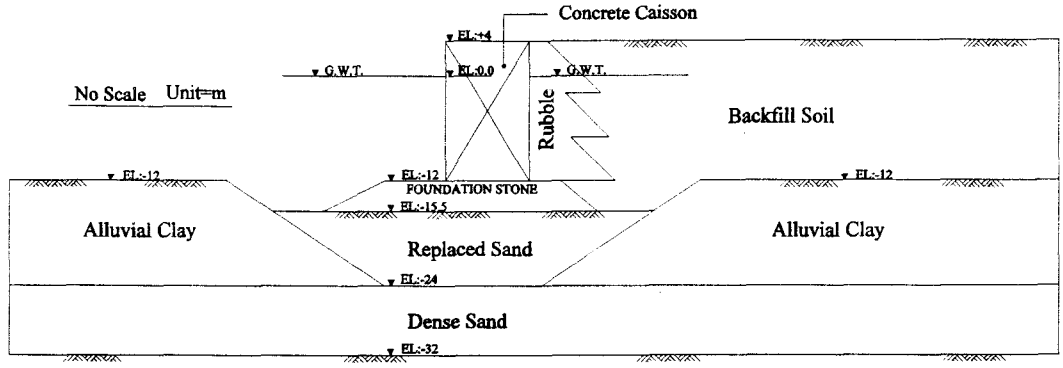

Figure 4-22: Geometry of Port Island model

Table 4-1: Input Soil Parameters for Port Island Model

Soil Type	ρ_d *(kg/m^3)*	ϕ *(deg.)*	G_m *(Pa)*	K_m *(Pa)*	κ *(m/sec)*	c *(Pa)*
Alluvial Clay	1700	30	7.5e7	3.5e8	1e-10	6000
Replaced Sand	1800	37	5.8e7	1.2e8	1e-8	0
Foundation and Backfill Rubble	2000	40	1.8e8	4.4e8	1e-2	0
Backfill Sand	1800	36	7.9e7	1.6e8	1e-7	0
Dense Sand	1600	38	6.5e7	1.3e8	1e-7	0
Soil in the Caisson	1750	35	8.0e7	1.6e8	-	0

Note: ρ_d = dry density; ϕ = friction angle; G_m = mean shear modulus; K_m = mean bulk modulus; κ = permeability; c = cohesion

The both sides of the model boundary are set far enough in order to avoid the boundary effect. The lateral boundaries are fixed in the horizontal direction, and the base is fixed in both the horizontal and vertical directions under static (gravity) loading. A static equilibrium under gravity loading to simulate the initial stresses existing insitu is first achieved under drained condition. The dynamic analysis is then

employed under plane strain and undrained conditions. At the side boundaries, free-field response motions are given through transmitting boundaries to approximate incident waves and radiation to and from the region set for the analysis. At the bottom boundary, the earthquake motion recorded at a depth of 32 m at Port Island, which corresponds to the base of the numerical model, is directly used as the input motion. In accordance with the direction of the caisson, East-West component of earthquake motion as shown in Figure 4-4, which is perpendicular to the caisson, with peak horizontal acceleration of 462 cm/sec^2 (0.47g) is used for the analysis. Rayleigh damping with a critical damping ratio of 0.05 at a frequency of 15 Hz determined from empirical formulas is used and pore pressure dissipation is not allowed during shaking.

The concrete caisson is represented by the beam element. The structure properties are defined by cross-sectional area, moment of inertia, and Young's modulus of the beam element as shown in Table 4-2. An interface between structure element and soil behind it is used to represent planes on which sliding or separation can occur. The interface is represented as normal and shear stiffness between two planes that may contact one another. The normal and shear stiffness of the interface are determined by the relationship of shear modulus and bulk modulus as follows:

$$Stiff = 10 \times Max\left(\frac{K + 4/3\, G}{\Delta Z_{\min}}\right) \tag{4-1}$$

where K = bulk modulus, G = shear modulus, ΔZ_{min} = the minimum distance between two adjacent grid points.

Table 4-2: Structure and Interface Properties for Port Island Model

Structure (Beam) Properties		*Interface Properties*	
Cross-sectional Area (m^2)	0.1	Normal Stiffness (Pa)	1.5e9
Moment of Inertia (m^3)	8.3e-3	Shear Stiffness (Pa)	1.5e9
Young's Modulus (Pa)	2.07e10	Interface friction angle (degree)	15

4.2.1.3.2 Results of Prediction (Port Island)

The deformed mesh at the end of shaking is shown in Figure 4-23. The residual displacements at the top of the caisson are 3.29 m and 0.95 m in the horizontal and vertical direction with an inclination of 1.2 degree, respectively. The predictions agree well with the observed displacements as shown in Figure 4-12 and 4-13, in which 2.34~3.2 m for horizontal displacement of the caisson with average value of 2.7 m and 0.8~1.1 m for settlement of the caisson with averaged vale of 0.9 m were observed. The predicted lateral displacement and settlement at the top of caisson are approximately overestimated by 18% and 5%, respectively, comparing to measured average value.

As seen from Figure 4-23, the mode of the deformation of the caisson tends to tilt into the foundation rubble beneath the caisson. This mode of deformation is consistent with the actual mode of deformation observed throughout the Port of Kobe. Full liquefaction ($r_u = 1$) was predicted at numerous locations in the backfill sand and partial liquefaction ($0 < r_u < 1$) in the replaced sand. The degree of liquefaction in the replaced sand was less than that in the backfill sand due to higher SPT-N values ($15 < N < 22$), hence, higher liquefaction resistance in the replaced sand layer. The pore

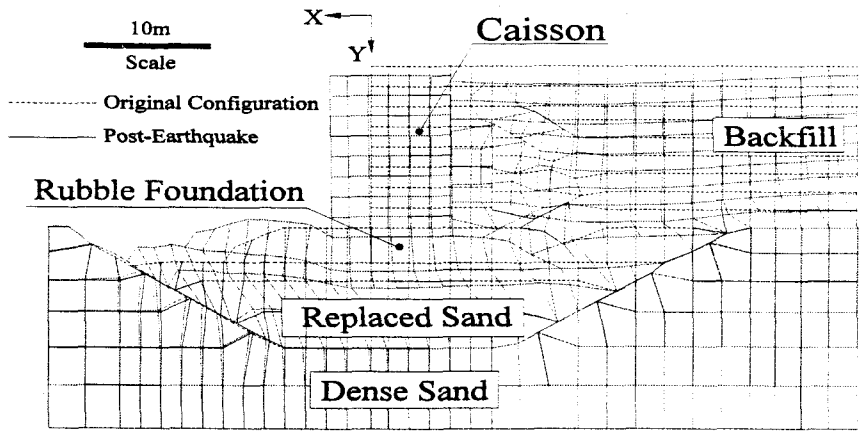

Figure 4-23: Deformed mesh of Port Island model

pressure ratios beneath the caisson and right behind the caisson were less than 0.7 and 0.6, respectively. Predicted liquefaction of the backfill sand is consistent with the sand boils observed in this area. Although the pore pressure ratio beneath the caisson has not reached unity, the excess pore water pressure has significantly increased during the shaking. The pore water pressures in the backfill sand were increased by 2~3 times of static pore water pressure and about 1.5~2 times in the replaced sand as shown in Figure 4-24 and Figure 4-25, respectively. Those increased pore water pressures significantly affected the deformation of the caisson.

Another indication of liquefaction in the backfill is shown in Figure 4-26 which shows the comparison of input acceleration time history to predicted acceleration time history at the top of the backfill. It can be observed that acceleration time history at the top of the backfill is de-amplified due to the liquefaction of the backfill. It is obvious that the performance of the caisson is significantly affected by

both high inertia force (a_{max} = 0.47g) and additional lateral pressure due to soil liquefaction in the backfill sand.

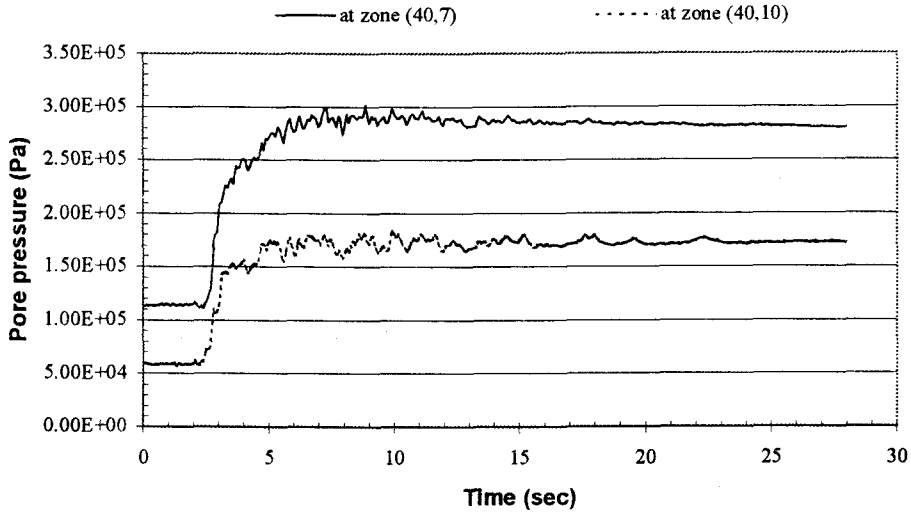

Figure 4-24: Pore water pressure distribution history in the backfill sand (Port Island)

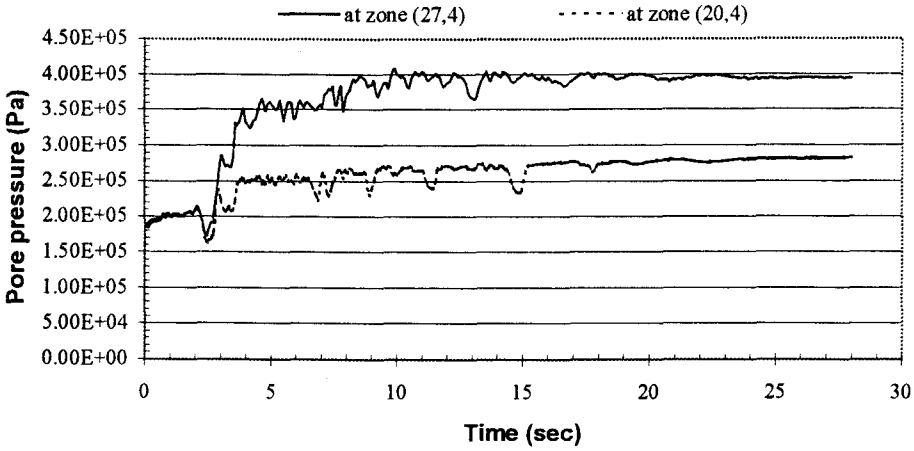

Figure 4-25: Pore water pressure distribution history in the replaced sand (Port Island)

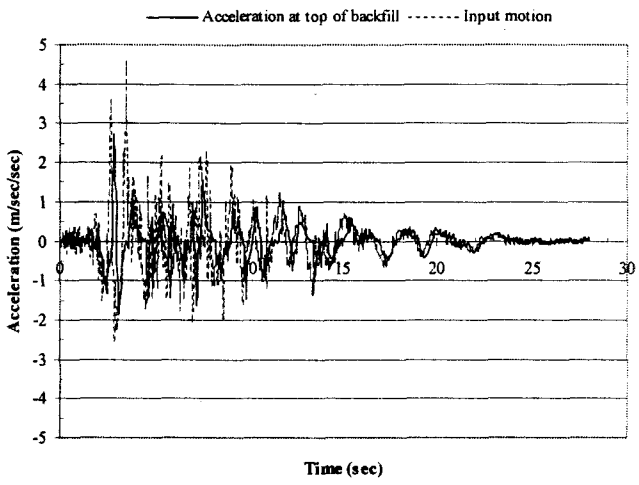

Figure 4-26: Comparison of input motion to acceleration time history at the top of the backfill (Port Island)

The slip plane between the caisson and the backfill soil was modeled. The relative settlement was predicted as 70 cm including the post-liquefaction volumetric strain settlement. This amount of settlement behind the caisson is in the range of observed settlement measured by Ishihara (1996). The comparison between predicted settlements and measured settlements in the backland is presented in Figure 4-27. It should be noted that measured settlements in Figure 4-27 were obtained from the fixed point (reference point) in the backland where no significant cracks were observed whereas predicted settlements were calculated from original ground surface elevation. The measured settlement distribution should be interpreted as a local variation with respect to the reference point. It is reported by the Development Bureau of Kobe City that the settlement in the interior of the Port Island due to earthquake was of the order of 20~100 cm. If the overall settlements are concerned, all settlement

curves shown in Figure 4-27 should be moved down by 20~100 cm. However, the pattern of settlements in the backland is consistent with actual measured values.

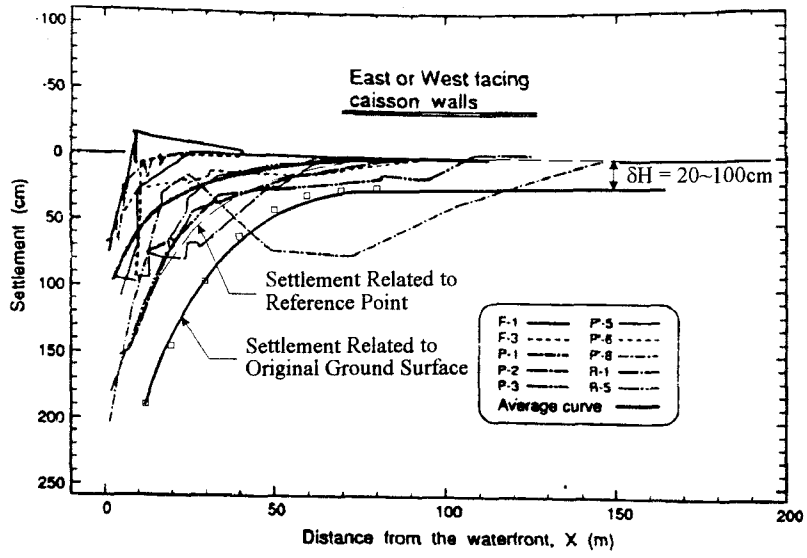

Figure 4-27: Comparison of observed settlements and predicted settlements in the backland at Port Island (after Ishihara et al., 1996)

The normalized lateral displacement (lateral displacement/lateral displacement at waterfront) versus normalized distance (distance from waterfront/distance of influence) from the waterfront along with predicted values is presented in Figure 4-28. The distance of influence is defined as a distance from the waterfront to the reference point where there is no visible cracks or fissures on the ground surface. It is also an upper limit for all data investigated at Port of Kobe and a distance of 150 meters is chosen as distance of influence. The lateral displacements are over-predicted within 45 meters (e.g., 0.3 on the x-axis) from the waterfront and under-predicted beyond that distance yet within the observed range. Since the lateral spreading is

accompanied by the ground distortion due to non-uniform distribution of soil deformation taking place in horizontal and vertical directions near waterfront, partial cracks or fissures could be filled with liquefied soils, hence, yield less measured lateral ground displacements. However, overall prediction of lateral ground displacement in the backland is in a reasonable agreement.

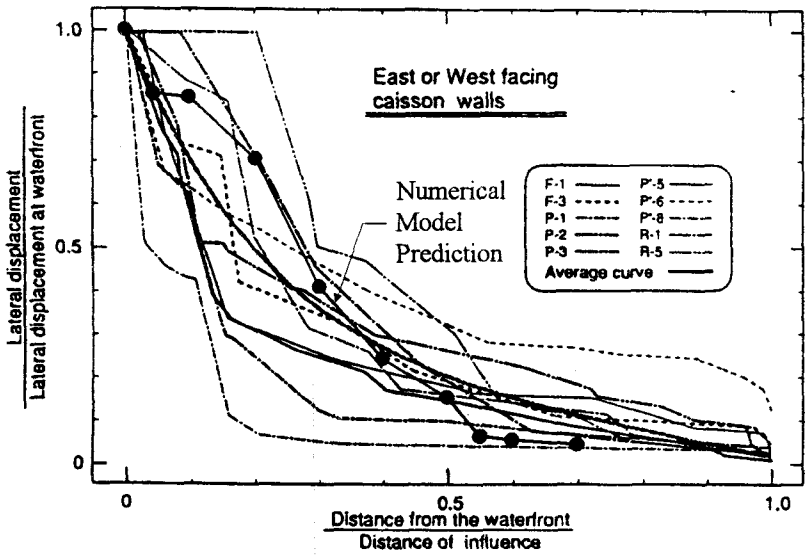

Figure 4-28: Normalized lateral displacements versus normalized distance from the waterfront for East or West facing quaywalls at Port Island (after Ishihara et al., 1997)

4.2.1.3.3 Rokko Island

The location of Rokko Island model indicated in Figure 4-2 with labeled as Case 2 is used. Rokko Island model has been setup in a similar manner to Port Island model in every aspect except that a layer of front sand fill is added and the earthquake motion component in the North-South direction at a depth of 32 m from ground

surface as shown in Figure 4-4 is used. This earthquake motion component is perpendicular to the face line of the caisson at Rokko Island, with peak horizontal acceleration of 544 cm/sec^2 (0.55g). The SPT-N values of 10 and 25 blows/0.3m for the backfill sand and replaced sand beneath the caisson are used, respectively. Also, the multi-lift rubble backfill used at Port Island has been replaced by a single-lift rubble backfill as shown in Figure 4-19.

4.2.1.3.4 Results of Prediction (Rokko Island)

The predicted residual displacements at the top of the caisson are 3.9 m and 1.21 m in the horizontal and vertical direction with an inclination of 3.6 degree, respectively. Comparing these predicted values to those measured values as shown in Figure 4-20 and 4-21, in which 3.92~5.23 m for the horizontal displacement of the caisson with averaged value of 4.5 m, and 1.4~2.2 m for settlement of the caisson with averaged value of 1.7 m, were observed, the predicted displacements are within a reasonable agreement. The predicted lateral displacement and settlement at the top of caisson are approximately underestimated by 13% and 30%, respectively, as compared to measured average value. The mode of the deformation of the caisson at Rokko Island is similar to that at Port Island, i.e., the caisson tends to tilt into the foundation rubble beneath the caisson. The residual displacements are larger than that at Port Island as a result of greater acceleration recorded in the North-South direction as described in section 4.2.1. The liquefaction has been predicted in the backfill and in the front sand fill. The pore pressure distributions in the backfill sand and replaced sand during shaking are presented in Figure 4-29 and Figure 4-30, respectively.

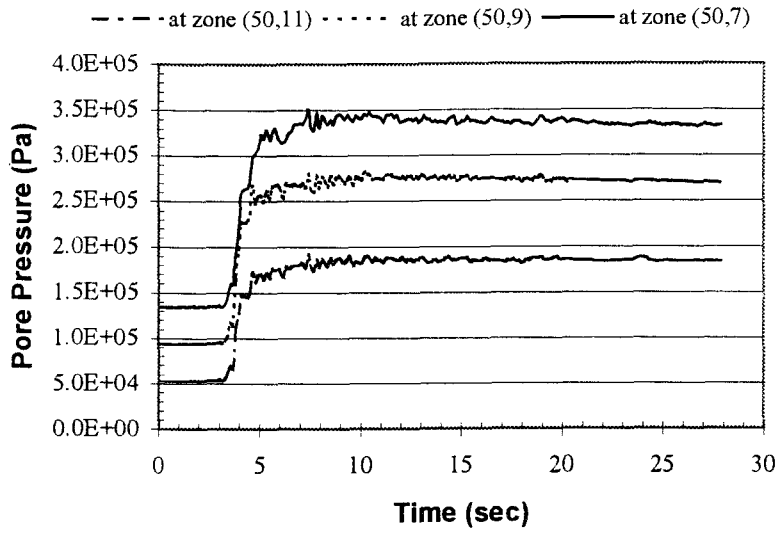

Figure 4-29: Pore pressure distribution history in the backfill (Rokko Island)

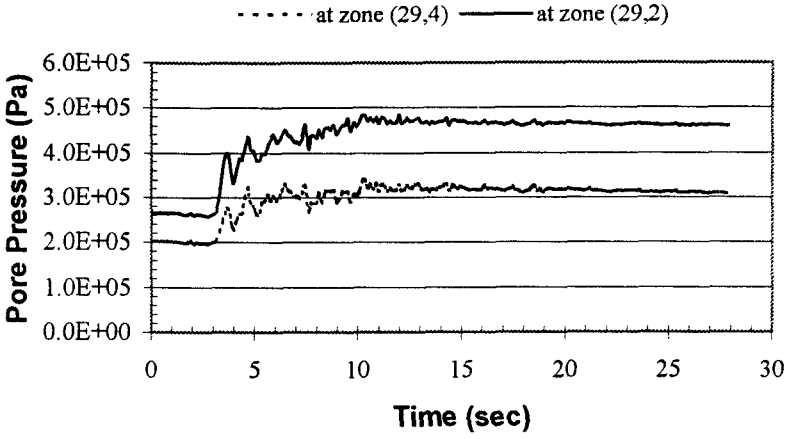

Figure 4-30: Pore pressure distribution history in the replaced sand (Rokko Island)

It can be seen that pore water pressures in the backfill were increased by 2.5~3.5 times of static pore water pressures and about 1.5~2 times in the replaced sand. The behavior of increased pore pressures is similar to that observed in Port

Island model in which less residual displacements at the top of the caisson were predicted. It may be reasonably assumed that for the quaywalls facing North or South direction at Rokko Island, the effect of strong inertia force contributes an important part in producing the lateral displacement of the quaywalls whereas the effect of the inertia force was moderate and the effect of liquefaction may be the factor for the quaywalls facing East or West at Port Island. However, the relatively quantitative contribution of the inertia force and liquefaction is not clear at present study.

The comparison between predicted settlements and measured settlements in the backland is presented in Figure 4-31. The R'-1 curve shown in this figure is close to the location of the quaywall being chosen for the analysis. As discussed in previous section, the order of 20~100 cm overall settlement should be added for all curves shown in Figure 4-31.

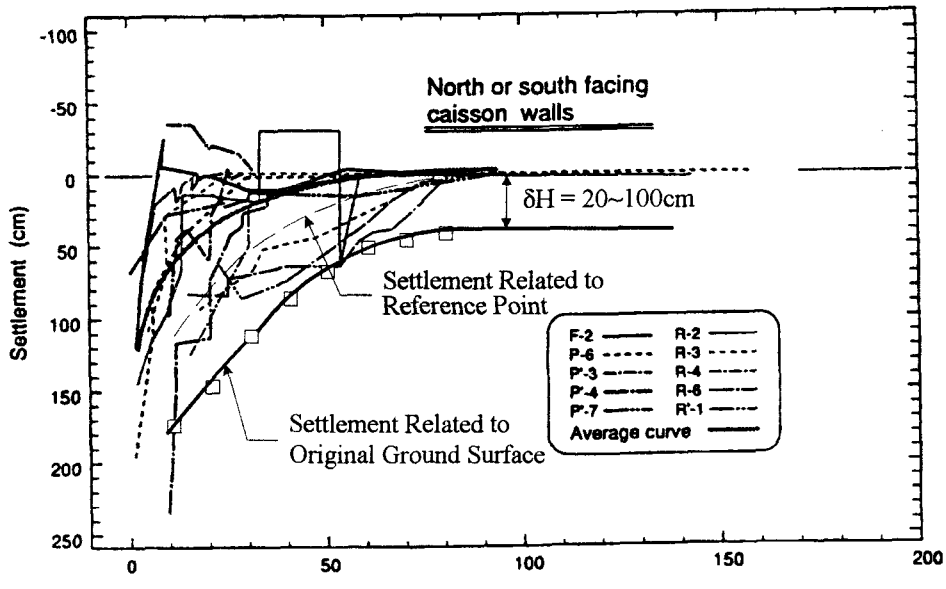

Figure 4-31: Ground settlements versus the distance from the waterfront at Rokko Island (after Ishihara et al., 1996)

The normalized lateral displacement versus normalized distance from the waterfront along with predicted values is presented in Figure 4-32. The predicted lateral ground displacements are over-predicted as compared to measured values. It may be the consequence that more factors are involved in producing larger displacements by stronger inertia force as compared to those induced by moderate inertia force and liquefaction at Port Island. This also shows uncertain behavior of lateral ground spreading influenced by factors regarding the strong earthquake shaking.

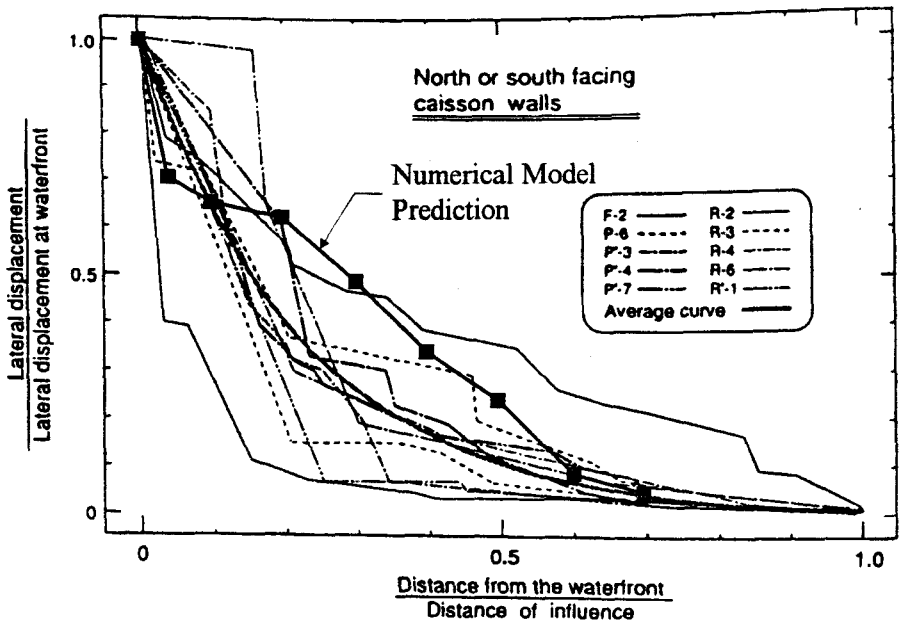

Figure 4-32: Normalized lateral displacements versus normalized distance from the waterfront for North or South facing quaywalls at Rokko Island (after Ishihara et al., 1996)

A comparison of measured averaged lateral displacements versus predicted displacements for Port Island and Rokko Island is shown in Figure 4-33. In this figure, two bold lines represent the measured values, which are average value of all measured values at both Port Island and Rokko Island, for the East-West facing walls and North-South facing walls. Interpolation curves of predicted values, represented by dot lines, for both East-West and North-South facing walls are also shown in Figure 4-33. The predicted curves are somewhat over-predicted close to caisson, i.e., 0.3 on the x-axis (= 45 m from the caisson in real scale), however, the predicted values agree favorably well afterwards.

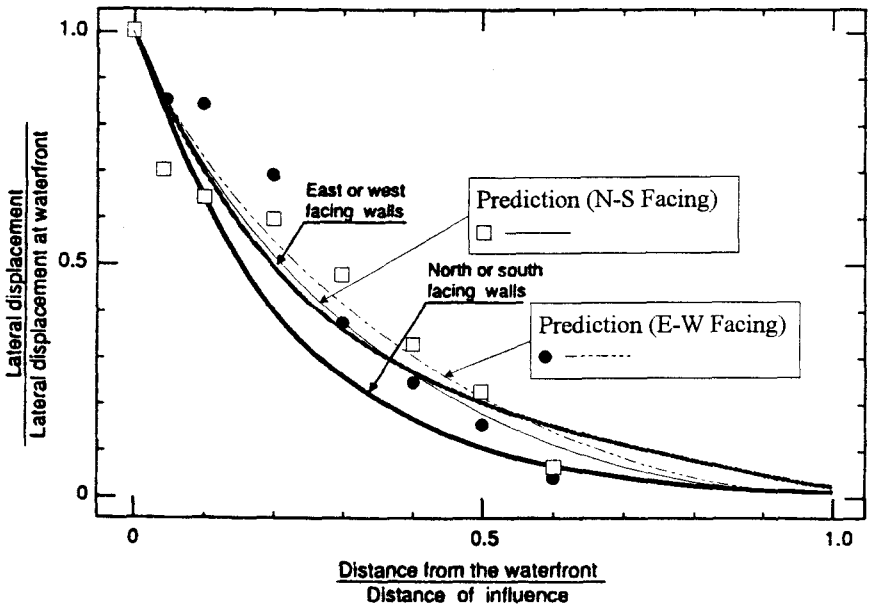

Figure 4-33: Comparison of measured averaged lateral displacement versus predicted lateral displacements in the backland area for Port Island and Rokko Island

4.2.2 *Kushiro-Oki Earthquake (Case 3 and Case 4, 1993)*

During the 1993 Kushiro-Oki Earthquake (M_{JMA} 7.8), many quay walls at Kushiro Port suffer damage due to liquefaction of unimproved backfill sand. The epicenter is located 15 km south of Kushiro City and focal depth is 107 km. The focal depth is much deeper than the ordinary focal depth of about 40 km for the earthquakes occurring around Japan. The Kushiro Port was shaken with a peak horizontal acceleration of 0.47g. The Kushiro Port is developed at the estuary of the Kushiro River as shown in Figure 4-34.

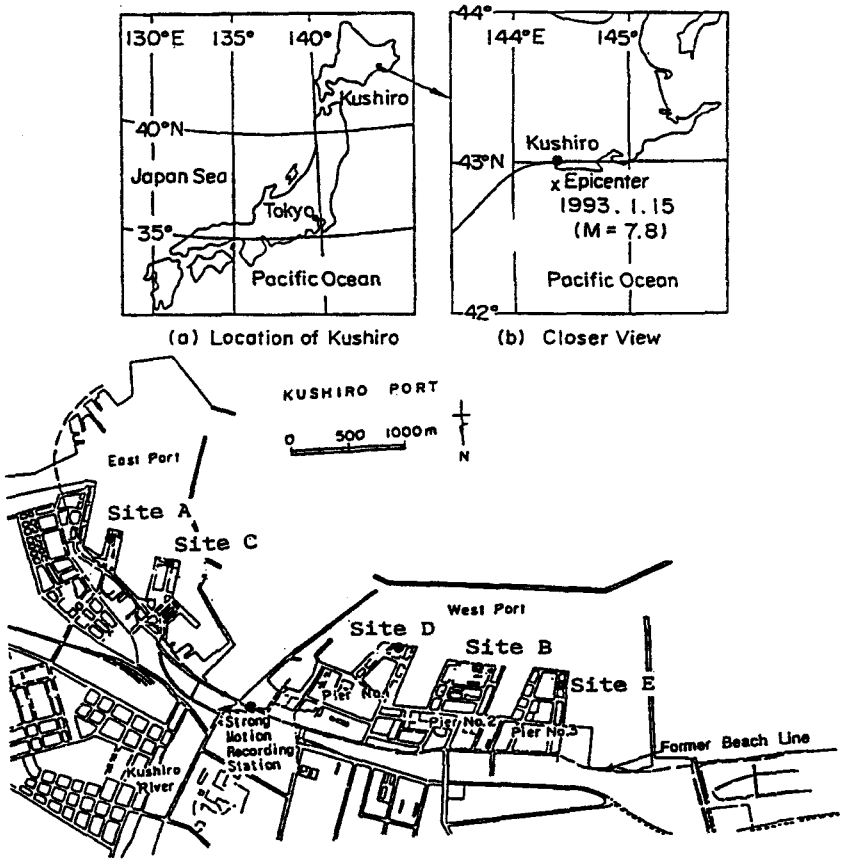

Figure 4-34: Location of Kushiro case studies (Iai et al., 1994b)

The strong motion recording station is located on the former beach line at the estuary of the Kushiro River. The boring log at the strong motion recording station is shown in Figure 4-35. The subsurface soil consists of several layers of dense to very dense sand with SPT N-values of 20 to greater than 50 down to a depth of about 50 meters below ground surface, underlain by a very dense sand with SPT N-values greater than 50 down to a depth of 77 meters, at which the downhole seismometer is installed. Thin silt layers occasionally appear and, when these layers are encountered, SPT N-values decrease to less than 10. Two accelerographs are obtained at strong motion recording station. One is from ground surface and the other is from a depth of 77 m below the ground surface. The peak accelerations on the ground surface are 4.68, 3.44 and 3.42 m/sec^2, whereas those at a depth of 77 m are 3.04, 2.65 and 1.10 m/sec^2 in the North-South, East-West and Up-Down directions, respectively.

The quay walls having improved backfill by sand compaction pile and gravel drain as measures against liquefaction performed well during the earthquake (Iai, et al., 1994b). In order to evaluate the effects of remedial measures against liquefaction, two case studies associated with unimproved (Pier 2 at site B) and improved (Pier 3 at site E) backfill sand layer, respectively, are presented in the following sections. It is also noted that those concrete caissons having the ratio of width-to-height close to unity only suffered slight damage even though the unimproved backfill sand liquefied.

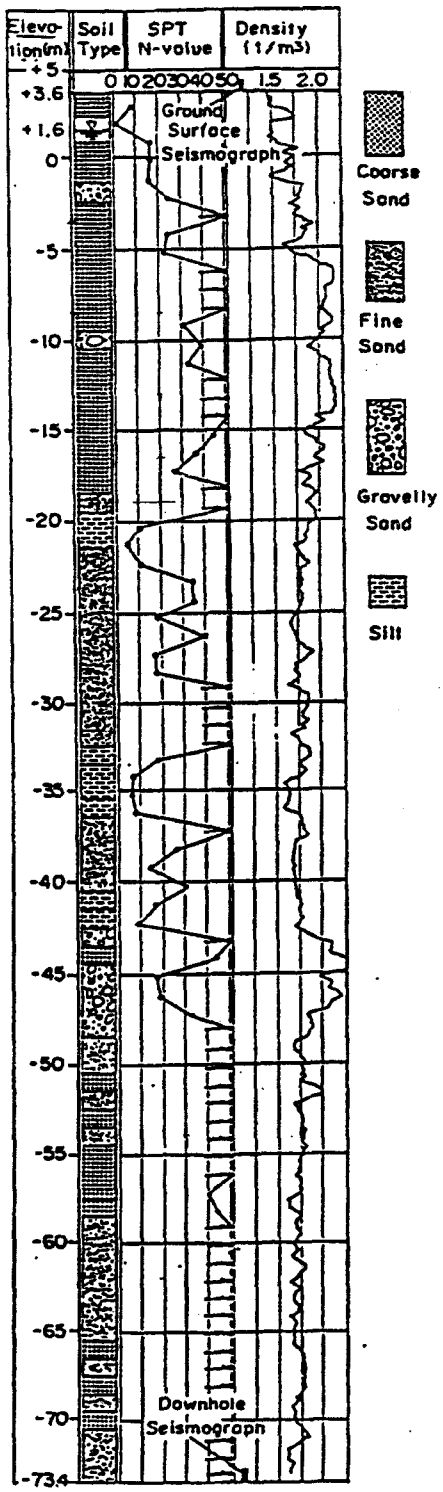

Figure 4-35: Soil condition at strong motion recording station at Kushiro Port (Iai et al., 1994b)

4.2.2.1 Case 3: Kushiro Port - Pier 2 at Site B (without Soil Improvement)

Most of the port area has been reclaimed from the sea by filling the sand dredged from nearby sea. The natural ground along the former beach line is sand dune origin with SPT N-values of about 50. The fill above the original ground gradually increases its thickness from none at the former beach line to about ten meters at the southern end of the piers in the West Port District. The gravity quay walls with the ratio of width-to-height close to unity as shown in Figure 4-36, located at the south end of the Pier 2 in the West Port District, experience only minor displacement. These quay walls were designed by pseudostatic method with seismic coefficient of 0.2. As noted from the ratio of width-to-height being close to unity, the quay wall was designed to resist relatively strong earthquake motions. The soil profile of the backfill, as shown in Figure 4-37, consists of about 10 m of coarse sand mixed with gravel underlain by 3 m of fine sand. The SPT N-value ranges from 2 to 10 blows/0.3m. The backfill soils having low SPT N-values are considered as highly liquefiable soils.

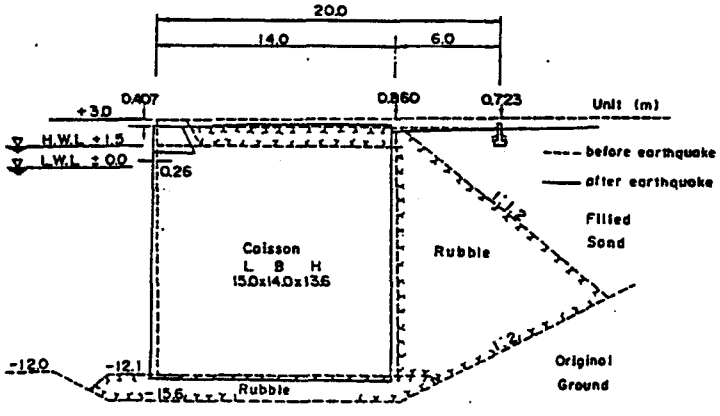

Figure 4-36: Typical cross section of quaywall at Site B (Iai et al., 1994b)

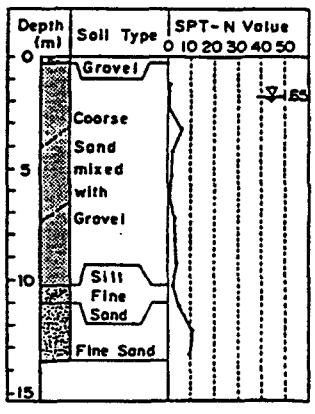

Figure 4-37: Soil condition at Site B (Iai et al., 1994b)

4.2.2.2 Case 4: Kushiro Port - Pier 3 at Site E (with Soil Improvement)

The gravity quay walls located at south end of the Pier 3 at site E in the West Port District are improved by sand compaction pile and gravel drain behind and above the rubble stone fill, respectively, as shown in Figure 4-38. The soil profile is similar as Pier 2 at site B except that the SPT N-value after soil improvement is increased up to 40 blows/0.3m.

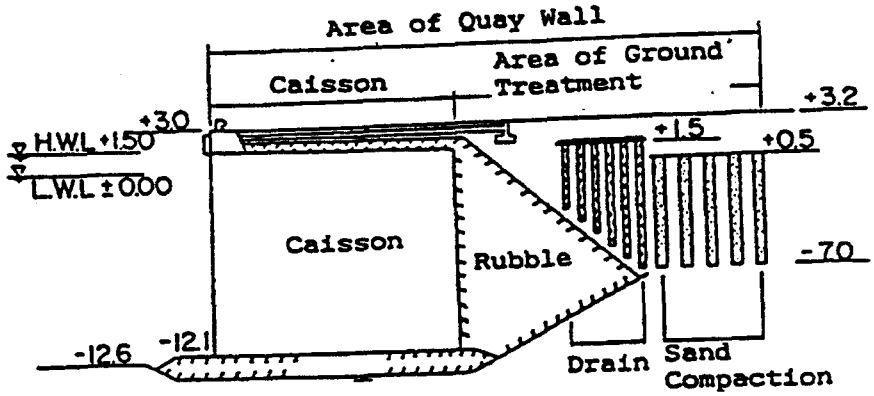

Figure 4-38: Employment of soil improvement at Site E (Iai et al., 1994b)

4.2.2.3 Analyses of Numerical Models at Kushiro Port

4.2.2.3.1 Pier 2 (without soil improvement)

The analytical model setup at Site B (Pier 2) of Kushiro Port is shown in Figure 4-39. The model is analyzed using a mesh of 40 by 15 zones. The input soil parameters for Pier 2 is shown in Table 4-3. At the bottom boundary, the earthquake motion, deconvoluted from the depth of 77 m to the base of the model by SHAKE91

program using the soil profile shown in Figure 4-35, is used. The input earthquake motion normal to the quay wall is shown in Figure 4-40.

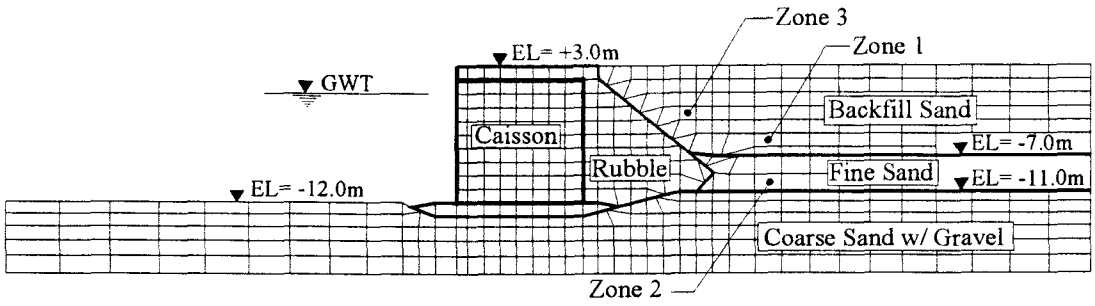

Figure 4-39: Analytical model setup at Site B (Pier 2) of Kushiro Port

Table 4-3: Input Soil Parameters for Kushiro Model

Soil Type	ρ_d *(kg/m³)*	ϕ *(deg.)*	G_m *(Pa)*	K_m *(Pa)*	κ *(m/sec)*	c *(Pa)*
Foundation and Backfill Rubble	2000	40	1.8e8	4.4e8	1e-1	0
Backfill Sand with gravel	1800	37	8e7	1.6e8	1e-7	0
Fine Sand	1800	36	9e7	1.8e8	1e-7	0
Coarse Sand with gravel	1600	38	1.1e8	2.2e8	1e-7	0
Soil in the Caisson	1750	35	8.0e7	1.6e8	-	0

Note: ρ_d = dry density; ϕ = friction angle; G_m = mean shear modulus; K_m = mean bulk modulus; κ = permeability; c = cohesion

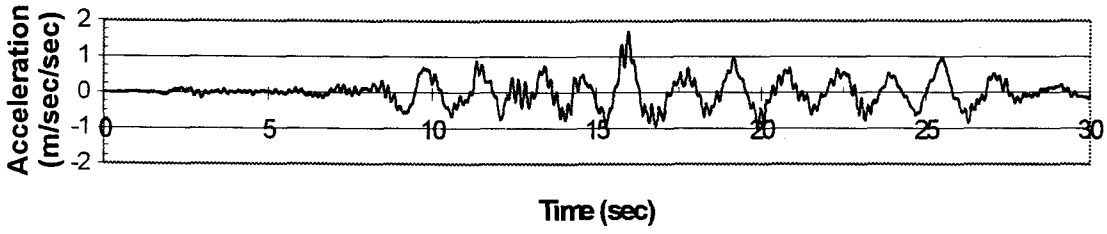

Figure 4-40: Input earthquake motion at the base of Kushiro model

4.2.2.3.2 Results of Prediction (Pier 2)

The deformed mesh of Pier 2 model at Site B of Kushiro Port (without soil improvement) before deformation and after deformation is shown in Figure 4-41. In order to clearly demonstrate the failure mechanism of the caisson, the deformed mesh was magnified by 4 times of its original size.

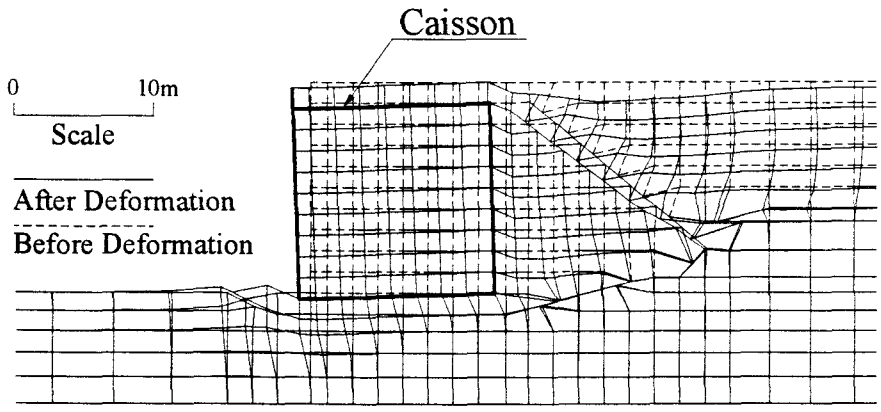

Figure 4-41: Deformed mesh of Pier 2 model at Site B of Kushiro Port (deformation is magnified by 4 times)

The residual displacements at the top of the caisson are found to be 0.33 m and 0.11 m in the horizontal and vertical direction, respectively. Comparing predicted displacements to measured displacements of 0.17~0.3 m in the horizontal direction and 0.24~0.47 m in the vertical direction, the results are somewhat over-predicted for the seaward horizontal displacement and under-predicted for the caisson settlement. The measured settlement (0.47m) was obtained around the corner of the quay wall face line and possibly it was affected by the settlement of quay walls on the other side. The horizontal displacement time history is shown in Figure 4-42. It can be seen

that the permanent displacements of the caisson occur about 25 seconds during the earthquake loading, beyond that time no further permanent displacements are observed. Figure 4-43 shows pore pressure distribution time history in the backfill and the fine sand layer. The pore pressure is increased 2 times of static pore pressure in the backfill (Zone 1 as indicated in Figure 4-39) and is increased about 3.6 times in the layer beneath the backfill (Zone 2).

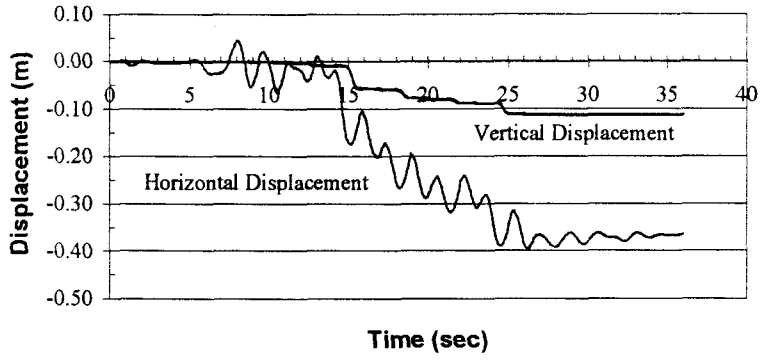

Figure 4-42: Horizontal and vertical displacement time history for Pier 2 model

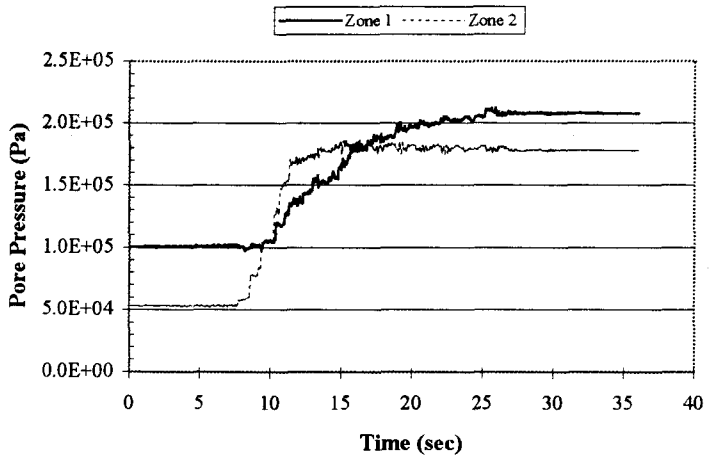

Figure 4-43: Pore pressure distribution time history in the backfill (Zone 1) and fine sand layer (Zone 2)

The predicted pore pressure ratio at various locations is shown in Figure 4-44. Full liquefaction (ru = 1) is predicted in the backfill soil, however, only partial liquefaction ($r_u \leq 0.5$) is observed in the fine sand layer although the pore pressure is increased about 3.6 times in this layer. The pore pressure ratio is gradually increased in the backfill and as peak acceleration occurs at the time of 15 seconds initial liquefaction has started. At this point, pore pressure ratio is approached to unity and backfill soil losses its shear strength, whereas the pore pressure ratio in the fine sand layer has only reached about 0.5 as a result of higher SPT N-values (higher liquefaction resistance). Pore pressure ratio at Zone 3 in the backfill is predicted as 0.8, less degree of liquefaction compared to Zone 1. It could be not only the result of high permeability of adjacent rubble backfill in which the excess pore pressures resulted from earthquake shaking dissipate rapidly but also due to seaward displacement of the caisson pulling out the backfill sand resulting in the reduction of the excess pore pressures. No liquefaction has been observed in the coarse sand layer beneath the caisson.

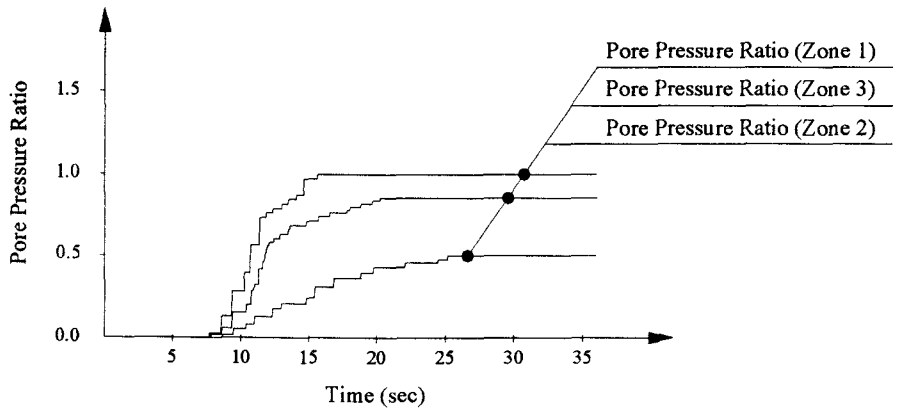

Figure 4-44: Pore pressure ratio at various locations for Pier 2 model

The tilted failure mechanism of the caisson was mainly due to the additional forces as a result of liquefaction in the backfill. No bearing capacity failure of foundation soil was observed and predicted. The approximate unity of width-to-height ratio of the caisson at Pier 2 of Site B was originally designed to resist earthquake loading. Although the liquefaction has been observed from the field investigation after earthquake, the caisson is tilted seaward only 0.3 meters.

4.2.2.3.3 Pier 3 (with soil improvement)

The model setup is the same as that in Pier 2 except that soil behind the caisson has been improved by 17 meters and the width-to-height ratio of the caisson is approximate 1.2, as shown in Figure 4-40. The SPT N-values of the soil in improved area increase from averaged value of 7 to 30 blows/0.3 m. The high soil strength in term of high SPT N-values (typically $N \geq 30$ blows/0.3m) in the improved area is considered as non-liquefiable soil in the model.

4.2.2.3.4 Results of Prediction (Pier 3)

The residual displacements at the top of the caisson are 0.09 m and 0.03 m in the horizontal and vertical direction, respectively. Comparing predicted displacements to measured displacement of 0.06~0.24 m in the horizontal direction and 0.05~0.18 m in the vertical direction, the results yield a good agreement with observed values. The effects of soil improvement and high width-to-height ratio significantly reduce the displacements of the caisson during earthquake loading. As much as four times of

displacements of the caisson has been reduced due to soil improvement. Soil improvement techniques have been considered as one of the well-suite methods to mitigate liquefaction hazards due to earthquake at harbors and ports around the world. An alternative method used as a countermeasure against liquefaction damage can be chosen to increase the width-to-height ratio as indicated in this case study. It is also interesting to note that the caisson with width-to-height ratio of unity without soil improvement at Maya Pier of Kobe Port only suffered minor damage comparing to averaged of 3~5 m seaward displacements of the caissons at Port Island and Rokko Island during 1995 Kobe Earthquake. As little as 0.5 m seaward displacements of the caissons was observed at Maya Pier, although the earthquake shaking level and characteristics of shear strength of the backfill sand were similar to other sites of Kobe Port. Detailed description of the effects of caisson width-to-height ratio will be presented in the latter section of parametric study.

4.2.3 Nihonkai-Chubu Earthquake (Case 5, 1983)

The Nihonkai-Chubu earthquake (M_{JMA} 7.7) occurred in the Japan Sea about 90 km west of Aomori Prefecture on May 26, 1983, causing severe damage to the coastal areas of the Tohoku region. Failure to the port facilities at Akita Port as shown in Figure 4-45(a) and 4-45(c) was mainly due to soil liquefaction in the backfill soils. The epicenter of the main shock was located on the bed of the Japan Sea, 100 km from the main island of Japan, as shown in Figure 4-45(b). The focal depth of the earthquake was about 14 km. According to the Japanese Meteorological Agency Scale as shown in Figure 4-45(d), the highest seismic intensity in this region was V, which

is roughly equivalent to VII-VIII on the Modified Mercalli Intensity Scale. Many waterfront quaywalls were tilted and slid towards the sea, aprons were crushed, and the function of the port was not operational (Noda et al., 1984). The earthquake-induced damage, including the subsidence and floating of structures, was also experienced during 1964 Niigata earthquake, therefore, many countermeasures against the recurrence of these kinds of damages have been developed and adopted in Japanese practice. However, it was first recognized for the permanent ground displacements induced by liquefaction at that time (Hamada, 1992b).

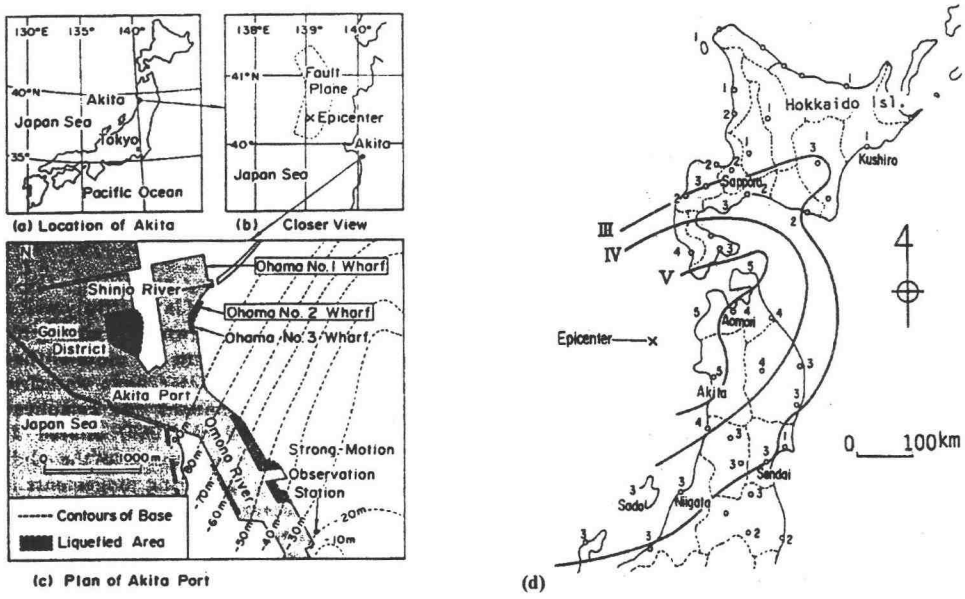

Figure 4-45: (a)~(c) Location of Akita Port; (d) Seismic intensity zones used in Japan (Iai et al., 1993)

4.2.3.1 Case 5: Gaiko Wharf at Akita Port

The Gaiko Wharf, which is newly reclaimed area, is located on the northwest part of the Akita Port as shown in Figure 4-45(c). A strong motion accelerograph was installed at the strong motion observation station as shown in the lower right corner of Figure 4-45(c). The maximum acceleration recorded at Akita Port were 0.223 g, 0.24 g, and 0.055 g in the North-South, East-West, and Up-Down directions, respectively, as shown in Figure 4-46. However, the horizontal design earthquake acceleration in this area according to the Japanese code is only equal to 0.1g that is well below peak ground acceleration recorded during the Nihonkai-Chubu Earthquake.

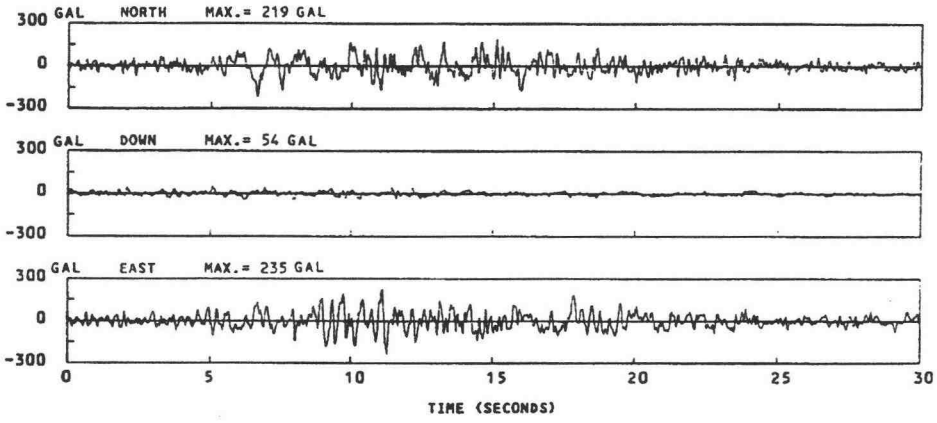

Figure 4-46: Recorded acceleration time history at Strong Motion Observation Station (Iai et al., 1993)

Two boring logs, as shown in Figure 4-47, were obtained at Gaiko Wharf (Pier C). The locations of two boring logs are shown in Figure 4-48. The subsurface consists of 3~4 m of loosely deposited hydraulic sand fill with SPT N-value of about 8 blows/0.3m underlain by approximately 13 m of medium dense sand with SPT N-

value of 5 blows/0.3m. The base of boring log consists of a thin layer of gravel and fine sand with SPT N-value of over 20 blows/0.3m.

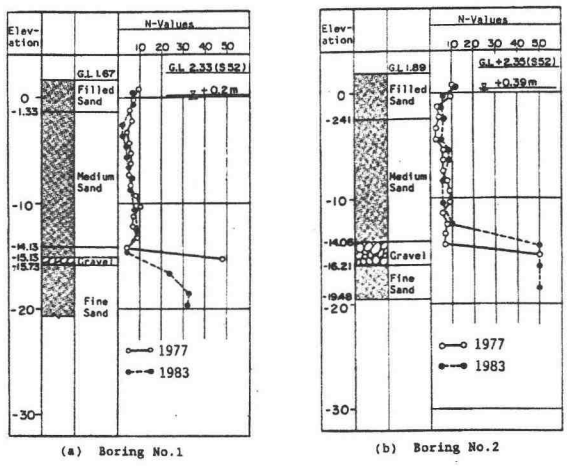

Figure 4-47: Soil conditions at Gaiko Wharf (Hamada, 1992b)

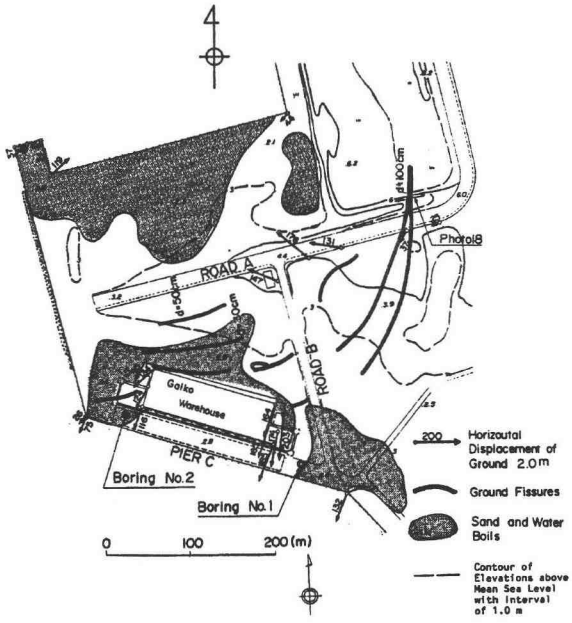

Figure 4-48: Ground displacements, ground fissures, and sand boils at Gaiko Wharf (Hamada, 1992b)

The liquefaction was observed along the perimeter of Akita Port as shown in Figure 4-49. As indicated in Figure 4-48 and Figure 4-49, Gaiko Wharf, South Pier, North Pier and Nakajima Pier were severely damaged due to soil liquefaction. Ground fissures and sand boils can be observed around Gaiko warehouse at Pier C as noted in Figure 4-48. The liquefaction-induced damage includes the collapse and large inclination of steel sheet pile, collapse of concrete-block quaywalls, and the seaward movements of caissons.

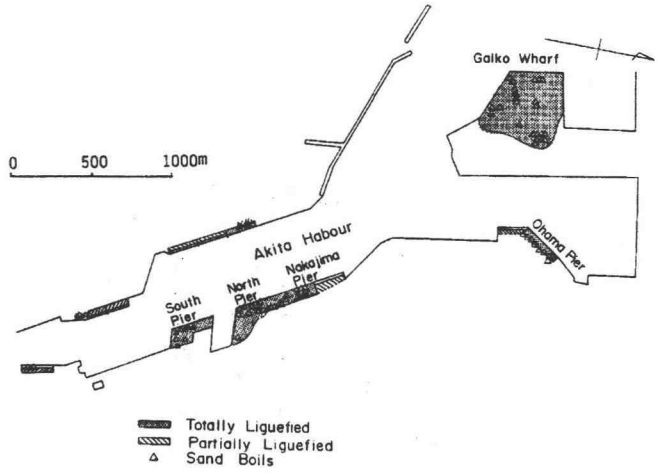

Figure 4-49: Locations of damage to quaywalls and liquefaction at Akita Port (Hamada, 1992b)

The typical cross section of caisson type quay wall of Pier C at Gaiko Wharf and measured seaward displacement and inclination of the top of the caissons are shown in Figure 4-50 and Figure 4-51, respectively. The caissons were moved on an average of 1.2 m and tilted to a maximum of 3 degrees. The magnitude of the displacement of the caissons mostly coincides with that of the surrounding ground measured by aerial survey.

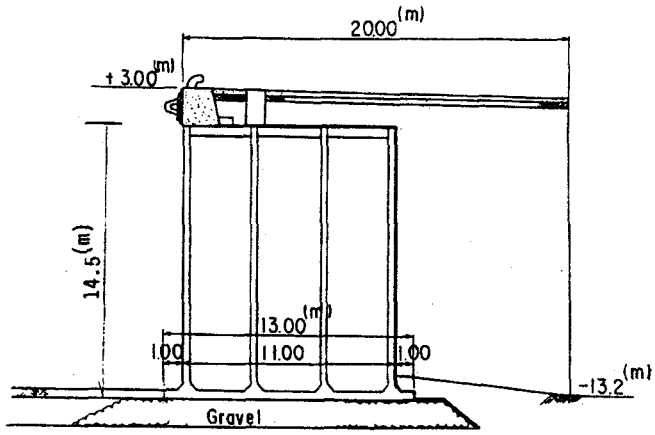

Figure 4-50: Geometry of caisson of Pier C at Gaiko Wharf (Hamada, 1992b)

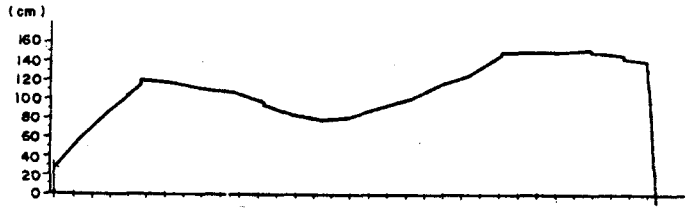

(a) Seaward displacement at the top of the caisson

(b) Seaward inclination of the caisson

Figure 4-51: Displacement and inclination of the caisson of Pier C at Gaiko Wharf (Hamada, 1992b)

Permanent ground displacements were measured by surveys based on aerial photographs taken before and after the earthquake. The ground displacement was evaluated by subtracting the coordinates of measuring points on the ground surface determined from pre-earthquake photograph from those of post-earthquake photographs. The Gaiko warehouse and ground around it was moved seaward with a maximum displacement of about 2 m. Behind the ground displacement, large ground fissures with a maximum width of about 1.0 m were observed. The ground fissures were generally perpendicular to the ground displacements, which had moved seaward due to soil liquefaction.

4.2.3.2 Analysis of Numerical Model at Akita Port

4.2.3.2.1 Description of Model

The model setup at Gaiko Wharf (Pier C) of Akita Port is shown in Figure 4-52. The model is analyzed using a mesh of 40 by 14 zones. The model consists of 15.5 m thick of backfill sand with SPT N-values ranging from 5 to 10, 6.5 m thick of fine sand and gravel with SPT N-values greater than 40, and 1.5 m thick of foundation rubble with SPT N-values greater than 50. The SPT N-values used in the model are based on the data of two boring logs as indicated in Figure 4-47. The soil parameters used in the model are listed in Table 4-4. The concrete caisson is presented by beam element and the properties of beam element are the same as those listed in Table 4-2.

As mentioned in section 4.2.3.1, the earthquake motions were recorded in strong motion observation station located about 20 m above the base rock as indicated

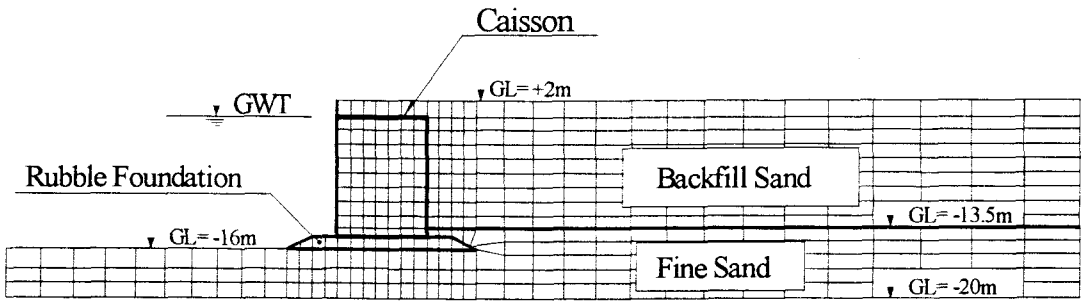

Figure 4-52: Model setup at Gaiko Wharf of Akita Port

Table 4-4: Input Soil Parameters for Akita Model

Soil Type	ρ_d *(kg/m^3)*	ϕ *(deg.)*	*G (Pa)*	*K (Pa)*	κ *(m/sec)*	*c (Pa)*
Backfill Sand	1800	37	5.77e7	1.25e8	1e-7	0
Fine Sand with gravel	1850	38	1.72e7	3.68e8	1e-7	0
Soil in the Caisson	1750	35	8.0e7	1.6e8	-	0
Foundation Rubble	2000	40	2.3e8	5e8	1e-1	0

Note: ρ_d = dry density; ϕ = friction angle; G = shear modulus; K = bulk modulus; κ = permeability; c = cohesion

with dashed lines in Figure 4-45(c). The soil deposit at the accelerograph site did not liquefy during the earthquake and, therefore, the accelerograph was not affected by soil liquefaction. In order to obtain input earthquake motion for Gaiko Wharf model, computer program, SHAKE91 (Idriss, et al., 1992), was employed. Considering the angle of the face of the quaywall at Gaiko District, EW and NS components of the earthquake motion, as shown in Figure 4-46, are first vectorly combined, and this

combined motion is then deconvoluted by the equivalent linear method (SHAKE91) to obtain input motion at the base of the model. The resulting input acceleration time history at the base of the model (-22 m) for the Akita case study is shown in Figure 4-53.

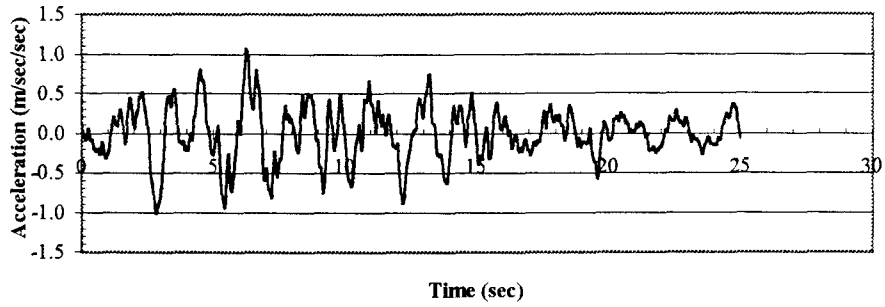

Figure 4-53: Input acceleration time history at the base of model

4.2.3.1.2 Results of Prediction (Gaiko Wharf)

Figure 4-54 shows deformed mechanism of the analytical model at Gaiko Wharf of Akita Port. The residual displacements at the top of the caisson are 1.19 m and 0.36 m in the horizontal and vertical direction, respectively. The inclination of the caisson is 1.9 degrees toward the sea. The measured seaward displacements at the top of the caisson as presented in Figure 4-51(a) are ranging 0.8 m to 1.5 m with averaged value of 1.2 m. The measured inclination as shown in Figure 4-51(b) is on an average of 1.5 degrees. The predicted seaward lateral displacement (1.19 m) and inclination (1.9 degrees) at the top of the caisson are matched very well comparing to measured average value of 1.2 m and 1.5 degrees, respectively. No information is available regarding the settlement of the caisson at Gaiko Wharf.

The pore pressure increases as much as 3.5 times of static pore pressure in the backfill. The pore pressure ratio has reached to unity at various locations in the backfill indicating that the damaging of liquefaction is primary cause of the failure of caisson since no failure of bearing capacity of rubble foundation beneath the caisson has been observed either in the field or in the prediction and the caisson was only subjected to relatively moderate earthquake motion.

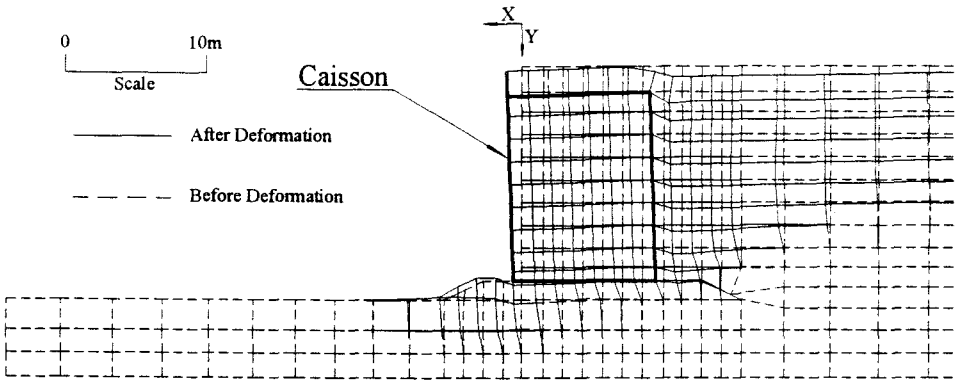

Figure 4-54: Deformed mesh of Akita model

4.3 Summary and Discussions of Case Studies

In view of the results of the aforementioned five case studies, the major findings of the seismic performance of the caissons are summarized as follows:

1. The magnitude and pattern of the predicted lateral displacements of the caissons agree with the measured displacements indicating that the present numerical model can be used to reasonably predict the seismic performance of concrete

caissons. The case studies have been particularly useful for calibrating the numerical model, evaluating the uncertainties associated with the model, and assessing the applicability of the model for computing the seismic behavior of gravity caissons in unimproved and improved soils. The results of case studies are summarized in Table 4-5 in which labeled number represents each case study.

Table 4-5: Summary of Five Case Study Results

Case Studies	X_d^* *(m)*			Y_d^{**} *(m)*		
	Predicted	***Measured***	***Average***	***Predicted***	***Measured***	***Average***
Hyogoken-Nanbu Earthquake						
① Port Island	3.3	2.3~3.2	2.7	0.95	0.8~1.1	0.9
② Rokko Island	3.9	3.9~5.2	4.5	1.21	1.4~2.2	1.7
Kushiro-Oki Earthquake						
③ Pier 2 (without improvement)	0.33	0.17~0.3	0.23	0.11	0.27~0.47	0.4
④ Pier 3 (with improvement)	0.09	0.06~0.24	0.168	0.03	0.05~0.13	0.11
Nihonkai-Chubu Earthquake						
⑤ Akita Port	1.19	0.8~1.5	1.2	0.36	N/A	N/A

Note: * seaward lateral displacements at the top of the caisson
** settlements at the top of the caisson

The subsidence in the backland area, in which post-liquefaction volumetric strain has been accounted for, can be predicted within a reasonable range as well. Figure 4-55 shows the comparison of numerical model predictions for lateral displacements at the top of the caissons to field average measured values in which detailed Kalamata case study will be discussed in the following chapter (Chapter 5). In Kobe Earthquake case studies, i.e., Case 1 and Case 2, the predicted

seaward lateral displacements at the top of the caisson are approximately over-predicted by 22% and under-predicted by 13% as compared to average measured lateral displacements for Case 1 and Case 2, respectively. And predicted settlements at the top of the caisson are approximately over-predicted by 6% and under-predicted by 29% as compared to average measured settlements for Case 1 and Case 2, respectively. In Kushiro Earthquake case studies, i.e., Case 3 and Case 4, the predicted seaward lateral displacements at the top of the caisson are within the observed values and approximately over-predicted by 43% and

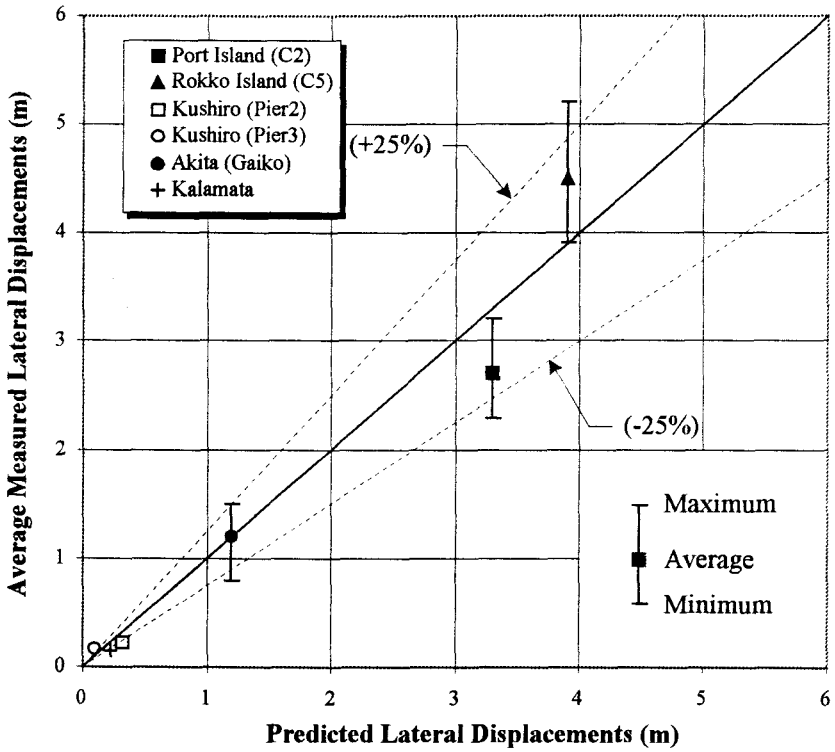

Figure 4-55: Comparison of predicted lateral displacements at the top of the caissons to average measured values

under-predicted by 46% as compared to average measured lateral displacements for Case 3 and Case 4, respectively. In Case 5, the predicted seaward lateral displacement of the caisson is matched pretty well, approximately under-predicted by 1%, as compared to average measured displacement and the predicted settlement appears to be acceptable although no measured information was available. Overall, numerical predictions for seaward lateral displacements are approximately within ±25% on average as compared to average field measured displacements. The predictions for settlements of the caisson are approximately under-predicted by 26% on average as compared to average field measured settlements. The uncertainties involved in numerical predictions are largely due to inherent uncertainties of field investigation for each case study including the soil properties, measured displacements, and characteristics of strong earthquake motions. As addressed in Chapter 2, numerous simplified assumptions were made in pseudostatic methods in order to make the problems easily to perform and interpret. Similar situations are usually encountered in numerical analyses as well. For example, in present study, (1) elastic-perfect plastic constitutive soil model usually simplifies the real soil behavior; (2) coupled pore pressure generation scheme was largely based on empirical correlations investigated from field data; (3) soil parameters for the models are not always available from each case study and are largely based on well-established geotechnical empirical correlations; and (4) the recorded earthquake motions can not always be directly applied to the models. Although these simplicities and uncertainties are noted in the numerical model, the numerical analysis approaches have been used for estimating the

deformation of waterfront structures by numerous researches (i.e., Roth and Inel, 1993; Inel et al., 1993; Inagaki et al., 1996; Dickenson and McCullough, 1998) and have been proved that predicted displacements were within reasonable ranges.

2. The failure mechanism of the caisson has been seaward tilting failure in all five case studies. No collapse and global instability was observed either in the field or in the modeling results. It should be noted that this failure mode of the caisson is not the same as that usually assumed in the limit equilibrium, sliding block methods of analysis. This indicates that the pseudostatic analysis methods are offset by the simplicity of failure mechanism for gravity type waterfront retaining structures especially if foundation soils are potentially liquefiable soils. The causes of the caisson failure, in addition to the effect of the strong shaking such as inertial force, hydrodynamic, and seismic lateral earth pressure, have been mainly due to soil liquefaction behind and/or beneath the caisson. The liquefaction of hydraulically placed backfill sand has significantly affected the seismic performance of the caisson, whereas the foundation condition beneath the caisson has relatively less significant influence on the caisson since it usually has been replaced or densified with higher shear strength soil, such as Port Island and Rokko Island at Kobe Port. Although partial liquefaction ($r_u \leq 0.5$) has been predicted in these replaced foundation soils in the Port Island and Rokko Island models (Case 1 and Case 2), it could be explained as a local failure of foundation soils. However, relative contribution to failure of the caisson due to liquefaction of backfill soil or deformation of foundation soil is not clear in present study. Although the mitigation of liquefaction hazards can be accomplished by

improving weaker soil shear strength through various soil improvement techniques, however, the promising extent of soils needed to be improved in order to maintain minimal operational serviceability at ports and the strategies of effectiveness of various soil improvement techniques are not well established.

3. The excess pore pressures induced by earthquake have increased as much as 2.5 times of static pore pressures in the backfill and about 1.5~2.0 times in the foundation soil beneath the caisson. The increased earthquake-induced excess pore pressures in the backfill sand have been proved, from case studies, as an important factor that significantly affected the seismic performance of the caisson.
4. The larger width-to-height ratio of the caisson (typically for Width / Height $\geq$ 1.2) performs favorably well during earthquake loading, such as Maya Pier of Kobe Port, Pier 2 (Case 3) and Pier 3 (Case 4) of Kushiro Port, although earthquake-induced liquefaction has been observed in these areas. The approach of high seismic resistant in terms of larger width-to-height ratio of the caisson along with the soil improvement techniques, such as Case 4, can be considered as one of alternative methods in the seismic design of gravity type walls.
5. The effects of soil improvement in the backfill have been proved (Case 4) to be a good countermeasure method against earthquake-induced liquefaction damage. These effects have been reflected in increasing the shear strength of the backfill and reducing the seaward displacement of the caisson. Comparing Case 3 (without soil improvement) to Case 4 (with soil improvement), seaward horizontal and vertical displacements of the caisson with soil improvement in the backfill are reduced up to three times less than those without soil improvement. The extent of

the soil improvement in the backfill soil is the function of earthquake characteristics (i.e., magnitude, peak acceleration, and duration), soil properties (i.e., shear strength of liquefiable and non-liquefiable soil), and geometry of the caisson (i.e., width-to-height ratio). In current practice, soft clay or silt beneath the caisson is usually replaced by sandy soil. If the replaced sands were not improved to a satisfactory level, it would also affect the deformation of the foundation soil and reduce the stability of the caisson during earthquake shaking.

6. From the results of case studies, the numerical model is considered to provide reasonable and representative prediction for seismic performance of concrete caisson. Since the numerical model is validated and calibrated by case studies, the model is used to perform sensitivity study of concrete caisson in unimproved and in improved soils in the following chapter.

5 GRAVITY RETAINING WALLS IN UNIMPROVED AND IN IMPROVED SOILS: PARAMETRIC STUDY

5.1 Introduction

Although soil improvement technology has been used to mitigate liquefaction hazards at numerous ports around the world, very few guidelines exist for specifying the extent of remedial soil treatment required to insure the serviceability of the waterfront components after a design-level earthquake. In view of the consequences of the earthquake-induced damage to waterfront retaining walls, this chapter has investigated the seismic response of concrete caisson in unimproved and in improved soils.

The present numerical model has been validated and calibrated by five case studies. The model has been proved that it can predict the seismic performance of the caisson in a reasonable agreement as discussed in the aforementioned chapter. The next phase of the project focuses on an extensive parametric study using the calibrated model for gravity retaining walls designed using the standard procedures for pseudostatic design (i.e., Ebeling and Morrison, 1993).

5.2 Parametric Study

The configuration of the model caisson and the surrounding soils is shown in Figure 5-1.

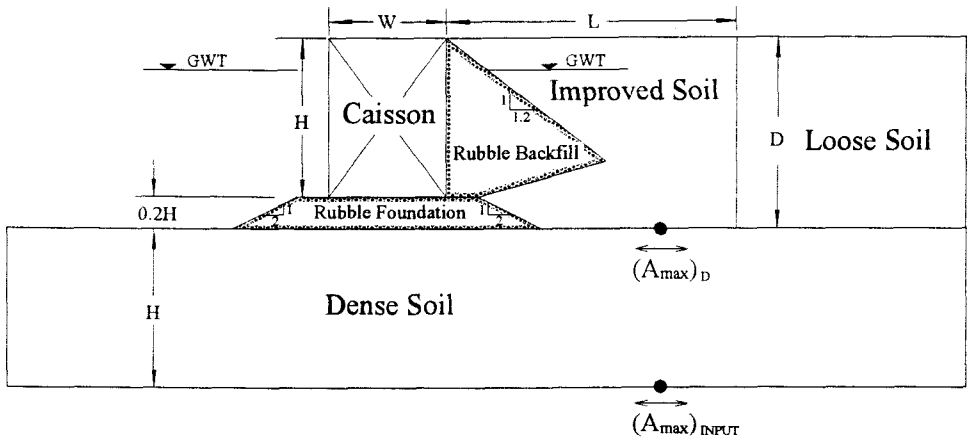

Figure 5-1: Cross section of model wall in parametric study

The differences among various models in the parametric studies are distinguished as the following characteristics:

I. *Wall Geometry*: Caisson heights of 15 m to 18 m are used with width-to-height (W/H) ratios of 0.7 and 1.2. The W/H ratios correspond to gravity structures designed to resist pseudostatic horizontal seismic coefficients of approximately 0.1 to 0.25 as presented in Figure 5-2, the range of interest for port engineers. The vertical seismic coefficient is assumed to be zero since vertical acceleration has less significant influence on the seismic performance of gravity type quay walls.

II. *Density of Soils*: The foundation and backfill soils are cohesionless materials, each layer modeled with uniform density. The range of densities used can be correlated with stress corrected standard penetration resistances ($(N_1)_{60}$) of ***(a)*** 25 blows/0.3 m in the foundation soil, ***(b)*** 10 to 20 blows/0.3m in unimproved backfill, and ***(c)*** 30 blows/0.3m in improved backfill. The depth of foundation

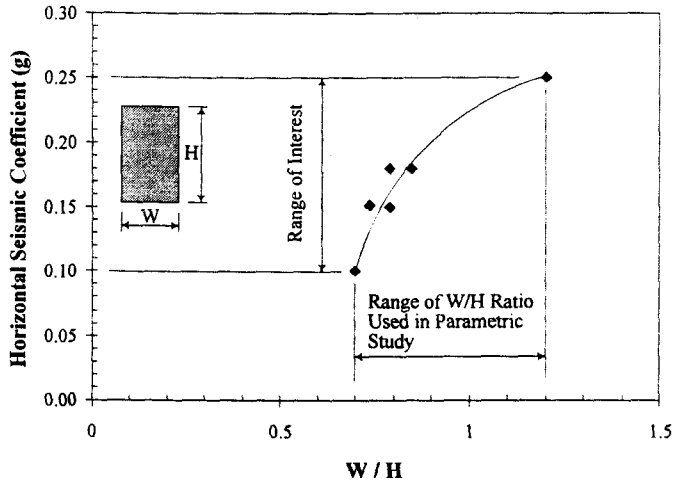

Figure 5-2: W/H ratio corresponding to pseudostatic horizontal seismic coefficients used in the design of caissons at Japanese ports

base is assumed to be the same as caisson height (H) and the depth of backfill soil is assumed to be 1.2 H. The soil improvement is modeled as providing a uniform increase in soil density throughout the zone of treatment. This is a simplification of the actual pattern of densification and variation in soil stiffness that would be expected from vibro-ground improvement techniques. No cohesion in the sandy backfill is modeled, therefore the results presented herein are not applicable for cases involving the use of ground treatment by grouting or soil cement techniques.

III. *Ground Motions*: The input motions are applied uniformly to the base of the dense soil underlying the caisson and fill soil. The lateral boundaries of the model are modeled as free field boundaries and set a distance far enough to eliminate boundary effects on the computed pattern of soil deformations. The

lateral and vertical deformations of the wall and surrounding soil, as well as the excess pore pressures in the backfill are calculated during the seismic loading. Ten earthquake motions covering the magnitude range of engineering interest (M_w 6 to 8) are selected for the parametric study. The information of input earthquake motions is listed in Table 5-1 and each acceleration time history is shown in Figure 5-3. A suite of recorded motions is utilized in order to account for the influence of varying ground motion characteristics (i.e. frequency content and duration) on the performance of the caissons. The selected acceleration time histories are slightly conservative in the sense that each one is characterized as having greater than average duration for that specific magnitude, thereby yielding slightly greater caisson displacements than would be computed using motions of average duration. Each motion is scaled to three different acceleration values ranging from 0.1g to 0.4g.

Table 5-1: Earthquake Information for Parametric Study

Earthquake	*Magnitude*	A_{max} *(m/sec²)*	*Location*
1984 Morgan Hill			
① Gilroy #4	6.2	2.17	Morgan Hill
1979 Imperial Valley			
② Bonds 140	6.6	5.76	Bonds Corner (140 degree)
③ Bonds 230		7.71	Bonds Corner (230 degree)
1940 El Centro			
④ El Centro	7.0	3.42	El Centro
1989 Loma Prieta			
⑤ Salinas	6.9	1.1	John and Work Street
⑥ Capitola		3.9	Capitola
1949 Western Wash.			
⑦ West Wash.	7.1	1.62	Highway Test Lab
1952 Kern County			
⑧ Taft	7.4	1.53	Taft, Kern County
1992 Landers			
⑨ Landers	7.5	2.68	Joshua Tree Fire Station
1985 Mexico			
⑩ Mexico	8.1	3.43	Mexico

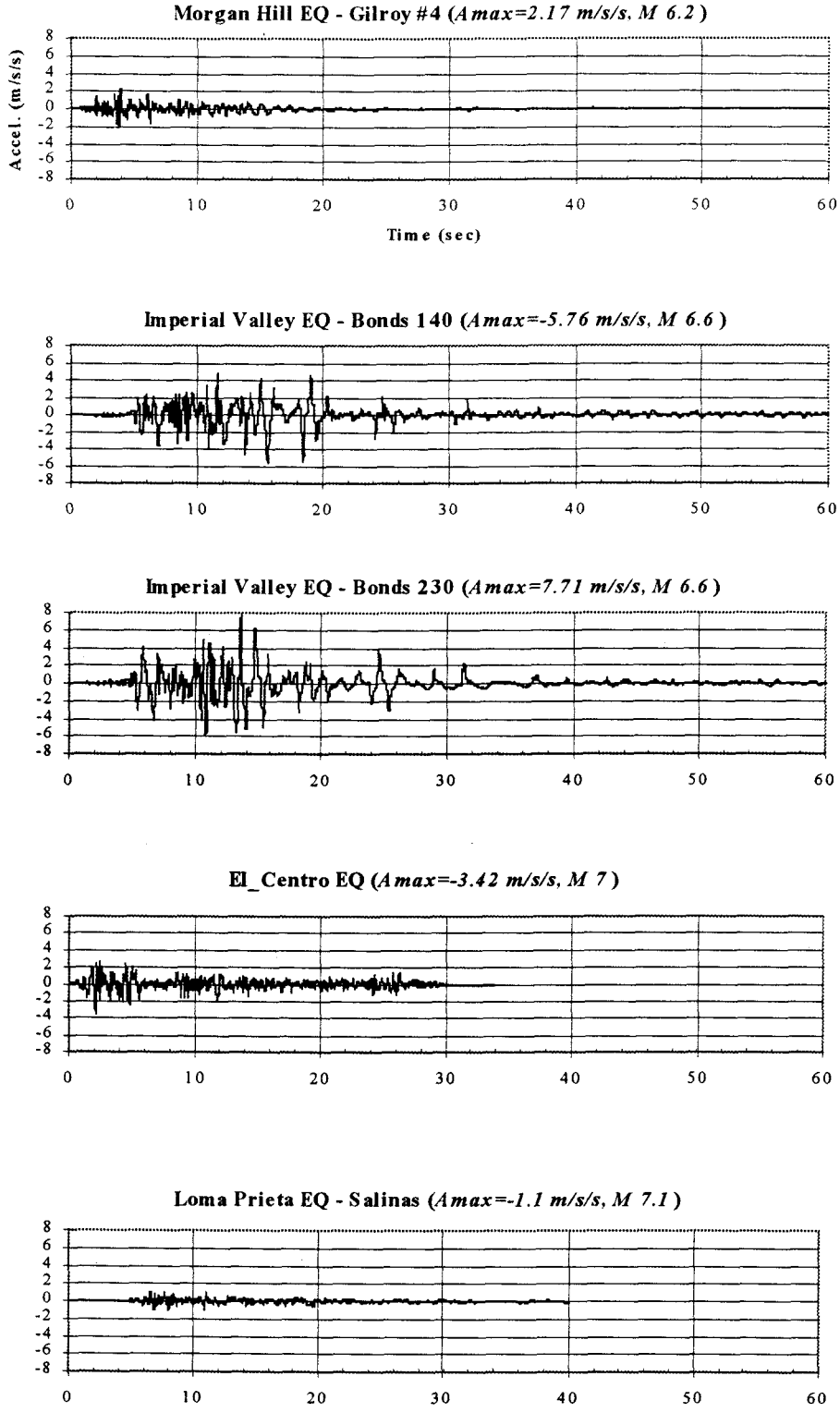

Figure 5-3: Input acceleration time history for parametric study of gravity retaining walls

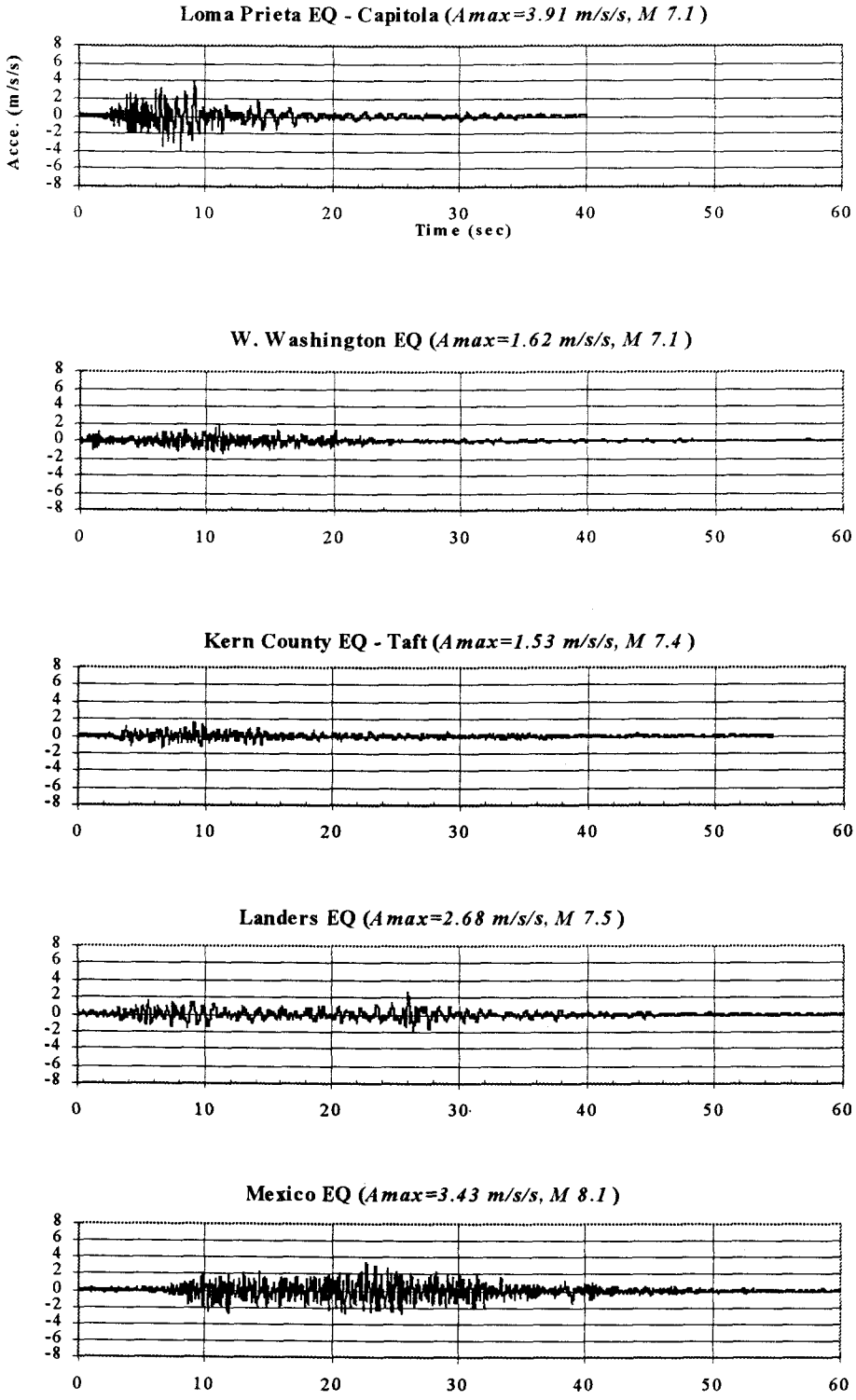

Figure 5-3 (Continued): Input acceleration time history for parametric study of gravity retaining walls

Notable specifications in the parametric study include; ***(a)*** no pore pressure generation in the foundation or improved backfill soils ($(N_1)_{60}$~30) implying that no liquefaction would occur in these layers, ***(b)*** the soil improvement extends to the base of the backfill (i.e. the same elevation as the dredge line) depth, ***(c)*** the water table is assumed to be constant on both sides of the caisson and no seepage force would occur during earthquake loading.

5.3 Results of Parametric Study

The results of the parametric study demonstrate the influence of ground motion characteristics, geotechnical parameters, and caisson geometry on the deformations of the caissons. These results have been synthesized into normalized parameters, where possible, to incorporate the key variables into straightforward design parameters. For example, the wall geometry has been expressed by *W/H* ratios as previously mentioned, the width of the zone of soil improvement is given as a function of the height of the wall *(L/H)*. In order to account for the duration of the earthquake motions, a normalized ground motion intensity has been used. This parameter is defined as the maximum horizontal acceleration at the top of the dense soil $(A_{max})_D$ (corresponding to the dredge line elevation in this study) divided by the appropriate magnitude scaling factor, MSF, (Arango, 1996). The magnitude scaling factors are provided in Table 5-2.

Table 5-2: Magnitude Scaling Factors (Arango, 1996)

Earthquake Magnitude	8.25	8	7.5	7	6	5.5
Magnitude Scaling Factor (MSF)	0.63	0.75	1	1.25	2	3

It is recommended that if a site specific seismic study is not performed to determine $(A_{max})_D$, then the peak ground surface acceleration can be reduced using the reduction factor (r_d) developed for estimating the variation of cyclic shear stress (or acceleration) with depth (Seed and De Alba, 1983). The values of r_d for 15 m and 7.5 m depth are approximately 0.78 and 0.95, respectively. It should be noted that the reduction factor was developed using one-dimensional dynamic soil response methods and this will yield approximate acceleration values for the two-dimensional soil-structure interaction applications discussed herein.

The computed data points of the parametric study are shown from Figure 5-4 to Figure 5-7. The normalized lateral displacements at the top of the caisson, X_d/H, are plotted versus the normalized width of the improved soil, L/H, and as functions of backfill density and the W/H ratios of the caissons. Notations in those figures are defined in Figure 5-1. Figure 5-4 and Figure 5-5 are normalized lateral displacements at the top of the caisson for backfill with $(N_1)_{60}$ = 10 blows/0.3m and ratio of caisson W/H=0.7 and W/H=1.2, respectively. Figure 5-6 and Figure 5-7 are plotted in the same fashion except for backfill with $(N_1)_{60}$ = 20 blows/0.3m. As seen from Figure 5-4, the computed data points in terms of normalized ground motion intensity

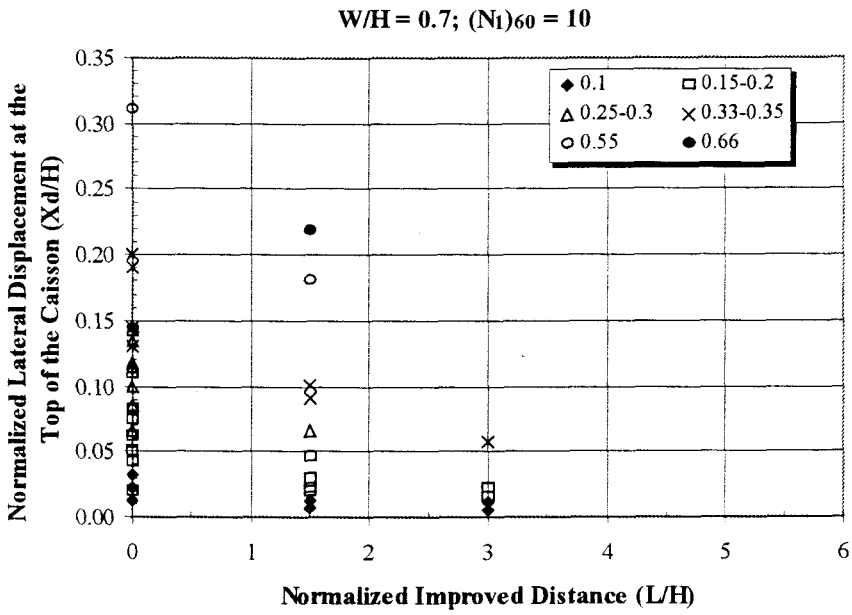

Figure 5-4: Normalized lateral displacements at the top of caisson for backfill with $(N_1)_{60}$ = 10 blows/0.3m and W/H ratio = 0.7 (data points are presented in the form of $A_{max,D}$ / MSF)

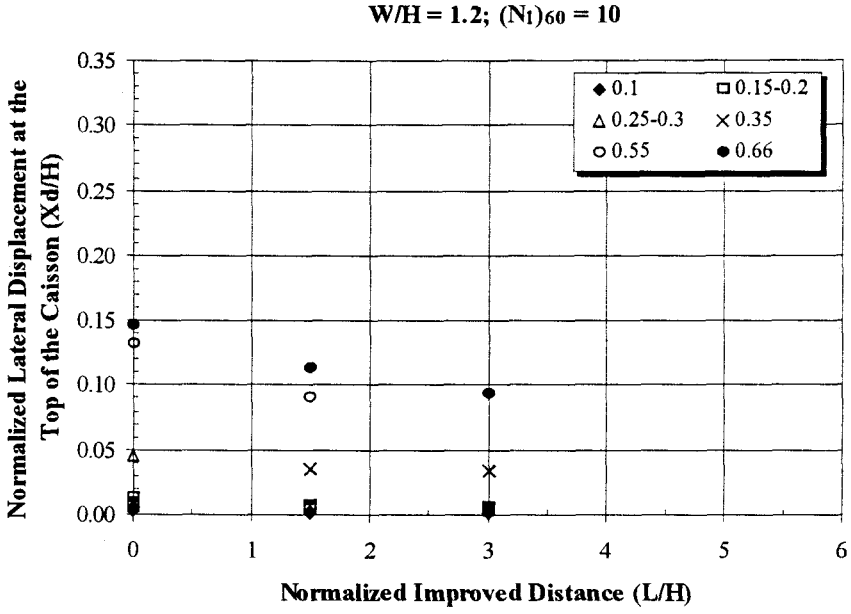

Figure 5-5: Normalized lateral displacements at the top of caisson for backfill with $(N_1)_{60}$ = 10 blows/0.3m and W/H ratio = 1.2 (data points are presented in the form of $A_{max,D}$ / MSF)

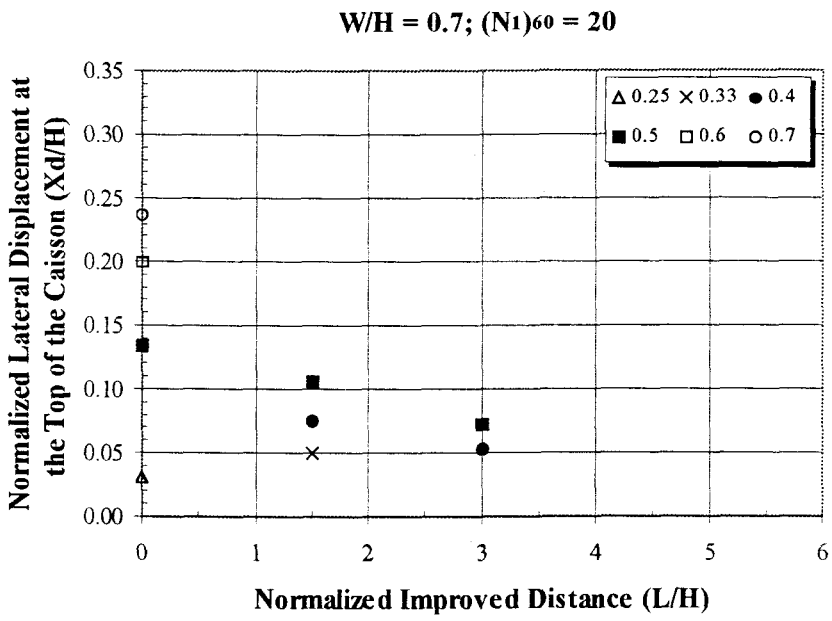

Figure 5-6: Normalized lateral displacements at the top of caisson for backfill with $(N_1)_{60}$ = 20 blows/0.3m and W/H ratio = 0.7 (data points are presented in the form of $A_{max,D}$ / MSF)

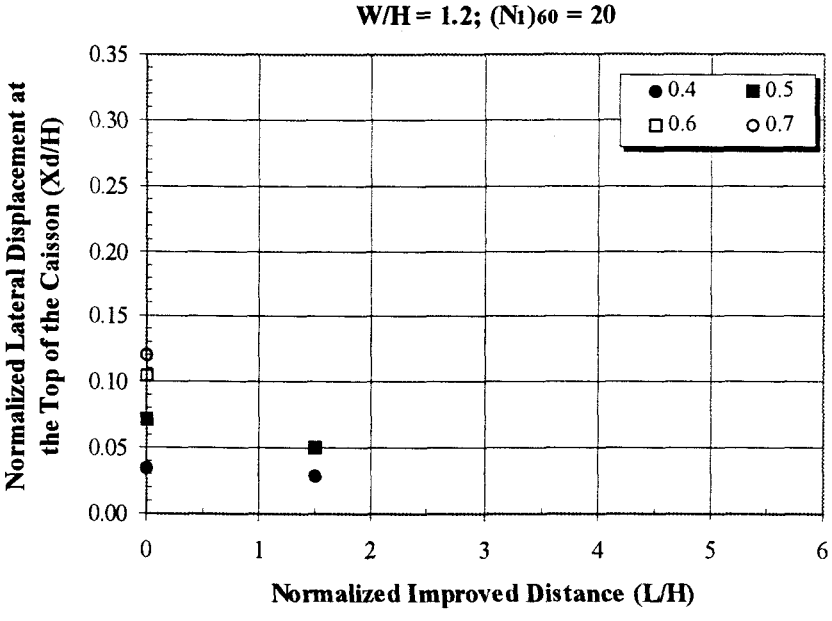

Figure 5-7: Normalized lateral displacements at the top of caisson for backfill with $(N_1)_{60}$ = 20 blows/0.3m and W/H ratio = 1.2 (data points are presented in the form of $A_{max,D}$ / MSF)

($(A_{max})_D/MSF$) are quite scatter due to inherent characteristics of earthquake motions used in the models.

By collecting the information from Figure 5-4 to Figure 5-7, the final results of the parametric study are plotted in Figure 5-8. The numbered triangles superimposed on the charts correspond to field case histories. The same numbered triangle but with two different values represents the upper and lower bound of the measured lateral displacement at the top of the caisson. Information pertaining to the strength of shaking, wall geometry, the penetration resistance of the backfill, and the observed displacements for the case studies is provided in Table 5-3. It should be noted that Figure 5-8 was prepared with width-to-height ratio (W/H) of 0.7 and 1.2, therefore, for the case of W/H not 0.7 or 1.2 (i.e., Case 4), the interpolation of lateral displacement corresponding to proper curves should be interpreted. By estimating peak horizontal acceleration at dredge line ($A_{max,D}$), along with appropriate magnitude scaling factor (MSF) and designed width-to-height ratio (W/H), the predicted lateral displacement at the top of the caisson can be obtained from Figure 5-8.

In Figure 5-8, the rubble fill adjacent to the caissons has been treated as non-liquefiable soil, thereby contributing to the "effect" width of the improved (i.e., non-liquefiable) soil. In the case of triangular, single-lift sections of rock fill the width of the rubble fill has been approximated as one half of the width of this fill at its base. The relationships provided in Figure 5-8 clearly demonstrate the benefit of ground treatment on the seismic performance of the caissons. It is also evident that the incremental benefit of a wider zone of ground treatment begins to decline once the

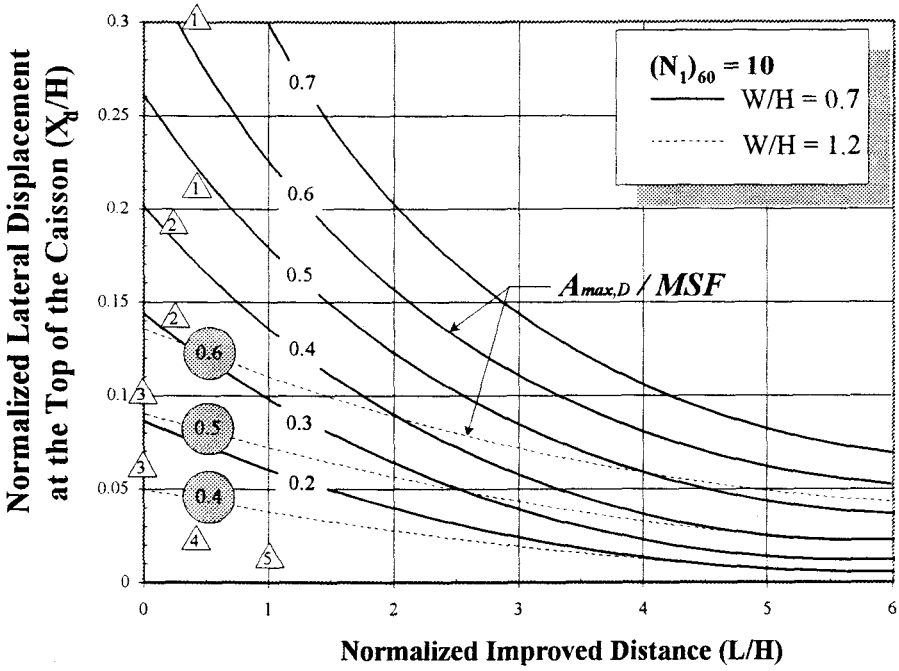

(a) Normalized lateral displacements for backfill with $(N_1)_{60}$ = 10

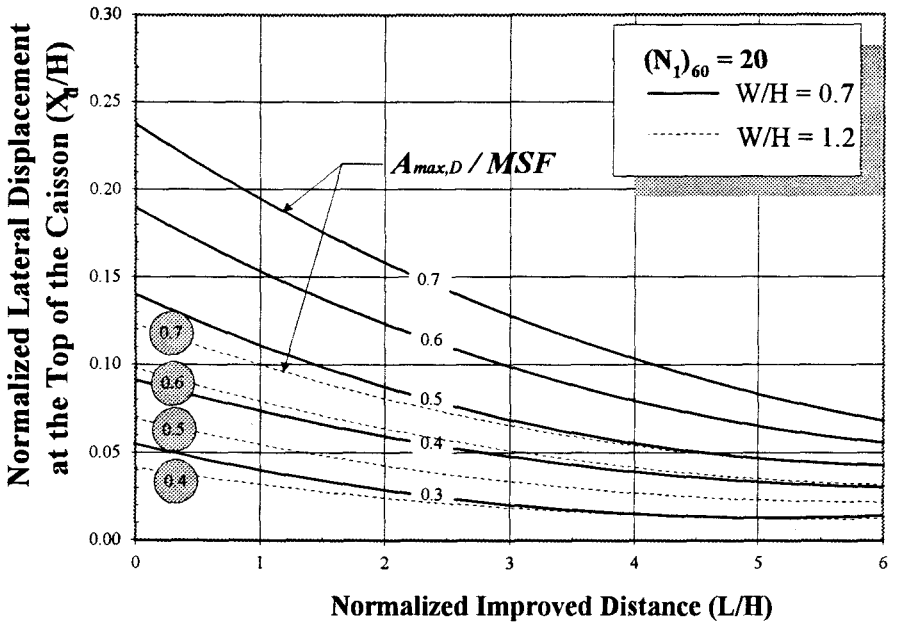

(b) Normalized lateral displacements for backfill with $(N_1)_{60}$ = 20

Figure 5-8: Simplified design charts for estimating lateral displacements of caissons

Table 5-3: Information on Case Studies

Case Study	$(A_{max})_D$ *(g)*	$(A_{max})_D/MSF$ *(g)*	*W/H*	X_d/H *(Measured)*	$(X_d/H)_{AVG}$	$(N_1)_{60,AVG}$
① Rokko Island	0.57	0.43	0.70	0.21~0.31	0.27	7.5
② Port Island	0.55	0.42	0.70	0.14~0.19	0.17	8
③ Akita	0.14	0.16	0.75	0.06~0.10	0.083	7.5
④ Kushiro (Pier 2)	0.16	0.18	1.03	0.022	0.022	4
⑤ Kushiro (Pier 3)	0.16	0.18	1.20	0.004~0.018	0.012	4
⑥ Kalamata*	0.15	0.08	0.52	8.6×10^{-3}~0.017	0.013	10

* The case study of Kalamata presented herein is for the comparison purpose and will be presented in the latter section.

soil improvement extends more than about 2.0 to 3.5 times the total height of the wall. At this point the cost of additional soil improvement may outweigh the benefits. It is interesting to note that the soil improvement guidelines prepared by the PHRI (1997) correspond to a normalized width of soil improvement of roughly 1.3 to 1.6.

A comparison of observed caisson displacements at various sites of Port of Kobe versus parametric study results is shown in Figure 5-9. Related information regarding peak horizontal acceleration at dredge line, W/H ratio, and soil penetration resistance are shown in the Table 5-4. The normalized ground motion intensity ($A_{max,D}$ / *MSF*) at Kobe Port is typically ranging within 0.4 and 0.5 as indicated in Table 5-3, i.e., 0.43 for Rokko Island and 0.42 for Port Island. In the case of Port Island, for example, enter normalized ground motion intensity of 0.42 into Figure 5-9 along with L/H = 0.25 (due to the rubble fill) and yield normalized lateral displacement of the

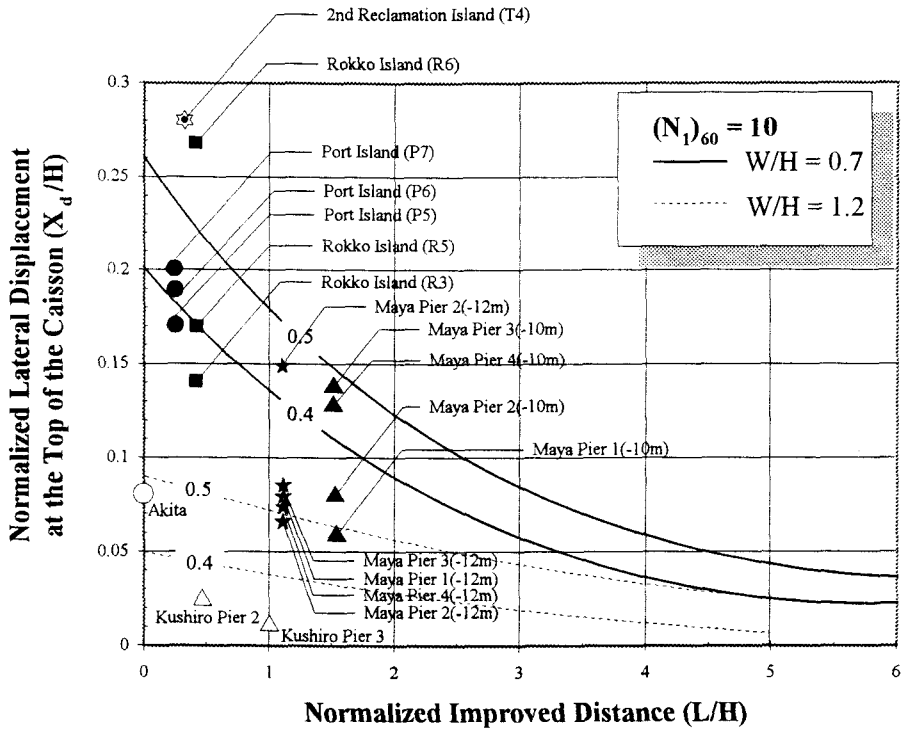

Figure 5-9: Compaison of field cases to the results of parametric study

Table 5-4: Field Data Information at Various Sites

Case Study	$(A_{max})_D$ *(g)*	$(A_{max})_D/MSF$ *(g)*	*W/H*	X_d/H *(Measured)*	$(X_d/H)_{AVG}$	$(N_1)_{60,AVG}$
① Port Island						
P5	0.55	0.42	0.68	0.14~0.19	0.17	8
P6	0.55	0.42	0.68	0.16~0.21	0.19	8
P7	0.55	0.42	0.68	0.14~0.30	0.20	8
② Rokko Island						
R3	0.57	0.43	0.70	0.09~0.19	0.14	7.5
R5	0.57	0.43	0.70	0.15~0.21	0.17	7.5
R6	0.57	0.43	0.70	0.21~0.31	0.27	7.5
③ 2nd Reclamation Island (T4)	0.57	0.43	0.60	0.17~0.41	0.28	7.5
④ Maya Wharf (-10m) Pier 1	0.55	0.42	1.00	0.03~0.10	0.06	8
Maya Wharf (-10m) Pier 2	0.55	0.42	1.00	0.06~0.10	0.08	8
Maya Wharf (-10m) Pier 3	0.55	0.42	1.00	0.14	0.14	8
Maya Wharf (-10m) Pier 4	0.55	0.42	1.00	0.12~0.13	0.125	8
⑤ Maya Wharf (-12m) Pier 1	0.55	0.42	1.00	0.05~0.10	0.08	8
Maya Wharf (-12m) Pier 2	0.55	0.42	1.00	0.05~0.09	0.07	8
Maya Wharf (-12m) Pier 3	0.55	0.42	1.00	0.088	0.088	8
Maya Wharf (-12m) Pier 4	0.55	0.42	1.00	0.074	0.074	8
⑥ Akita Port	0.14	0.16	0.75	0.06~0.10	0.08	7.5
⑦ Kushiro Port (Pier 2)	0.16	0.18	1.20	0.022	0.022	4
⑧ Kushiro Port (Pier 3)	0.16	0.18	1.20	0.004~0.018	0.012	4

caisson (X_d/H) of approximately 0.2. The measured X_d/H values are ranging from 0.14 to 0.3 with averaging of 0.19. Once again, the lateral displacement of the caisson is the function of W/H ratio, therefore, those cases where W/H ratios are not equal to 0.7 or 1.2, interpolation of the lateral displacement should be made in order to obtain appropriate values from Figure 5-9. It shows that predicted displacements of the caissons are in reasonable agreement with observed displacements in various locations at Kobe Port.

As a screening tool for estimating the seismically induced displacements of caissons, the recommended procedures for utilizing the results of the parametric study include:

1. Design the wall using standard pseudostatic limit equilibrium methods to determine the wall geometry *(W/H)*.
2. Determine $(A_{max})_D$ based on a site response analysis or approximate with empirical soil amplification factors to yield the peak ground surface acceleration and the reduction factor (r_d).
3. Select the magnitude scaling factor *(MSF)* for the specified earthquake magnitude, and compute the ground motion intensity factor as $(A_{max})_D/MSF$.
4. Given the standard penetration resistance of the backfill soils, the width of the ground treatment behind the caisson, and the ground motion intensity factor, enter Figure 5-8(a) or Figure 5-8(b) and obtain the normalized lateral displacement. From this, the deformation at the top of the wall (X_d) can be estimated.

5.4 Comparison of Field Case with the Design Chart

Comparison of Kalamata Harbor case study (Case 6) to parametric study results in Table 5-3 is made in order to examine the applicability of parametric study results to known seismic performance of concrete block type gravity wall. The information regarding 1986 Kalamata Earthquake are tabulated in Table 5-5.

Table 5-5: 1986 Kalamata Earthquake Information

Magnitude	$A_{max,D}$ *(g)*	$A_{max,D}/MSF$ *(g)*	*W/H*	*L/H*	*N (blows/0.3m)*	*Measured (cm)*	*Predicted (cm)*
6.2	0.153	0.085	0.52	0.56	10	15±5	23

For the magnitude of 6.2 (MSF = 1.8 in Table 5-2) with peak horizontal at dredge line of 0.153g, the normalized motion intensity is calculated as 0.085g. The width (W) and height (H) of the wall are 6 m and 11.6 m, respectively, therefore, W/H ratio is determined as 0.52. The averaged width of the rubble backfill (L) treated as "effect" of soil improvement is 6.55 m. The value of 0.56 for L/H ratio is obtained. Entering Figure 5-8(a) with $A_{max,D}/MSF = 0.085$, $L/H = 0.56$, $W/H = 0.52$, and SPT-N values of 10, $X_d/H \cong 0.02$ is determined. Then, the lateral displacement of the wall of 0.02×1160 cm = 23 cm is predicted. Comparing the predicted value to measured value (15±5 cm), the resulting design chart is over-predicted about 53 % in average.

5.5 Comparison of Permanent Displacement-Based Approach to Parametric Study Results

In Section 2.3 the permanent displacement-based approaches have been outlined. In order to compare those approaches to the results of parametric study, a caisson at Rokko Island (R6 Type) is used for comparison purpose. Detailed caisson displacement calculations based on both Richards-Elms method and Whitman-Liao method are shown in Appendix. Only the results of both methods are summarized herein. The predicted results along with parametric study results and measured value are listed in Table 5-6. It should be noted that in both Richards-Elms and Whitman-Liao methods peak ground velocity and acceleration are used, whereas peak horizontal accelerations at dredge line are used in the parametric study. The recorded peak horizontal accelerations ($A_{max,D}$) near dredge line in the direction of North-South, East-West, and Up-Down are 0.576g, 0.55g, and 0.8g, respectively. Dividing these values of $A_{max,D}$ by magnitude scaling factor of 1.25 (M_w 6.9), normalized ground motion intensity ($A_{max,D}/MSF$) can be determined as 0.46, 0.44, and 0.64. In the cases of liquefiable backfill, entering 0.46, 0.44, and 0.64 into Figure 5-8(a) along with W/H = 0.7 and accounting for the "effect" of improved zone of L/H = 0.5 due to rubble backfill, normalized lateral displacements at the top of the caisson (X_d/H) can be computed as 0.205, 0.195, and 0.32. The lateral displacements of the caisson (H=17.5 m) are then determined as 359 cm, 341 cm, and 560 cm in the North-South, East-West, and Up-Down direction as shown in Table 5-6, respectively. In the cases of no liquefaction in the backfill, entering these values into Figure 5-8(a) along with L/H = 6, normalized lateral displacements (X_d/H) can be obtained as 0.03, 0.03, and

0.06. The lateral displacements of the caisson are determined as 53 cm, 53 cm, and 105 cm in the North-South, East-West, and Up-Down direction, respectively.

Table 5-6: Comparison of Proposed Method to Displacement-Based Approaches

Methods / *Displacements*	*Richards-Elms (cm)*	*Whitman-Liao(cm)*		*Parametric Study(cm)*	*Measured(cm)*	
		mean	d_{allow} [1]		*range*	*average*
Liquefaction in the Backfill:						
North-South	247	48	192	359	315~465	390
East-West	48	11	44	341		
Up-Down	473	37	148	560		
No Liquefaction in the Backfill:						
North-South	1.3	0.03	0.12	53	—	—
East-West	0.3	2×10^{-3}	8×10^{-3}	53		
Up-Down	2.5	0.42	1.68	105		

Note: [1] d_{allow} = allowable displacement of wall

It is obvious that both displacement-based approaches underestimate the performance of the caisson during earthquake even though the effect of liquefaction in the backfill has been accounted for in the analysis. The Richards and Elms method was developed based on the initial choice of a specified limiting wall displacement similar to the Newmark's sliding block analysis. This procedure computes the weight of the wall required to prevent motion greater than that specified. It can be done by combining an incremental relative displacement model with the Mononobe-Okabe analysis. Since Richards and Elms method was developed in a manner of sliding block type approach, it overlooked the tilting failure mechanism of the wall, which

has been observed in many historic earthquakes, such as aforementioned case studies. The research by Siddharthan, et al. (1992), considering the combination of tilting and sliding failure mechanism, indicates that tilting failure mechanisms generally increase wall displacements over those produced by sliding-only models. Whitman and Liao proposed an enhancement of Richards and Elms method considering the effects of various uncertainties, such as soil resistance and ground motion, and the permanent displacement then can be calculated as a log-normal distribution with mean value. Also, there is ample evidence (Seed and Whitman, 1970, Evans, 1971) that in practice, earthquake effects on retaining walls are greater than those predicted by the Mononobe-Okabe analysis. In practice, the response of gravity type retaining walls, especially in the waterfront and the occurrence of soil liquefaction, under seismic loading conditions is more complicate and generally is nonlinear behavior. However, those approaches, either pressure-based or displacement-based approaches, provide simplified and straightforward means to estimate seismic loading and earthquake-induced displacement of the gravity type walls. Actually, some of the cases designed by conventional approaches perform well during earthquake due to higher safety factor involved and conservative consideration embedded in static wall design. Those methods should be use and interpreted carefully.

More sophisticated nonlinear analysis method as proposed in this chapter is obviously more appropriate to represent the soil-structure response under seismic loads. Based on the results of parametric study, as evidences in Table 5-6, the proposed model is capable of accounting for nonlinear and plastic behavior of the soil, earthquake-induced liquefaction and excess pore pressures, ground motion

characteristics, irregular soil and wall geometry, and interfaces between the soil and structure.

5.6 Summary and Conclusions

This investigation has highlighted the following pertinent aspects of the seismic design and performance of caisson retaining walls:

1. From a practical perspective, the "failure" of a caisson quay wall can be considered as corresponding to lateral deformations in the range of 10 cm to 30 cm, due to the damage incurred by adjacent cargo handling equipment and facilities. The allowable deformations will therefore reflect the sensitivity of appurtenant structures.
2. The factors of safety computed with standard pseudostatic design methods are not adequately correlated with the wall deformations to facilitate estimates of seismically-induced lateral deformations. Therefore, deformation-based analyses that account for the generation of excess pore pressures in the backfill are recommended.
3. Simplified design charts have been developed to aid in the performance-based seismic design of gravity caissons. The proposed procedures to predict earthquake-induced lateral displacement of the caisson under various conditions such as soil density, ground motion characteristics, and wall geometry, have also been introduced. The proposed nonlinear, effective stress analysis has been proved that it is a more appropriate method to simulate the seismic performance of the caisson as compared to conventional design approaches. It is more efficient

especially when excess pore pressure generation and liquefaction have occurred in the backfill. Due to the limitation of modeling consideration, uncertainties involved in parametric study are estimated to be within ±20% in association with available soil parameters and ground motion characteristics. This statement is especially true as modeling case studies where the soil properties and ground motions are not always available.

4. The relationships provided in Figure 5-8 clearly demonstrate the benefit of ground treatment on the seismic performance of the caissons. It is also evident that the incremental benefit of a wider zone of ground treatment begins to decline once the soil improvement extends more than about 2.0 to 3.5 times the total height of the wall. At this point the cost of additional soil improvement may outweigh the benefits.
5. The design charts are robust with respect to seismically-induced excess pore pressure in that r_u vales ranging from 0 to 1 are accounted for. Therefore, the charts can be used for cases with non-liquefiable backfill as well as liquefiable soils.

6 SEISMIC BEHAVIOR OF PILE-SUPPORTED WHARVES

6.1 Introduction

The seismic performance of pile foundations in liquefiable soil deposits is a major issue for many new and existing waterfront structures. Pertinent examples including the 1964 Niigata earthquake, the 1989 Loma Prieta earthquake, and recent the 1995 Hyogoken-Nanbu earthquake, have shown that earthquake-induced soil liquefaction and lateral ground displacement have caused extensive damage to pile foundations (Hamada, 1992a; Tokimatsu et al., 1996; Werner et al., 1998). Soil-pile interaction in liquefied soil is not well understood, and the available well-documented case histories are still too limited in number and detail to develop reliable design methodologies. Current pseudostatic analyses of the peak loading conditions for single pile systems either use back-calculated apparent reduction factors in the p-y curves of piles in liquefiable sand (Miura and O'Rourke, 1991), or include soil movement as a part of the soil-pile interaction analysis, in which the residual shear strength of liquefiable soil is used (Wang and Reese, 1998). Furthermore, previous investigations of lateral load versus pile deflection relationships have been mainly based on piles founded in sands and clays with a level ground surface. To evaluate the lateral load capacity of vertical piles embedded in a sloping rock fill, which is a common geometry for pile-supported wharves, it is necessary to modify the p-y relationships to reflect the properties of the rock fill and the effect of the sloping surface.

The seismic analyses of the soil-pile interaction problems have been investigated by numerous researchers (Boulanger, et al., 1997; Chaudhuri, et al., 1995; Finn, et al., 1994; Hamada, 1992a, Johnson et al., 1998; Kagawa, 1992; Matlock, et al., 1981; Miura, et al., 1991; Mori, et al., 1992; Naesgaard, 1992; Ohtomo, et al., 1994; Stewart, et al., 1988; Tokida, et al., 1992; Wang, et al., 1998). In general, current design methods associated with lateral loading from horizontal soil movements resulting from earthquake-induced liquefaction acting on piles or pile groups may be classified into four groups as follows:

- *Empirical methods*: the response of the pile is estimated in terms of maximum bending moment, maximum shear force, and pile head deflection on the basis of charts developed from field or laboratory data;
- *Pressure-based methods*: a lateral pressure distribution acting against the piles is estimated in a relatively simple manner, and is generally only used to calculate the maximum bending moment in the piles;
- *Displacement-based methods*: the distribution of lateral soil displacement is first estimated by free field (absence of piles) site response including liquefaction, and then lateral soil movement is used as input for near field (presence of piles) site response. The resulting pile deflection, maximum shear force, and bending moment distribution are calculated;
- *Numerical methods (finite element or finite difference method)*: the piles and soils are represented in the sophisticated manner to take into account more complicate geometry of the model, i.e., irregular soil layers and sloping ground surface, and overall soil-pile interaction responses are calculated.

A common soil-pile interaction model is based on the Beam on Nonlinear Winkler Foundation (BNWF) method. In the BNWF analysis the pile is represented by a series of elastic beam elements and each attached with discrete nonlinear springs which represent the soil resistance. The behavior of these nonlinear soil springs is represented by the relationship of soil ultimate resistance versus relative pile displacement (nonlinear p-y curves). The assumption of Winkler type foundation is that the soil-pile interaction force at any depth is related to the pile shaft displacement at that depth only, therefore independent of the interaction forces above and below. Soil behavior near the pile is strongly influenced by soil deformations associated with pile displacements. Since these soil-pile interaction effects decrease with distance from the pile, soil-pile models often discretize the soil into free field and near field components. The results of free field site response including liquefaction potential, lateral soil movement, pore pressure generation, and acceleration time history, are first evaluated and estimated. The resulting lateral soil movement or acceleration time history is then utilized as input data in the BNWF analysis. In this research, a similar approach has been adopted except for two aspects: (1) a simplified bilinear elasto-plastic force-displacement relationship (p-y curves) is adopted to simulate soil-pile interaction; (2) the free field site response including liquefaction and pore pressure generation is coupled with these bilinear p-y curves in the pile-soil interaction analysis.

6.2 Calibration of the FLAC Model for the Lateral Loading of Piles

In order to evaluate the seismic performance of pile-supported structures at ports, the behavior of soil-pile interaction in the FLAC model was first validated by application to three static laterally loaded tests, one dynamic centrifuge test, and one well-documented field case study. The objectives of these analyses are to (1) compare the response of numerical models to field tests and then calibrate numerical models with pile foundations in level or in sloping ground; (2) compare the computed response to the measured seismic performance of a pile-supported wharf; and (3) improve the applicability of soil parameters used for pile foundations in subsequent parametric studies. The properties of the soil and the pile used in the following sections are either directly obtained from the laboratory tests provided by authors or estimated using well-established geotechnical correlations.

6.2.1 Static Lateral Loading of Single Piles on Horizontal Ground

Two static lateral load tests on piles were selected and comparisons of the load test results to the computed response are examined. Test No. 1 is setup in laboratory scale for an aluminum pile in a dry sand. Test No.2 is established in field scale for a concrete pile in saturated sand with level ground conditions. These two static tests provide an opportunity to evaluate and justify the soil-pile interaction parameters used in the numerical model to rather simple field static tests

6.2.1.1 Lateral Load Pile Test 1 (Gandhi et al., 1997)

All tests were carried out using the setup shown in Figure 6-1 with a 0.7×0.7×0.6 m test tank filled with dry river sand in laboratory scale. The lateral load was applied to the pile using dead weights as shown in Figure 6-1. The test soil used was clean and fine to medium river sand and aluminum pipe pile with outer diameter of 18.2 mm and wall thickness of 0.75 mm was used as model pile.

The properties of sand and pipe pile are tabulated in Table 6-1(a) and Table 6-1(b), respectively. Piles were instrumented for measuring bending moment by pasting electrical-resistance-type strain gauges. The lateral load was applied by 10 equal increments. The horizontal displacement of the pile head was measured using mechanical dial gauges. Each load increment was maintained for a minimum of 10 minutes till the lateral displacement of pile head stabilized with no further movement. Vertical settlement of the pile head was also measured and found negligible.

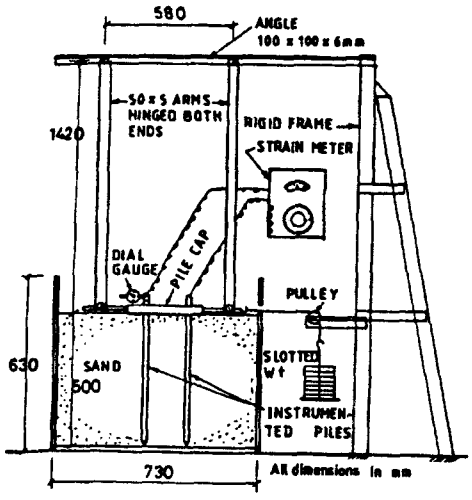

Figure 6-1: Experimental setup for static lateral test 1 (Gandhi et al., 1997)

Table 6-1 (a): Properties of Test Sand for Test 1

Description	γ_{max} *(kN/m³)*	γ_{min} *(kN/m³)*	ρ_d *(kg/m³)*	ϕ *(deg)*	c *(N/m²)*	ν	G_m *(N/m²)*	K_m *(N/m²)*
Test Sand	17.3	14.61	1600	35	0	0.25	6.4×10^6	1.1×10^7

Note: γ_{max}=Maximum unit weight; γ_{min}=Minimum unit weight; ρ_d=Dry density; ϕ=Friction angle; c=Cohesion; ν=Poisson's ratio; G_m=Mean shear modulus; K_m=Mean bulk modulus

Table 6-1 (b): Properties of Test Pipe Pile for Test 1

Description	d_{out} *(mm)*	d_{in} *(mm)*	t *(mm)*	L *(mm)*	A *(mm²)*	*Perimeter (mm)*	E_p *(N/mm²)*	I_p *(mm⁴)*
Aluminum Pipe Pile	18.2	16.7	0.75	500	41.1	57.2	55000	1565

Note: d_{out}=Outer diameter; d_{in}=Inner diameter; t=Wall thickness; L=Length; A=Area; E_p=Modulus of elasticity; I_p=Moment of inertia

6.2.1.1.1 FLAC Model Setup

The laboratory model was analyzed in the numerical model using a mesh of 10×10 zones. A comparison run was made by increasing the size of the mesh to 30×10 and 10 times of coordinate in the horizontal direction to avoid the effect of side boundary. No significant change in pile and soil displacement was observed and the computed deformations varied by less than 2%.

The side boundaries are fixed in the horizontal direction and the base boundary is fixed in both the horizontal and vertical directions. The sand layer is modeled with Mohr-Coulomb materials. The shear and bulk moduli are required to define the elastic behavior of the soil. The soil shear strength is defined by the

cohesion and the friction angle. The geotechnical parameters used in FLAC are provided in Table 6-1(a).

The pile in the test is modeled using "pile" element in FLAC and the pile is divided into five equal length segments of 10 cm each. The pile nodes can be defined separately from the soil nodes. The pile nodes and soil nodes are connected by nodal joint elements having shear and normal stiffness and maximum shear and normal forces. In this manner, an approximate representation of the development of lateral resistance with relative soil-pile movement and ultimately the limiting soil pressure acting on the piles is simulated. This approach is similar to "p-y" curves procedures currently used for the analysis of laterally loaded piles. Input data for pile elements required are pile flexural stiffness (EI), area (A), perimeter (P), and length of pile (L). The density of the pile is ignored. The lateral loads are applied at the top of the pile in 6 equal increments (25 N each) ranging from 50 N to 200 N. The structural parameters used in FLAC are provided in Table 6-1(b).

The properties needed to characterize the response of the pile/soil interaction in FLAC model are shear coupling springs and normal coupling springs. If the failure associated with the pile/soil response is assumed to occur in the soil, then the lower limits for shear coupling spring friction resistance and cohesive strength can be related to the angle of internal friction of the soil and the soil cohesion times the perimeter of the pile, respectively. In this case, 35° and zero are used for shear coupling spring friction and cohesion, respectively. The normal coupling spring properties, as indicated in Chapter 3, are obtained from running a test pile with the same pile geometry and soil properties as in the FLAC model. The stiffness of normal

coupling spring is obtained by calculating the slope of maximum normal coupling spring strength versus relative displacement between soil and pile. The cohesive and friction resistances of the normal spring are calculated from the interception and slope of maximum normal coupling spring strength versus effective confining stress at the depth of interest, respectively. The representative shear and normal coupling spring properties for an individual test pile is listed in Table 6-2.

Table 6-2: Properties of Pile/Soil Interaction for Test 1

Description	*Test 1*
Shear coupling spring stiffness (Pa/m)	4.55×10^{6}
Shear coupling spring cohesion (Pa/m)	0
Shear coupling spring friction (degree)	35
Normal coupling spring stiffness (Pa/m)	4.55×10^{6}
Normal coupling spring cohesion (Pa/m)	1.5×10^{3}
Normal coupling spring friction (degree)	60

6.2.1.1.2 Results of Static Lateral Load Test 1

The predicted and measured pile head deflections and bending moments at pile deflection of 10 mm are shown in Figure 6-2 and Figure 6-3, respectively. The predicted pile deflections at the load stages of 75 N and 100 N are slightly underestimated comparing to measured values by approximately 10% and 20%, respectively. The predictions within the load stages of 125 N to 200 N generally match well with measured values. Both computed and measured maximum bending moments are obtained at the depth of 200 mm and the computed maximum bending

moments are over-predicted by approximately 7%. The overall agreement between predicted and measured deflections as well as the bending moments is good.

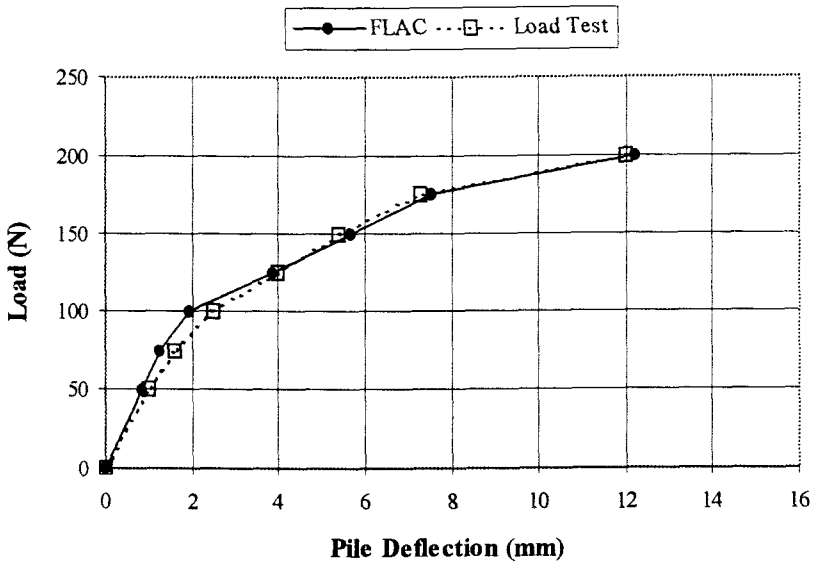

Figure 6-2: Measured pile head deflections of lateral test 1 versus FLAC predictions

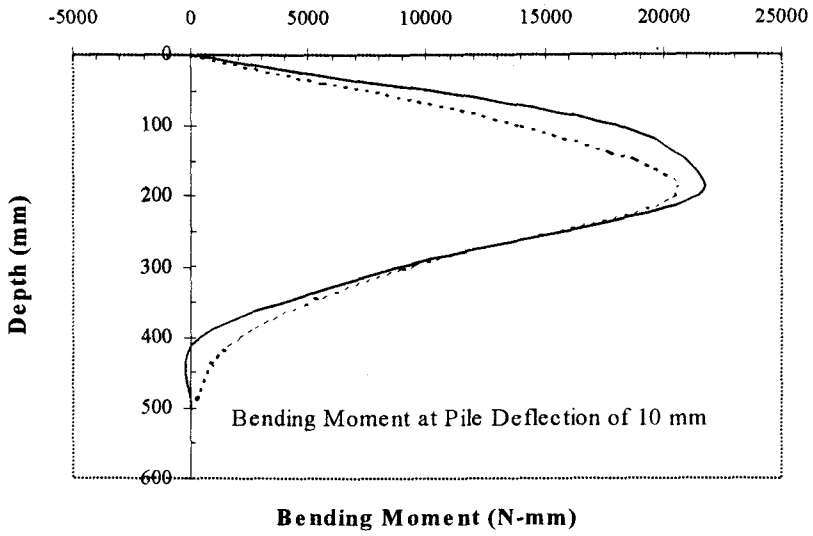

Figure 6-3: Measured bending moments at pile head deflection of 10 mm versus FLAC predictions in lateral test 1

6.2.1.2 Lateral Load Pile Test 2 (Alizadeh et al., 1970)

The soils at Lock and Dam 4 are medium to fine sands and silty sands with averaging the standard penetration resistance of 32 blows/ft in the upper 60 feet. The angle of internal friction of the sands ranged from 31° to 35° and the submerged unit weight averaged 62.8 lbs/ft^3. The total of 11 piles has been tested at the site in order to determine the lateral loading-deformation behavior for individual vertical and batter piles. The No. 5 square concrete pile (16 inches) at Lock and Dam 4 is chosen as test 2. The properties of soil and test pile obtained from Mansur and Hunter (1970) are tabulated in Table 6-3(a) and Table 6-3(b), respectively.

For practical purposes, all test piles at Lock and Dam 4 site may be considered as single isolated pile not influenced by adjacent piles (Alizadeh and Davisson, 1970). Test pile is loaded normal to its axis with a calibrated hydraulic jack. The loading arrangement is shown in Figure 6-4. Deflections normal to the pile axis are measured with two dial indicators reading to 0.001 in. placed at the ground line.

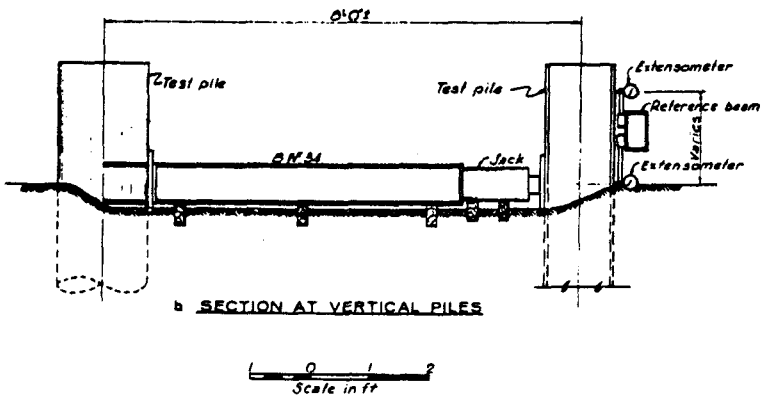

Figure 6-4: Lateral testing frame for lateral test 2 (Alizadeh et al., 1970)

Table 6-3 (a): Properties of Soil for Test 2

Description	ρ_d *(slug/ft³)*	c *(lb/ft²)*	ϕ *(deg.)*	ν	n	k *(ft/sec)*	G_m *(lb/ft²)*	K_m *(lb/ft²)*
Sand	3.42	0	35	0.32	0.35	1.3×10^{-3}	4×10^{6}	1.2×10^{7}

Note: ρ_d=Dry density; c=Cohesion; ϕ=Friction angle; ν=Poisson's ratio; n=Porosity; k=Permeability; G_m=Mean shear modulus; K_m=Mean bulk modulus

Table 6-3 (b): Properties of Pile for Test 2

Description	d *(in)*	L *(ft)*	A *(ft²)*	*Perimeter (ft)*	E_p *(lb/ft²)*	I_p *(ft⁴)*
Concrete Pile	16	55	1.778	5.333	9.072×10^{8}	2.63×10^{-1}

Note: d=Pile width; L=Length; A=Area; E_p=Modulus of elasticity; I_p=Moment of inertia

6.2.1.2.1 FLAC Model Setup

The procedure of model setup for test 2 is similar as test 1. The model is analyzed using a mesh of 20×10 zones. The lateral loads are applied at the top of the pile head from the range of 10 to 30 kips by 4 equal increments (5 kips each). The representative shear and normal coupling spring properties in FLAC model for an individual pile are shown in Table 6-4.

Table 6-4: Properties of Pile/Soil Interaction for Test 2

Description	*Test 2*
Shear coupling spring stiffness (lb/ft²/ft)	2.0×10^{6}
Shear coupling spring cohesion (lb/ft²/ft)	0
Shear coupling spring friction (degree)	35
Normal coupling spring stiffness (lb/ft²/ft)	2.0×10^{6}
Normal coupling spring cohesion (lb/ft²/ft)	2.0×10^{4}
Normal coupling spring friction (degree)	65

6.2.1.2.2 Results of Static Lateral Load Test 2

The predicted and measured pile head deflections are shown in Figure 6-5. No measured bending moment is available for No. 5 pile. The analytical result for pile head deflection compare very favorably with measured deformation.

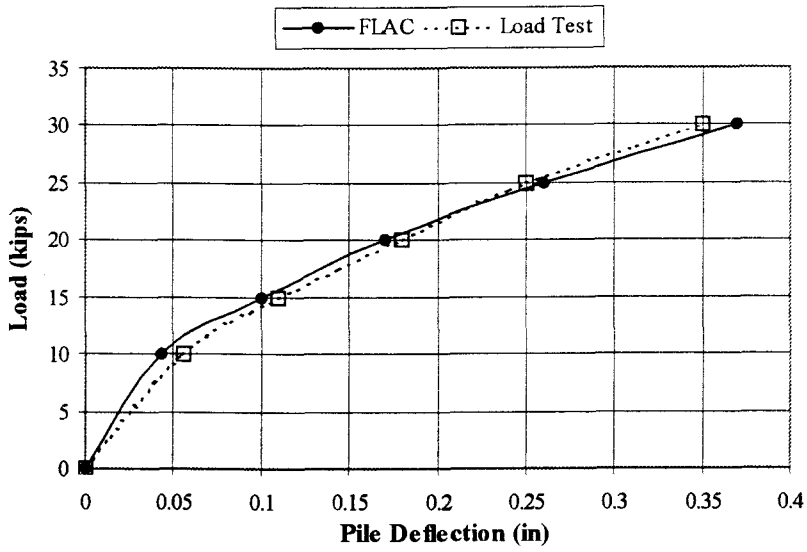

Figure 6-5: Measured pile deflection of lateral test 2 versus FLAC predictions

The results of static lateral load test 1 and test 2 show that current numerical model has a potential ability to predict pile head deflection and bending moment within a reasonable agreement either in the dry soil (Test 1) or in the saturated soil (Test 2) for level ground surface. The soil-pile interaction in sloping ground is not the same as that with a level ground surface due to decreased lateral soil resistance on piles on downhill side and increased lateral soil resistance on the uphill side. This condition is especially significant for piles under seismic shaking, in which applied

loading is a two-way motion. Therefore, the behavior of pile under static lateral load condition in the sloping ground is first conducted in the following section.

6.2.2 Static Lateral Loading of Piles in Sloping Ground

Lateral load tests of two production piles in sloping rock fill were performed for a new container wharf constructed at the Port of Los Angles (Diaz et al., 1984). This test provides a good opportunity to examine the influence of the sloping conditions on the lateral behavior of prestressed concrete piles.

The wharf section is shown in Figure 6-6. Two instrumented production piles, noted as reaction and test pile, were driven in the back row as indicated in Figure 6-6. An instrumented reaction pile was driven approximately six feet (center to center) behind each test pile. All test and reaction piles were 24 in. octagonal prestressed concrete piles with 80 feet long. The test pile setup is shown in Figure 6-7. Each pair of test piles was loaded by hydraulic jack between the test pile and reaction pile in step of 8, 16, 24, and 32 tons (71, 142, 214, and 285 kN). Each load step was applied at a rate of approximately two tons (18 kN) per minute and deflections of the piles were recorded at one-half minute interval during loading. Static and repeated loading situations were made for two test piles. The wharf deck was not constructed during the lateral load tests.

The subsurface conditions consist of rockfill at a slope ratio of 1.5:1 (horizontal to vertical) underlain by silty sand and silt. The properties of soils and test piles are listed in Table 6-5(a) and Table 6-5(b), respectively.

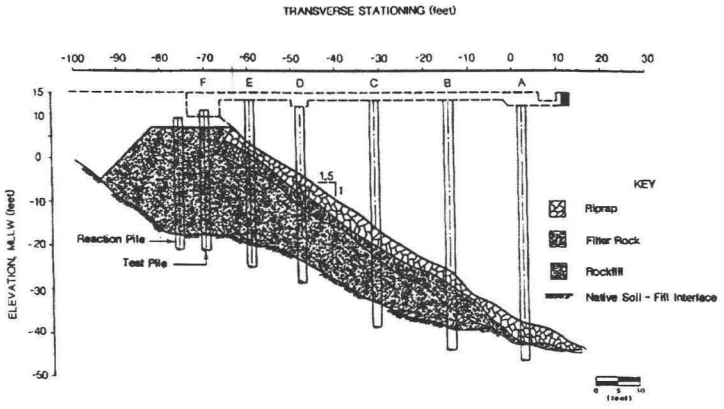

Figure 6-6: Wharf and actual slope cross-section for static lateral test in sloping ground (Diaz et al., 1984)

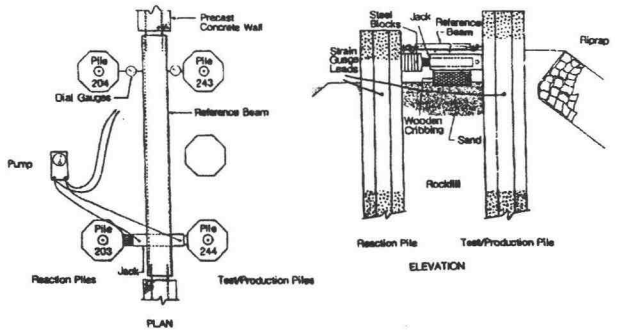

Figure 6-7: Test pile setup (Diaz et al., 1984)

Table 6-5 (a): Properties of Soils for Static Lateral Load Test in Sloping Ground

Soil Type	ρ_d *(slug/ft^3)*	c *(lb/ft^2)*	ϕ *(deg.)*	ν	k *(ft/sec)*	G_m *(lb/ft^2)*	K_m *(lb/ft^2)*
① Riprap	4.10	0	47	0.20	1×10^{-1}	7×10^{7}	9.3×10^{7}
② Rockfill	4.00	0	45	0.20	1×10^{-1}	6×10^{7}	8×10^{7}
③ Silty Sand	3.36	0	35	0.23	1×10^{-4}	2.5×10^{6}	5.5×10^{6}
④ Silt	3.30	0	25	0.25	5×10^{-5}	2.3×10^{6}	8.1×10^{6}
⑤ Sand and Silty Sand	3.36	0	37	0.23	1×10^{-4}	2.5×10^{6}	5.5×10^{6}

Note: ρ_d=Dry density; c=Cohesion; ϕ=Friction angle; ν=Poisson's ratio; k=Permeability; G_m=Mean shear modulus; K_m=Mean bulk modulus

Table 6-5 (b): Properties of Pile for Static Lateral Load Test in Sloping Ground

Description	*d (in)*	*L (ft)*	*A (ft^2)*	*Perimeter (ft)*	*E_p (lb/ft^2)*	*I_p (ft^4)*
Octagonal Prestressed Concrete Pile	24	80	3.31	6.6584	5.8×10^{8}	8.76×10^{-1}

Note: d=Pile width; L=Length; A=Area; E_p=Modulus of elasticity; I_p=Moment of inertia

6.2.2.1 FLAC Model Setup

The model was analyzed using a mesh of 50×10 zones. Both side boundaries (left and right) were set far enough to avoid the effects of side boundary. The model setup was shown in Figure 6-8. The soil properties for each layer shown in Table 6-5(a) were used for the analysis. The properties of the 24 in. octagonal prestressed concrete pile were given in Table 6-5(b).

It should be noted that the results of previous two static lateral tests (Test 1 and Test 2) were based on piles embedded in dry or saturated sands in a level ground surface. It is necessary to take the effect of the sloping surface on the properties needed to characterize the response of pile/soil interaction, i.e., shear coupling spring and normal coupling spring properties, into account. The difference between pile founded in the sandy soil with level surface and pile founded in the rockfill with sloping surface is reflected on the reduction of lateral resistance of soil acting on pile due to sloping ground.

The representative shear and normal coupling spring properties for an individual pile used in FLAC model were adjusted by the reduction factor proposed by Diaz, et al. (1984) as follows.

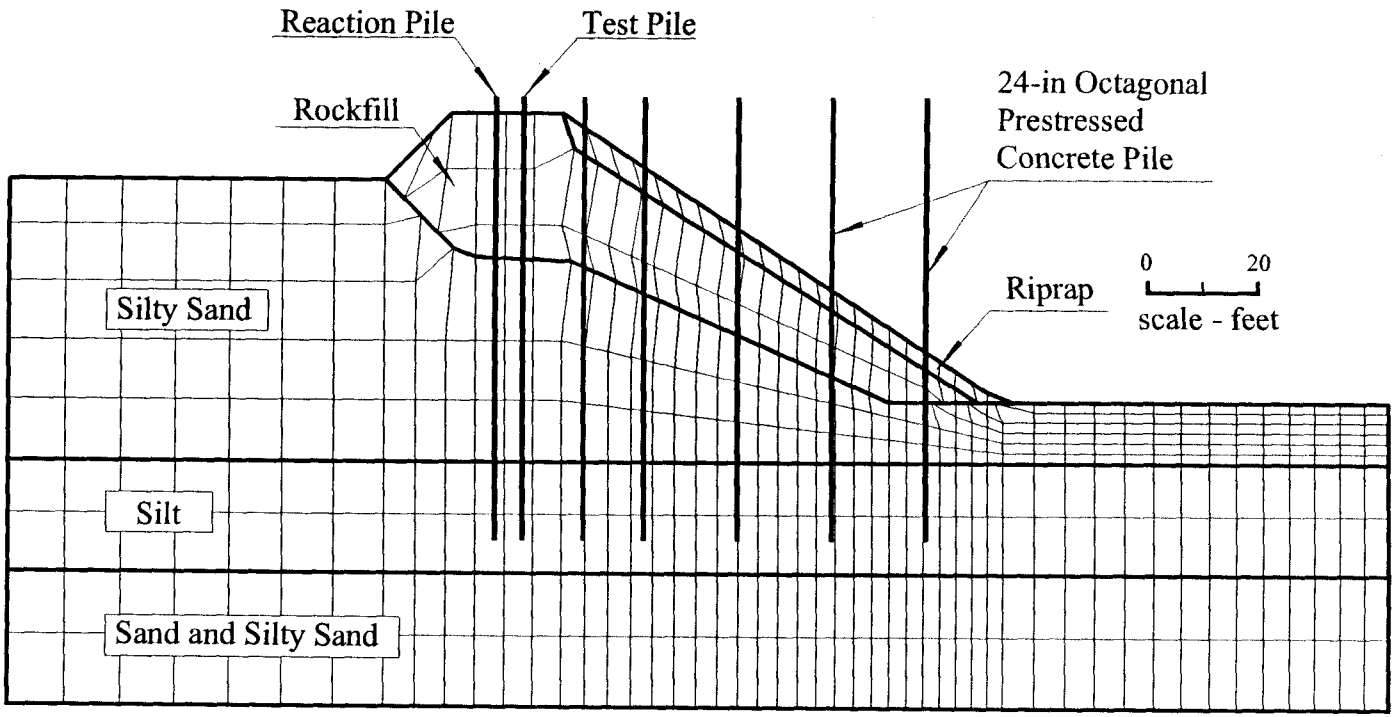

Figure 6-8: FLAC model setup for static lateral load test in sloping ground

$$\beta = \frac{K_{ps} - K_{as}}{K_p - K_a} \tag{6-1}$$

where

β = Lateral resistance slope reduction factor;

K_{ps} = Coulomb passive earth pressure coefficient (vertical wall, sloping backfill)

K_{as} = Coulomb active earth pressure coefficient (vertical wall, sloping backfill)

K_p = Coulomb passive earth pressure coefficient (vertical wall, horizontal backfill)

K_a = Coulomb active earth pressure coefficient (vertical wall, horizontal backfill)

The active and passive pressure coefficients were obtained with $\alpha = 34°$ (angle of rockfill slope) The reduction factor for pile loading in the down slope direction was then calculated as 0.6 using equation 6-1. Therefore, the reduction factor, β, ranges from 0.6 to 1.0 for slope angles of 34° to 0° (i.e., $\alpha = 0$ and $\beta = 1$), respectively. In order to account for the effect of riprap, a reduction factor of 0.9 was applied to the representative shear and normal coupling spring properties of pile used in FLAC model and the values are shown in Table 6-6.

Table 6-6: Properties of Pile/Soil Interaction for Pile in Sloping Ground

Description	***Test #2***
Shear coupling spring stiffness (lb/ft^2/ft)	2.0×10^7
Shear coupling spring cohesion (lb/ft^2/ft)	0
Shear coupling spring friction (degree)	45
Normal coupling spring stiffness (lb/ft^2/ft)	2.0×10^7
Normal coupling spring cohesion (lb/ft^2/ft)	2.0×10^5
Normal coupling spring friction (degree)	80

A comparison of pile displacements computed using LPILE (Reese, 1990) and FLAC was also made in order to minimize the uncertainties involved in the numerical modeling. The soil profile used in LPILE analysis is shown in Figure 6-9.

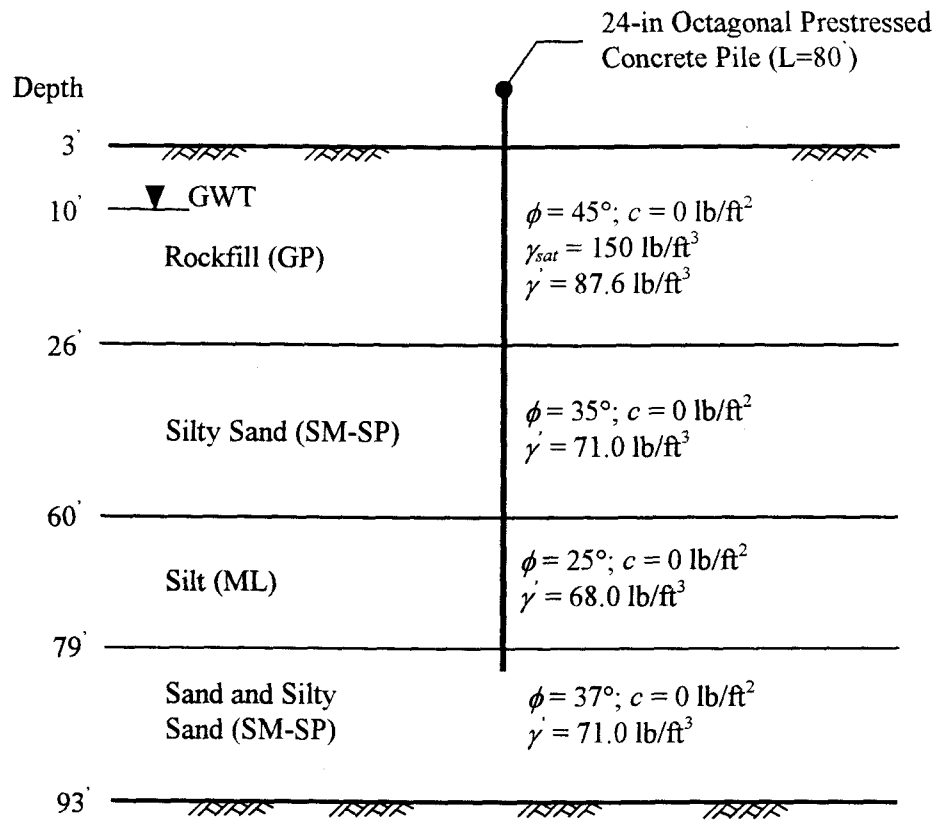

Figure 6-9: Soil profile used in "LPILE" analysis

The version of LPILE used in the analysis can not account for sloping surface, therefore, some modifications were required. The rockfill was treated as a cohesionless soil in LPILE and rock shear strength parameters (i.e., c=0 and $\phi = 45°$) were used. The constant of modulus of subgrade reaction (k_s) was reduced to account for the effect of sloping surface. The trial values of k_s were not obtained until the

curve of predicted pile head deflection corresponding to each loading step (8, 16, 24, and 32 tons) was matched within the curves of measured pile head deflection. A series of soil resistance (p) versus pile deflection (y) curves were obtained from this iterative procedure. The p-y curves for various depths were then used as input p-y curves in LPILE. The pile deflections were then predicted at various loading steps.

6.2.2.2 Results of Static Lateral Load Test in Sloping Ground

The predicted pile head deflections in the sloping rockfill using FLAC and LPILE along with the measured pile head deflections from the various test conditions (static and repeat loading) are shown in Figure 6-10. Also, a comparison of moments measured from strain gauge data to moments predicted using FLAC and LPILE is shown in Figure 6-11.

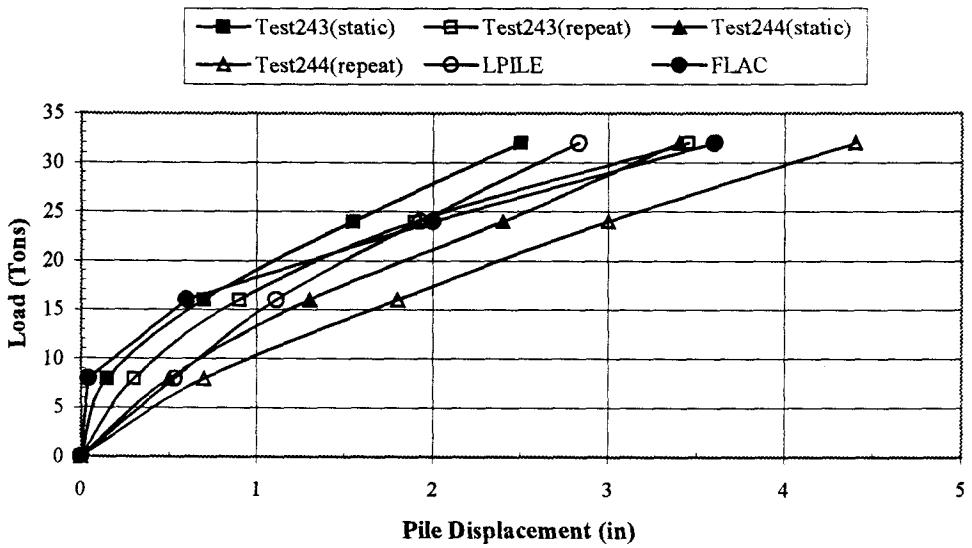

Figure 6-10: Measured and predicted pile head deflections using LPILE and FLAC

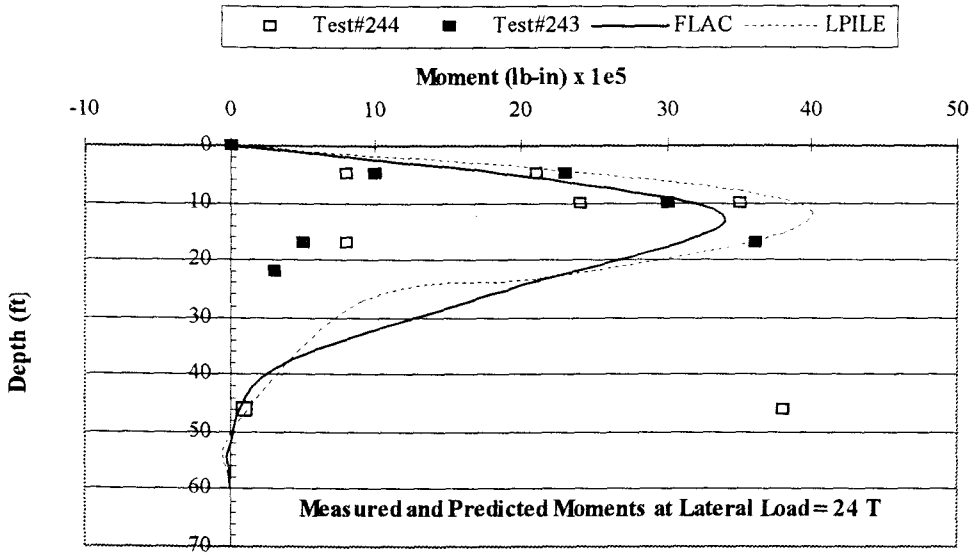

Figure 6-11: Comparison of moments measured from strain gauge data to moments predicted using LPILE and FLAC at lateral load = 24 tons

The predicted pile head deflections using FLAC (Figure 6-10) are in reasonable agreement with the measured values, although the pile deflections are underestimated at lower loading steps, i.e., 8 and 16 tons. The properties of shear and normal coupling springs including spring stiffness and spring yield strength used in FLAC were obtained using average values over the depth of rockfill, i.e., at about the middle depth of sloping rockfill where the soil confining stress was higher than that near ground surface. In this manner, the effect of soil-pile interaction in terms of stiffness and yield strength of coupling springs, which simulate resistance behavior of the soil, will be more significant at higher loading stages than those at lower loading stages. Hence, predicted pile deflections were more representative and matched well at the higher loading stages whereas underestimated at the lower loading stages. However, overall predictions of the pile head deflections in FLAC were satisfactory.

The predicted pile head deflections obtained from LPILE were also matched well with measured pile head deformations. Due to the lack of systematic procedures in LPILE for piles embedded in sloping rockfill, the most representative p-y curves at various depths were difficult to establish.

It can be seen in Figure 6-11 that both the predicted and measured bending moment profiles are quite similar along the upper portion of the pile however the measured bending moments exhibit greater scatter. The strain gauge data was used to calculate the pile moments induced by the lateral loads. The moments calculated using the strain gauge data assumed an uncracked section using the formula $M = E \times \varepsilon \times I / y$ where M = pile moment, E = modulus of elasticity of pile, ε = strain from strain gauge, I = moment of inertia of pile, y = distance from neutral axis to strain gauge. Diaz reported that most of strain gauge data resulted in wide scatter, and in some cases unrealistic data, due possibly to moisture infiltrating the field splices.

A comparison of the computed bending moments is made in Figure 6-11. The results show that the prediction of maximum bending moment using LPILE is approximately 18% higher than that using FLAC. In FLAC analysis, the effect of adjacent piles near test pile is taken into account as shown in Figure 6-8 whereas the single pile is used in LPILE analysis. The efficiency of a pile group for a given spacing reduces with the increasing in number of piles in the group due to the increased number of overlapping zones of passive and active wedges. The bending moment increases with increase in pile spacing. This phenomenon is also observed in the laboratory test (Gandhi, 1997). Therefore, the prediction of bending moments along the pile in LPILE analysis tends to be higher than that in FLAC analysis.

However, the depths of maximum bending moment from both FLAC and LPILE analysis were very close. Due to wide scatter of strain gauge data, the measured bending moments along the pile shaft become inconclusive.

The comparison of the results of previous three static lateral load tests, i.e., two static lateral load tests in level ground and one test in sloping ground, to FLAC model demonstrates a good agreement and indicates that the FLAC model can be used to predict the behavior of the soil-pile interaction in static lateral load conditions within a reasonable range. In dynamic analysis, especially when earthquake-induced liquefaction and excess lateral soil movement are involved, the soil-pile interaction becomes more complex. In order to calibrate the numerical model for the influence of liquefaction and excess lateral soil movement, the model is applied to a physical model case. The detailed description and discussion will be conducted in the following section.

6.2.3 Dynamic Loading of Single Pile in Liquefiable Soils

The centrifuge model (Abdoun et al., 1997) was to simulate a reinforced concrete pile that was deformed by lateral spread under NFCH building during the 1964 Niigata Earthquake. The model setup is shown in Figure 6-12. The inside dimensions of the laminar box were 45.72 cm (length) by 25.4 cm (width) by 26.39 cm (height). The model pile was made of 0.95 cm in diameter polytherimide rod. Under 50g centrifugal acceleration, this model simulates a prototype pile of diameter d = 47.5 cm (18.7 in) and flexural stiffness EI = 8000 kN-m^2. The model pile was assumed to be uncracked section of pile and remains elastic during the test. The strain

gauges were waterproofed by microcrystalline wax and a soft plastic shrink tube. Sand grains were glued to the shrink tube surface in order to develop an adequate pile-soil roughness. The soil profile consisted of two layers of cemented sand, interposed with a Nevada sand layer. Nevada sand was placed at a relative density of 40% and was assumed to be potentially liquefiable soil. The soil profile was fully saturated with water and the laminar box was inclined 2° to the horizontal direction. Both model scale and prototype scale of the model are given in Figure 6-12. Input acceleration time history was a sinusoidal motion with amplitude of 1.96 m/sec^2 (0.2g), frequency of 2 Hertz, and duration of 23 seconds. The input sinusoidal motion was applied at the base of the model.

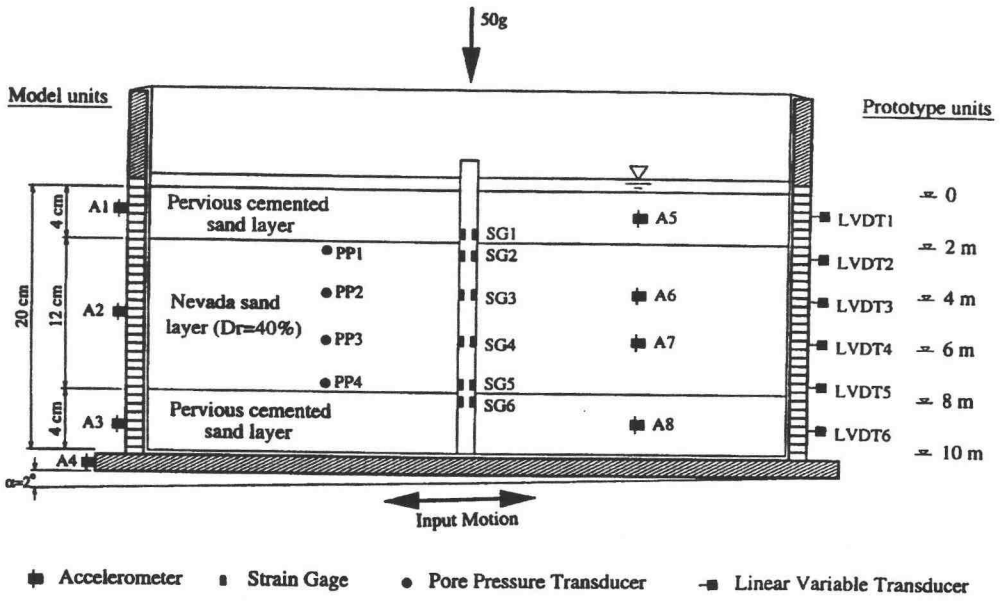

Figure 6-12: Centrifuge test model setup (Abdoun et al., 1997)

6.2.3.1 FLAC Model Setup

The model was analyzed using a mesh of 30×10 zones. The model was to simulate prototype scale under 1g condition. The properties of soil and pile used in the analysis are tabulated in Table 6-7(a) and Table 6-7(b), respectively. The properties of pile to represent the response of pile/soil interaction are listed in Table 6-8. The bottom sand layer with high SPT $(N_1)_{60}$ = 30 blows/0.3m was assumed to be non-liquefiable soil, whereas the top sand layer with moderate SPT $(N_1)_{60}$ = 15 blows/0.3m had a liquefaction potential. The Nevada sand layer with low SPT $(N_1)_{60}$ = 10 blows/0.3m was assumed to be liquefiable soil.

The procedures of modeling were similar as those in previous static lateral load tests except that pore pressure generation and lateral soil spreading due to excitation motion were included. Before conducting dynamic analysis, a static analysis of soil and pile under gravity loading was first completed.

Table 6-7 (a): Properties of Soils Used in FLAC Analysis for Centrifuge Test Model

Description	ρ_d *(N/m³)*	c *(N/m²)*	ϕ *(deg)*	ν	k *(m/sec)*	G_m *(N/m²)*	K_m *(N/m²)*	*SPT*
① Top Cemented Sand	1800	6.4×10^5	35	0.35	9.8×10^{-4}	7×10^7	2.1×10^8	15
② Nevada Sand Liquefiable Layer	1700	0	34	0.20	6.6×10^{-5}	5×10^7	6.7×10^7	10
③ Bottom Non-Liquefiable Cemented Sand	1800	6.4×10^5	40	0.35	9.8×10^{-4}	4×10^8	1.2×10^9	30

Note: ρ_d=Dry density; c=Cohesion; ϕ=Friction angle; ν=Poisson's ratio; k=Permeability; G_m=Mean shear modulus; K_m=Mean bulk modulus; SPT=$(N_1)_{60}$ blows/0.3m.

Table 6-7 (b): Properties of Pile Used in FLAC Analysis for Centrifuge Test Model

Description	*d (m)*	*L (m)*	*A (m^2)*	*Perimeter (m)*	*E_p (N/m^2)*	*I_p (m^4)*
Concrete Pile	0.475	11	0.177	1.49	3.2×10^9	2.5×10^{-3}

Note: d=Pile width; L=Length; A=Area; E_p=Modulus of elasticity; I_p=Moment of inertia

Table 6-8: Properties of Pile/Soil Interaction for Pile in Dynamic Loading

Description	*Layer ①*	*Layer ②*	*Layer ③*
Shear coupling spring stiffness (*Pa/m*)	2.2×10^8	2.0×10^7	2.2×10^8
Shear coupling spring cohesion (*Pa/m*)	2.0×10^6	2.0×10^5	2.0×10^6
Shear coupling spring friction (*degree*)	35	30	35
Normal coupling spring stiffness (*Pa/m*)	2.2×10^8	2.0×10^7	2.2×10^8
Normal coupling spring cohesion (*Pa/m*)	2.0×10^6	2.0×10^5	2.0×10^6
Normal coupling spring friction (*degree*)	65	30	65

6.2.3.2 Results of Dynamic Loading Model

Figure 6-13 shows a comparison of predicted pile displacement at various depths in FLAC model to the measured deformations from the centrifuge test. Overall, the predictions along the pile shaft are excellent with the exception of slightly underestimated pile displacement near ground surface (variation ~ 5%). The pile displacements were only measured at three locations, i.e., at the depth of 0 m, -6 m, and –10m, in the centrifuge test. The pile displacements in the range of two adjacent measured points are unknown and are inconclusive. However, the behavior of the pile displacement can be somewhat estimated from adjacent soil movement since the pile and adjacent soils usually move together as subjected to lateral movements.

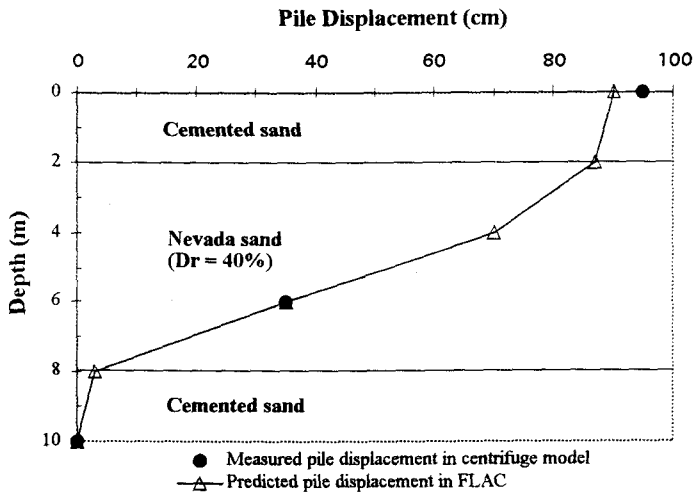

Figure 6-13: Comparison of predicted pile displacements at various depths in FLAC to measured in centrifuge test

The predicted lateral soil movements and measured values along with pile displacements at various depths during shaking are shown in Figure 6-14. The pattern of soil movement profile has mainly resulted from the liquefaction-induced lateral soil movement in the middle layer of liquefied sand, causing a uniform soil movement in the top of sand layer. The soil profile in the middle layer tends to be nonlinear varying with depth, whereas it is linear variation predicted in centrifuge test. The maximum lateral soil movement after shaking was predicted 90 cm at ground surface in FLAC model. This value is slightly higher (~12%) than that measured in the centrifuge test due to the occurrence of partial liquefaction ($(N_1)_{60}$~15) near the soil-pile interface where soils fail around the pile in the top sand layer. The pore pressure ratios near the pile as well as in the middle soil layer are shown in Figure 6-15. From this figure, pore pressure ratios reached unity at the lower interface of liquefiable layer indicating that pile deflection was significantly affected by excess lateral soil flow due to soil

liquefaction, whereas the pile in the bottom soil layer, where the soil is not liquefied, basically remains unchanged.

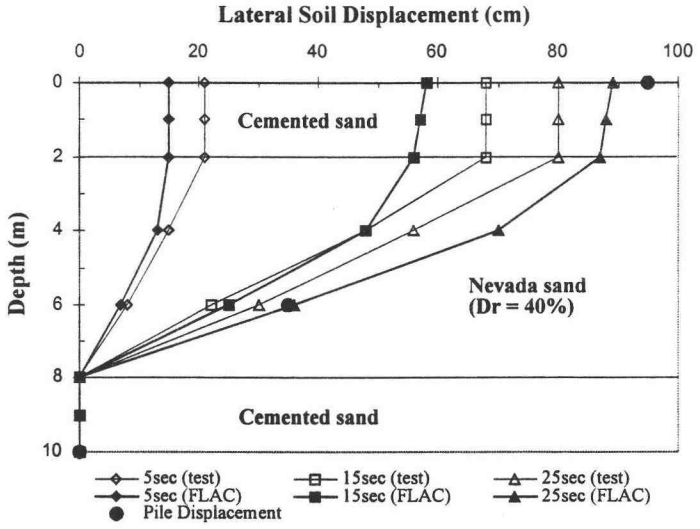

Figure 6-14: Comparison of predicted lateral soil movements in FLAC to measured in centrifuge test along with pile displacements during shaking

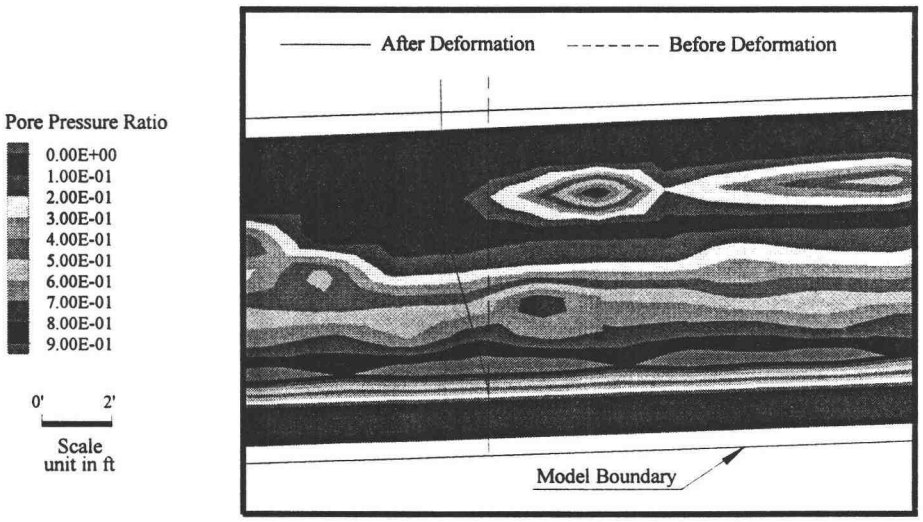

Figure 6-15: Contour of pore pressure ratio after shaking in FLAC model

Figure 6-16 shows the comparison of predicted bending moments in FLAC model to measured values in the centrifuge test. From Figure 6-15, the failure slip plane is observed at the lower interface of liquefiable layer resulting in excess bending moment on pile as shown in Figure 6-16. The predicted maximum bending moment at the lower interface of liquefiable layer matches very well with measured value. At the upper interface of liquefiable layer, the predicted maximum bending moment is higher than that of measured value due to partial soil liquefaction around the pile in the top soil layer as shown in Figure 6-15, therefore providing more bending moment on pile in FLAC model, whereas in the centrifuge test the top soil layer is specified as non-liquefiable. This additional lateral force also causes deeper location of maximum bending moment due to soil liquefaction resulting from not only the top soil layer but also the middle soil layer.

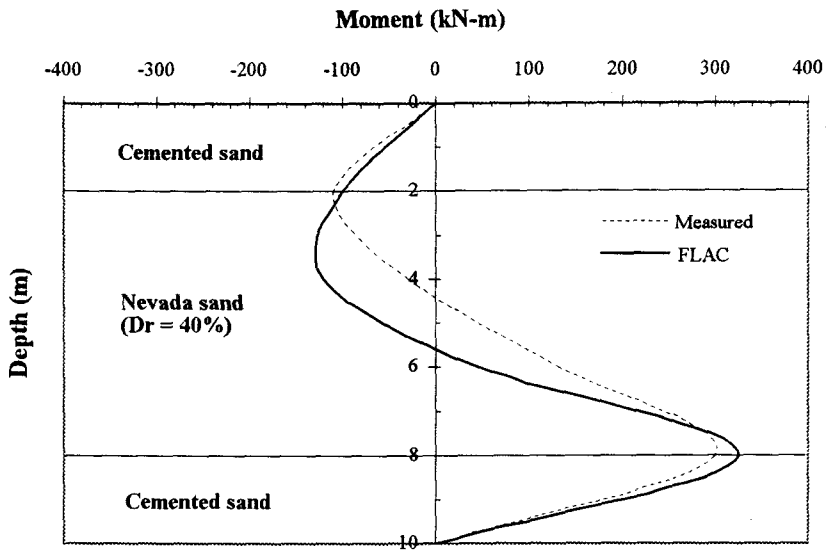

Figure 6-16: Comparison of predicted bending moments in FLAC to measured in centrifuge test

The predicted soil and pile displacements in FLAC model together with measured pile displacement in centrifuge test are shown in Figure 6-17. It can be seen that the pile moves the same magnitude as that of soil indicating that the pile displacement is primarily caused by lateral soil spreading due to soil liquefaction in the middle soil layer. The pattern and mode of soil as well pile displacements were also observed after 1964 Niigata Earthquake. Overall, the prediction of pile displacement agrees favorably well with test result.

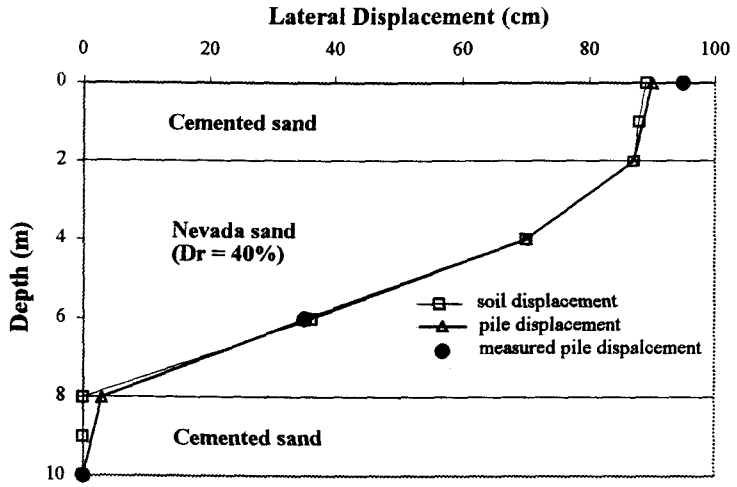

Figure 6-17: Predicted soil displacements and pile displacements in FLAC together with pile displacements measured in centrifuge test

It is noted that this centrifuge test is to simulate the pile response to soil liquefaction during 1964 Niigata Earthquake. Hence, it is interesting to compare current model results to those observed after Niigata Earthquake. Figure 6-18 presents the comparison of predicted pile displacements to measured values after 1964 Niigata Earthquake (Yoshida and Hamada, 1991). Dashed line in Figure 6-18 represents the

soil profile at NFCH building site during the 1964 Niigata Earthquake. The similar pattern of both pile displacements can be observed. As aforementioned in this section, partial liquefaction is observed in the top soil layer of FLAC model, whereas non-liquefiable soil layer is assumed for that same layer in the Niigata model, therefore, FLAC model prediction yields slightly higher pile displacement. Although the soil and motion characteristics in the current FLAC model (in a manner of approximate representation) are slightly different from NFCH building site, the prediction of deformed magnitude and pattern of pile is quite comparable to that measured after shaking in the 1964 Niigata Earthquake.

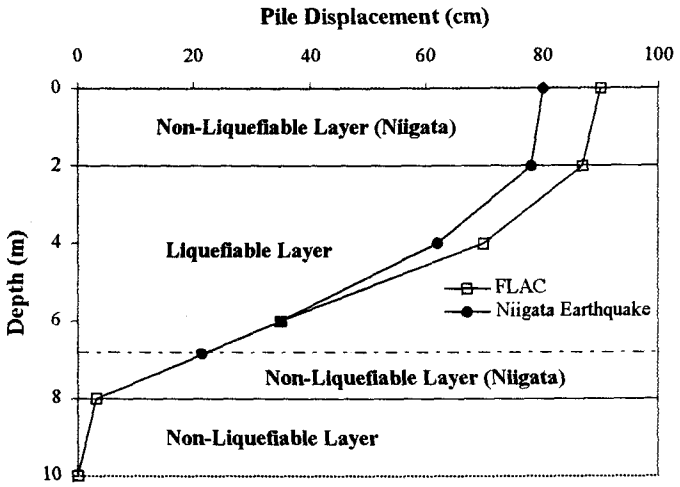

Figure 6-18: Comparison of predicted pile displacement in FLAC to measured after 1964 Niigata earthquake

The analytical results of pile behavior, either in static lateral load test models or in dynamic centrifuge test model, are very consistent with the measurements provided by various modeling conditions. A field case study, located at Seventh Street

Marine Terminal at the Port of Oakland, California, during 1989 Loma Prieta Earthquake was then selected in order to investigate the uncertainties and analytical accuracy involved in modeling considerations for pile-supported wharf to known performance under seismic loading.

6.2.4 Dynamic Loading of a Pile-Supported Wharf – Field Case Study

During 1989 Loma Prieta Earthquake (M_w 6.9), the Seventh Street Marine Terminal at Port of Oakland, California, suffered damage due primarily to earthquake-induced liquefaction and excess settlement in the sand fill as well native silty sand beneath and behind the perimeter rockfill dike. The location of the Seventh Street Terminal and active faults in the San Francisco Bay Area is shown in Figure 6-19. Initial estimates set the Port of Oakland earthquake damage repair at $75 million. Damage occurred primarily at the Seventh Street Complex and the Middle Harbor; the Inner Harbor and Outer Harbor were relatively undamaged (Benuska, 1990).

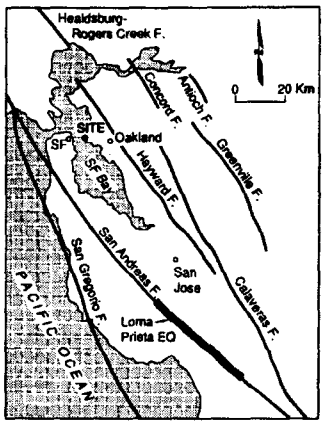

Figure 6-19: Location of Seventh Street Terminal and active faults in the San Francisco Bay Area (Egan et al., 1992)

6.2.4.1 Site Description

The Port of Oakland occupies 19 miles of shoreline on the eastern side of San Francisco Bay and is surrounded by several major faults as shown in Figure 6-19. The Seventh Street Terminal has a number of pile-supported wharves. The typical of cross section through the wharf, rock dike, and backfill fill at the Seventh Street Terminal is shown in Figure 6-20. The wharf deck is supported on 16 in square prestressed concrete piles. Piles on the backland are battered at an inclination of 1 to 3 (H:V) and all other piles that support wharf deck are vertical. The piles spacing in the transverse direction are ranging from 11.33 ft to 14.5 ft, and are ranging 16 ft to 18 ft in the longitudinal direction.

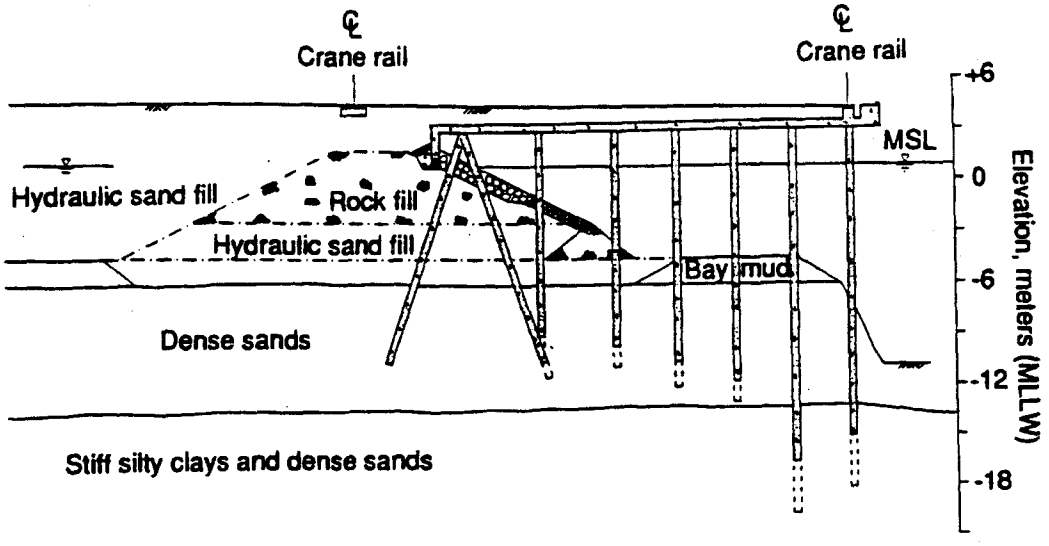

Figure 6-20: Typical cross section of the Seventh Street Terminal wharf (Egan et al., 1992)

The wharves are supported by piles that extend through perimeter dikes constructed by hydraulically placing sand and rock fill into the waters of the bay. The areas behind these rock dikes and wharves have been developed by hydraulic sand fill. The hydraulic sand dike fills are loose to medium dense, having $(N_1)_{60}$ values in the range between 9 and 20 blows/ft, with an average value of 14 blows/ft. The soil layer beneath the rock dike fill is native sand stratum of 37 ft to 50 ft thick, consisting of medium dense to dense silty or clayey sands. The upper native sands are medium dense with $(N_1)_{60}$ values ranging from 13 to 18 blows/ft. The deeper native sands are dense to very dense with $(N_1)_{60}$ values exceeding 30 blows/ft. The native sand layer is underlain by stiff silty clays and dense sands (Old Bay Mud) up to the depth of –120 ft. It is expected that these hydraulically placed sand fills either beneath or behind the rock dike are potentially liquefiable soils due to their lower penetration resistance, rock dike are potentially liquefiable soils due to their lower penetration resistance, averaging $(N_1)_{60} \sim 11$ blows/ft in the back fill layer and $(N_1)_{60} \sim 14$ blows/ft in the base of rock dike fill.

The horizontal and vertical peak ground acceleration recorded at the Terminal 25, located approximately 2 km northeast of the Seventh Street Terminal, is 0.29g and 0.07g, respectively. Due to the similarity of soil conditions for at Terminal 25 and Seventh Street Terminal, it is anticipated that ground motion levels experienced at the Seventh Street Terminal are close to those recorded at the Terminal 25, i.e. A_{max} = 0.29g.

6.2.4.2 Earthquake Damage

Damage to port facilities was variable depending on the location during the 1989 Loma Prieta Earthquake. The most severe damage was observed at the Seventh Street Terminal. Liquefaction of the sand fill was widespread in the hydraulically placed sand fill as evidenced by the formation of sand boils through cracks in the asphalt pavement of the backland. The differential settlement in the backland relative to pile-supported wharf was estimated up to maximum of about 1 ft. Due to this differential settlement, the large bridge cranes at the terminal became inoperational. In addition to settlement, bayward lateral spreading of the perimeter dikes and backfill has been observed in the formation of horizontal crack openings in the asphalt behind the wharf. The degrees of lateral spreading were variable, ranging from 4 inches to maximum of 14 inches around the perimeter of rock dike. Figure 6-21 shows that settlement and lateral spreading of the fill supporting inboard bridge crane rail.

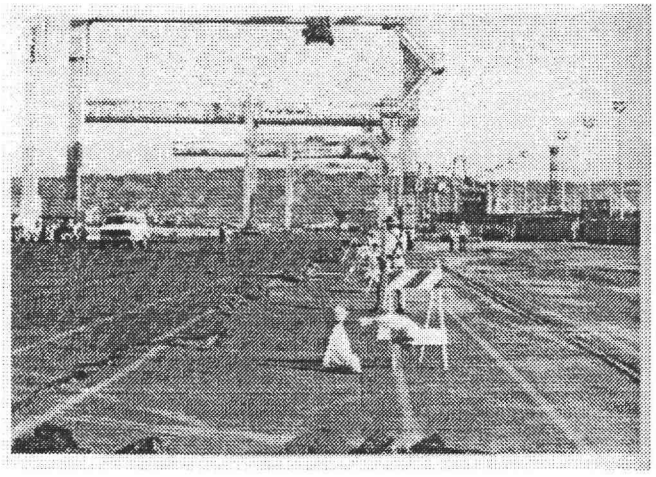

Figure 6-21: Settlement of fill supporting inboard bridge crane rail (photograph by Marshall Lew)

The vertical piles were generally survived as a result of their flexible characteristics, whereas the batter piles were damaged by tensile failures at or near the tops of most of the rearmost line at the inboard wharf edge. Figure 6-22 shows that the shear failure of batter piles supporting wharf at the Seventh Street Terminal. It is interesting to note that the Howard Terminal, which is similar to the Seventh Street Terminal except that the dike is made entirely of rock and no batter piles are used to support the wharf, suffered only minor damage and no apparent lateral movements or pile breakage, indicating that batter piles are generally not behaved satisfactory during earthquake shaking. As a result of widespread damage to the batter piles, the port replaces the batter pile system with a system of vertical piles designed to resist lateral loads. The Seventh Street Terminal was fully inoperational about six months and had limited crane capability for twenty-two months after the earthquake while repair work proceeded.

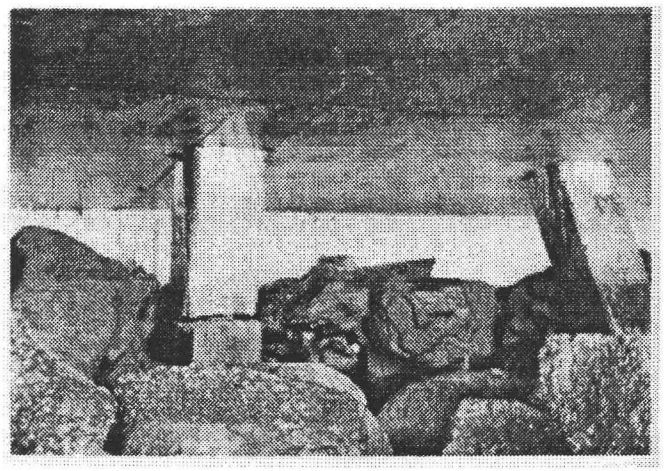

Figure 6-22: Failure of batter piles at the Seventh Street Terminal (photograph by Geomatrix Consultants)

6.2.4.3 FLAC Model Setup

The results of previous static case studies of pile behavior are consistent with laboratory and field performance. The soil/pile interaction under seismic loading is complicated due to appropriate representing soil strength and pile ultimate resistance characteristics, generation of excess pore pressures, and ground motion intensity. This case study provides an opportunity to investigate the performance of existing pile-supported wharf to earthquake damage, to calibrate the modeling uncertainties for the soil/pile interaction with known performance.

The model is analyzed using a mesh of 40×14 zones. The model setup is presented in Figure 6-23. The soil properties are obtained directly from investigation of laboratory and field data. The soil properties are tabulated in Table 6-9.

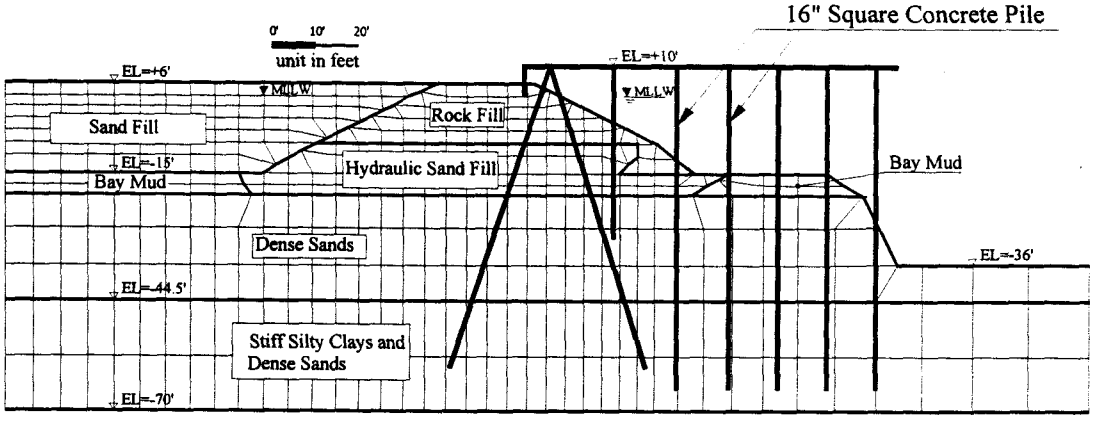

Figure 6-23: FLAC model setup for the case study of the Seventh Street Terminal

Table 6-9: Properties of Soils for the Case Study of the Seventh Street Terminal

Soil Type	ρ_d *(slug/ft³)*	c *(lb/ft²)*	ϕ *(deg.)*	ν	k *(ft/sec)*	G_m *(lb/ft²)*	K_m *(lb/ft²)*
Sand Fill	3.05	0	30	0.35	1×10^{-4}	3.1×10^{5}	9.4×10^{5}
Rock Fill	3.57	0	45	0.20	1×10^{-1}	1.8×10^{6}	2.5×10^{6}
Bay Mud	2.30	See Note 2	0	0.35	1×10^{-7}	3.7×10^{5}	1.1×10^{6}
Dense Sand	3.50	0	42	0.35	1×10^{-4}	1.9×10^{6}	5.6×10^{6}
Stiff Silty Clays and Dense Sands	2.83	1440	37	0.35	1×10^{-5}	1.4×10^{6}	4.5×10^{6}

Note:

1. ρ_d=Dry density; c=Cohesion; ϕ=Friction angle; ν=Poisson's ratio; k=Permeability; G_m=Mean shear modulus; K_m=Mean bulk modulus
2. Bay Mud : $S_u / p' = 0.38$

The piles supporting the wharf were modeled with pile elements representing 16 in. square prestressed concrete pile. The moment capacity of the piles was also simulated in the model. The condition of increasing deformation with a limiting resisting moment that results in a discontinuity in the rotational motion is called a plastic hinge. The portion of the pile in which the plastic moment occurs can continue to deform without providing additional moment resistance after it reaches plastic moment. Once the maximum bending moment capacity of piles is reached, the plastic hinge at pile nodes is formed. It is assumes that pile elements behave elastically until they reach the plastic moment. In order to limit the moment that is transmitted between pile elements, the moment capacity at the nodes is specified as 400 kips-ft in the model.

As described in Chapter 3, the FLAC program employs an explicit finite difference method for modeling nonlinear static and dynamic problems in plane strain condition in a way of approximating the three-dimensional nature of the problem to

two-dimension. Reducing three-dimensional problems involving regularly spaced piles in the out-of-plane direction to two-dimensional problems involves averaging the effect in three-dimension over the distance between the elements. The element spacing, *S*, can be used to scale the structural element properties, i.e., pile stiffness, pile perimeter, pile plastic moment, and shear and normal strength of the spring elements. The pile properties are tabulated in Table 6-10.

As noted in Section 6-2-2, earthquake shaking is usually applied on piles in both seaward and landward directions. In order to account for the effects of sloping ground surface along the seaward side of the rock dike, in which the soil passive resistance on piles was reduced, the reduction factor of 0.8 was applied to the normal coupling spring cohesion, whereas a factor of 1.1 was applied to the normal coupling spring tension in the landward direction in which the effect of increased soil passive resistance was taken into account. The properties of pile to represent the response of pile/soil interaction are listed in Table 6-11.

The penetration resistances ($(N_1)_{60}$) for sandy soils behind and beneath the wharf were 11 and 13 blows/ft based on *insitu* investigation, respectively. At the levels of shaking, the sand fill was considered potentially liquefiable and excess pore pressures were monitored during the shaking.

The acceleration time histories recorded at the Oakland Outer Harbor Station No. 58472 of 35 degree and 305 degree were first combined vectorially to produce the acceleration time history acting normal to the wharf. The acceleration used at the base of the FLAC model was then computed from this acceleration time history using the equivalent linear dynamic soil response program SHAKE91 (Idriss and Sun, 1992).

The input acceleration time history at the base of model is shown in Figure 6-24. The Rayleigh damping of 5% and frequency of 5 Hz were used.

Table 6-10: Properties of Pile for the Case Study of the Seventh Street Terminal

Description	*d* (ft)	*A* (ft^2)	*Perimeter* (ft)	E_p (lb/ft^2)	I_p (ft^4)
Concrete Pile	1.33	1.78	5.33	5.8×10^8	0.263

Note: d=Pile width; L=Length; A=Area; E_p=Modulus of elasticity; I_p=Moment of inertia

Table 6-11: Properties of Pile/Soil Interaction in the Field Case Study

Description	*Values*
Shear coupling spring stiffness ($lb/ft^2/ft$)	2.0×10^7
Shear coupling spring cohesion ($lb/ft^2/ft$)	0
Shear coupling spring friction (*degree*)	45
Normal coupling spring stiffness ($lb/ft^2/ft$)	2.0×10^7
Normal coupling spring cohesion ($lb/ft^2/ft$)	2.4×10^5
Normal coupling spring tension ($lb/ft^2/ft$)	3.3×10^5
Normal coupling spring friction (*degree*)	80

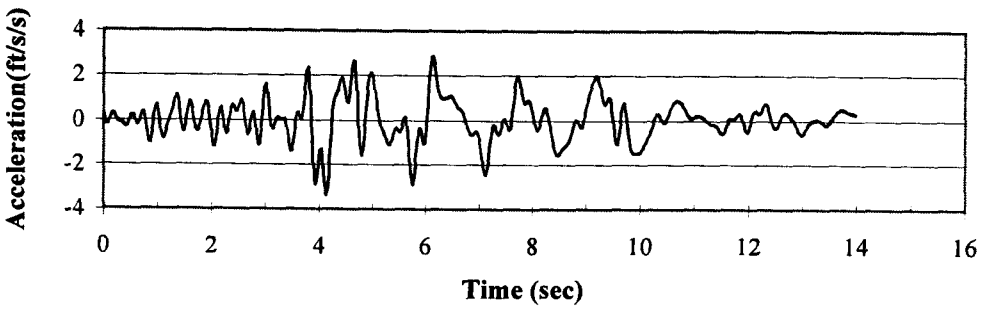

Figure 6-24: Acceleration time history used at the base of the FLAC model

6.2.4.4 Results of Case Study at the Seventh Street Terminal, Port of Oakland

The predicted seaward lateral displacement and settlement at the top of the rock dike at the Seventh Street Terminal is shown in Figure 6-25. The lateral movement of the rock dike has significantly increased after approximately 4 seconds and has reached the permanent displacement of 9 in. at 10 seconds. It has then remained permanent throughout the 4 seconds of ground shaking. The similar pattern of the rock dike settlement was observed as well. The maximum settlement at the top of the rock dike was computed to be 5.8 in.. The measured seaward lateral movement starting from the middle portion in the inland to the edge of deck was made by summarizing the horizontal ground openings parallel to the deck alignment. It is assumed that ground cracks were caused by the movement of the rock dike at both sides of the wharf. The measured lateral movements were estimated in the range of 4 in. to as high as 15 in. with the averaged value of 12 in.. The measured settlement was made by measuring the vertical offset at various crack locations near the edge of the deck. The vertical offsets around the perimeter of the deck are ranging 4 in. to 7 in.. The predicted lateral displacement (9 in.) and settlement (5.8 in.) of the rock dike are consistent with the measured values observed for the perimeter dike following the Loma Prieta Earthquake. It is noted that the measured seaward lateral movements are quite scattered, ranging from 4 in. to 15 in. The seismic behavior of pile-supported wharf system is quite different from the gravity type caisson retaining structures in which uniform seaward lateral movement was observed, as an example of the Port of Kobe during 1995 Kobe Earthquake as described in Chapter 4. This implies that more

factors are involved in the seismic performance of pile-supported systems not only in the nonlinear pile-soil interaction but also construction of landfill process.

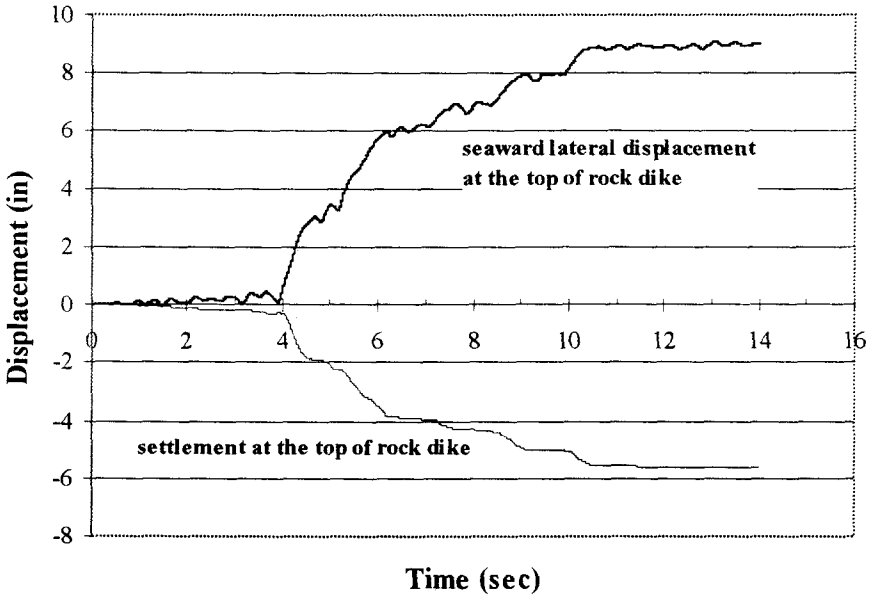

Figure 6-25: Predicted time history of seaward lateral displacement and settlement at the top of rock dike

Figure 6-26 shows the acceleration time history predicted at the top of the sand fill along with input motion at the base of the model. The horizontal peak acceleration was estimated to be 0.27g. This value is consistent with the recorded horizontal peak acceleration of 0.29g at the Port's Berth 25 Wharf, located approximately 2 km northeast of the Seventh Street Terminal. It is believed that the same order of magnitude for the horizontal peak ground acceleration would be anticipated at the Seventh Street Terminal due to similar subsurface conditions. It is obvious that shaking level simulated in the model is within reasonable ranges.

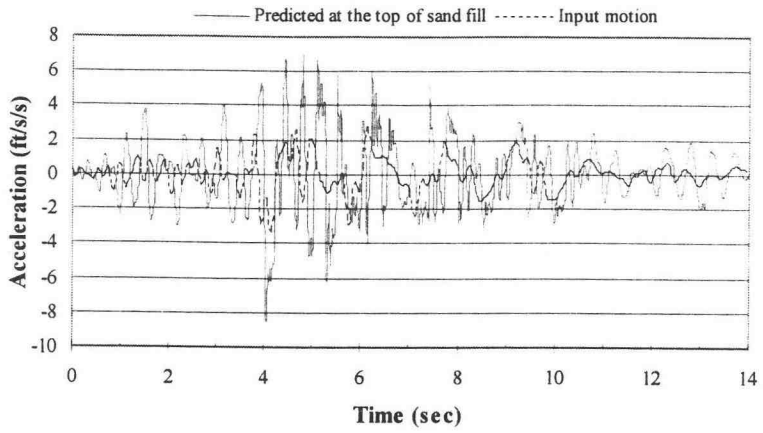

Figure 6-26: Acceleration time history predicted at the top of sand fill

A number of liquefaction-induced sand boils and depressions at the surface were observed at the Seventh Street Terminal after the Loma Prieta Earthquake. To examine the degree of liquefaction in the sand fill beneath and behind the rock dike, accumulated pore pressure ratios were computed and monitored during shaking. Figure 6-27 shows the contour of pore pressure ratio (r_u) in the sand fill beneath and behind the rock dike.

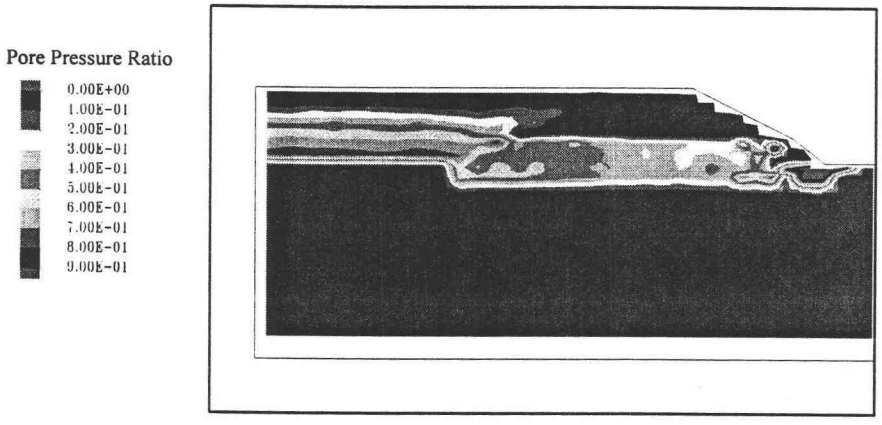

Figure 6-27: Contour of pore pressure ratio after shaking

Full liquefaction ($r_u = 1$) at the front end of sand fill beneath the rock dike was predicted whereas partial liquefaction ($r_u \leq 0.8$) was predicted in the backfill area. The causes of lateral movement and settlement of the rock dike can be reasonably assumed as a result of the failure of sand fill beneath the rock dike and excessive lateral spreading of the backfill, due to earthquake-induced liquefaction.

The deformed soil meshes and pile elements before and after shaking are shown in Figure 6-28. It should be noted that both soil and pile deformations were magnified 3 times for more clearly demonstration purpose. It can be seen from Figure 6-28 that larger residual soil displacements were found at the toe of rock dike due to loss of passive resistance and excessive lateral pressures resulted from liquefaction around that area as well as from the backfill, thus primarily affecting post-earthquake stability of the rock dike.

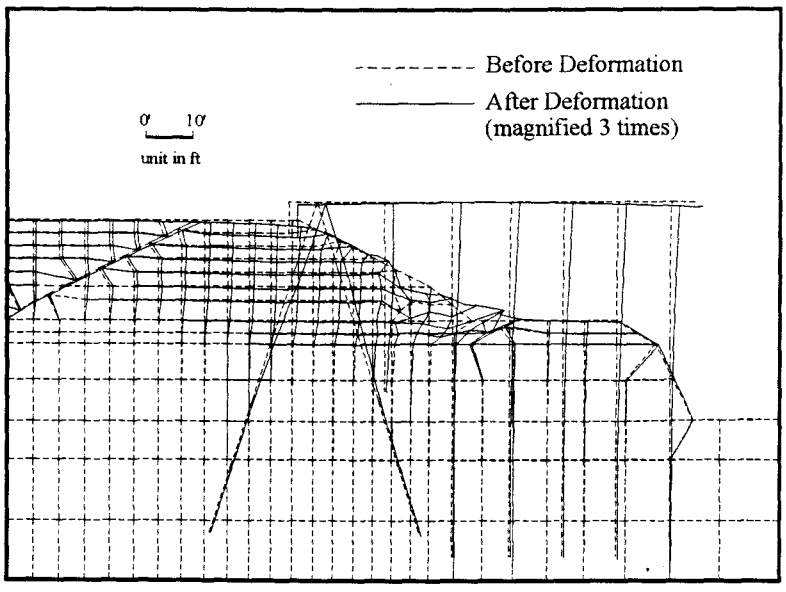

Figure 6-28: Deformed model mesh (both soil and pile displacements were magnified by 3 times)

Figure 6-29 shows pile deformation before and after shaking. It is noted that the pile deformation has been magnified by 12 times of its actual deformation. The predicted seaward displacement of the pile was approximately 7.2 in. The seaward pile movement was basically consistent with rock dike movement. The plastic hinges along two batter piles were found near the interface of upper rock dike and sand fill beneath it due to seaward soil spreading in the sand fill caused by liquefaction exceeding the plastic moment of the batter piles. The rest of vertical piles have remained elastic behavior throughout the analysis. The predicted behavior of the piles is consistent with the observed behavior as addressed in previous section. The analytical results show that the magnitude of predicted seaward pile deformation is within the observed values in terms of the summation of ground horizontal movements.

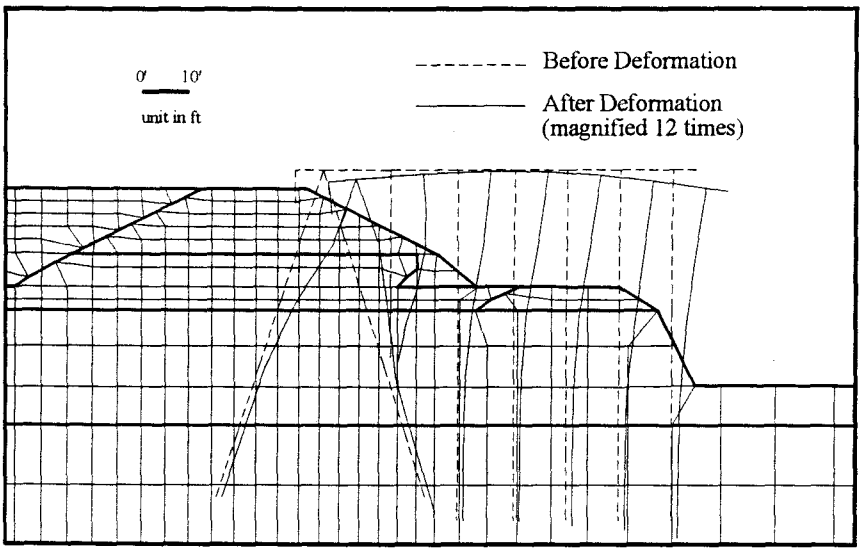

Figure 6-29: Pile deformation before and after shaking (pile deformations were magnified by 12 times)

The predicted lateral movement of rock dike of 9 in. is underestimated the averaged measured value of 12 in. by 25%, but within the ranges of measured values around the perimeter of the Seventh Street Terminal, i.e., 4 in. to 15 in.. The seaward maximum pile deformation of 7.2 in. is predicted to be 20% less than that of rock dike movement. This rather scatter failure degree of rock dike and pile deformation reflects the complicate characteristics of pile-soil interaction subjected to liquefaction-induced lateral soil movement as compared to those rather uniform failure mode observed from historic gravity type caissons.

7 PARAMETRIC STUDY OF PILE-SUPPORTED WHARVES IN SLOPING ROCKFILL

7.1 Introduction

As outlined in Chapter 6, the numerical model for soil-pile interaction has been calibrated for lateral load tests and a field case study of the seismic performance of a pile-supported wharf. The results of prediction under various conditions, i.e., static tests in laboratory and in field scale, sloping ground surface, dynamic loading, and known performance of case study, provide representative results. A comparison of the numerical modeling results with the physical model study and field case histories indicates that the numerical uncertainties in the modeling is on the order of ±25%. The case studies have been particularly useful for investigating the causes of earthquake damage to existing pile-supported wharves, for calibrating the numerical model, and to begin formulating methods for mitigating earthquake damage to these structures.

The earthquake-induced liquefaction of hydraulically placed sand fill is a major cause of damage to pile-supported systems. The lateral movement of liquefied soils applies excessive lateral forces and moments on pile foundations resulting in buckling or yielding failure of piles. The use of apparent reduction factors in the p-y curve analysis, or treating lateral soil movement as a part of the soil-pile interaction analysis by either reducing the stiffness of the liquefied soil or using undrained residual shear strength of liquefiable soil, is the common analytical method for piles in liquefiable soils. From two series of full-scale pile load tests Lam et al. (1995)

concluded that the potential dynamic gapping and cyclic degradation effects tended to result in a significant reduction in the soil stiffness, as much as 80 to 90 percent in soil resistance. From centrifuge mode tests, a degradation coefficient of 0.1 for soil lateral resistance in fully liquefied soil was reported by Liu and Dobry (1995). Subsequent centrifuge tests revealed that the presence of the pile did not significantly affect the free field response and lateral spreading of the liquefied soils (Abdoun et al., 1997), indicating that the soils around the pile were essentially free to flow and the soils were not taking advantage of stiffness of pile.

Soil-pile interaction in the liquefiable soils is a complex phenomenon and has been greatly simplified in dynamic analysis and design. As addressed in Chapter 3, the coupling spring approach used in FLAC model is similar as those used in the conventional p-y curves method except that the simplified bilinear elasto-plastic force-displacement relationship, in which the generation of excess pore pressure resulted from earthquake loading can be accounted for, is adopted. In spite of this simplicity, this approach for modeling pile-supported wharf in liqufiable soils has been found to yield reasonable displacements as compared to known performance of field case study at the Seventh Street Terminal as described in Chapter 6.

If the bending moments and deformations induced in the piles can be estimated accurately, then more cost effective design and construction procedures may be implemented. In view of this, it is necessary to evaluate how the pile-supported systems respond to earthquake loading in unimproved and in improved soils; what the effectiveness of improved area is required to ensure that the port is operational under design level earthquake. Since the analytical model has been used

in the Seventh Street Terminal case study, a series of parametric studies pertaining to pile-supported systems in improved soil were conducted. Detailed discussions of various factors affecting the seismic performance of a pile-supported wharf, regarding the effects of (1) earthquake-induced liquefaction; (2) ground motion intensity; (3) pile stiffness, and (4) the pile reinforcement, will be first evaluated for a pile-supported wharf in liquefiable soils. By collecting the information presented herein, the needed extents and soil improvement scenarios thus mitigating earthquake damage to pile-supported wharves to a minimal degree were conducted. Empirical design charts considering ground shaking intensity, pile stiffness, soil density, and various extents of improved area were then determined.

7.2 Analytical Model Setup of Pile-Supported Wharves

The analysis was performed using two-dimensional finite difference code FLAC (version 3.4). The detailed descriptions of this code have been addressed in Chapter 3. The specific modeling considerations for parametric study of pile-supported wharves in sloping rockfill subjected to the effect of earthquake-induced liquefaction will be presented in the following sections.

7.2.1 Soil Model Setup

The Mohr-Coulomb elastic-plastic constitutive soil model coupling with empirical-based pore pressure generation scheme was used to model soil behavior. The pore pressure generation and liquefaction resistance of cohesionless soil was

modeled using an incremental form of the simplified, stress-based procedures developed by Seed and his co-workers (Seed and De Alba, 1986). The liquefaction resistance of the soil was adjusted to account for initial static shear stresses and overburden stresses as described by Seed and Harder (1990). Effective stresses were continually updated as pore pressures increased in loose-to-medium dense sandy soils. The effective stresses and corresponding soil strength were monitored until the state of initial liquefaction was reached. At this point the strength of the soil was modeled using undrained residual strengths (Stark and Mesri, 1992). In addition, the post-liquefaction volume change of the sand deposits was estimated using the established relationship between the factor of safety against liquefaction and volumetric strain (Ishihara and Yoshimini, 1991).

After reviewing wharf configurations in the western coast of United States, the wharf configuration of Port of Long Beach, California, was chosen for the parametric study due to more and more applicability of multi-lift rock dike at many ports. The configuration of the generalized pile-supported wharf and the surrounding soil is shown in Figure 7-1. The Mean Lower Low Water (MLLW) was assumed to be located at elevation of 0 ft and a water depth of 50 ft was used. The slope of rock dike was specified as a 1:1.5 (vertical:horizontal). The undrained shear strength ratio (S_u/σ'_v) of 0.4 was used in the clay layer. The hydraulically placed sand fill with SPT-N values ($(N_1)_{60}$) of 10 blows/ft is considered representative of field conditions at many ports where hydraulically placed sand fill has been used during reclamation. The foundation soils, i.e., dense sand and firm sand base, with SPT-N values ($(N_1)_{60}$)

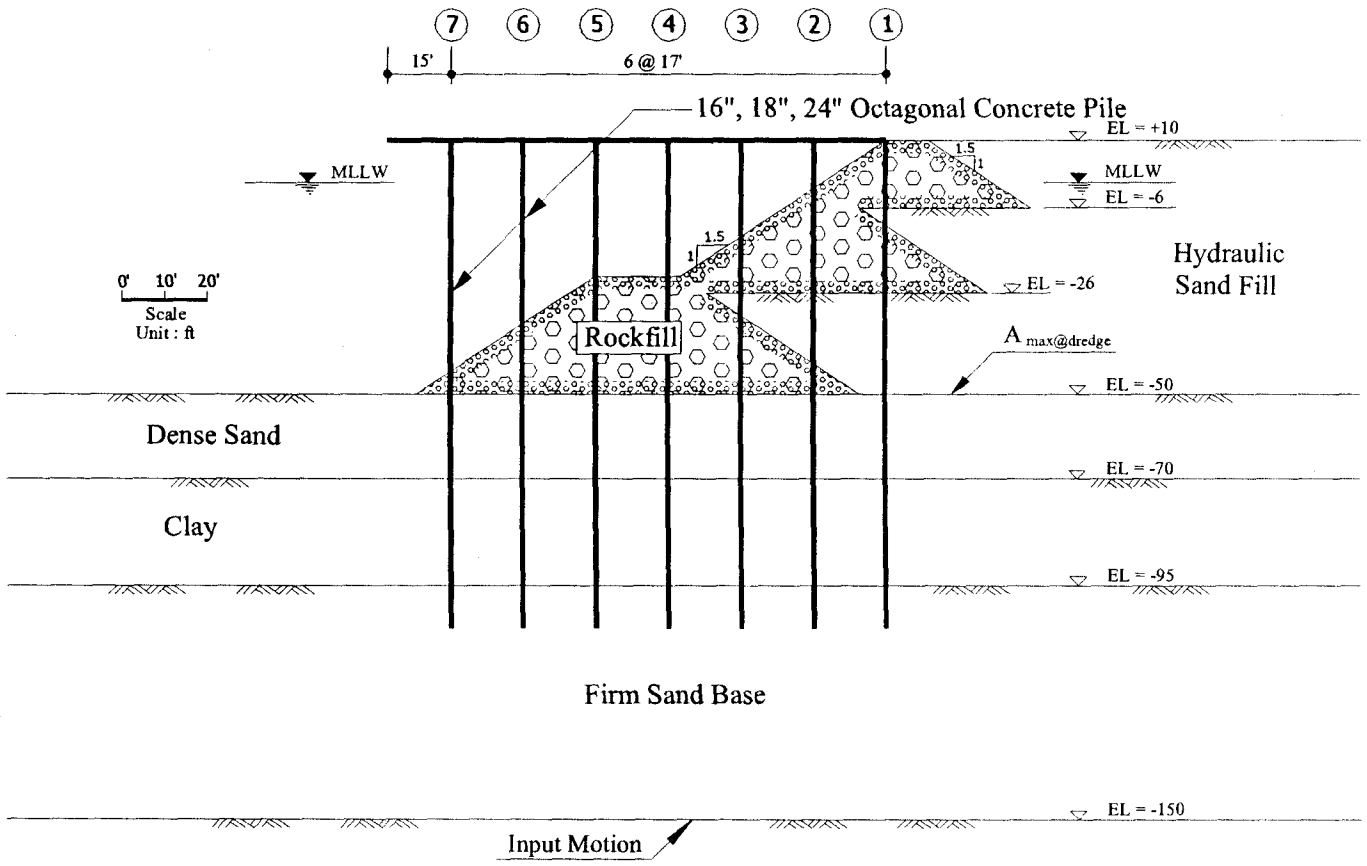

Figure 7-1: Configuration of pile-supported wharf and surrounding soils for parametric study

greater than 30 blows/ft were treated as non-liquefiable soils. The representative soil properties in the model for each layer are listed in Table 7-1.

Table 7-1: Properties of Soils for Parametric Study

Description	*Unit Weight (pcf)*	*Cohesion (psf)*	*Friction Angle (deg.)*	*Poisson Ratio*	K^1	n^1	$(N_1)_{60}$ *(blows/ft)*
Sand Fill	125	0	30	0.35	650	0.7	10
Rock Dike	133	0	45	0.20	3000	0.6	> 30
Dense Sand	128	0	36	0.35	850	0.7	30
Clay	120	See note 2	0	0.35	550	0.7	-
Base Sand	130	0	38	0.35	850	0.7	30
Improved Soil	130	0	39	0.35	900	0.7	30

Note:

1. $G = Kp_a\left(\frac{\sigma'_m}{p_a}\right)^n$ where G = shear modulus, p_a = atmospheric pressure, σ'_m = mean effective stress, K and n = dimensionless material constant.
2. Undrained shear strength ratio: $S_u / \sigma'_v = 0.4$.

7.2.2 Pile Model Setup

Three different diameters of prestressed octagonal concrete piles were used in the analysis, i.e., 16 in., 18 in., and 24 in.. The seven vertical piles denoted as 1 to 7 were spaced 17 ft in the transverse direction and were spaced 16 ft in the longitudinal direction. The embedded length of piles in the firm base sand layer was set as 10 ft and total length of pile was 115 ft. The wharf deck and supporting piles were modeled using pile elements in which soil movement around the pile can be approximated in the model. The pile heads are loaded with lumped masses representing the weight of wharf deck, soils, and the pavement above it. The rigid pile head fixity condition preventing pile head rotation but not deflection was used in the model. The pile nodes

were defined separately from the soil nodes, and the two were connected by nodal joint elements, i.e., two sets of coupling springs (normal coupling spring and shear coupling spring), having shear and normal stiffness and maximum shear and normal force. This allows an approximate representation of the development of lateral resistance with relative movement between the soil and pile, and ultimately the full limiting soil pressure acting on the piles, similar to a p-y curve that is used in other forms of analysis for laterally loaded piles but in a simplified way. The cracked section can be specified in the pile elements. Once the moment capacity in a pile node was exceeded, a plastic hinge will be formed which precluded additional moment resistance. The properties of pile are tabulated in Table 7-2 and Table 7-3.

Table 7-2: Properties of Piles Used in the Parametric Study

Description	*Area* (ft^2)	*Perimeter* (*ft*)	*Length* (*ft*)	*Modulus of Elasticity** (lb/ft^2)	*Moment of Inertia* (ft^4)
24" Pile	3.31	6.6584	115	5.8×10^8	0.876
18" Pile	1.86	5	115	5.8×10^8	0.275
16" Pile	1.472	4.417	115	5.8×10^8	0.1732

Note: * Based on concrete compressive strength of 5000 psi; $E_c = 57000\sqrt{f'_c}\,(psi)$

Table 7-3: Properties of Pile/Soil Interaction in the Parametric Study

Description	*Values*
Shear coupling spring stiffness ($lb/ft^2/ft$)	2.0×10^7
Shear coupling spring cohesion ($lb/ft^2/ft$)	0
Shear coupling spring friction (*degree*)	45
Normal coupling spring stiffness ($lb/ft^2/ft$)	2.0×10^7
Normal coupling spring cohesion ($lb/ft^2/ft$)	2.0×10^5
Normal coupling spring tension ($lb/ft^2/ft$)	2.75×10^5
Normal coupling spring friction (*degree*)	80

In reducing actual 3D problem to 2D plane strain model, the properties representing pile stiffness and ultimate strength of springs were divided by pile spacing in the out-of-plane direction and this would be the most common and the simplest approach used in current practice. In order to account for the effects of sloping ground surface regarding soil resistance on the pile, the limiting resistance of the pile springs was reduced by a factor of 0.8 near seaward sloping side whereas a factor of 1.1 was used on the inland sloping side. The full gap effect is specified allowing the gap to close before the pile will reload the soil under seismic shaking.

7.2.3 Input Motions

Three earthquake motions covering the magnitude range of engineering interest (M_w 6 to 8) were selected in the analysis. They are M_w 6.2 1984 Morgan Hill earthquake (Gilroy #4, A_{max} = 0.22g), M_w 6.9 1989 Loma Prieta earthquake (Capitola, A_{max} = 0.40g), and M_w 7.5 1992 Landers earthquake (Joshua Tree Fire Station, A_{max} = 0.27g), as tabulated in Table 5-1 and Figure 5-3. Each recorded free-field motion was scaled to three different maximum acceleration values in the range of 0.1g to 0.4g. These ground motion levels correspond to CLE and OLE shaking levels at many ports in the western United States. As addressed in Chapter 5, the selected acceleration time histories were conservative in the sense that each one was characterized as having greater than average duration and therefore input energy for that specific magnitude, thereby yielding greater displacements than would be computed using motions of average duration. The Rayleigh damping of 5% and frequency of 5 Hz are used in the analyses.

7.3 Assessment of Seismic Performance of Pile-Supported Wharves in Unimproved Soils

Various factors affecting the seismic performance of pile-supported systems are evaluated in this section including:

- *elastic/plastic behavior of pile* – the elastic and plastic behavior of piles during seismic loading are compared;
- *ground motion intensity* – a range of ground motions with widely varying characteristics with respect to intensity duration and frequency content are evaluated;
- *stiffness of pile* – the effect of various pile stiffness on pile deformation are examined;
- *influence of liquefaction* – the hydraulically placed sand fill behind the pile-supported wharf is evaluated for varying degrees of pore pressure generation;
- *"pile pinning" effect* – the seismic performance of rock dike is evaluated by presence of piles and absence of piles.

7.3.1 Effect of Elastic/Plastic Behavior of Piles

In this section, three scenarios on the performance of pile-supported wharf subjected to CLE and OLE event shaking levels are investigated as follows: **(a)** treating the piles without consideration of spacing effect in the out-of-plane direction (i.e., as continuous walls) with full stiffness; **(b)** treating the piles as continuous walls with reduced stiffness over spacing but without plastic hinge formation (elastic

behavior of piles); **(c)** treating the piles as continuous walls with reduced stiffness over spacing with plastic hinge formation (plastic behavior of piles).

The hydraulically placed sand fill as shown in Figure 7-1 with very low SPT-N values ($(N_1)_{60}$ = 10 blows/ft) was considered to be highly liquefiable soil layer, while the foundation dense sand with $(N_1)_{60} \geq 30$ blows/ft was treated as non-liquefiable soil layer. The models were subjected to various input acceleration levels ranging from 0.1g to 0.4g.

The results of the effect of pile elastic and plastic behavior on pile-supported wharf deformations under various modeling considerations are shown in Figure 7-2 and model information is tabulated in Table 7-4. The normalized ground motion intensity ($A_{max@dredge}$ / MSF), defined as peak horizontal acceleration at dredge line divided by appropriate magnitude scaling factor (Arango, 1996), was used for comparison. The use of magnitude scaling factor is to account for the duration of various earthquake magnitudes used in the analysis. The results of various pile model considerations using simplified, bilinear p-y curves embedded in FLAC indicate that the pile head displacements are essentially proportional to normalized ground motion intensity ($A_{max@dredge}$ / MSF), but rather less significant for the normalized ground motion intensity greater than 0.4g.

Comparison of elastic pile model to plastic pile mode from Figure 7-2 shows that both pile models behave elastically for ground motion intensity of 0.2g and there is no difference between both models. The behavior of these two pile models becomes different for ground motion intensity greater than 0.4g due to the elastic pile model

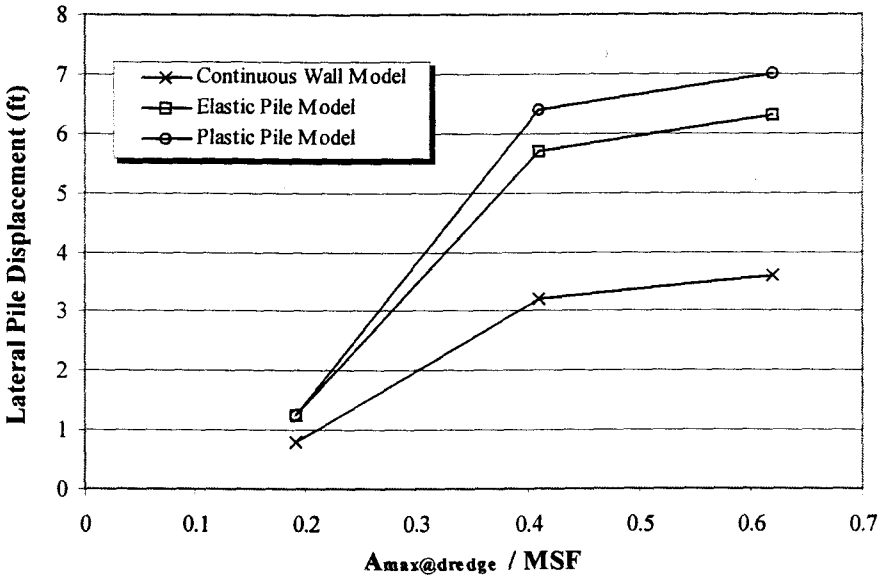

Figure 7-2: Comparison of lateral pile head displacements for various pile models

Table 7-4: Comparison of Various Pile Models on Pile Displacements

Description	*Continuous Wall with Full Stiffness*	*Elastic Pile with Reduced Stiffness*	*Plastic Pile with Reduced Stiffness*
	y_p *(ft)*	y_p *(ft)*	y_p *(ft)*
Capitola Input Motion: A_{max} = 0.1g (at model base) $A_{max@dredge}$ = 0.24g $A_{max@dredge}$ / *MSF* = 0.192g	0.8	1.26	1.26
Capitola Input Motion: A_{max} = 0.4g (at model base) $A_{max@dredge}$ = 0.512g $A_{max@dredge}$ / *MSF* = 0.41g	3.2	5.7	6.4
Landers Input Motion: A_{max} = 0.4g (at model base) $A_{max@dredge}$ = 0.62g $A_{max@dredge}$ / *MSF* = 0.62g	3.6	6.3	7.0

Note:
1. y_p = pile displacement of 24 in. prestressed octagonal concrete pile.
2. *MSF* = 1.25 for M_w = 6.9 (Capitola); *MSF* = 1.0 for M_w = 7.5 (Landers).

having infinite pile moment capacity, whereas the plastic pile model having limited moment capacity. Once the moment capacity of the piles (600 kips-ft) in the plastic model is exceeded, the plastic hinges have formed at pile nodes without providing additional moment resistance to external earthquake loading, but pile deformation can be continued to computed in the model. The resulting bending moments of both elastic and plastic models on row 1 pile, as shown in Figure 7-1, subjected to horizontal peak acceleration ($A_{max,\ h}$) of 0.4g at the base of the model are shown in Figure 7-3. Bending moments of as much as 1800 kips-ft is observed in the dense sand layer for the elastic model. The piles actually behave plastically, i.e., failure, as a result of plastic hinge formation after plastic moment of 600 kips-ft (24 in. prestressed octagonal concrete pile) is reached. Without limiting the pile capacity, the piles in the elastic model tend to provide more moment resistances (as many as three times of pile ultimate moment capacity) on pile displacements, hence reducing the pile displacements.

The effect of plastic hinge formations on increasing pile displacement is found to be approximately 10% comparing plastic pile model to elastic pile model. It is noted that the pile displacements either in elastic model or in plastic model are rather large and the maximum bending moments are observed in the sand fill layer and dense sand layer. This is because the sand fills immediately beneath and behind the rock dike have liquefied and the effect of earthquake-induced liquefaction tends to provide excessive lateral forces on piles and cause the instability of rock dike.

In order to examine the factors causing large pile head displacements, the contour of pore pressure ratio beneath and behind the rock dike for horizontal peak

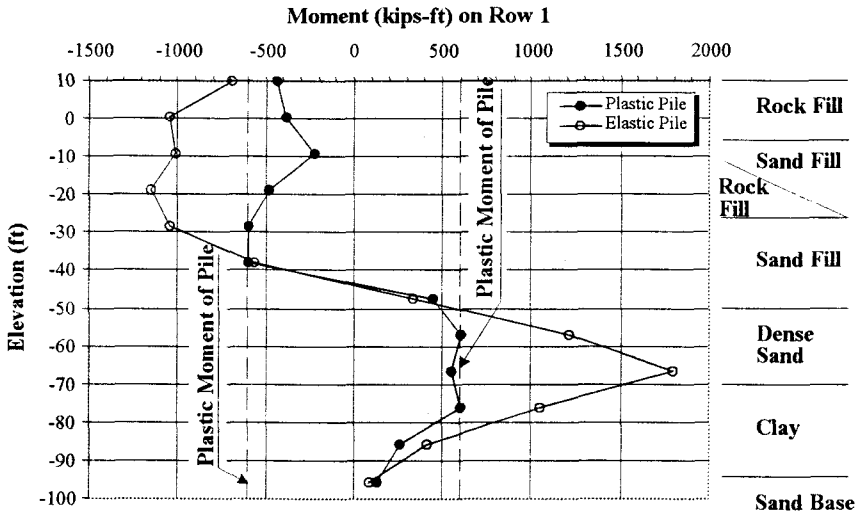

Figure 7-3: Bending moment of row 1 pile subjected to peak horizontal acceleration of 0.4g at the base of the model in the plastic and elastic pile model

acceleration of 0.4g and 0.1 g at the base of the model are plotted in Figure 7-4 and Figure 7-5, respectively. The pore pressure ratios of unity are observed at various locations in Figure 7-4 ($A_{max,\,h}$ = 0.4g) but are primarily concentrated beneath the rock dike; whereas the pore pressure ratios are less than 0.6 in the backland and somewhat close to unity beneath second-lift rock dike for the case of $A_{max,\,h}$ = 0.1g as shown in Figure 7-5. As excess pore pressures, generated by earthquake shaking, are gradually increased, the shear resistance of bottom sand fills is dramatically reduced. The excess pore pressures continue to accumulate until the soils completely lose their shear strength (zero shear strength). The generation of pore pressures resulting in reduction of shear strength of the soils beneath rock dike has primarily affected the instability of rock dike. The progressive failure of instability of the rock dike is not stopped until

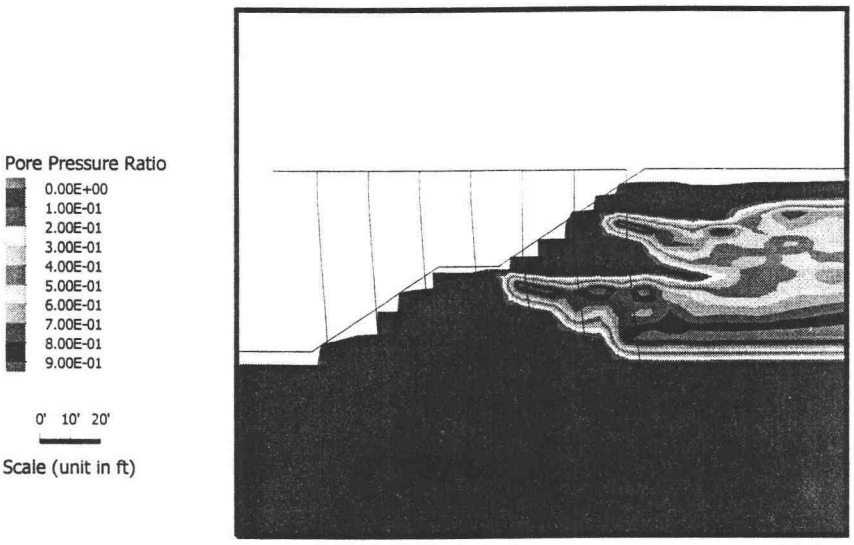

Figure 7-4: Contour of pore pressure ratio beneath and behind the rock dike ($A_{max,h}$ = 0.4g at the base of the model)

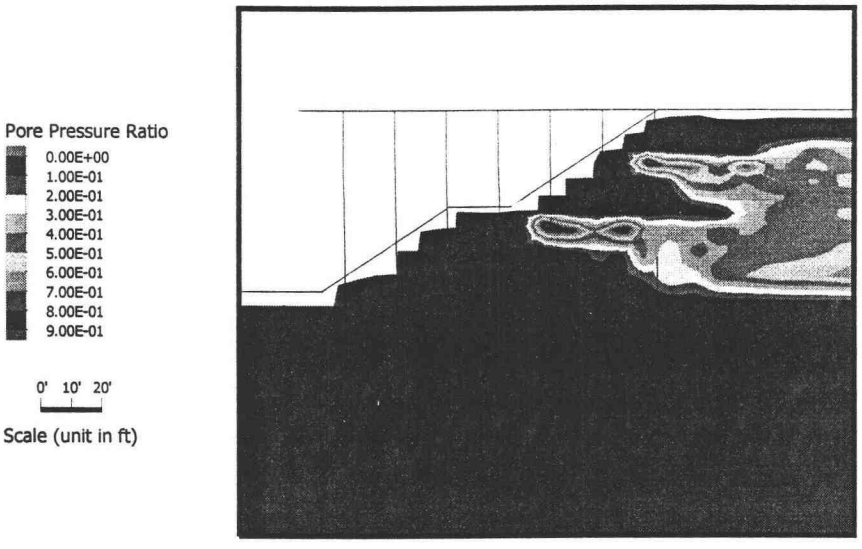

Figure 7-5: Contour of pore pressure ratio beneath and behind the rock dike ($A_{max,h}$ = 0.1g at the base of the model)

the external and internal forces are equilibrium. The piles are forced to deform essentially in accordance with the magnitude of rock dike displacements due to this progressive failure of slope. The additional lateral forces resulted from liquefaction in the sand fill layer tend to induce more bending moments on piles either in the elastic or plastic model as evident in Figure 7-3. It can be then reasonable assumed that for normalized ground motion intensity greater than 0.4g (typically for peak horizontal acceleration $\geq$ 0.4g), in which full liquefaction has been observed, the effect of plastic hinge formations on increasing pile displacement is 10% between elastic and plastic model. For normalized ground motion intensity of 0.2g (typically for peak horizontal acceleration = 0.1g), in which the degree of liquefaction is rather minor, there is no significant difference between elastic and plastic model since the ultimate pile capacity is not exceeded and essentially both pile models behave elastically under this level of shaking. The effect of liquefaction of backfill sand fill on pile deformation will be investigated in the latter section.

Comparison of continuous wall model to plastic model indicates that continuous wall model reduces the pile displacement by approximate 50% of that in the plastic model. However, without considering the spacing effect in the out-of-plane direction, the continuous wall model appears to result in too conservative pile displacements and is considered to be inappropriate approach for the analysis of soil/pile interaction.

7.3.2 Effect of Pile Stiffness and Ground Motion Intensity

In previous section the causes of failure modes for rock dike and piles and the difference between various pile modeling considerations have been investigated. In this section, the effects of various levels of ground motion intensity and the stiffness of piles, i.e., 16, 18, 24 in. prestressed octagonal concrete piles, on the performance of pile-supported wharf are evaluated. All piles in this section are using plastic pile model as described in previous section, in which cracked section of piles is modeled.

Figure 7-6 presents the normalized displacement (*Ys*), defined as seaward displacement at the top of the rock dike (y_s) divided by pile diameter (d), subjected to a range of ground motions. The circled numbers in Figure 7-6 represent the normalized ground motion intensity ($A_{max@dredge}$ / *MSF*) and h denotes the depth of liquefiable sand fill (i.e., 60 ft). The data for $h/d = 0$ represent that the backfill sands are specified as non-liquefiable soils. It is obvious from Figure 7-6 that higher ground motion intensity causes larger lateral displacement of rock dike than that under lower levels of ground motion intensity, as expected. However, the rock dike displacements between normalized ground motion intensity of 0.4g and 0.6g become less significant since a very severe liquefaction condition has occurred under these high shaking levels and the difference of rock dike displacement between these two values is primarily caused by inertial forces. On the contrary, the differences of displacements between ground motion intensity of 0.2g and 0.25g become significant because the degree of liquefaction is rather minor for ground motion intensity of 0.2g, whereas the degree of liquefaction is more severe for ground motion intensity of 0.25g, as described in Section 7.3.1. In particular, the rock dike displacements at the ground

motion intensity in the range of 0.2g to 0.25g are about one-third of those induced at the ground motion intensity in the range of 0.4g to 0.6g.

It is also observed from Figure 7-6 that the stiffer piles (smaller *h/d* ratio) tend to provide more resistance to dike displacement than those of softer piles (larger *h/d* ratio). This tendency is greater (steeper slope of curves) under higher ground motion intensity but rather less obvious under lower ground motion intensity because the piles essentially remain elastic behavior without plastic hinge formation at pile nodes under lower level of shaking.

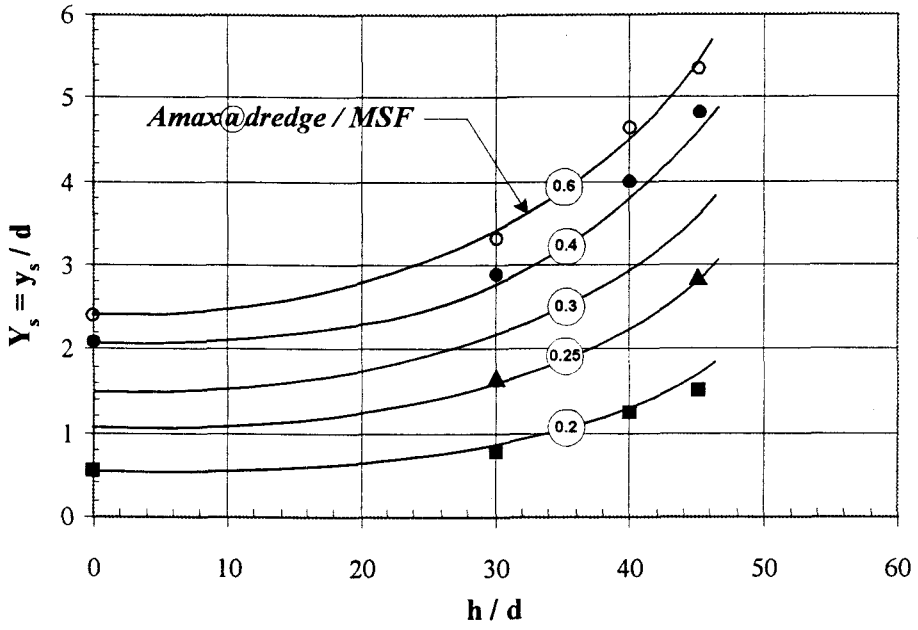

Figure 7-6: Normalized displacements at the top of rock dike subjected to a range of ground motions

Figure 7-7 shows that the effect of pile stiffness on pile deformation subjected to a range of ground motions in terms of normalized pile deflection (Y_p), defined as

maximum pile head deflection (y_p) divided by pile diameter (d), versus relative stiffness between pile and soil. The pile/soil relative stiffness, S_r, is defined as follows:

$$S_r = \frac{E_p I_p}{E_r y_s^4} \tag{7-1}$$

where E_p = Young's modulus of pile, I_p = moment of inertia of pile, E_r = pre-liquefaction or post-liquefaction stiffness of sand fill from Figure 7-8, and y_s = displacement at the top of the rock dike obtained from Figure 7-6. The S_r is a dimensionless measure of the flexibility of the pile relative to the soil and has limiting values of ∞ for an infinitely rigid pile and zero for an infinitely long pile. This formulation is consistent with the work by Stewart et al. (1994).

From Figure 7-7, the data can be divided by two curves which represent excess pore pressure ratio (r_u) of 1 and 0. For r_u =1 (full liquefaction), the increased gradients at lower S_r were caused by an increased soil displacement (y_s) due to higher normalized ground motion intensity (for $A_{max@dredge}/MSF \geq 0.25$g). The plastic hinges were essentially formed at pile nodes as a result of high ground motion intensity and excessive lateral soil spreading caused by liquefaction. This plastic behavior of piles became insignificant once S_r exceeded approximately 60, beyond which the piles essentially behaved elastically corresponding to lower normalized ground motion intensity of 0.2g. For r_u =0 (no liquefaction), similar pattern of pile head deflections was found for higher normalized ground motion intensity but pile head deflections essentially remained constant for S_r greater than 30.

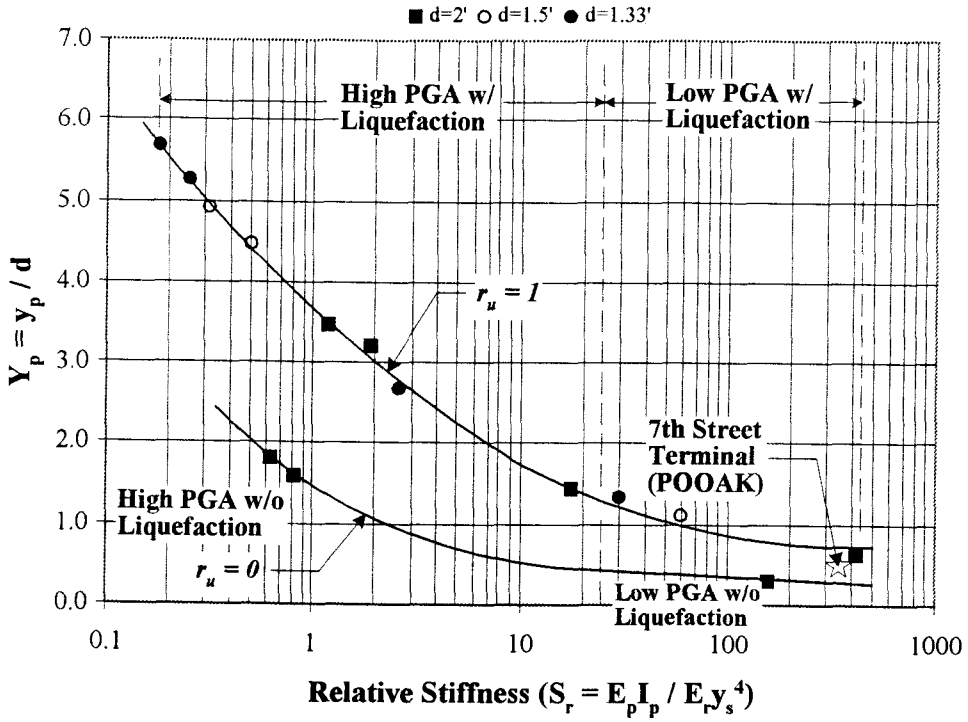

Figure 7-7: Effect of pile stiffness on pile displacements subjected to a range of ground motions

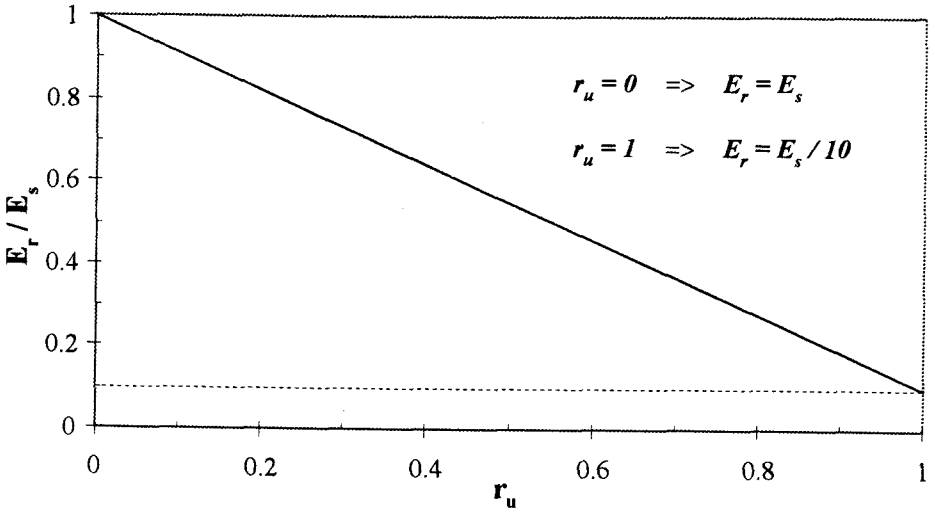

Figure 7-8: Pre-liquefaction and post-liquefaction stiffness of sand fill

It should be noted that the soil stiffness, E_r, used in equation 7-1 should account for seismically-induced excess pore pressure. A simplified linear relationship between E_r and r_u is illustrated in Figure 7-8. From two series of full-scale pile load tests Lam et al. (1995) reported that the potential dynamic gapping and cyclic degradation effects tend to result in a significant reduction in the soil stiffness as much as 80 to 90 percent in soil resistance. Also, from centrifuge mode tests Liu and Dobry (1995) reported a degradation coefficient of 0.1 for soil lateral resistance in fully liquefied soil. In this study, a reduction factor of 0.1 in soil stiffness for $r_u = 1$ was adopted. In this way, soil stiffness, E_r, equals to pre-liquefaction soil stiffness, E_s, for $r_u = 0$ and equals to 10% of pre-liquefaction soil stiffness for $r_u = 1$.

The case study of the Seventh Street Terminal, Port of Oakland, during 1989 Loma Prieta Earthquake is superimposed in Figure 7-7 with the star. It should be noted that the geometry of pile-supported wharf for this parametric study was based on multi-lift rock dike whereas single-lift rock dike was used at the Seventh Street Terminal. The reasonable agreement between the case study and the proposed relationship indicates that it is robust with respect to excess pore pressure, and applicable to single- as well as multi-lift dike structures. This latter observation is tentative in light of the limited number of case histories.

The relationship in Figure 7-7 also suggest that pile deformations (y_p) are roughly proportional to $(E_pI_p)^{-0.25}$ and $(E_pI_p)^{-0.4}$ for normalized ground motion intensity of 0.4g ~ 0.6g and 0.2g ~ 0.25g, respectively. Therefore, by increasing the pile diameter by 1.5 times, say from 16 in. pile to 24 in. pile, the pile deformation will be reduced by 10% and 30% for ground motion intensity of 0.4g ~ 0.6g and 0.2g ~

0.25g, respectively. It should be noted that these two correlations were based on the fact that the backfill sands were fully liquefied during seismic loading. For those back fills that are not liquefiable soils or less degree of excess pore pressure generation, the percentage of reduction on pile deformation for different pile stiffness would be expected to be different. Stewart et al. (1994) suggested that a doubling in pile stiffness at a given site would be expected to lead to an increase in maximum bending moment of between 5% and 25%, and a reduction in pile cap deflection of about 30% for piles subjected to lateral soil movement generated by embankment from centrifuge and field test data. However, no liquefaction effects on pile deflections are account for in those data.

The plastic hinge formation at various depths under different levels of shaking and different pile stiffness for the third row pile is shown in Figure 7-9 and Figure 7-10, respectively. The M_h denotes moments occurred at hinge nodes caused by earthquake inertia forces and liquefaction-induced excessive lateral soil spreading and M_p denotes plastic moment (ultimate pile moment capacity) of the piles. Once M_h is equal to M_p, the plastic hinges would be formed at pile nodes. Figure 7-9 shows that plastic hinges were formed primarily within the rock dike and sand fill layers under higher ground motion intensity (0.41g and 0.62g), while the piles essentially behave elastically under lower ground motion intensity (0.192g). These plastic hinges, resulted from liquefaction-induced lateral soil spreading in the backfill sand layer and instability of rock dike due to weaker zones immediate beneath it, caused large pile deformations.

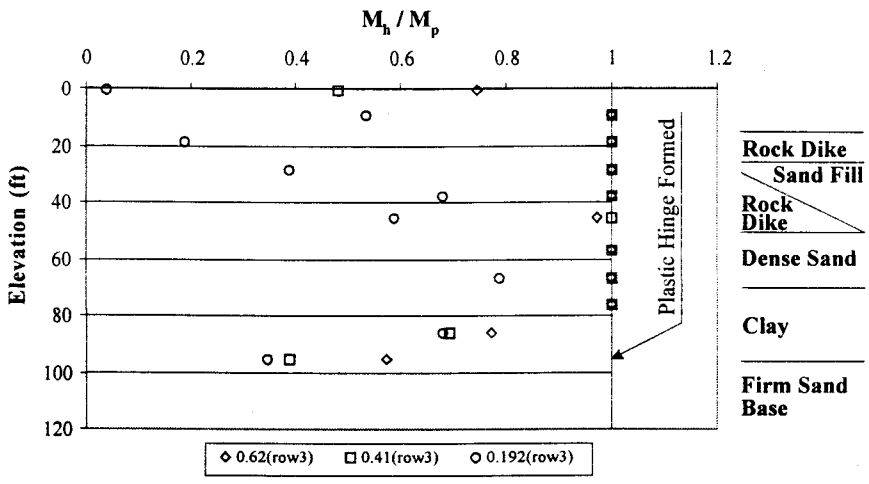

Figure 7-9: Plastic hinge formation on row 3 pile with depth subjected to various ground motion intensity (M_h=hinge moment; M_p=plastic moment)

Figure 7-10 shows the pile behavior for different pile stiffness subjected to ground motion intensity of 0.41g. The results indicate that stiff piles deflect as a rigid body and attract high forces and moments at higher shaking levels, whereas flexible piles essentially track with the soil and are subjected to low forces and moments.

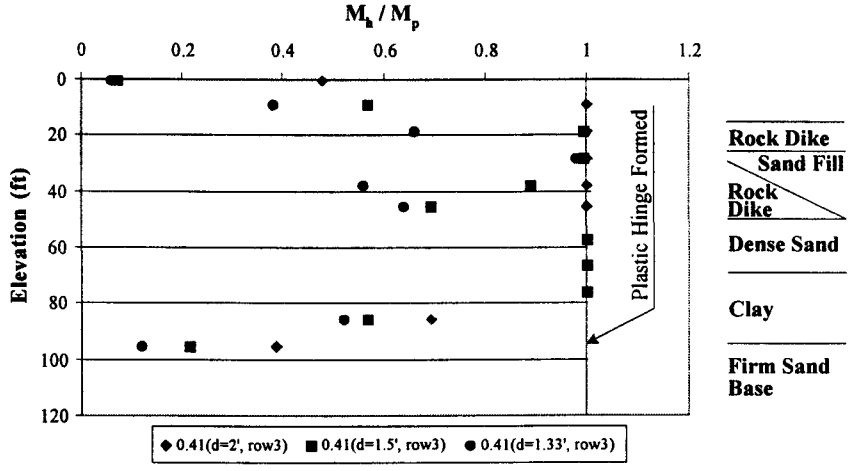

Figure 7-10: Plastic hinge formation on row 3 pile with depth for different pile stiffness (M_h=hinge moment; M_p=plastic moment)

It is obvious that the seismic performance of rock dike and pile-supported wharf is significantly affected by earthquake-induced liquefaction. The liquefaction primarily affects the stability of the rock dike, and induces the excessive lateral soil spreading causing high forces and moments on piles. In order to examine the quantitative contribution of liquefaction-induced lateral soil spreading, a comparison of the effect of liquefaction on the seismic performance of piles is investigated under various shaking levels in the following section.

7.3.3 Effect of Liquefaction-Induced Lateral Soil Spreading

In this section, the influence of liquefaction-induced lateral soil deformation on the performance of piles is evaluated. The pile-supported wharf is subjected to various ground motion intensity as described in previous two sections but the backfill sand layer is specified as non-liquefiable soil. The results of this section provide a direct comparison to those from Section 7.3.2. The comparison can be used to evaluate the relative quantity on pile displacements between these two soil conditions, i.e., liquefiable backfill and non-liquefiable backfill.

The results of the effect of liquefaction on rock dike and pile displacements are provided in Table 7-5. The comparisons of non-liquefiable backfill to liquefiable backfill subjected to the horizontal peak accelerations in the range of 0.1g to 0.4g indicated that the seaward rock dike displacements were essentially reduced by approximately 30%, while pile deformations were reduced by approximately 50%. The reduction of rock dike displacement reflects on the facts that in the case of non-liquefiable backfill scenario the sand fill layer immediate beneath rock dike between

elevation of –26 ft to –50 ft apparently increases the shear resistance against instability of rock dike, whereas in the case of liquefiable backfill scenario the shear strength of the liquefied soils approaches to zero extending over a depth of 24 ft beneath the rock dike, hence the piles are forced to deform in the same magnitude of rock dike displacements.

Table 7-5: Comparison of Liquefiable Backfill to Non-liquefiable Backfill on Rock Dike and Pile Displacements

Description	*Liquefiable*		*Non-Liquefiable*		*Reduction*	
	y_s *(ft)*	y_p *(ft)*	y_s *(ft)*	y_p *(ft)*	y_s *(%)*	y_p *(%)*
Capitola Input Motion: A_{max} = 0.1g (at model base) $A_{max@dredge}$ = 0.24g $A_{max@dredge}$ / *MSF* = 0.192	1.53	1.26	1.17	0.6	24	52
Capitola Input Motion: A_{max} = 0.4g (at model base) $A_{max@dredge}$ = 0.512g $A_{max@dredge}$ / *MSF* = 0.41	5.9	6.38	4.2	3.2	29	50
Landers Input Motion: A_{max} = 0.4g (at model base) $A_{max@dredge}$ = 0.62g $A_{max@dredge}$ / *MSF* = 0.62	6.64	6.96	4.45	3.62	33	48

Note:
1. y_s = rock dike top displacement; y_p = pile displacement.
2. *MSF* = 1.25 for M_w = 6.9 (Capitola); *MSF* = 1.0 for M_w = 7.4 (Landers).

It is noted that the pile displacements are less than the rock dike displacements for lower shaking level in which the piles essentially behave elastically. For higher shaking levels, the pile displacements are greater than those of rock dike because the piles behave plastically as a result of formation of plastic hinge due to the exceedance of pile resisting moment capacity under these high shaking levels. The pile displacements are 5% ~ 8% higher than those of rock dike, typically for ground

motion intensity greater than 0.4g. As presented in Section 7.2.1, the difference of pile displacements for elastic and plastic pile model is about 10%. If the piles behave elastically under these high shaking levels, the displacements of piles are compatible to those of rock dike.

Figure 7-11 shows the bending moment of row 1 pile for liquefiable backfill and non-liquefiable backfill. It is evidence that the pile remains elastically without forming plastic hinges at pile nodes as the backfill sand fill is not liquefied, hence reducing the pile displacements dramatically. The amounts of lateral backfill soil spreading on pile displacements are significantly reduced as comparing 6.38 ft to 3.2 ft for ground motion intensity of 0.41g. As much as 50% of pile displacement reduction has been observed.

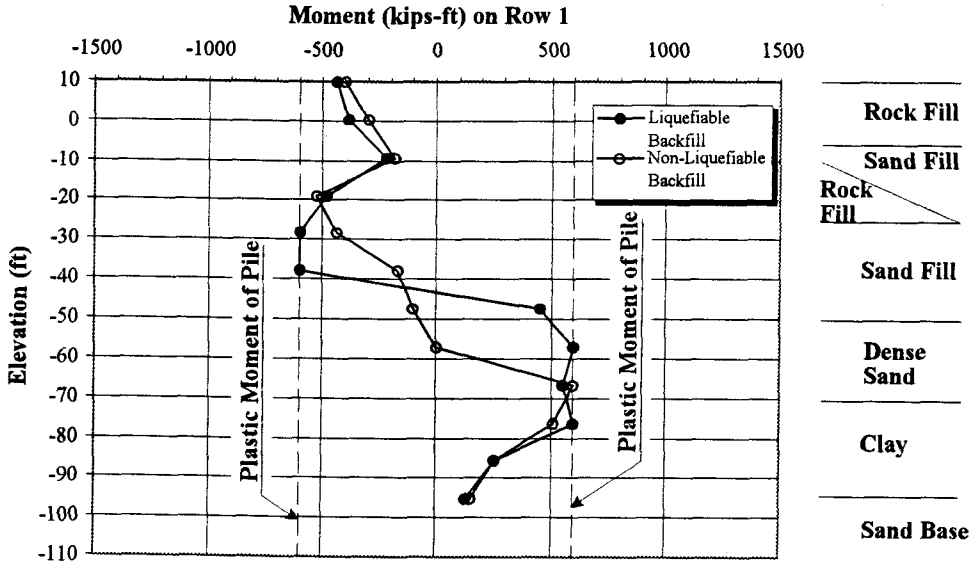

Figure 7-11: Bending moment of row 1 pile in liquefiable backfill and in non-liquefiable backfill subjected to $A_{max,h}$ = 0.4g

It then can be concluded that the performance of pile-supported wharf is largely affected by liquefiable backfill. The effects of earthquake-induced liquefaction in the backfill have primarily: (1) induced additional lateral forces and moments on piles; (2) caused the instability of rock dike; (3) resulted in the formation of plastic hinges at pile nodes in which the piles lose the capacity of resisting external moments, and (4) forced the piles moving in accordance with rock dike displacement.

7.3.4 Effect of Pile Pinning

In previous section, the effects of liquefaction-induced lateral soil spreading on pile displacements have been conducted. In this section, the effect of pile reinforcement on rock dike displacement is investigated. Comparisons of rock dike displacements with piles to without piles for liquefiable backfill subjected to shaking levels in the range of 0.1g to 0.4g are examined.

The results of pile pinning effect on rock dike displacement are tabulated in Table 7-6. The results indicated that the effects of pile pinning have reduced the rock dike displacement by approximately 23% for $A_{max,h}$ = 0.4g and by 50% for $A_{max,h}$ = 0.1g, respectively.

For severe liquefaction condition, i.e. at a higher level of acceleration, in which the shear strength of the liquefied soils was close to zero ($r_u \sim 1$), the reinforcement effect of piles in these liquefied soils essentially was relatively small, i.e. 21% and 25% reduction of rock dike displacement for ground motion intensity of 0.62g and 0.41g, respectively, due to lower values of normal and shear resisting strength of pile-soil interaction defined as simplified bilinear p-y curves used in the

model. The reinforcement effect of piles in providing resistance forces on rock dike in the liquefied soil layers, i.e. from Row 1 to Row 3 in Figure 7-1, was insignificant and the liquefied soils were essentially free to flow around the piles regardless of the stiffness of the piles. The piles embedded in the rock dike in front of liquefied backfill sand and underlying dense sand layer, i.e. from Row 4 to Row 7, provided large proportion of resisting forces on reducing the rock dike displacements.

For less severe liquefaction condition, i.e. at a lower level of acceleration, in which the excess pore pressures were about 0.4 to 0.6 of initial effective overburden stress (r_u = 0.4 to 0.6) as indicated in Figure 7-5, the pinning effect of piles apparently provided more resisting forces on rock dike displacement since higher values of normal and shear resisting strength of pile-soil interaction due to less degree of excess pore pressure generation were expected. As much as 50% of reduction on rock dike displacement due to pile pinning effect was observed at a lower level of acceleration.

It is noted that the deep-seated slope failure through the relatively thick clay layer (EL=-70 ft ~ EL=-95 ft) between dense sand layer and firm sand base layer was not observed. The sliding mode of failure primarily occurred at the interface of liquefied sand fill and the underlying dense sand due to massive liquefaction scenario. The pinning effect of the pile depends primarily on the higher stiffness of dense sand layer beneath the weak shear zone. For severe liquefaction condition, the reinforcement of piles became less significant since the soils around the piles were essentially free to flow and large portion of resisting forces against instability of rock dike came from the pile stiffness in the non-liquefiable soils near the toe of rock dike.

For less severe liquefaction condition, the soils were taking advantage of stiffness of piles, hence reducing the rock dike displacements significantly.

Table 7-6: Comparison of Pile Pinning Effects on Rock Dike Displacements for Liquefiable Backfill

Description	*No Piles with Liquefied Backfill*	*Piles with Liquefied Backfill*	*Reduction*
	y_s *(ft)*	y_s *(ft)*	y_s *(%)*
Capitola Input Motion: A_{max} = 0.1g (at model base) $A_{max@dredge}$ = 0.24g $A_{max@dredge}$ / *MSF* = 0.192g	2.97	1.53	50
Capitola Input Motion: A_{max} = 0.4g (at model base) $A_{max@dredge}$ = 0.512g $A_{max@dredge}$ / *MSF* = 0.41g	7.89	5.90	25
Landers Input Motion: A_{max} = 0.4g (at model base) $A_{max@dredge}$ = 0.62g $A_{max@dredge}$ / *MSF* = 0.62g	8.38	6.64	21

Note:
1. y_s = rock dike top displacement.
2. *MSF* = 1.25 for M_w = 6.9 (Captola); *MSF* = 1.0 for M_w = 7.4 (Landers).

7.4 Parametric Study for Pile-Supported Wharves in Improved Soils

In Section 7.3, various factors affecting the seismic performance of pile-supported wharf and rock dike have been examined. The failure modes of pile-supported wharf have been primarily due to a massive liquefaction zone scenario causing instability of rock dike through the weaker shear zone layer beneath the rock dike. The generation of excess pore pressure induced by earthquake shaking in these weaker zones has largely increased the pile and rock dike displacements. The presence of piles in liquefiable soils essentially do not provide the enough shear

resistance to reduce rock dike displacements efficiently. In view of these major causes on seismic performance of pile and rock dike, the next phase of the project focuses on an extensive parametric study for pile-supported wharf in various extents of improved zones.

7.4.1 Case 1: Soil Improvement in the Adjacent Areas of the Rock Dike

In this section, the effectiveness of the soil improvement were evaluated in the areas including the areas immediate beneath the first-lift and the second-lift of the rock dike and the areas behind the rock dike.

7.4.1.1 FLAC Model Setup

The configuration of the model pile-supported wharf and the surrounding soils was the same as shown in Figure 7-1 except that various extents of improved zones were implemented as shown in Figure 7-12. Three scenarios of improved zones, denoted as Case A, Case B, and Case C, according to the findings of previous sections have determined to be used in the analysis in order to determine the most beneficial extent of improved zone. In Figure 7-12, L and D denote the width and the depth of improved zone, respectively. No pore pressure generation in the foundation or improved backfill soils ($(N_1)_{60}$~30) implying that no liquefaction would occur in these layers. The depth of soil improvement extends to the base of the backfill, i.e., the same elevation as the dredge line. The mean lower low water (MLLW) is assumed to

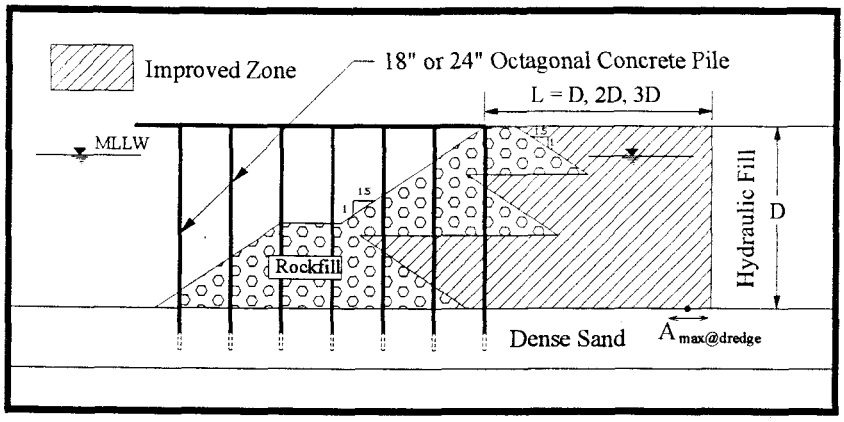

Case A

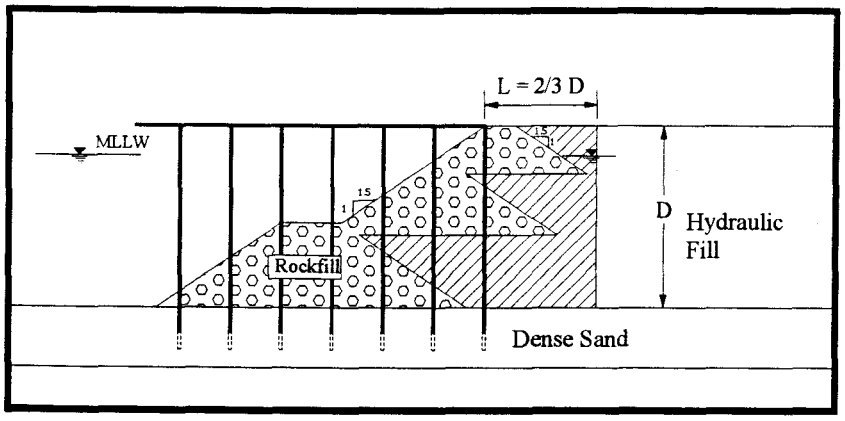

Case B

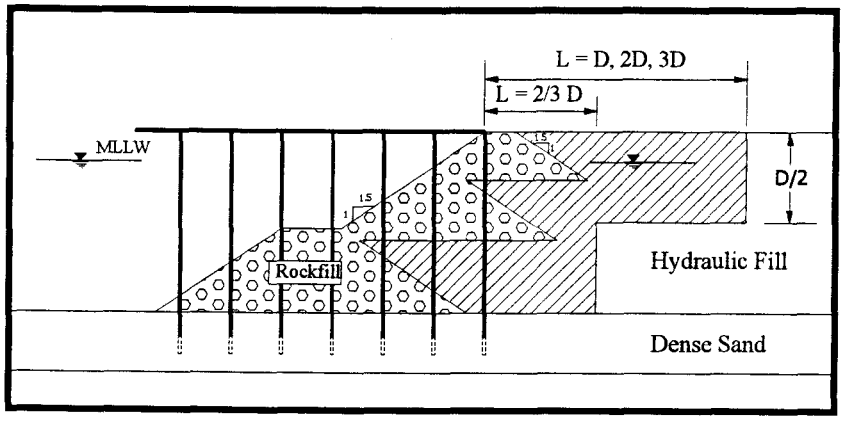

Case C

Figure 7-12: Geometry of models for various improved widths (L) and depths (D) in parametric study of Case 1

be constant on both sides of the model wharf and no seepage forces would occur during earthquake loading.

Other pertinent differences among various models in the parametric studies include:

I. *Pile Stiffness*: Two pile models representing 24 in. and 18 in. prestressed octagonal concrete pile were used in the analyses. The pile properties are the same as those tabulated in Table 7-2.

II. *Density and Strength of Soils*: The foundation and backfill soils were cohesionless materials except for the clay layer with undrained shear strength ratio (S_u/σ'_v) of 0.4 between foundation dense sand and base sand layers. Each layer was modeled with uniform density. The range of densities used can be correlated with stress corrected standard penetration resistances ($(N_1)_{60}$) of ***(a)*** 30 blows/ft in the foundation soils, ***(b)*** 10 blows/ft in unimproved backfill, and ***(c)*** 30 blows/ft in improved backfill. The soil properties are shown in Table 7-1. No cohesion in the sandy backfill was modeled, therefore the results presented herein are not applicable for cases involving the use of ground treatment by grouting or soil cement techniques.

III. *Ground Motions*: The input motions were applied uniformly to the base of the firm base sands. The lateral boundaries of the model were modeled as free field boundaries and set a distance of five times the hydraulic sand fill depth on both side boundaries to eliminate boundary effects on the computed pattern of soil deformations. The lateral and vertical deformations of the pile-supported wharf and surrounding soil, as well as the excess pore pressures in

the backfill were calculated and monitored during the seismic loading. Three earthquake motions covering the magnitude range of engineering interest (M_w 6 to 8) were selected for the parametric study. The information of input earthquake motions is listed in Table 5-1, denoted as ①, ⑥, and ⑨, and each acceleration time history is shown in Figure 5-3. A suite of recorded motions was utilized in order to account for the influence of varying ground motion characteristics (i.e. frequency content and duration) on the seismic performance of the pile-supported wharf. Each record motion was scaled to three different maximum acceleration values, i.e., 0.1g, 0.2g, and 0.4g.

7.4.1.2 Results of Parametric Study for Case 1

The results of the parametric study for pile-supported wharf in improved soils are presented in the form of the normalized pile head displacement versus the ratio of improved soil width (L) to depth (D). The normalized pile displacement is defined as follows:

$$\frac{y_p E_p I_p}{P H^3} \tag{7-2}$$

where y_p is the calculated pile lateral displacement, E_p is Young's modulus of pile, I_p is moment of inertia of pile, P is the pressures applied by the liquefied backfill sand behind the improved soil, and H is the depth of backfill sand layer, equivalent to the D defined previously. This dimensionless parameter is chosen by reference to the

approximate solutions for deflection of a beam subjected to concentrated load *P*. The values of P can be estimated by the procedures as follows:

Step 1: Estimate the pressures applied by the liquefied backfill behind the improved soil

Consider the pressures applied at the boundary of improved soil as shown in Figure 7-13.

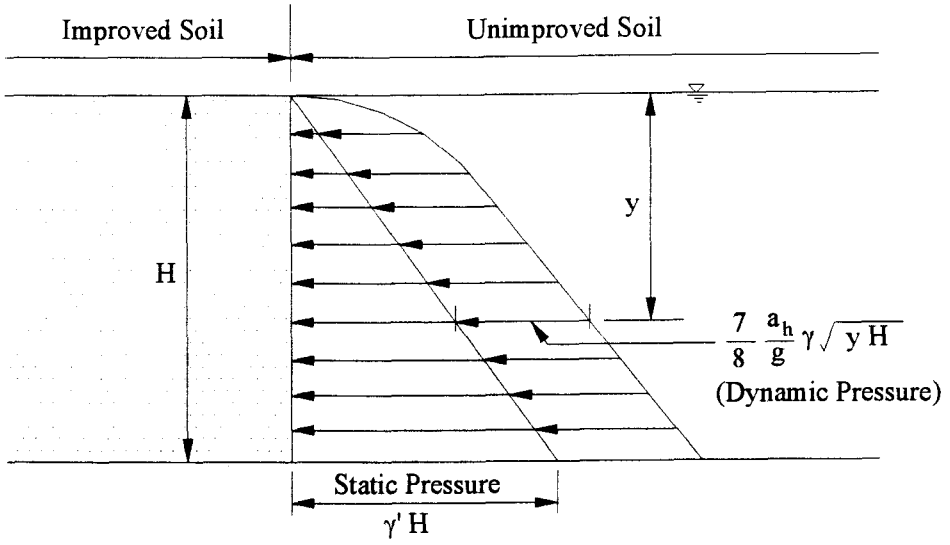

Figure 7-13: Pressures applied at the boundary of improved soil (after PHRI, 1997)

where H = improved soil depth, a_h = pseudostatic horizontal acceleration (g), γ = unit weight of saturated sand, and γ' = buoyant unit weight of saturated sand. At the boundary between improved soil and unimproved soil, a dynamic pressue and a static pressure corresponding to an earth pressure coefficient K = 1.0 are applied due to

liquefaction of unimproved soil. Then, total pressures applied by the liquefied backfill sand behind the improved soil can be computed as follows.

$$P_{static} = \frac{1}{2}\gamma' H^2 K \tag{7-3}$$

$$P_{dynamic} = \frac{7}{12}\frac{a_h}{g}\gamma H^2 \tag{7-4}$$

$$P = P_{static} + P_{dynamic} \tag{7-5}$$

Step 2: Estimate the pseudostatic horizontal acceleration, a_h

The pseudostaic horizontal acceleration associated with the design earthquakes is determined to calculate $P_{dynamic}$ as indicated in equation 7-4.

The results of the parametric study for pile-supported wharf in improved and in unimproved soils for pile diameter of 24 in. and 18 in. are shown in Figure 7-14 and Figure 7-15, respectively. The curves in both figures represent the relationship of normalized pile head displacement ($y_p E_p I_p / PH^3$) versus improved soil ratio (L/D) for various normalized ground motion intensities defined as peak horizontal acceleration at dredge line over magnitude scaling factor ($A_{max@dredge}/MSF$). The definition of the normalized ground motion intensity was described in Section 5-3. It should be noted that a_h vaules of 0.1g, 0.2g, and 0.4g in equation 7-4 correspond to 0.2g, 0.25g~0.3g, and 0.4g~0.6g in Figure 7-14 and Figure 7-15 due to the use of various earthquake motions (i.e., different frequent contents and durations) and the magnitude scaling factor.

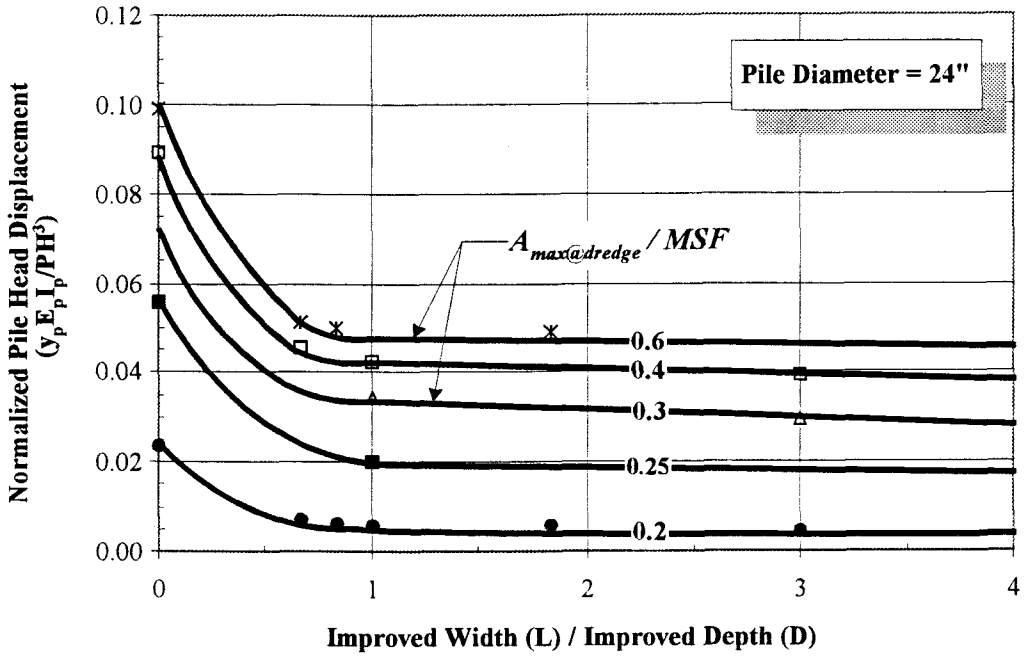

Figure 7-14: Normalized pile head displacement for pile diameter = 24 in.

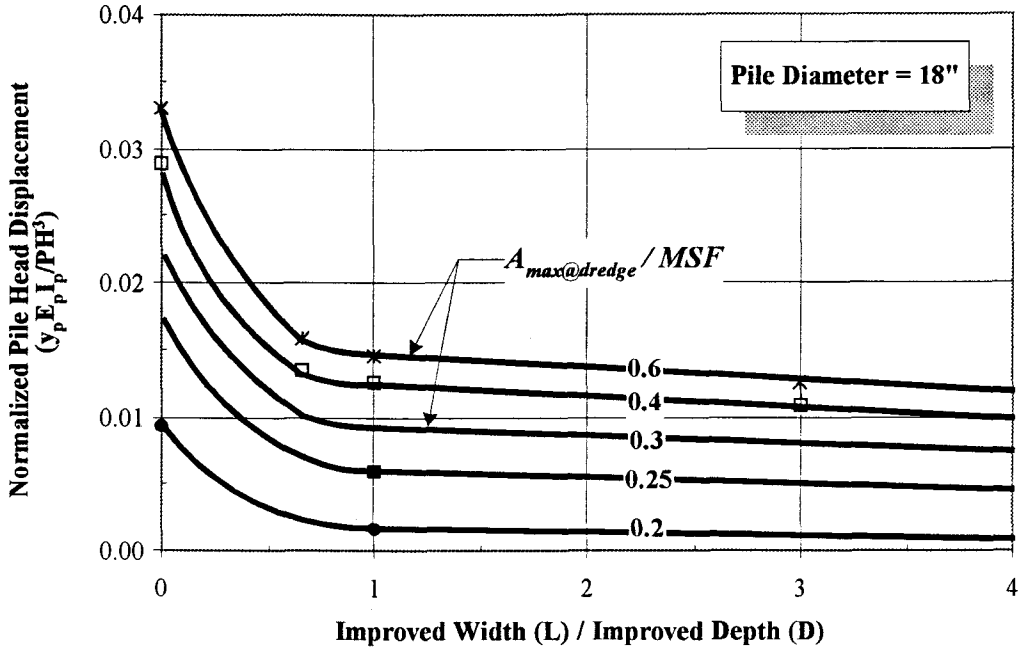

Figure 7-15: Normalized pile head displacement for pile diameter = 18 in.

It is recommended that if a site specific seismic study is not performed to determine $A_{max@dredge}$, then the peak ground surface acceleration can be reduced using the reduction factor (r_d) developed for estimating the variation of cyclic shear stress (or acceleration) with depth (Seed and De Alba, 1983). The values of r_d for 50 ft and 25 ft depth are approximately 0.78 and 0.95, respectively. By estimating peak acceleration at dredge line, $A_{max@dredge}$, along with appropriate magnitude scaling factor, *MSF*, and designed pile diameter, the predicted lateral pile head displacement in improved and in unimproved soils can be obtained from Figure 7-14 or Figure 7-15.

From Figure 7-14 and Figure 7-15, the benefits of soil improvement on reducing the lateral pile displacements are clearly demonstrated. The incremental benefit of a wider improved zone became insignificant once the soil improvement extended more than 1 to 1.5 times the depth of backfill. By treating rock dike and pile-supported wharf section as a rigid box (in an approximate way), these ranges are compatible with soil improvement guidelines complied by PHRI for caisson type retaining systems as shown in Figure 1-3, in which the normalized soil improvement width of 1.3 to 1.6 were suggested.

It is also noted that the difference of pile displacements between Case A (L/D = 1, 2, and 3) and Case B (L/D = 0.67) was rather small, i.e. Case A reducing pile displacement by averaging 10% more than that of Case B, implying that once the weaker zones immediate beneath the first-lift and second-lift of rock dike have been improved, the effectiveness of soil improvement for wider extents is rather insignificant (i.e., 15% lesser pile displacements for $L/D > 1$ as compared to case of

L/D = 1). In order to fit in the charts using the data from Case C, an equivalent ratio of width to depth corresponding to full depth of improved zone was used. Both Case B and Case C indicate that it is necessary, at least, to design an improvement zone so that there is no influence of liquefaction in the active failure zone. This improvement zone was found to be approximately at the ratio of improved soil width to soil depth of 1.5 for the 24 in. prestressed octagonal concrete pile from the parametric study. Beyond that point, the cost for additional soil improvement may outweigh the benefits.

The results of limited data for 18 in. pile showed similar patterns of pile displacement as for 24 in. pile. The most beneficial extent was approximately located at L/D ratio of 2.

The uncertainties involved in the charts are approximately estimated to be 30% for computed pile displacements regarding the characteristics of input earthquake motions, and rock dike geometry. The selected acceleration time histories are conservative due to each one characterized as having greater than average duration for that specific magnitude even introducing appropriate magnitude scaling factors, thereby yielding greater displacements than would be computed using motions of average duration. The 30% uncertainty is estimated from the result of case study in previous section in which similar modeling approaches were used. The available case histories for pile-supported wharf in improved soils are too limited in number and detail to make a comparison. However, these charts can be used as preliminary design charts as an upper bound of possible pile displacement subjected to either CLE or OLE event shaking levels.

7.4.2 Case 2: Soil Improvement behind the Rock Dike

In previous section, various soil improvement areas including the soils immediate beneath the first-lift and the second-lift rock dike have been investigated. For a newly constructed rock dike, the improved soil areas immediate beneath the multi-lift rock dike could be more conveniently accomplished by improving the weaker soils lift by lift. However, in practice, it is not so easy to improve the weaker soils immediate beneath the multi-lift rock dike for existing wharves. In this section, only the soils behind the multi-lift rock dike are improved and the soils immediate beneath the rock ike are left unimproved.

7.4.2.1 FLAC Model Setup

The FLAC model setup was the same as Section 7.4.1 except that extents of improved zones were implemented as shown in Figure 7-16.

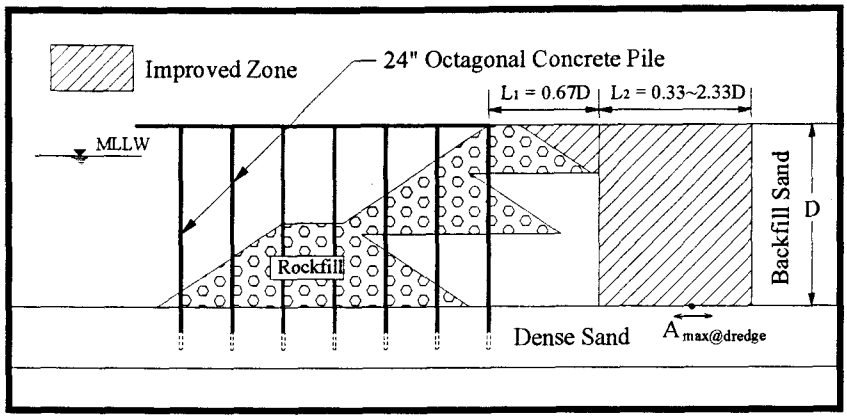

Figure 7-16: Geometry of models for various improved widths (L) and depths (D) in parametric study of Case 2

7.4.2.2 Results of Parametric Study for Case 2

The results of the parametric study for pile-supported wharf in improved and in unimproved soils for Case 2 scenario is shown in Figure 7-17. In this figure, lateral slope displacements at the top of the rock dike were plotted versus various impoved soil ratio subjected to a range of shaking levels. It should be noted that the soil improvement scenario in this section (Case 2) is different from that in Section 7.4.1 (Case 1), therefore, the results of these two sections should not be used interchangeably. Furthermore, from the results of Section 7.3, the pile displacements are essentially moved in accordance with the slope displacements of rock dike. In order to avoid confusing the results from these two sections, lateral slope displacements at the top of the rock dike computed from the numerical model were used.

From Figure 7-17, it is evident that the incremental benefit of a wider zone of ground treatment begins to decline once the improved width (L_2) extends more than about 0.5 to 1.0 times the depth of the backfill. At this point the lateral slope displacements were largely dependent on the intensity of inertia forces and the magnitude of slope displacements was caused by the degree of excess pore pressure generation of weaker soils immediate beneath first-lift and second-lift of the rock dike. The most beneficial extent was found approximately to be located at L_2/D ratio of 1.0 corresponding to approximately 100 ft behind the top of the rock dike (or 60 ft of L_2 improved soil width). Behind this point, the effectiveness of additional soil improvement may not be significant.

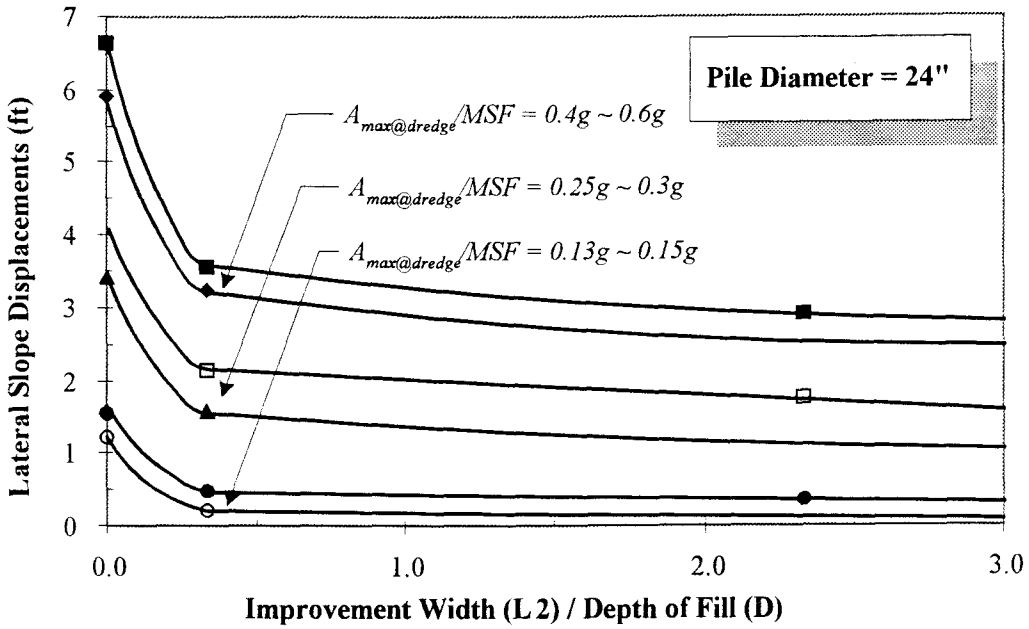

Figure 7-17: Lateral slope displacement versus improved soil ratio under a range of shaking levels

7.5 Recommended Procedures for Estimating Earthquake-Induced Displacements of Pile-Supported Wharves in Unimproved or in Improved Soils

As a screening tool for estimating the seismically-induced displacements of pile-supported wharves, the recommended procedures for using the results of parametric study include:

1. Estimate the potential liquefiable depth (H), designed pile properties (i.e., pile diameter,d, and pile flexural stiffness, E_pI_p).
2. Determine $(A_{max})_D$ based on a site response analysis or approximate with empirical soil amplification factors to yield the peak ground surface acceleration and the reduction factor (r_d).

3. Select the magnitude scaling factor *(MSF)* for the specified earthquake magnitude, and compute the ground motion intensity factor as $(A_{max})_D/MSF$.
4. Estimate the pile/soil relative stiffness (S_r) using equation 7-1. Enter Figure 7-7 to obtain the normalized pile displacement in which seismically-induced excess pore pressure ratio, r_u, ranging from 0 to 1 can be accounted for. From this, the maximum pile head displacement (y_p) in liquefiable or in non-liquefiable backfill soils can be estimated.
5. Determine the ratio of improved soil width (L) to improved soil depth (D) using either Case 1 or Case 2 scenario.
6. Determine the pseudostaic horizontal acceleration, a_h, associated with the design earthquakes. Estimate the pressures applied by the liquefied backfill sand behind the improved soil, P, using equation 7-3 ~ 7-5.
7. For Case 1 scenario, given pile diameter (d), the ratio of improved soil width to improved soil depth (L/D) and the ground motion intensity factor($(A_{max})_D/MSF$), enter Figure 7-14 or Figure 7-15 and obtain the normalized lateral pile head displacement. From this, the maximum pile head displacement (y_p) can be estimated.
8. For Case 2 scenario, given the ratio of improved soil width to improved soil depth (L/D) and the ground motion intensity factor($(A_{max})_D/MSF$), enter Figure 7-17 and obtain the lateral slope displacement at the top of the rock dike. For estimating maximum pile head displacememt, multiple slope displacement by an averaging factor of 1.15.

7.6 Summary of Parametric Study Results

The seismic performance of pile-supported wharves in sloping rock dike in unimproved and in improved soils have been evaluated. The resulting findings lead to following conclusions.

1. Higher ground motion intensity caused larger pile displacements but this tendency was less significant for ground motion intensity greater than 0.4g since the backfill sand were essentially fully liquefied and plastic hinges have formed at pile nodes under these high levels of shaking. For lower ground motion intensity, the piles essentially behaved elastically because the degree of excess pore pressure generation was relatively minor, hence inducing relatively smaller pile displacements. The pile displacements were roughly proportional to $(E_pI_p)^{-0.25}$ and $(E_pI_p)^{-0.4}$ for ground motion intensity of 0.4g ~ 0.6g and 0.2g ~ 0.25g, respectively. By increasing the pile diameter by 1.5 times, the pile displacements will be reduced by 10% and 30% for ground motion intensity of 0.4g ~ 0.6g and 0.2g ~ 0.25g, respectively.
2. The effects of earthquake-induced liquefaction in the backfill and in the soil immediate beneath first-lift and second-lift of the rock dike on the seismic performance of pile-supported wharves have primarily (1) induced additional lateral forces and moments on piles; (2) caused the instability of rock dike; (3) resulted in the formation of plastic hinges at pile nodes in which the piles lose the capacity of resisting external moments, and (4) forced the piles moving in accordance with rock dike displacement. The liquefaction-induced lateral soil

spreading has caused 2 times more pile displacements than those resulted from earthquake inertial forces only.

3. The deep-seated slope failure through the relatively thick clay layer (EL=-70 ft ~ EL=-95 ft) between dense sand layer and firm sand base layer was not observed. The sliding mode of failure primarily occurred at the interface of liquefied sand fill and the underlying dense sand due to massive liquefaction scenario. The pinning effect of the pile depends primarily on the higher stiffness of dense sand layer beneath the weak shear zone. For severe liquefaction condition, the reinforcement of piles became less significant since the soils around the piles were essentially free to flow regardless of the stiffness of piles and large portion of resisting forces against instability of rock dike came from the pile stiffness in the non-liquefiable soils near the toe of rock dike. For less severe liquefaction condition, the soils were taking advantage of stiffness of piles, hence reducing the rock dike displacements significantly. The effects of pile reinforcement have reduced the rock dike displacements by 50% and 23% for ground motion intensity of 0.2g and 0.4g ~ 0.6g, respectively.

4. The design charts for estimating the maximum lateral pile head displacement in unimproved or in improved soils have been developed. The chart for estimating the maximum lateral pile head displacement in unimproved soils can account for seismically-induced excess pore pressure in that r_u values are ranging from 0 to 1. Hence, the chart can be used for piles in liquefiable or in non-liquefiable soils.

5. Two soil improvement scenarios have been proposed. The results of parametric study indicate that it is necessary, at least, to design an improvement zone so

that there is no influence of liquefaction in the active failure zone. For Case 1 scenario, i.e., improving the areas immediate beneath the first-lift and second-lift of the rock dike and behind the rock dike, the most beneficial extents of soil improvement, starting from the top of the rock dike on the seaward side, are approximately estimated to be 1 ~ 1.5 times and 2 times the depth of liquefiable backfill for 24 in. and 18 in. octagonal prestressed concrete piles, respectively. For Case 2 scenario, i.e., improving areas only behind the rock dike and the areas immediate beneath the first-lift and second-lift of the rock dike are left unimproved, the most beneficial extents of soil improvement is approximately estimated to be 1.7 ~ 2.0 times the depth of liquefiable backfill for 24 in. octagonal prestressed concrete piles. Beyond those points, the cost of the additional soil improvement may outweigh the benefits.

8 SUMMARY AND CONCLUSIONS

8.1 Summary

A number of port facilities throughout the world are located in highly seismic regions, and recent experience demonstrates that waterfront retaining structures are vulnerable to earthquake damage. The loss of port functions has significant economic impact on lifeline systems as well as widespread economic consequences on industries relying on ports for commerce. The seismic performance of ports in the Osaka Bay region during the Hyogoken-Nanbu (Kobe) Earthquake of January 17, 1995 provides pertinent examples of the seismic vulnerability of port facilities. The widespread damage to the Port of Kobe during this earthquake caused $5.5 billion repair cost and $6 billion of indirect losses due to closure of the Kobe Port during only the first year after the earthquake.

The poor seismic performance of these facilities has been due, in large part, to the deleterious foundation and backfill soils that are commonly prevalent in the marine environment and the lack of design standards for many of the waterfront structures that make up the port system. The poor seismic performance of port facilities and economic impact of earthquake-induced damage highlight the need for improved performance-based design methods. These performance-based design methods improve the limitation of conventional force-based seismic design methods which are not well suited for conditions involving liquefiable sandy soils. Very few guidelines exist for specifying the performance-based design procedures in current standards-of practice.

Soil improvement techniques have been widely used as a countermeasure against liquefaction and thereby mitigating seismic hazards due to ground failures. Uncertainties involved in the application of soil improvement techniques include: (1) to what degree (i.e., minimum relative density, ground replacement ratios) the soils should be treated, and (2) the lateral and vertical extent of ground treatment required to insure acceptable seismic performance of the waterfront facilities.

In light of the importance of port components on economic impact, the primary objectives of this research were to (1) evaluate the seismic response of waterfront retaining structures and pile-supported wharves during earthquakes; (2) establish a representative numerical model for the seismic analysis of waterfront structures; (3) evaluate the seismic performance of piles in liquefiable soils; and (4) develop straightforward, practice-oriented design charts and performance-based guidelines for the analysis and design of waterfront structures.

Current pseudostatic methods of seismic analysis and design for gravity type walls were presented in Chapter 2. Two approaches, seismic pressure-based approach and permanent displacement-based approach, have been outlined.

State-of-art numerical method (Finite Difference Method) for dynamic analysis of soil-structure interaction problems was introduced in Chapter 3. This chapter addressed numerical modeling considerations used in the dynamic analysis of waterfront structures. These modeling considerations regarding constitutive soil model, pore pressure generation, soil parameters, and structural elements have been outlined.

The applicability of numerical model to known performance of gravity type retaining walls from case histories was addressed in Chapter 4. Five well-documented case histories for the seismic performance of gravity walls to earthquake damage in unimproved and in improved soils were chosen. The proposed numerical model was validated and calibrated by field performance. The evaluation of field seismic performance of concrete caissons consisted of comparisons of computed lateral displacements and settlements at the top of the caisson to average measured values, lateral soil movements and settlements including post-liquefaction volume strain in the backland area, and pore pressure generation. The major causes of failure of gravity walls, and the effects of countermeasures against earthquake-induced liquefaction used in the case histories in terms of soil improvement and width-to-height ratio, were discussed. Additionally, the uncertainties involved in the numerical model were also addressed.

Parametric studies of the seismic performance of gravity walls, using calibrated numerical model, in unimproved and in improved soils was outlined in Chapter 5. The parametric studies evaluated the factors affecting the seismic performance of caisson in association with backfill soil densities ($(N_1)_{60}$=10 ~ 20 blows/0.3m), a suite of ground motions intensity (M 6 ~ 8) , wall geometries (width-to-height ratio, W/H = 0.7 ~ 1.2), and the extent of soil improvement (L/H = 1 ~ 3). Following the analyses, the results of parametric study incorporated into the straightforward practice-oriented design charts for estimating seaward lateral displacement of the caisson. Comparison of field cases, i.e., five case histories from Chapter 4, and a concrete block quay wall case study at Kalamata Harbor, to design

charts were made in order to examine the applicability of design charts to known seismic performance of concrete caisson. The comparisons of permanent displacement-based approach results to parametric study results were also made in order to examine the difference between pseudostatic method and numerical method.

Chapter 6 evaluated the seismic behavior of pile-supported wharves. The proposed model was validated and calibrated by (1) two static lateral loading of single pile on horizontal ground, (2) a static lateral loading of single pile in sloping ground, (3) a dynamic loading of single pile in liquefiable soils, and (4) a case study of pile-supported wharf at Port of Oakland during 1989 Loma Prieta earthquake. The evaluation of piles subjected to lateral loading consisted of comparisons of computed pile displacements, pile bending moments, soil lateral movements to field measurements. These comparisons validated the soil-pile interaction characteristics, either in static lateral loading condition for piles on level ground and in sloping ground, or in dynamic loading condition for piles in liquefiable soils.

Chapter 7 presented parametric study of pile-supported wharves in sloping rockfill. The factors affecting the seismic performance of pile-supported wharf in unimproved soils, such as soil liquefaction, ground motion intensity, and pile stiffness, was first conducted. The causes and failure mechanism of pile-supported wharf and rock dike were evaluated and discussed. Following the analyses of seismic performance of pile-supported wharf in unimproved soils, parametric studies considering various ground motions, pile stiffness, and the extent of soil improvement were then determined. The results of parametric study were incorporated into simplified design charts for estimating the maximum pile head deformation.

8.2 Conclusions

The major findings and conclusions of this research have been drawn based on the areas studied as follows:

8.2.1 Gravity Type Concrete Caisson

- The waterfront retaining structures at ports are usually encountered with several unique conditions such as saturated soils, balanced static water forces, and hydraulically placed loose sandy soils. These loose sandy soils are very susceptible to liquefaction. The application of pseudostatic methods for marine environment does not directly account for strain softening behavior in liquefiable soils. Furthermore, the important aspects of soil-structure interaction are not modeled. These conditions limit the applicability of pseudostatic methods for waterfront structures. The seismic coefficient used in standard pseudostatic design methods for gravity type waterfront retaining walls are not adequately correlated with the wall deformations to facilitate estimates of seismically-induced lateral deformations in liquefiable soils. The performance-based design methods improve the limitation in the conventional seismic design methods that are based on the force balance against the designed seismic force. Therefore, performance-based (or deformation-based) analyses, which account for the generation of excess pore pressures in the backfill, to insure the serviceability of the waterfront components after a design-level earthquake are recommended.

- Gravity walls usually fail by rigid-body mechanisms, such as sliding, overturning, or deep-seated (global) instability. Under static conditions, retaining walls are acted upon by body forces related to the mass of the wall, by soil pressures, and by external forces. A properly designed retaining wall will achieve equilibrium of these forces without inducing shear stresses that approach the shear strength of the soil. During an earthquake, inertial forces and changes in soil strength (partially due to soil liquefaction) may violate force equilibrium and cause the loss of bearing capacity of foundation, deep-seated failure, additional earth pressure induced by liquefaction, as well as the permanent deformation of the wall. The failure mechanism of caissons in the case studies presented herein has been seaward tilting failure. It is noted that this failure mode of the caisson is not the same as that usually assumed in the limit equilibrium, sliding block methods of analysis. This indicates that the simplicity of pseudostatic analysis methods is offset by the failure mechanism for gravity type waterfront retaining structures especially if foundation soils are potentially liquefiable soils. The causes of the caisson failure, in addition to the effect of the strong shaking such as inertial force, hydrodynamic, and seismic lateral earth pressure, have been mainly due to soil liquefaction behind and/or beneath the caisson. The liquefaction of hydraulically placed sand fill has significantly affected the seismic performance of the caisson, whereas the foundation soil beneath the caisson has relatively less significant influence on the caisson since it usually has been replaced or densified with higher shear strength soil, such as Port Island and Rokko Island at Kobe Port.

- The nonlinear, effective stress analysis has been shown to provide a more representative method to simulate the seismic performance of the waterfront retaining walls as compared to conventional design approaches. It is more applicable especially when excess pore pressure generation and liquefaction have occurred in the backfill. Overall, numerical prediction for seaward lateral displacements of the caissons is approximately within ±25% on average as compared to average field measured displacements as indicated in Figure 4-55 and is approximately under-predicted by 26% on average for vertical displacements.
- Two simplified design charts for estimating lateral displacements of the caisson in unimproved and in improved soils have been proposed. The design charts are robust with respect to seismically-induced excess pore pressure in that r_u vales ranging from 0 to 1 are accounted for. Therefore, the charts can be used for cases with non-liquefiable backfill as well as liquefiable soils. The relationships provided from parametric studies clearly demonstrate the benefit of ground treatment on the seismic performance of concrete caisson. It is evident that the incremental benefit of a wider zone of ground treatment begins to decline once the soil improvement extends more than about 2.0 to 3.5 times the total height of the caisson. At this point the cost of additional soil improvement may outweigh the benefits.
- From a practical perspective, the "failure" of a caisson quay wall can be considered as corresponding to lateral deformations in the range of 10 cm to 30 cm, due to the damage incurred by adjacent cargo handling equipment and

facilities. The allowable deformations will therefore reflect the sensitivity of appurtenant structures. It was found that to limit the lateral displacements of caisson to acceptable levels for specifications used at ports in improved soils under higher shaking levels (typically $A_{max,h} \geq 0.3g$) was difficult. Alternative approaches to reduce the displacements of the caisson are required. The larger width-to-height ratio of the caisson (typically for Width/Height $\geq$ 1.2) performed favorably well during earthquake loading, even earthquake-induced liquefaction has been observed. The approach of high seismic resistant in terms of larger width-to-height ratio of the caisson along with the soil improvement techniques, such as Case 4 in Section 4.2.2.2, can be considered as a countermeasure against liquefaction for the seismic design approach of gravity type wall.

8.2.2 Seismic Performance of Piles in Liquefiable Soils

- Simplified design chart (Figure 7-7) for piles in unimproved soils has been developed to facilitate fast assessment of estimating the maximum pile head deformation. The chart can be used to account for seismically-induced excess pore pressure in that r_u values are ranging from 0 to 1. Hence, it can be used for piles in liquefiable or in non-liquefiable soils. At low relative pile/ soil stiffness, earthquake-induced soil liquefaction beneath the rock dike has induced excessive lateral forces and moments on piles, has caused the formation of plastic hinges at pile nodes in which the piles lose the capacity of resisting

external moments, and hence has resulted in large pile displacement. With increasing relative pile/soil siffness in which the degree of the excess pore pressure is rather low and the soil is taking advantage of the pile stiffness, the piles essentially behave elastically without yielding. For pile in non-liquefiable soil (r_u = 0), the pile displacements remain constantly once the relative pile/soil stiffness exceeds roughly 30 to 60.

- The results of parametric study reveal that the important parameters affecting lateral pile seismic response include the extent of liquefiable backfill, pile stiffness, the shear strength of liquefied soils, the stiffness of soil beneath the rock dike, and levels of shaking. The seismic performance of pile-supported wharf is largely affected by the extent of liquefaction adjacent to the foundation. The effects of earthquake-induced liquefaction in the backfill have primarily caused the instability of rock dike through the weaker shear zone layer beneath the rock dike and forced the piles moving in accordance with rock dike displacement. As much as two times of those simply caused by inertial forces only was observed.
- The predictions of piles in liquefiable soils accounting for the effect of sloping rockfill, i.e., reducing passive resistance on the seaward side, indicate that the pile displacements are approximately 25% and 10% higher than those without the consideration of slope effect for lower and higher shaking levels, respectively. At present, the analytical methods using the theory of subgrade reaction for the seismic performance of pile in liquefiable soils have largely developed in level ground. Without considering the slope effect, current p-y

curves approaches tend to underestimated the lateral pile displacements even the effect of earthquake-induced liquefaction being accounted for. From the results of five field load tests for piers constructed on slopes (non-liquefiable soils), Gabr et al. (1990) reported that as much as 50% of underestimation were observed.

- The parametric studies suggest that maximum pile head deformations are roughly proportional to $(E_pI_p)^{-0.25}$ and $(E_pI_p)^{-0.4}$ in the liquefiable soils for normalized ground motion intensity of 0.4g ~ 0.6g and 0.2g ~ 0.25g, respectively. Therefore, by increasing the pile diameter by 1.5 times (corresponding to increasing 5 times of pile stiffness), say from 16 in. pile to 24 in. pile, the pile deformation in the liquefiable soils will be reduced by 10% and 30% for ground motion intensity of 0.4g ~ 0.6g and 0.2g ~ 0.25g, respectively. Stewart et al. (1994) suggested that a doubling in pile stiffness at a given site would be expected to lead to an increase in maximum bending moment of between 5% and 25%, and a reduction in pile cap deflection of about 30% for piles subjected to lateral soil movement generated by embankment from centrifuge and field test data. However, no liquefaction effects on pile deflections are account for in those data.
- The pinning effect of the pile depends primarily on the higher stiffness of dense sand layer beneath the weak shear zone. For severe liquefaction condition, the reinforcement of piles on rock dike deformations becomes less significant since the soils around the piles are essentially free to flow regardless of pile stiffness.

For less severe liquefaction condition, the soils are taking advantage of stiffness of piles, hence reducing the rock dike deformations significantly.

- Simplified design charts for estimating the maximum lateral pile head displacement in improved soils, in which two soil improvement scenarios are used, have been developed. The results of parametric study indicate that it is necessary, at least, to design an improvement zone so that there is no influence of liquefaction in the active failure zone. For Case 1 scenario, i.e., improving the areas immediate beneath the first-lift and second-lift of the rock dike and behind the rock dike, the most beneficial extents of soil improvement, starting from the top of the rock dike on the seaward side, are approximately estimated to be 1 ~ 1.5 times and 2 times the depth of liquefiable backfill for 24 in. and 18 in. octagonal prestressed concrete piles, respectively. For Case 2 scenario, i.e., improving areas only behind the rock dike and the areas immediate beneath the first-lift and second-lift of the rock dike are left unimproved, the most beneficial extents of soil improvement is approximately estimated to be 1.7 ~ 2.0 times the depth of liquefiable backfill for 24 in. octagonal prestressed concrete piles. Beyond those points, the cost of the additional soil improvement may outweigh the benefits.
- For the cases with very loose backfill that are improved to reasonable densities but subjected to high shaking levels, limiting the pile displacements to acceptable degree is found to be difficult due to strong inertial forces. However, these pile displacements are essentially much less than those that occur in unimproved soils.

- The uncertainties involved in the charts are approximately estimated to be 30% for computed pile displacements regarding the characteristics of input earthquake motions, and rock dike geometry. The 30% uncertainty is estimated from the result of case study of Port of Oakland in which similar modeling approaches were used. The selected acceleration time histories are conservative due to each one characterized as having greater than average duration for that specific magnitude, thereby yielding greater displacements than would be computed using motions of average duration. However, these charts can be used as preliminary design charts as an upper bound of maximum pile displacement subjected to either CLE or OLE event shaking levels.

8.2.3 Strengths and Limitations of the Numerical Model

- The primary strengths of numerical model include (1) capable of accounting for nonlinear, plastic behavior of the soil in a simplified manner, and modeling the interfaces between the soil and wall elements; (2) irregular embankment and structure geometries can be modeled; (3) dynamic soil behavior, strain softening of liquefiable soils, soil-structure interaction, and permanent deformations can be more accurately evaluated than in pseudostatic methods; (4) transient, dynamic effects of earthquake motions can be more reasonably represented; (5) it is easy to perform sensitivity studies for the influence of various parameters on the seismic response of soils and structures.
- Limitations and uuncertainties in the numerical models usually arise from the facts that (1) several potentially important aspects of dynamic soil behavior are

not modeled in the simple Mohr-Coulomb constitutive soil model (e.g., soil modulus degradation due to cyclic straining, strain-hardening, or dialatancy) (2) requisite soil parameters for a constitutive soil model may not be always available and engineering judgement based on geotechnical correlations will lead to uncertainty; (3) given the highly variable nature of ground motion characteristics, the use and interpretation of earthquake motions may result in quite variable computed structure deformations; (4) very few well-documented case histories of seismic performance of retaining structures and pile-supported wharves exist, thereby limiting opportunities to calibrate the numerical model.

8.3 Recommendations for Future Research

- The results of this research have been based on nonlinear, effective stress numerical model. The soil and soil-pile interaction properties used in the numerical model have largely based on empirically geotechnical relations developed from field test data. Futhermore, the use of 20% reduction factor in the bilinear p-y curve relationship for accounting for piles in the sloping rockfill has been based on the data as compared to limited field case study. The accuracy of the prediction can be improved if the model is validated and calibrated by more case histories or experimental data. However, the available field case histories for waterfront structures in improved soils are too limited in number and detail. Future study based on experimental data, such as centrifuge test , shaking table test, to improve the proposed model is recommended.

- The soil improvement was modeled as providing a uniform increase in soil density throughout the zone of treatment that would be expected from vibro-compaction improvement techniques. However, improvement near sensitive utilities may require the use of controlled displacement techniques such as grouting or soil mixing. Future soil improvement scenario used in the model can be extended by considering various soil improvement strategies.
- In practice, many waterfront structures are designed using pseudostatic analysis methods. It would be beneficial to relate, where possible, the numerical modeling results with more standard pseudostatic methods. Future work to incorporate the numerical modeling results into standards-of-practice design methods for waterfront structures is recommended.
- The performance-based design methods have improved the limitation in the conventional seismic design methods. The poor seismic performance of port facilities and economic impact of earthquake-induced damage also highlight the need for improved performance-based design methods. Future work associated with reducing the uncertainties, establishing measures of uncertainties and randomness, and developing a methodology that accounts for these aspects in the design and evaluation process for the design of waterfront structures is recommended.

BIBLIOGRAPHY

Abdoun, T., Dobry, R., and O'Rourke, T.D. (1997) "Centrifuge and Numerical Modeling of Soil-Pile Interaction during Earthquake Induced Soil Liquefaction and Lateral Spreading" *Geo-Institute*, 97'.

Alizadeh, M. and Davisson, M.T. (1970) "Lateral Load Tests on Piles-Arkansas River Project" *Journal of Geotechnical Engineering*, ASCE, Vol. 96, No. SM5, September pp.1583-1603.

Arango, I. (1996) "Magnitude Scaling Factors for Soil Liquefaction Evaluations" *Journal of Geotechnical Engineering*, ASCE, Vol. 122, No. 11, pp. 929-936.

Benuska, L. (ed., 1990) "Loma Prieta Earthquake Reconnaissance Report" *Earthquake Spectra*, Supplement to Volume 6, EERI, May.

Boulanger, R.W., Wilson, D.W., Kutter, B.L., and Abghari, A. (1997) "Soil-Pile-Superstructure Interaction in Liquefiable Sand" *Transportation Research Record*, No. 1569, pp.55-64.

Byrne, P.M., Anderson, D.L., and Janzen, W. (1984) "Response of Piles and Casings to Horizontal Free-field Soil Displacements" *Canadian Geotechnical Journal*, Vol. 21, June, pp. 720-725.

Byrne, P.M., Jitno, H., Anderson, D.L., and Haile, J. (1994) "A Procedure for Predicting Seismic Displacements of Earth Dam", *XIII ICSMFE*, 1994, India. pp. 1047-1052.

Chaudhuri, D., Toprak, S., and O'Rourke, T.D. (1995) "Pile Response to Lateral Spread: A Benchnark Case" *Proceedings* of the Fourth U.S. Conference on Lifeline Earthquake Engineering, Technical Council on Lifeline Earthquake Engineering Monograph No. 6, August, pp. 755-762.

Chen, L.T. and Poulos, H.G. (1997) "Piles Subjected to Lateral Soil Movements" *Journal of Geotechnical Engineering*, ASCE, Vol. 123, No. 9, September, pp. 802-811.

Contri, G., Noce, G., and Fedolino, M. (1986) *Precast Elements in Harbour Works*, Permanent International Association of Navigation Congresses (PIANC) Bulletin 56.

Cundall, P.A. (1976) "Explicit Finite Difference Methods in Geomechanics" *Proceedings* of the EF Conference on Numerical Methods in Geomechanics, Blacksburg, Virginia, June, Vol., pp.132-150.

Cundall, P. and M. Board. (1988) "A Microcomputer Program for Modeling Large-Strain Plasticity Problems." *Proceedings* of 6th International Conference on Numerical Methods in Geomechanics. Innsbruck, Austria. pp 2101-2108.

Diaz, G.M., Patton, B.W., Armstrong, G.L., and Joolazadeh, M. (1984) "Lateral Load Tests of Piles in Sloping Rock Fill" *Proceedings* of Analysis and Design of Pile Foundations, ASCE, Oct. 1-5, pp.214-231.

Dickenson, S.E., and McCullough, N. (1998) "Mitigation of Liquefaction Hazards to Anchored Sheet Pile Bulkheads" *Proceedings* of Port '98 Conference, ASCE, Long Beach, CA, March.

Empfehlungen des Arbeitsausschusses Ufereinfassungen (EAU) (1990) *Recommendations of the Committee for Waterfront Structures*, Sixth English Edition, Ernst and Sohn, Berlin.

Ebeling, R.M., and Morrison, E.E. (1993) "The Seismic Design of Waterfront Retaining Structures", *Technical Report R-939*, Office of Navy Technology and Department of the Army, NCEL, Naval Civil Engineering Laboratory, Port Hueneme, CA, 256 p.

Egan, J.A., Hayden, R. F., Scheibel, L.L., Otus, M., and Serventi, G.M. (1992) "Seismic Repair at Seventh Street Marine Terminal" Proceedings of Groutings, Soil Improvement and Geosynthetics, ASCE, New Orleans, LA, February 25-28, pp. 867-878.

Erickson B.P., Ferritto J., Hebert D.C., and Werner, S.D. (1998) "Seismic Design and Analysis" *Chapter 5 of Seismic Guidelines for Ports*, Technical Council on Lifeline Earthquake Engineering Monograph No. 12, ASCE, March.

Evans, G.L. (1971) "The Behavior of Bridge Under Earthquake" *Proceedings* of New Zealand Roading Symposium, Vo. 2, pp.664-684.

Ferritto, J. (1997) "Seismic Design Criteria for Soil Liquefaction" *Technical Report TR-2077-SHR*, U.S. Naval Facilities Engineering Services Center, Port Hueneme, CA, June.

Finn, W.D.L., Wu, G., and Ledbetter, R.H. (1994) "Recent Developments in the Static and Dynamic Analysis of Pile Groups" *Deep Foundations*, Vancouver geotechnical Society, May, pp. 1-24.

Franklin, A.G. and Chang, F.K. (1977) "Earthquake Resistance of Earth and Rock Fill Dams; Report 5: Permanent Displacement of Earth Embankments by Newmark's Sliding Block Analysis" *Misc. Paper S-71-17*, Soil and Pavement Lab., U.S. Army Engineer Waterways Experiment Station, Vicksburg, Mississippi, November.

Gabr, M.A. and Borden, R.H. (1990) "Lateral Analysis of Piers Constructed on Slopes" *Journal of Geotechnical Engineering*, ASCE, Vol. 116, No. 12, December, pp.1831-1850.

Gandhi, S.R. and Selvam S. (1997) "Group Effect on Driven Piles under Lateral Load" *Journal of Geotechnical Engineering*, ASCE, Vol. 123, No. 8, August, pp.702-709.

Goh, A.T.C., Teh, C.I., and Wong, K.S. (1997) "Analysis of Piles Subjected to Embankment Induced Lateral Soil Movements" *Journal of Geotechnical Engineering*, ASCE, Vol. 123, No. 9, September, pp. 792-801.

Hamada, H. (1992a) "Large Ground Deformations and Their Effects on Lifelines: 1964 Niigata Earthquake" *Technical Report NCEER-92-0001*, Case Studies of Liquefaction and Lifeline Performance during Past Earthquakes, Volume 1-Japanese Case Studies, February 17.

Hamada, H. (1992b) "Large Ground Deformations and Their Effects on Lifelines: 1983 Nihonkai-Chubu Earthquake", *Technical Report* NCEER-92-0001, Case Studies of Liquefaction and Lifeline Performance during Past Earthquakes, Vol. 1.

Hamada, M., Isoyama, R., and Wakamatsu, K. (1996) "Liquefaction-Induced Ground Displacement and Its Related Damage to Lifeline Facilities" *Soils and Foundations*, Special Issue on Geotechnical Aspects of the January 17 1995 Hyogoken-Nanbu Earthquake, Jan., pp. 81-97.

Hardin, B.O. (1978) "The Nature of Stress-Strain Behavior for Soils" *Proceedings* ASCE Specialty Conference on Earthquake Engineering and Soil Dynamics, Pasadena, CA, Volume 1, pp.3-90.

Housner, G.W. (1975) *Earthquake Design Criteria for Long Beach Harbor*, December.

Iai, S. and Kameoka, T. (1993) "Finite Element Analysis of Earthquake Induced Damage to Anchored Sheet Pile Quay Walls" *Soils and Foundations*, Vol. 33, No. 1, March, pp. 71-91.

Iai, S. (1994a) "Area of Ground Compaction Against Soil Liquefaction", *XIII International Conference of Soil Mechanics and Foundation Engineering*, 1994, New Delhi, India. pp. 1075-1078.

Iai, S., Matsunaga, Y., Morita, T., Miyata, M., Sakurai, H., Oishi, H., Ogura, H., Ando, Y., Tanaka, Y., and Kato, M. (1994b) "Effects of Remedial Measures against Liquefaction at 1993 Kushiro-oki Earthquake" *Proceedings* of Fifth U.S.-Japan Workshop on Earthquake Resistant Design of Lifeline Facilities and Countermeasures against Soil Liquefaction, NCEER Technical Report NCEER-94-0026, O'Rourke and Hamada (eds.), pp.135-152.

Idriss, I.M. and J.I. Sun. (1992) *User's Manual for SHAKE91*. Center for Geotechnical Modeling, Dept. of Civil and Environmental Engineering, University of California, Davis.

Inagaki, H., Iai, S., Sugano, T., Yamazaki, H., and Inatomi, T. (1996) "Performance of Caisson Type Quay Walls at Kobe Port" *Soils and Foundations*, Special Issue on Geotechnical Aspects of the January 17 1995 Hyogoken-Nanbu Earthquake, Jan., pp. 119-136.

Inel, S., Roth, W.H., and Rubertis, C. (1993) "Nonlinear Dynamic Effective-Stress Analysis of Two Case Histories" *Proceedings* of the Third International Conference on Case Histories in Geotechnical Engineering, St. Louis, Missouri, June 1-4, Paper No. 14.14, pp. 1735-1741.

Itasca Consulting Group, Inc. (1998) *FLAC User's Manual*, Version 3.4, Itasca, Minneapolis, MN.

Ishihara, K. and Yoshimine, M. (1991) "Evaluation of Settlements in Sand Deposits Following Liquefaction during Earthquakes", *Soils and Foundations*, V. 32, pp. 173-188.

Ishihara, K., Yasuda, S., and Nagase, H. (1996) "Soil Characteristics and Ground Damage" *Soils and Foundations*, Special Issue on Geotechnical Aspects of the January 17 1995 Hyogoken-Nanbu Earthquake, Jan., pp. 109-118.

Johnson, R.K., Riffenburge, R., Hodali, R., Moriwaki, Y., and Tan, P. (1998) "Analysis and Design of A Container Terminal Wharf at the Port of Long Beach" *Ports '98*, Vol. One, pp. 436-444.

Kagawa, T. (1992) "Lateral Pile Response in Liquefying Sand" *Proceedings* of the Tenth World Conference on Earthquake Engineering, July 19-24, Spain, pp.1761-1766.

Lam, I. P. and Cheang, L. (1995) "Dynamic Soil-Pile Interaction Behavior in Submerged Sands" *Proceedings* of the Earthquake-Induced Movements and Seismic Remediation of Existing Foundations and Abutments, Geotechnical Special Publication No. 55, ASCE, pp. 110-135.

Liu, L. and Dobry, R. (1995) "Effects of Liquefaction on Lateral Response of Piles by Centrifuge Model Tests" *NCEER Bulletin*, SUNY-Buffalo, NY., pp. 7-11.

Mansur, C.I. and Hunter, A.H. (1970) "Pile Tests – Arkansas River Project" *Journal of Geotechnical Engineering*, ASCE, Vol. 96, No. SM5, paper 7509, September, pp. 1545-1582.

Martin, G.R., Dinn, W.D.L., and Seed, H.B. (1975) "Fundamentals of Liquefaction under Cyclic Loading" *Journal of Geotechnical Engineering*, ASCE, Vol. 101, No. GT5, pp. 423-438.

Martin, G.R., and Lam, I.P. (1995) "State of the Art Paper Seismic Design of Pile Foundations: Structural and Geotechnical Issues" *Proceedings* of Third International Conference on Recent Advances in Geotechnical Earthquake Engineering and Soil Dynamics, St. Louis, Missouri, April.

Matlock, H. and Reese, L.C. (1960) "Generalized Solutions for Laterally Loaded Piles" *Journal of Soil Mechanics and Foundation Division*, ASCE, Vol. 86, SM5, pp.63-91.

Matlock, H. Martin, G.R., Lam, I.P., and Tsai, C.F. (1981) "Soil-Pile Interaction in Liquefiable Cohesionless Soils during Earthquake Loading" *International Conference on Recent Advances in Geotechnical Earthquake Engineering and Soil Dynamics*, Vol. II, April 26-May 3, pp. 741-748.

Mayne, P.W. and Kulhawy, F.H. (1982) "Ko-OCR Relationships in Soil" *Journal of Geotechnical Engineering*, ASCE, 108 (6), pp.851-872.

Meyersohn, W.D., O'Rourke, T.D., and Miura, F. (1992) "Lateral Spread Effects on Reinforced Concrete Pile Foundations" *Proceedings* of the Fifth U.S.-Japan Workshop on Earthquake Disaster Prevention for Lifeline Systems, Tsukuba, Japan, Oct. 26-30.

Miura, F. and O'Rourke, T.D. (1991) "Nonlinear Analysis of Piles Subjected to Liquefaction-Induced Large Ground Deformation" *Technical Report NCEER-91-0001*, 3rd U.S.-Japan Workshop on Earthquake-Resistance Design of Lifeline Facilities and Countermeasures for Soil Liquefaction, NCEER, Buffalo, NY, February, pp. 497-512.

Miura, F., Stewart, H.E., and O'Rourke, T.D. (1991) "The effects of Liquefaction-Induced Lateral Spreading on Pile Foundations" *Journal of Soil Dynamics and Earthquake Engineering*, Vol. 10, No. 5, July, pp. 271-279.

Mononobe, N. and Matsuo, H. (1929) "On the Determination of Earth Pressures during Earthquakes" *Proceedings*, World Engineering Congress.

Mori, S., Ikeda, T., Takimoto, Y., Muto, M., and Tohaya, T. (1992) "Influence of Soil Liquefaction on Dynamic Response of Structure on Pile Foundations" Proceedings of the Tenth World Conference on Earthquake Engineering, July 19-24, Madrid, Spain, pp. 1777-1780.

Nadim, F. (1980) "Tilting and Sliding of Gravity Retaining Walls" *Master Thesis*, Department of Civil Engineering, Massachusetts Institute of Technology, Cambridge, Massachusetts.

Nadim, F. and Whitman, R. (1983) "Seismically Induced Movement of Retaining Walls" *Journal of Geotechnical Engineering*, Volume 109, No. 7, pp. 915-931.

Naesgaard, E. (1992) "Lateral Load Tests to Examine Large-Strain (Seismic) Behavior of Piles" *Canadian Geotechnical Journal*, Vol. 29, pp. 245-252.

Newmark, N.M. (1965) "Effects of Earthquakes on Dams and Embankments" *Geotechnique*, London, England, Vol. 15, No. 2, pp. 139-160.

Noda, S., Uwabe, T., and Chiba, T. (1975) "Relation between Seismic Coefficient and Ground Acceleration for Gravity Quaywall." *Report of the Port and Harbour Research Institute*. Vol 14, No 4. pp 67-111.

Nozu, A., Uwabe, T., Sato, Y. and Shinozawa, T. (1997a) "Relation Between Seismic Coefficient and Peak Ground Acceleration Estimated from Attenuation Relation." *Technical Note of the Port and Harbour Research Institute*. Ministry of Transport, Japan. (in print). (in Japanese).

Nozu, A., Uwabe, T., and Sano, T. (1997b) "Loss of Regional Economy at Kushiro Port due to Kushiro-Oki Earthquake in 1993" *Technical Note*, PHRI, Japan.

Ohtomo, K. and Hamada, M. (1994) "Soil force Acting on Pile in Laterally Flowing Ground by Soil Liquefaction" *Proceedings* of Fifth US national Conference on Earthquake Engineering, Vol., IV, July 10-14, pp. 241-250.

Okabe, S. (1926) "General Theory of Earth Pressures" *Journal of the Japan Society of Civil Engineering*, Vol. 12, No. 1.

O'Rourke T.D., Meyersohn, W.D., Shiba, and Chan (1994) "Evaluation of Pile Response to Liquefaction-induced Lateral Spread" *Technical Report NCEER-94-0026,* the Fifth U.S.-Japan Workshop on Earthquake Resistance Design of Lifeline Facilities and Countermeasures against Soil Liquefaction, November, pp. 457-479.

Port and Harbour Research Institute (1994) "Damage to Port Structures by the 1993 Kushiro-Oki Earthquake", *Technical Report* No. 766, PHRI, Ministry of Transport, Japan.

Port and Harbour Research Institute (1997) *Handbook on Liquefaction Remediation of Reclaimed Land*, A.A. Balkema Publishers, Brookfield, VT, 312 p.

Reese, L.C. (1990) *LPILE User's Manual*, Version 3.0, Austin, Texas.

Reese, L.C. and Wang, S.T. (1993) "Documentation of Computer Program LPILE Version 4.0", Ensoft, Inc., Austin, Texas.

Reese, L.C., and Cox, W.R. (1975) "Field Testing and Analysis of Laterally Loaded Piles in Stiff Clay" *Proceedings* of Offshore Technology Conference, Houston TX, OTC 2312.

Richards, R. and Elms, D. (1979) "Seismic Behavior of Gravity Retaining Walls", *Journal of Geotechnical Engineering*, ASCE, Vol. 105, No. GT4, pp449-464.

Roth, W.H., and Inel S. (1993) "An Engineering Approach to the Analysis of VELACS Centrifuge Tests" *Proceedings* of the International Conference on the Verification of Numerical Procedures for the Analysis of Soil Liquefaction Problems, Davis, CA, Oct. 17-20.

Seed, H.B., and Whitman, R.V. (1970) "Design of Earth Retaining Structures for Dynamic Loads" *Proceedings* of Specialty Conference on Lateral Stresses in the Ground and Design of Earth Retaining Structures, ASCE, Ithaca, New York, pp. 103-147.

Seed, H.B. and De Alba (1986) "Use of SPT and CPT Tests for Evaluating the Liquefaction Resistance of Soils" *Proceedings*, Insitu '86, ASCE.

Seed, R.B. and Harder, L.F. (1990) "SPT-based analysis of cyclic pore pressure generation and Undrained Residual Strength" *Proceedings* of H. Bolton Seed Memorial Symposium, University of California, Berkeley, Vol. 2, pp. 351-376.

Siddharthan, R., Ara, S., and Norris, G.M. (1992) "Simple Rigid Plastic Model for Seismic Tilting of Rigid Walls" *Journal of Structural Engineering*, ASCE, Vol. 118, No. 2, pp. 469-487.

Shibata, T., Oka, F., and Ozawa, Y. (1996) "Characteristics of Ground Deformation due to Liquefaction" *Soils and Foundations*, Special Issue on Geotechnical Aspects of the January 17 1995 Hyogoken-Nanbu Earthquake, Jan., pp. 65-79.

Stark, T. D., and Mesri, G. (1992) "Undrained Shear Strength of Liquefied Sands for Stability Analysis", *Journal of Geotechnical Engineering,* ASCE, Vol. 118, No. 11, pp. 1727-1747.

Stewart, D.P., Randolph, M.F., and Jewell, R.J. (1994) "Recent Development in the Design of Piles Loaded by Lateral Soil Movements" *Proceedings* of International Conference on Design and Construction of Deep Foundations, Vol. II, December, pp. 992-1006.

Stewart, H.E., Miura, F., and O'Rourke T.D. (1988) "Pile Damage due to Large Ground Displacement" *Proceedings* of 1st Japan-U.S. Workshop on Liquefaction, Large ground Deformation and Their Effects on Lifeline Facilities, November 16-19, Tokyo, Japan, pp. 173-182.

Toki, K. (1995) Committee of Earthquake Observation and research in the Kansai Area.

Tokida, K., Matsumoto, H., Towhata, I., and Sasaki, Y. (1992) "Study on Prediction of Lateral Ground Flow by Soil Liquefaction and Its Influence on Piles" Proceedings of the 24th joint Meeting Of Wind and Seismic Effects, pp. 271-284.

Tokimatsu, K., Mizuno, H., and Kakurai, M. (1996) "Building Damage Associated with Geotechnical Problems" *Soils and Foundations*, Special Issue on Geotechnical Aspects of the January 17 1995 Hyogoken-Nanbu Earthquake.

Wang, S., Kutter, B.L., Chacko, M.J., Wilson, D.W., Boulanger, R.W., and Abghari, A. (1998) "Nonlinear Seismic Soil-Pile Structure interaction" *Earthquake Spectra*, Vol. 14, No. 2, May, pp. 377-396.

Wang, S.-T. and Reese, L.C. (1998) "Design of Pile Foundations in Liquefied Soils" *Proceedings* of Specialty Conference, Geotechnical Special Publication No. 75, Geotechnical Earthquake Engineering and Soil Dynamics III, ASCE, Volume 2, August 3-6, pp.1331-1343.

Watanabe, K. (1981) "Development of Kobe Port Island and Foundations of Structures in the Island" *The Foundation Engineering and Equipment*, Vol. 9, No.1, pp. 83-91 (in Japanese).

Werner, S.D. and Hung S.J. (1982) "Seismic Response of Port and Harbor Facilities" *Report*, No. R-8122-5395, National Science Foundation Grant No. CEE8012337.

Werner, S.D. and Dickenson, S.E. (1995) "Hyogoken-Nanbu Earthquake of January 17, 1995: A Post-Earthquake Reconnaissance of Port Facilities" *Report* by the Committee of Ports and Harbors Lifelines of the Technical Council of Lifeline Earthquake Engineering (TCLEE), ASCE September.

Werner, S.D. (ed., 1998) "Seismic Guidelines for Ports" *Technical Council on Lifeline Earthquake Engineering Monograph No. 12*, ASCE, March.

Westergaard, H. (1931) "Water Pressure on Dams during Earthquakes" *Transactions of ASCE*, paper No. 1835, pp. 418-433.

Whitman, R.V. and Liao, S. (1985) "Seismic Design of Retaining Walls" *Misc. Paper GL-85-1*, U.S. Army Engineer Waterways Experiment Station, Vicksburg, Mississippi.

Wong, C. (1982) "Seismic Analysis and Improved Seismic Design Procedure for Gravity Retaining Walls" *Research Report 82-32*, Department of Civil Engineering, Massachusetts Institute of Technology, Cambridge, Massachusetts.

Yasuda, S., Ishihara, K., harada, K., and Shinkawa, N. (1996) "Effect of Soil Improvement on Ground Subsidence due to Liquefaction" *Soils and Foundations*, Special Issue on Geotechnical Aspects of the January 17 1995 Hyogoken-Nanbu Earthquake, Jan., pp. 99-107.

Yoshida, N. and Hamada, M. (1991) "Damage to Foundation Piles and Deformation Pattern of Ground due to Liquefaction-induced Permanent Ground Deformations" *Technical Report NCEER 91-0001*, the 3rd Japan-U.S. Workshop on Earthquake-Resistance Design of Lifeline Facilities and Countermeasures for Soil Liquefaction, NCEER, Buffalo, NY, February, pp. 147-161.

APPENDIX

COMPARISON OF THE PSEUDOSTATIC METHODS TO THE PARAMETRIC STUDY RESULTS OF CAISSON TYPE WALL

APPENDIX: COMPARISON OF THE PSEUDOSTATIC METHODS TO THE PARAMETRIC STUDY RESULTS OF CAISSON TYPE WALL

Introduction

In order to compare pseudostatic approaches to the parametric study results of caisson type wall, a caisson at Rokko Island (R6 Type) of Kobe Port, Japan, is used for comparison purpose. The calculations of caisson displacement for the cases of non-liquefiable backfill and liquefiable backfill based on both Richards-Elms method and Whitman-Liao method are presented.

Richards and Elms Method

No Excess Pore Pressure Consideration in the Backfill

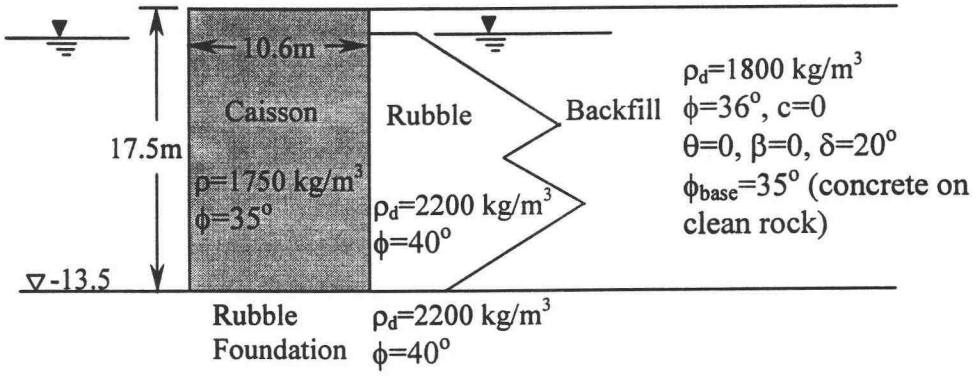

Soil and caisson profile at Rokko Island (R6 Type caisson)

Step 1: The weight of the caisson

$$W = 17.5 \times 10.6 \times 1750 \times 9.81 = \underline{3.2\times10^6}\ (\text{N/m})$$

Step 2: Trial of pseudostatic acceleration, k_h

Assume a trial pseudostatic acceleration of 0.2g and use Equation (2-2) and (2-3) to obtain total active thrust by Mononobe-Okabe method.

$$\psi = \tan^{-1}(k_h / 1\text{-}k_v) = \tan^{-1}(0.2 / 1\text{-}0) = \underline{11.3°}$$

M-O method:

$$K_{AE} = \frac{\cos^2(40-0-11.3)}{\cos 11.3\cos(20+11.3)\left[1+\sqrt{\frac{\sin(20+40)\sin(40-11.3)}{\cos(20+11.3)\cos(0-0)}}\right]^2} = \underline{0.32}$$

$$P_{AE} = \tfrac{1}{2}(0.32)(2000\times 9.81)\times 17.5^2 = \underline{9.6\times 10^5}\ (\text{N/m})$$

Step 3: Determination of yield acceleration, a_y

From Equation (2-18)

$$a_y = \left[\tan 35 + \frac{9.6\times 10^5 \sin 20 \tan 35 - 9.6\times 10^5 \cos 20}{3.2\times 10^6}\right] g = 0.49g > 0.2g(assumed)$$

Because the computed yield acceleration (0.49g) is inconsistent with the assumed pseudostatic acceleration (0.2g), another iteration is required.

Step 4: Another iteration of k_h

Try $k_h = 0.35$g

$\psi = \tan^{-1}(0.35) = \underline{19.3°}$

$K_{AE} = \underline{0.45}$

$P_{AE} = \tfrac{1}{2}(0.45)(2000 \times 9.81)(17.5)^2 = \underline{1.35\times 10^6}$ (N/m)

$a_y = 0.4\text{g} > 0.35\text{g}$ (assumed)

Based on Step 3 and Step 4, yield acceleration, a_y, is determined to be 0.37g.

Step 5: Determination of permanent displacement of caisson

Recorded ground acceleration, velocity, and displacement at Rokko Island are shown as follows.

Earthquake Information at Rokko Island

North-South Accel./Velocity/Displ. (gal/kine/cm)	*East-West Accel./Velocity/Displ. (gal/kine/cm)*	*Up-Down Accel./Velocity/Displ. (gal/kine/cm)*
340.6/81.6/34.3	284.2/47.3/26.9	555.6/54.2/21.9

a_y can then be calculated based on Equation (2-20).

$$d = 0.087\frac{81.6^2(340.6)^3}{(0.37\times 981)^4} = \underline{1.3cm} \text{ (N-S)} \tag{A-1}$$

$$d = 0.087\frac{47.3^2(284.2)^3}{(0.37\times 981)^4} = \underline{0.3cm} \text{ (E-W)} \tag{A-2}$$

$$d = 0.087\frac{54.2^2(555.6)^3}{(0.37\times 981)^4} = \underline{2.5cm} \text{ (U-D)} \tag{A-3}$$

Whitman-Liao Method

From Equation (2-22), the *mean* or *expected* value of permanent displacement is calculated by

$$\bar{d} = \frac{37(81.6)^2}{340.6}\exp\left(\frac{-9.4\times 0.37\times 981}{340.6}\right) = \underline{0.03cm} \text{ (N-S)}$$

$$\bar{d} = \frac{37(47.3)^2}{284.2}\exp\left(\frac{-9.4\times 0.37\times 981}{284.2}\right) = \underline{2\times 10^{-3}\,cm} \text{ (E-W)}$$

$$\bar{d} = \frac{37(54.2)^2}{555.6}\exp\left(\frac{-9.4\times 0.37\times 981}{555.6}\right) = \underline{0.42cm} \text{ (U-D)}$$

$$d_{llow} = 4\bar{d} = 4\times 0.03 = \underline{0.12cm} \text{ (N-S)} \tag{A-4}$$

$$d_{llow} = 4\bar{d} = 4\times 2\times 10^{-3} = \underline{8\times 10^{-3}\,cm} \text{ (E-W)} \tag{A-5}$$

$$d_{llow} = 4\bar{d} = 4\times 0.42 = \underline{1.68cm} \text{ (U-D)} \tag{A-6}$$

Excess Pore Pressure Consideration in the Backfill

If liquefaction effect is considered, both methods can be modified based on the procedures in Section 2.2.3.

Account for excess pore pressure in the backfill and assumed $r_u = 0.8$:

Step 1: The weight of the caisson

$$W = \underline{3.2\times10^6} \text{ (N/m)}$$

Step 2: Trial of pseudostatic acceleration, k_h

For the case of completely saturated backfill, soil thrusts may be calculated as follows.

$$\gamma_b = \rho_b g = \frac{G_s - 1}{G_s}\rho_d g = \frac{2.65-1}{2.65}(2000\times9.81) = \underline{12216} \text{ (N/m}^3\text{)}$$

Assuming that $k_h = 0.08$g, $r_u = 0.8$ and from Equation (2-11)

$$\psi = \tan^{-1}\left[\frac{\gamma_{sat}k_h}{\gamma_b(1-r_u)(1-k_v)}\right] = \tan^{-1}\left[\frac{(12216+9810)0.08}{12216(1-0.8)(1-0)}\right] = \underline{36^\circ}$$

$$K_{AE} = \frac{\cos^2(40-36)}{\cos 36\cos(20+36)\left[1+\sqrt{\dfrac{\sin(20+40)\sin(40-36)}{\cos(20+36)}}\right]^2} = \underline{1.25}$$

$$\gamma = \gamma_b(1-r_u) = 12216(1-0.8) = \underline{2443} \text{ (N/m}^3\text{)}$$

$$P_{AE} = \frac{1}{2}\gamma H^2(1-k_v)K_{AE} = \frac{1}{2}\times2443\times17.5^2\times1.26 = \underline{4.7\times10^5} \text{ (N/m)}$$

$$P_{ws} = \frac{1}{2}\gamma_{eq} H_w^2 = \frac{1}{2}(\gamma_w + r_u \gamma_b) H_w^2 = \frac{1}{2}(9810 + 0.8 \times 12216) 15.1^2 = \underline{2.23 \times 10^6} \text{ (N/m)}$$

$$P_{total} = P_{AE} + P_{ws} = 4.7 \times 10^5 + 2.23 \times 10^6 = \underline{2.7 \times 10^6} \text{ (N/m)}$$

Step 3: Determination of yield acceleration, a_y

$$a_y = \left[\tan 35 + \frac{2.7 \times 10^6 \sin 20 \tan 35 - 2.7 \times 10^6 \cos 20}{3.2 \times 10^6} \right] g = 0.11g > 0.08g \text{ (assumed)}$$

Choose a_y = 0.1g.

Step 4: Determination of permanent displacement of caisson

Richards-Elms Method

$$d = 0.087 \frac{81.6^2 (340.6)^3}{(0.1 \times 981)^4} = \underline{247cm} \text{ (N-S)} \quad \text{(A-7)}$$

$$d = 0.087 \frac{47.3^2 (284.2)^3}{(0.1 \times 981)^4} = \underline{48cm} \text{ (E-W)} \quad \text{(A-8)}$$

$$d = 0.087 \frac{54.2^2 (555.6)^3}{(0.1 \times 981)^4} = \underline{473cm} \text{ (U-D)} \quad \text{(A-9)}$$

Whitman-Liao Method

$$\bar{d} = \frac{37(81.6)^2}{340.6} \exp\left(\frac{-9.4 \times 0.1 \times 981}{340.6} \right) = \underline{48cm} \text{ (N-S)}$$

$$\bar{d} = \frac{37(47.3)^2}{284.2} \exp\left(\frac{-9.4 \times 0.1 \times 981}{284.2} \right) = \underline{11cm} \text{ (E-W)}$$

$$\bar{d} = \frac{37(54.2)^2}{555.6} \exp\left(\frac{-9.4 \times 0.1 \times 981}{555.6} \right) = \underline{37cm} \text{ (U-D)}$$

$$d_{allow} = 4\bar{d} = 4 \times 48 = \underline{192cm} \text{ (N-S)} \quad \text{(A-10)}$$

$$d_{allow} = 4\bar{d} = 4 \times 11 = \underline{44cm} \text{ (E-W)} \quad \text{(A-11)}$$

$$d_{allow} = 4\bar{d} = 4 \times 37 = \underline{148cm} \text{ (U-D)} \quad \text{(A-12)}$$